"Synthesis, Binding Studies and Click Modification of Diazido Acridine Intercalators: A Versatile Two-Step Approach to Functional Nanomaterials"

Shahrbanou Moradpour Hafshejani

Doctor of Philosophy

School of Chemistry

October 2013

Abstract

Two diazido acridine drivatives, N,N'-(acridine-3,6-diyl)bis(2-azidoacetamide), **PD** and 3,6-bis(2-azidoacetamido)-10-methylacridin-10-ium, **PDMe**$^+$ were prepared from 3,6-diamino acridine, **Pf**. The azide groups were exploited by click chemistry to synthesise functional intercalators by reaction with the alkyne-bearing groups, ethynyl ferrocene **EFc**, phenylacetylene, N-pentynyl-2-(2-thienyl)-pyrrole **pent-TP** and acetylene-PEG4-carboxyrhodamine, **APCR**. The click reaction products were characterised by ^{1}H NMR spectroscopy, ^{13}C NMR spectroscopy, ES-MS, IR and, where appropriate, cyclic voltammetry. IR studies showed the disappearance of the azide and alkynyl stretching signals at 2114 cm^{-1} and 2112 cm^{-1} respectively after the click reaction. Cyclic voltammetry revealed that the click product with **EFc** was redox active, E = 346 mV compared to 441 m V for the free **EFc**, a negative shift due to the electron donating effect of the triazole ring.

Intercalation of **PD** and **PDMe**$^+$ into DNA, were studied by UV/vis, fluorescence, circular dichroism (CD), linear dichroism (LD) and DNA denaturation experiments. The titration of **Pf** and **PDMe**$^+$ with DNA showed bathocromic and hypochromic effects in the absorption spectra. However, for **PD** an interesting phenomenon, a bathochromic and hyperchromic effect was observed. The pKa of **PD** (4.3) suggests that as **PD** approaches DNA it becomes protonated due to the low local pH and so aids binding to DNA. Both UV and fluorescence titrations gave DNA binding constants for **Pf**, **PD** and **PDMe**$^+$ of $\geq 3.8 \times 10^6$, 5.3×10^5 and 2×10^6 respectively. These findings were consistent with the observed increasing stabilisation of the double helix by the intercalators, **PD** < **PDMe**$^+$ < **Pf.**

DNA complexes of **PD** and **PDMe**$^+$ were click modified with **EFc**, **pent-TP** and **APCR** and characterised by ES-MS, UV/vis, IR, fluorescence microscopy, LD, atomic and electrostatic force microscopy (AFM and EFM), and cyclic voltammetry. As for the free reaction, cyclic voltammetry, IR and UV/vis spectroscopy confirmed the successful click reaction of the DNA complexes, but could not confirm **PD** or **PDMe**$^+$ remained intercalated after click modification. AFM studies confirmed DNA retained its natural wire-like topology after intercalation and click functionalization. Fluorescence microscopy images of DNA complexes with **PD** and **PDMe**$^+$ that had been click modified with **APCR** showed illuminated strands 17 μm in length, comparing well with the dimensions of λ-DNA. LD experiments indicated that **PDMe**$^+$ reamains inserted into the DNA helix after the click reaction was performed *in-situ* using **pent-TP**.

Acknowledgments

List of Abbreviations and Symbols

Å	Angstrom
AFM	atomic force microscopy
c-AFM	conducting atomic force microscopy
CT-DNA	calf thymus DNA
DC	direct current
	diameter
DMF	dimethylformamide
DNA	Deoxyribonucleic acid
eV	electron volt
EFM	electrostatic force microscopy
	ferric chloride
E_{Km}	kinetic energy
E_B	binding energy
FTIR	Fourier transmission infrared
FWHM	full-width-at-half-maximum
f_0	resonance frequency
$\emptyset$	conductance
HOMO	highest occupied molecular orbital
HOPG	highly oriented pyrolytic graphite
h°	Photon energy
HL-60	Human promyelocytic leukemia cells
i-V	current-voltage
IC	Integrated Circuit
K	Kelvin
IPA	isopropanol
l	Length
LUMO	lowest unoccupied molecular rbital
Min	minutes
mM	milli molar
nm	nanometre
n	integer number
pA	pico amperes
Pin	polyIndole
Py	pyrrole
PPy	polypyrrole
PR	photoresist
QCM	quartz crystal microbalance
RT	room temperature
s	second
SCM	scanning capacitance microscopy
SPM	scanning probe microscopy
XPS	X-ray photoelectron spectroscopy
μm	micrometre
λ-DNA	Lambda DNA from bacteriophage
θ	reflection angle (theta)
λ	wavelength
UV	ultraviolet
R	resistance
ρ	resistivity

S	Siemens (conductance unit)
σ	conductivity
VRH	variable-range hopping
UV-Vis	ultraviolet-visible
Ω	ohm (resistance unit)
TP	thiophenyl pyrrole
XRD	x-ray diffraction
CD	circular dichroism
LD	linear dichroism
P/D	nucleotide phosphate/ dye ratio
Pf	proflavine
PD	N,N'-(acridine-3,6-diyl)bis(2-azidoacetamide)
PDMe$^+$	3,6-bis(2-azidoacetamido)-10-methylacridin-10-ium
CT-DNA	calf thymus DNA
[poly(dA-dT)]$_2$	poly(deoxyadenylic-thymidylic) acid
[poly(dG-dC)]$_2$	poly(deoxyguanylic-cytidylic) acid
EFc	ethynyl ferrocene
Pent-TP	N-pentynyl-2-(2-thienyl)-pyrrole
APCR	acetylene-PEG4-carboxyrhodamine

Table of Contents

Chapter 1 – *Introduction*

Chapter 1- Introduction

1. Introduction

The last decade has seen a dramatic growth in the efforts to form new nanoscale materials with individual and exquisite properties using biomolecules such as DNA.[1] These new materials rely on the self-recognising and self-organising properties inherent to biology.[1-5] Building blocks constructed on the nanoscale exhibit new properties relative to bulk materials on the macroscopic scale.[6, 7] The new properties of nanomaterials result from the limitation of electron motion on movement to the nanoscale dimension because of the effects of quantum confinement.[8] These properties can be exploited to design and create new devices. Research on the quantum effect has been highlighted as a key area of future research in nanoscience and nanotechnology.[9] Nanobiotechnology is the interface between nanotechnology and biology and has applications in a vast number of fields. One key goal of nanotechnology is the development of miniaturized structures with the generation of predicted patterns and shapes with feature sizes up to 100 nm.[10]

Biological systems already build their structural components on the nanoscale. In addition, biological nanostructures such as proteins and nucleic acids possess the key ability to recognize molecules leading to self-assembly and the scaffolding of atoms and molecules into larger structures. DNA is a readily available biopolymer and is perhaps the best candidate as a template or scaffold for nanofabrication. The self-assembly of two complementary DNA strands into the double helix and their exploitation to form nanostructures according to programmable patterns make it an ideal tool for the nanobiotechnologist.[11-14]

In this thesis a novel approach is employed to integrate nanomaterial with DNA. The two processes involved are intra-base pair intercalation and the Cu catalysed click coupling reaction. These methods enable modification of the DNA structure without any molecular changes to the nucleobases or disruption to the base-pairing interactions.

Therefore, this chapter reviews the current state-of-the-art in the formation of nanomaterials with a particular emphasis on the fabrication of 1-D nanowires and the role of DNA as a template and scaffold to form nanomaterials. Finally, the project goals and the contents of the proceeding chapters are outlined.

1.1 Nanomaterials

In nanomaterial fabrication, the bottom-up approach applies single molecules to assemble in a supramolecular fashion of high order. Nanomaterials are dimensionally divided into three types that have at least one dimension between 1-100 nm. Nanomaterials that possess zero dimensions include quantum dots and nanoparticles.[15, 16] Nanoparticles exhibit beneficial properties as a result of their small size and high surface area to volume ratio. Therefore, these nanomaterials are ideal and important for diffusing in or out of cells for drug delivery and imaging applications.[16]

However, the control of material growth along a single dimension is a feature that is essential to this project to produce a uniform wire-like structure. However, this is not an easy challenge and considerably more difficult than the fabrication of either 0-D or 2-D nanomaterials.
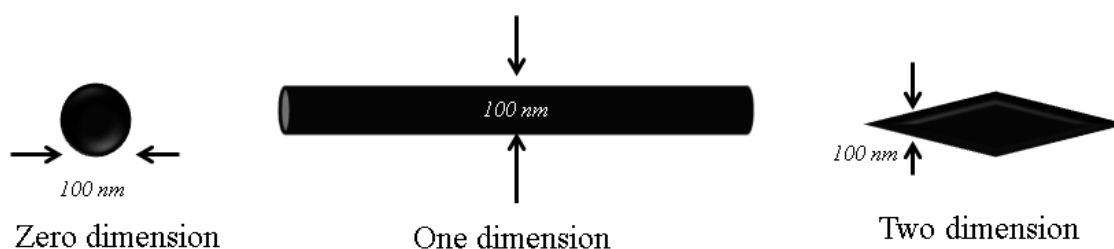
Figure 1. Illustration of 0D, 1D and 2D nanomaterials.

The conductivity of bulk materials has been widely investigated. 2D nanostructures such as films exhibited high conductivity as noted extensively in the literature.[17] On the other hand, and similar to the case of nanoparticles, there are still difficulties in the control of the direction of electron flow across a 2-D film.

Recent findings indicate that 1D organic structures show conductivities which are higher than 2D materials due to the channelling of this electron flow down a wire-like structure.[18] A variety of examples have shown that the properties of nanomaterials such as electrical and thermal features change with switching to lower dimensions. Researchers are now discovering how the properties of one dimensional materials vary during the synthesis process.[19]

Semiconductor materials for example π-conjugated organic polymers have been used as nanowires and their conductivities are controllable and tunable via doping in

experienced challenges.[20] The semiconductor nanowire research has seen considerable growth since the 1990's.[21, 22]

Semiconductor nanowires are similar to rod-like semiconductor material structures with height scale less than 100-200 nm. Recently, nanowires have been obtained with smaller size with diameters of 5 nm.[23]

One-dimensional nanowires have been grown by a variety of methods, for instance metals can be arranged as seed to grow nanowires.[24] The type of metal ions determines the diameter size of the wire.[25] Nanowires have provided an opportunity for miniaturising electronics. The control of the size, length, position and direction is vital for nanowires. A large number of nanowires can be aligned and will permit for a denser packing of wires onto a chip, hence increasing the transistor density and becoming a more powerful computational resource.

The construction of nanowires can be divided into the synthesis of organic and inorganic based systems. These two research areas are discussed in the following sections.

1.1.1   Inorganic 1-D nanomaterials

An early report on the construction of semiconductor 1-D inorganic material was presented by Tenne *et al*. by forming nanotubes of WS_2 in 1992.[26] The natural needle-like structures of transition metal oxide crystals such as MoO_x and WO_x can act as a template to aid the longitudinal growth of the nanotubes upon sulfurization with H_2S. The constructed nanotubes indicate a layer structure which can result in both amorphous and polycrystalline tubes.[26]

Consequently, a number of chalcogenide nanotubes have been synthesised in the same way, such as CdS, CdSe and ZnS.[27, 28] Goldberger *et al*. constructed monocrystalline nanotubes from GaN which was synthesised by epitaxial growth on ZnO nanowires .[24]

ZnO having dimensions of 2-5 µm in length and 30-200 nm in diameter was used as a templating material, see Figure 2a. The deposition of GaN on the template was performed through adding trimethylgallium and ammonia using chemical vapour deposition techniques at 600-700 $^{\circ}$C. Finally, the template was eliminated by treating with 10% H_2 in argon at 600 $^{\circ}$C and the single crystal GaN nanotube appeared as an uniform array with inner dimensions of a 30-200 nm diameter and a wall thickness of

5-50 nm, see Figure 2b. This technique was also used by Hu *et al*. to produce single crystal Si nanotubes.[29]

While the above example demonstrated how to produce nanotubes possessing semiconductor properties the technique needs considerable energy which can not be economically viable.
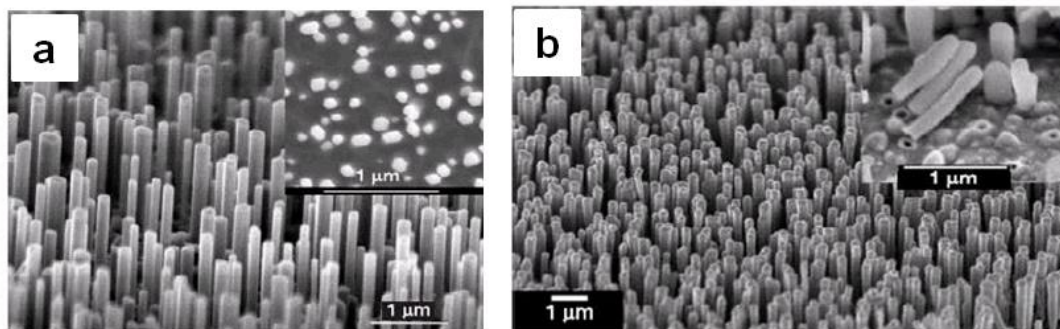
Figure 2. (a) SEM of ZnO precursor template and (b) SEM of GaN nanotubes array with ZnO template removed.[24]

There are several restrictions on the production of inorganic nanotubes. Firstly, the difficulties of the controlling their dimensions and structural morphology and secondly, purification techniques.[30, 31] As a result achieving the generation of inorganic nanotubes can be challenging.

1.1.2 Organic 1-D nanomaterials

Organic semiconductor materials can be modified through chemical modification or doping to access higher conductivities.[32] In 1991 carbon nanotubes were found by Iijima. Carbon nanotubes are a kind of 1D organic materials and are good conductors. In those nanotubes, carbon atoms have hexagonal forms and have needle-like and helical structures similar to fullerenes. They indicate outstanding conductivity measurements, owing to their 1D structure electrons can proceed without scattering along the length of the tube and as a result the currents are high.[33] However, the growth of carbon nanotubes and their structure are not easily controlled.

Carbon nanotubes are divided into two categories, single wall nanotubes (SWNT) or multi-walled nanotubes (MWNT). Single-walled nanotubes are formed by wrapping a one atom thick layer of graphite and consequently conductivities are similar to semiconductor and metallic behaviour. Chemical modification can be harmful for the nanotube conductive attributes as it breaks the C=C bonds and results in a decrease in conductivity.

MWNT comprise multi layers of graphite folded into a tube. MWNT compared to SWNT are more resistant to changes in their properties after chemical modification.[34] In addition, while semiconductor materials can be adjusted to regulate the band gap through doping, carbon nanotubes do not have this feature. As a result, semiconducting nanowires are often more preferable than carbon nanotubes for electronic applications.

Xiao and co-workers synthesised organic nanowires from a single crystalline nanostructure. Hexabenzocornene (HBC) is a planar polycyclic aromatic compound which forms nanofibres by overlapping $\pi-\pi$ interaction in a self-organising process (Figure 3).[35]
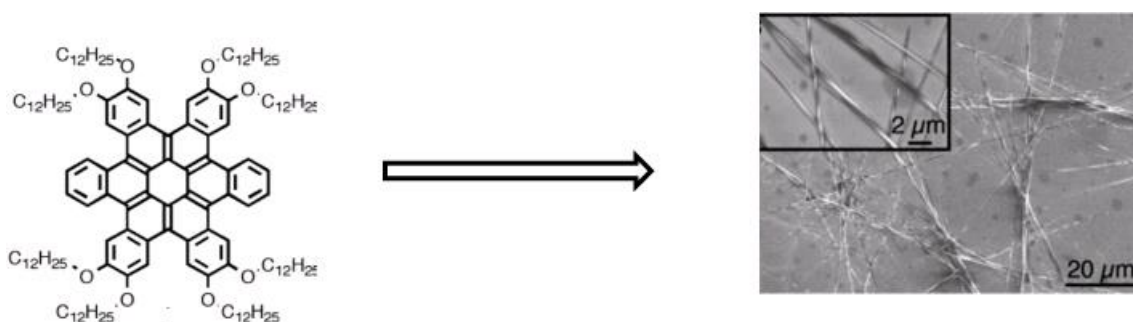
Figure 3. The structure of octa-substituted HBC and an SEM image of the self-organised nanofibres of HBC[35]

The self-assembly of The HBC molecules in the direction of the $\pi-\pi$ stacking leads to 1-D structures. The formation of organic crystalline wires in just one direction is a challenge that is only met by large pre-designed molecules such as HBC. Carrier mobility examinations illustrated that the large range and diverse morphologies of the fibres, emphasised the fact that achieving the generation of single crystalline nanostructures with uniform properties can be challenging.

Organic π-conducting polymers have increasingly been investigated as films and coatings and are popular substrates due to their ease of modification compared to inorganic materials. The preparation of single 1-D nanowires from bulk-conducting polymers is however difficult due to the uncontrollable growth of conducting polymers, usually not in only one direction.

If the growth of polymers can be regulated to give 1-D forms, i.e. nanowires, these can be aligned on surfaces for possible electronic purposes. Therefore, to achieve this target, DNA, as a biopolymer is a suitable candidate as a nanofabrication template due to its nanoscale diameter ~2 nm and wire-like structure.[36-38] In addition, the length and

sequence of DNA can be used to control the templating and so be exploited for nanomaterial designs.[39, 40]

1.2 DNA as a tool for 1-D nanomaterial fabrication

DNA is an outstanding molecule to fabricate nanoscale functional materials due to its specific structure. The DNA double helix comprises of two single strands that compose of a set of nucleotides linked via phosphodiester bonds to give the DNA backbone.[39, 41-43]

Each nucleotide consists of one of the purine (guanine, adenine) or pyrimidine (cytosine, thymine) bases, one sugar ring and a phosphate group. According to Watson and Crick base pairing,[44] the association of adenine to thymine and cytosine to guanine via two and three hydrogen bonds respectively builds the double helix DNA as shown in Figure 4. The spacing between nucleotides is approximately 0.34 nm with a duplex diameter of ~2 nm.[45] DNA can exist in diverse lengths between both the nanoscale and microscale due to it's polymeric nature. Several kinds of DNA with different lengths are commercially accessible such as Calf Thymus (CT), 3 µm and Lambda (λ), 17 µm.[46] On the other hand, long DNA duplexes of many microns in length can be constructed by enzymatic extensions of DNA oligomers.[47, 48]
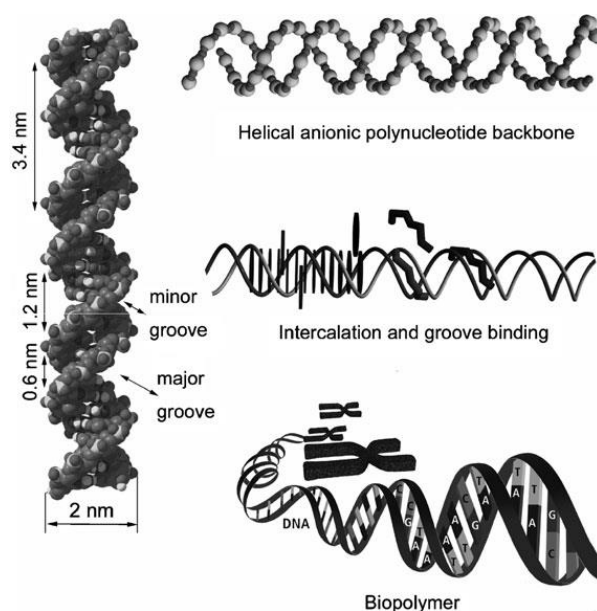
Figure 4: Basic features of naturalDNA.[49]

DNA has been recognized as an insulator despite a huge interest in it's possible conductivity. [50, 51] Therefore, DNA itself cannot be used for electronic purposes. On the other hand, DNA contains different functional groups and features such as self-

organising and self-assembling which can be modified to form materials which are applicable in electronic or biosensing devices.

The self-assembly and genetic coding properties of DNA serve as tools in the nanofabrication of DNA-based higher ordered supramolecular structures. The chemical and structural approaches that have been reported to generate DNA-hybrid architectures are illustrated in the following sections.

1.2.1 DNA nanostructures

During the last three decades, various methods have been used to fabricate DNA nanostructures, for example Seeman *et.al* exploited branched DNA molecules with sticky ends to form cube- like molecular complexes (Figure5).[36, 52]
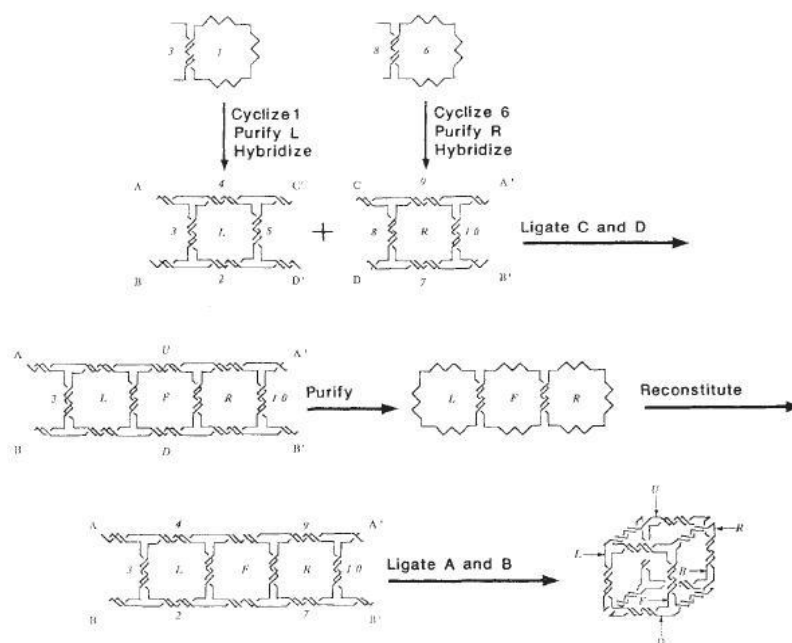
Figure 5 Synthetic scheme of to form a cube –like DNA molecule.[52]

DNA molecules are covalently ligated with help from their complementary sticky ends and form interconnected rings to construct the cube. Every face of the cube comprises of a circle of DNA molecules joined to four neighbour strands along the edges. The edges of the cube are made up of identical lengths of double helical DNA and vertices act as branched junction points.

Winfree *et.al* demonstrated how to construct two dimentional DNA crystals using antiparallel DNA double-crossover (DX) motifs. DNA DX molecules consist of two side by side double helixes joined to each other by two adjacent crossover junctions, see figure 6.[10, 53, 54]

Figure 6 Design of DX molecular structure and arrangement into 2-D lattices[54]

Niemeyer.*et.al* indicated another approach to assemble nanostructures with the use of bisbiotinylated DNA and the biotin-binding protein streptavidin (STV) to construct supramolecular DNA-STV nanocircles.[55] The STV despite having four binding capacities in the reaction with bisbiotinylated DNA exploits only two or three valances which results in linear and two dimentional DNA-STV supramolecular assemblies. The thermal denaturation of these oligomers generates supramolecular DNA nanocircles and linear DNA-STV molecules as the two principal products. The initial concentration of DNA-STV oligomers and the cooling rate after thermal denaturation process change the yield of these products, see Figure 7.

Figure 7 Synthesis of supramolecular DNA-streptavidin nanocircles (4 a-g)[55]

Rothemund demonstrated a novel strategy to construct nanostructures called DNA origami.[56] In DNA origami a long-single strand of DNA is folded with the aid of staple short-single strands of DNA to form 2-D/3-D shapes. This procedure is carried out programmatically and the desired shapes are designed through computer aided modeling. The creation of addressable positions on the scaffold is a considerable feature of DNA origami and helps progress the need for accurate nanoscale material modification, see Figure 8.
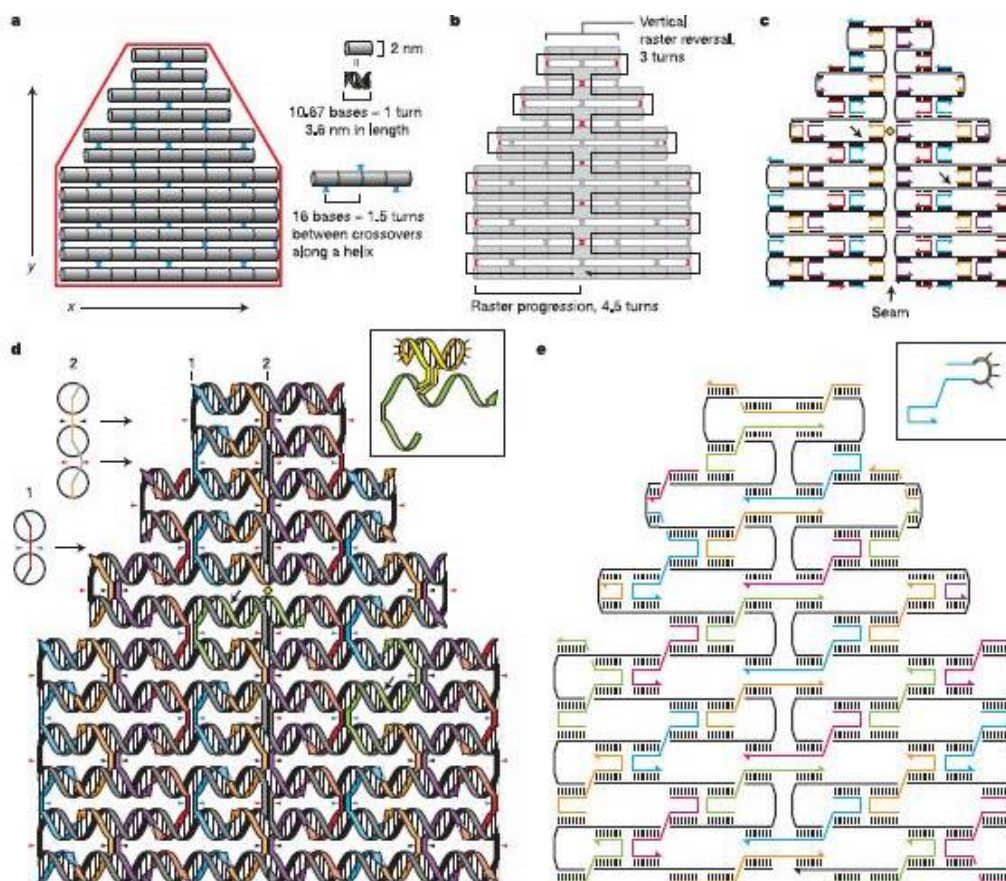
Figure 8 Design of DNA origami.[56]

1.2.2 DNA as a template

DNA templating is one of the two common approaches to incorporate nanomaterials along the DNA helix. In this manner, DNA acts as a guide to grow materials along the duplex of DNA. Therefore, the nanomaterial structures templated on DNA possess the topology similar to the underlying DNA, see Figure 9.
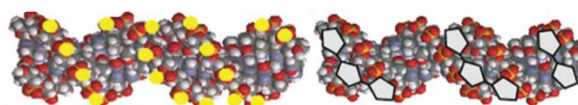
Figure 9. Schematic representation of DNA-hybrid material utilizing the DNA duplex as a template of metal ions (left side) and organic polymers (right side).

The backbone of DNA comprises of phosphate groups with one negative charge per base. Therefore, DNA can be employed as a polyanion to which metal ions and polycationic groups can electrostatically bind. This approach known as DNA templating and can be used to enhance the electrical conductivity of DNA.[57, 58] Investigations into DNA templating show that the specific binding sites on DNA are used to assemble metal ions or conducting polymers which bear positive charges. The length of the

templated material is determined from the length of the DNA and the final dimensions are somewhat larger than the bare-DNA template.

1.2.2.1 DNA templated metals

Metallisation of DNA can take place either electrostatically or via coordination chemistry. DNA can template metals by electrostatic interaction between positively charges on metal ions and the negative charges of the DNA phosphate backbone. The earliest conductive metallic DNA-templated nanowires were reported by *Braun.*[59] He constructed silver DNA nanowires via depositing silver ions onto DNA immobilised between two gold electrodes.[59] In this work short oligonucleotides containing sticky ends joined two gold electrodes via interaction of thiol-gold interactions at both 3' ends. A bridge between the electrodes was formed from a piece of complementatry λ–DNA and silver ions were deposited along the DNA bridge via ion exchange. Subsequently the reduction of the silver-DNA complex resulted in a conductive DNA-metallic nanostructure.

Despite the simplicity of this method, the lack of control over the growth of the silver/DNA hybrid nanowires creates non-uniform material as seen in Figure 10a. The lack of uniformity along the wires denoted a lower conductivity compared to crystalline silver.[59] Therefore attempts to improve the quality and conductance of nanowires containing metals such as gold, silver, palladium, platinum and copper have been fabricated.[45, 60, 61]

Palladium templated onto DNA was reported by Richter. DNA was first activated by Pd acetate, followed by reduction to Pd nanoclusters and finally absorption as Pd-DNA onto a grid surface covered with carbon for analysis.[45] Some long DNA structures were seen, up to 5 μm in solution, but they tended to form loops. Therefore, this deviation from the natural linear geometry of the DNA helix creates less wire-like structures. Moreover, when metallic DNA grows to diameters of 20-40 nm it begins to bend from the native structure of DNA and consequently breaks the DNA strands. As a result, it was identified that DNA could be used to deposit and immobilise growing metal clusters with a diameter of 3-5 nm. On the other hand, larger Pd clusters can aggregate up to 40 nm over longer periods, see Figure 10b.

Mertig *et al* synthesised smaller diameters of invariable Pt nanowires of just a few nanometers in diameter, see Figure 10c.[61] Initially Pt(II)-DNA complexes act as nucleation sites on DNA and in further steps the reduction of Pt(II) to Pt constructs nanoclusters of platinum metal. Pt^{2+} coordinates to guanine at the N7 position, within

several minutes. This method indicates the possibility for site directed binding of Pt by DNA. The size of nanoclusters is can be controlled by adjusting the activation time.

Woolley and co-workers originally investigated copper templated onto DNA, see Figure 10d.[60] The templating was carried out in several steps. Firstly a silicon wafer surface was treated by poly-L-lysine to produce a polycationic surface for loading polyanionic DNA and secondly it was treated with $Cu(NO_3)_2$ to bind Cu^{2+} ions electrostatically along the negative DNA backbone. Finally, the reduction of Cu^{2+} to metallic copper is performed using ascorbic acid. There were several problems as the copper coverage along the DNA was not uniform and some DNA segments existed without any copper coverage at all. Furthermore, the reduction of Cu^{2+} ions to Cu^0 was not easy to control and consequently the metallised DNA did not show any conductivity.
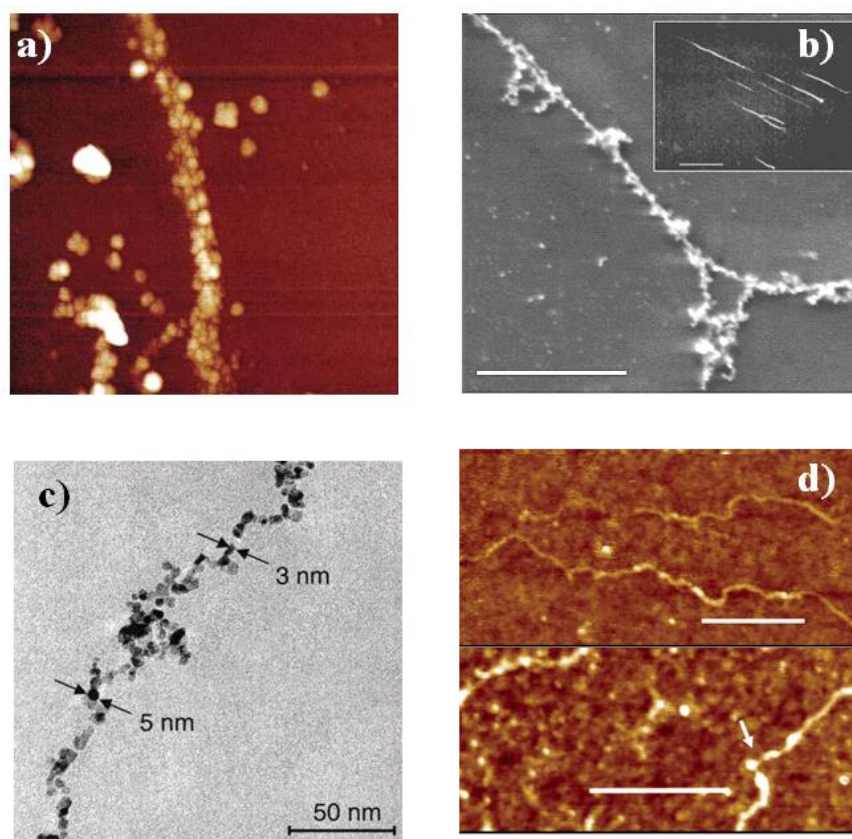
Figure 10. a) AFM image of silver template DNA produced by Braun et al. exhibited a diameter of 100 nm and length of 15 μm[59] b) SEM image of Pd-metalized-DNA , scale bar = 1 μm 40 nm thick on a glass surface (with fluorescence inset)[45] c) TEM image of Pt nanoparticles grown on a single molecule of DNA[61]d) 3D AFM image of DNA deposited on silicon (top) and DNA treated twice with Cu^{2+} and ascorbic acid (bottom).[60]

The difficulties to produce uniform metallic nanowires via templating metal onto DNA by weak electrostatic interactions between the positive metal ions and the negative DNA backbone are highlighted in Figure 10a, 10b and 10c. Therefore, to eliminate the

aforementioned problems a second method is required to produce metallic nanowires which are reproducible and can be applied in electronics.

A second route to the metallisation of DNA can occur via coordination chemistry. Lee and co-workers[62] presented the fabrication of metallic DNA complexes via the coordination of divalent metal ions such as (Zn^{2+}, Co^{2+}, Ni^{2+}) with DNA. Although those transition metals increase the DNA conductivity, the DNA structure and its stability would change due to interference with the hydrogen binding between base pairs.

Controlling the precise locations along the DNA of metal ions was introduced by Shinonoya.[63] He synthesised oligonucleotides with metal-mediated base pairs where metal-coordination sites took the place of hydrogen binding sites, see Figure 11.
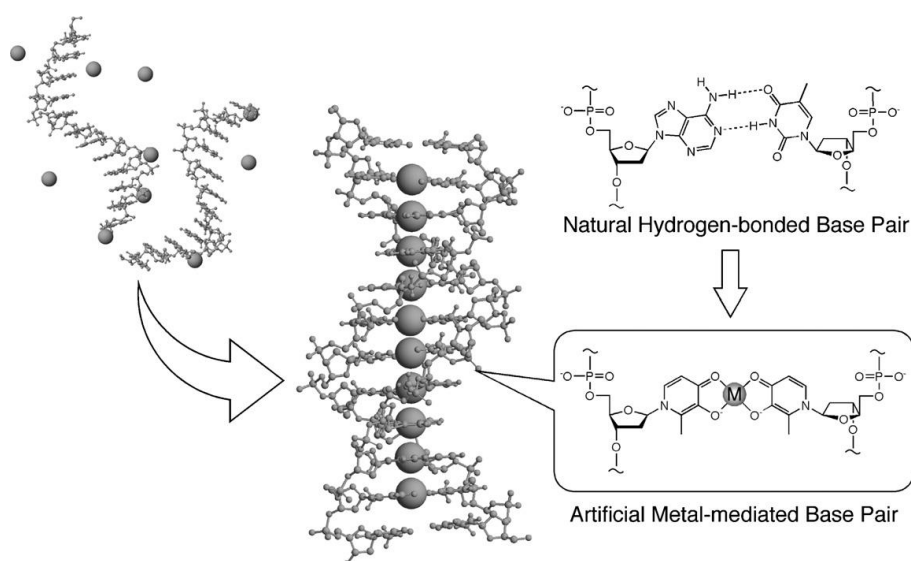
Figure 11. An example of an artificial metal-mediated base pair produced by Shinonoya *et al* where the bases have been replaced by more coordination bonds. [63]

This method was feasible for the coordination of Pd^{2+} ions between two artificial base pairs prepared by the covalent binding of an amine ligand to the ribose instead of a native DNA nucleoside.

In another example, the coordination of two different transition metals into DNA was presented. Cu (II) ions were coordinated between two hydroxy pyridone units of adjacent strands to form a planar "base pair", while two pyridyl units simultaneously formed a complex with a Hg (II) ion, [63] see Figure 12.
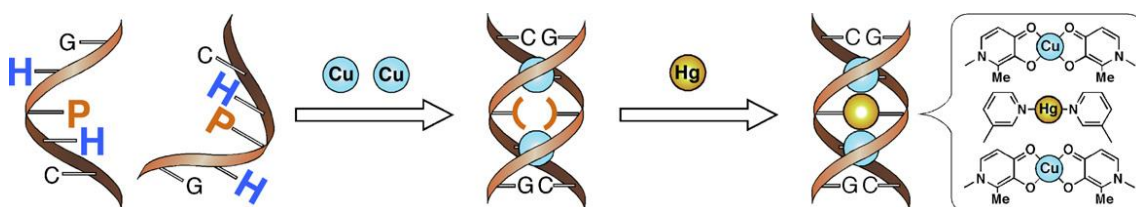
Figure 12. An example of an artificial metal-mediated base pair, H and P represent hydroxyl pyridone and pyridyl units respectively. [63]

While metallo-DNA exhibit higher conductivity, there are several restrictions with DNA metalisation. Firstly, disruption of the initial DNA structure and deviation from the native configuration of DNA and secondly, the difficulty for further modification of the metallic-DNA/hybrid material. In contrast to metallic nanowire fabrication, further modification of an organic polymer DNA/hybrid system may be more attractive to add more functionality through established organic synthetic reactions.

1.2.2.2 DNA templated organic material

Organic polymers are often conducting organic polymers as polycationic and can electrostatically template with the polyanionic backbone of DNA, in a similar way to the metal ions discussed in an earlier section. The oxidation of monomers such as pyrrole, thiophene and aniline during polymerisation forms a range of polycataionic oligomers and polymers. The polymer conductivity is chemically tunable via doping and this is a benefit of using such polymers.[64]

In contrast to metal ions, organic polymers after binding electrostatically with the DNA backbone can be designed to allow for further modification.[65] In addition, organic polymers templated onto DNA tend to form more uniform nanowires due to their flexibility. The metallic beads-on-a-string structures seen in Figure 13a is due to the lack of contact between adjacent nanoparticles.[18, 59]
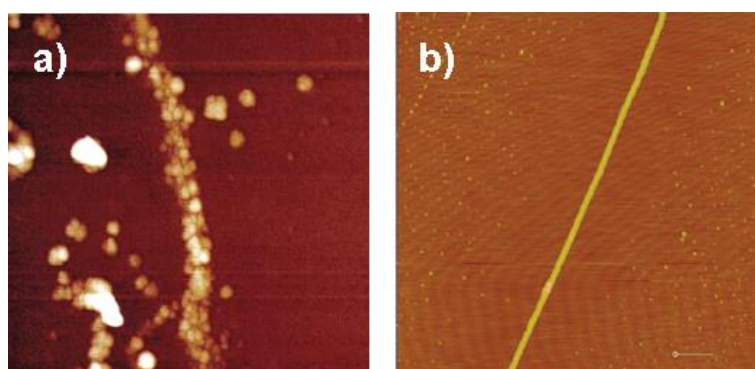
Figure 13. Comparison of a) silver-DNA hybrid nanowire with the appearance of "beads-on-a-string" and b) conductive polyindole nanowire templated onto DNA (scale bar 1 μm). [18, 54]

Polyindole templated on DNA is an example of an organic polymer templated onto DNA and exhibited conductivities between 2.5–40 Scm^{-1}, which are higher than the bulk conductivities of polyindole.[18] The conductivity of bulk films of polyindole has been reported as 10^{-2} and 10^{-1}Scm^{-1}. As a result, the higher conductivity of DNA template with polyindole results from the polymer growth in 1-D allowing for the controlled direction of electron flow. [18]

Other examples of DNA templating use polymers such as polypyrrole[66, 67] and polyaniline. [68, 69] Coating the surface of DNA strands with polyaniline provides a route to controllable electrical conductivity. The construction of polyaniline nanowires were achieved during the following steps. In the first step, DNA templates are added to a solution of aniline monomers. Then, the protonated aniline monomers align along the DNA strand via electrostatic interactions with the negatively charged phosphate backbone. In the next step free aniline monomers are washed away and subsequently the polymerization of aniline monomers along the DNA strand is achieved by using horseradish peroxidise, see Figure 14.[68-70]
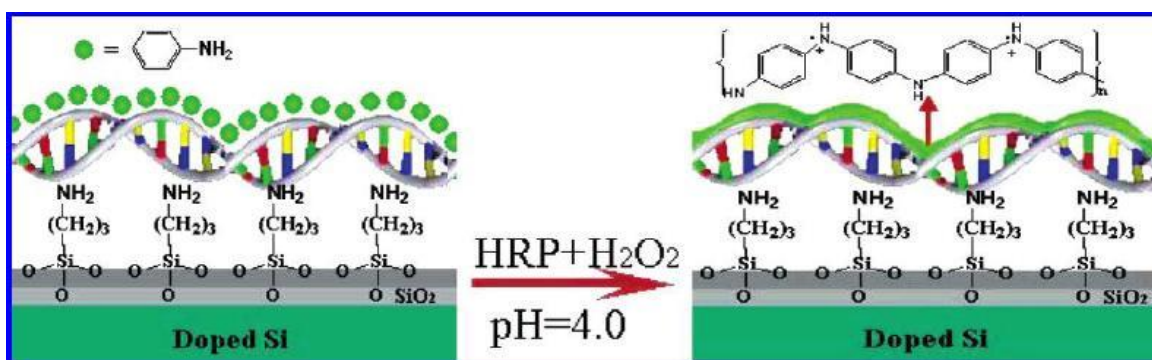
Figure 14 Fabrication of a polyaniline nanowire immobilized on a si surface[70]

Polyaniline compared to polyindole has a conductivity of 40×10^{-7} S. cm^{-1}, lower than polyindole. The lower conductivity of polyaniline is explainable due to the lack of continuity and uniformity along the polyaniline wire. The continuity of these polyaniline wires was improved via controlling the pH. At the optimum pH of 4.0 uniform nanowires were observed. On the other hand, low pH can initiate denaturation of DNA duplex,[70] an as a result, polyaniline is not an appropriate conductive polymer if the DNA structure is to be retained.

Houlton *et al* paid considerable attention to form DNA nanowires from the conductive polymers, polypyrrole.[66, 67] Under oxidative polymerization, polypyrrole-cationic polymers are formed and can electrostatically bind to the negative charge along the

DNA backbone. The conductivity of polypyrrole is up to 4 Scm^{-1} similar to polyindole and higher than bulk materials. [66, 67]

The conductive DNA hybrid nanowires described above have higher conductivities than bulk materials and further functionalization can occur on monomer units even after polymerisation. As a result, they may hold promise in future electronic applications.

One major restriction on DNA templating is that the DNA nucleosides do not have any special role in the assembly of the material. In addition, although DNA templating is easily carried out in a short time with high yield, a lack of reproducibility and control in the final dimensions of the material is observed. Therefore, to target certain bases of DNA stoichiometrically for assembling nanomaterials, the modification of DNA nucleobases through covalent bond formation was performed as illustrated in the following section.

1.3 DNA as a molecular scaffold

In the previous sections on DNA templating, the modification of DNA was carried out by the addition of materials through non-covalent interactions. In contrast, in DNA scaffolding, the modification of the DNA structure is carried out via covalent linkages to the DNA. [71-78] The DNA scaffold can be modified at various sites, for example the substitution of nucleobases. Pseudo-bases containing functional groups varying from fluorescent to redox active moieties have been incorporated into oligonucleotides via chemical or enzymatic synthesis with great success.[71-73] In this way, although the DNA building blocks have been modified, the self-coding of DNA can still be accessible. Modified nuclebases can be incorporated via phosphoramidite chemistry in automated DNA synthesis or enzymatically using polymerases. These methods provide an opportunity to form modified DNA duplexes to build more complex DNA nanostructures through self-assembly.

Typically, modifying the 2' and 4' positions on the ribose ring or modifying the 3' or 5' ends of the DNA strands is performed. The nucleobases themselves can also be modified at various positions, the C5 position of the pyrimidines being a common approach.[72] DNA scaffolding signifies precise placement of modified groups and affords subsequent control of the final structure when building either short oligomers or duplexes up to several microns in length.

Carell *et al* have eliminated some disadvantages regarding DNA templating by the covalent modification of nucleosides and providing binding sites for metals into the nucleosides[74-78] as shown in Figure 15.
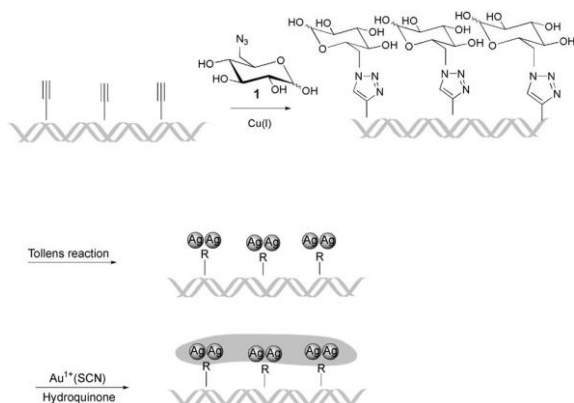
Figure 15 General scheme for the metallization procedure.[77]

They exploited the modification of 5-iodo-2-deoxycytosine triphosphate via the Sonogashira reaction with a di-alkyne linker to produce the alkyne-modified nucleoside. Enzymatic incorporation of the modified cytosine building block by the polymerase chain reaction gave a modified DNA template of up to 900 bp. Later, the modification of the alkyne linker was performed by a click reaction with an azide-bearing sugar group to build triazole linked products. Silver was selectively deposited onto the sugar triazole-modified DNA by the Tollens reaction. To construct silver nanowires 300 nm in length as observed by AFM. This work indicated a highly uniform and selective metallization process. [77]

In DNA scaffolding, the assembly of nanomaterial is carried out with precise control and reproducibility is another positive attribute of this approach. On the other hand, this approach requires considerable time, in synthesis, and often without any economic justification.

Therefore, to eliminate the restrictions of DNA scaffolding, an intermediate approach for the assembly of material along the DNA duplex is required and is detailed in the following section.

1.4 DNA intercalation

DNA is able to bind small molecules through three possible binding modes. Molecules which contain positively charged ions can interact with the negative phosphate groups on the backbone through simple electrostatics. Furthermore, another set of molecules can be accommodated into the grooves of DNA via hydrogen binding, hydrophobic interactions and electrostatics. These are typical of groove-binding drugs.[49, 79, 80] A third

mode of binding includes small molecules such as flat polycyclic aromatic chromophores which can be intercalated into DNA by non-covalent binding. Acridines and their derivatives are intercalators which have antibacterial and anticancer properties and can be inserted into DNA. DNA can be slightly unwound to open a space between adjacent base pairs to position the intercalators within the helix. Therefore, one way to modify DNA is to accommodate functional groups on the intercalators and then modify these sites after insertion into DNA.[79-81] Figure 16, presents some intercalators that have been extensively studied for a range of applications and have briefly been described.

Ethidium bromide

Proflavine

Daunomycin

Nogalamycin

Anthracene-9,10-diones

m-AMSA
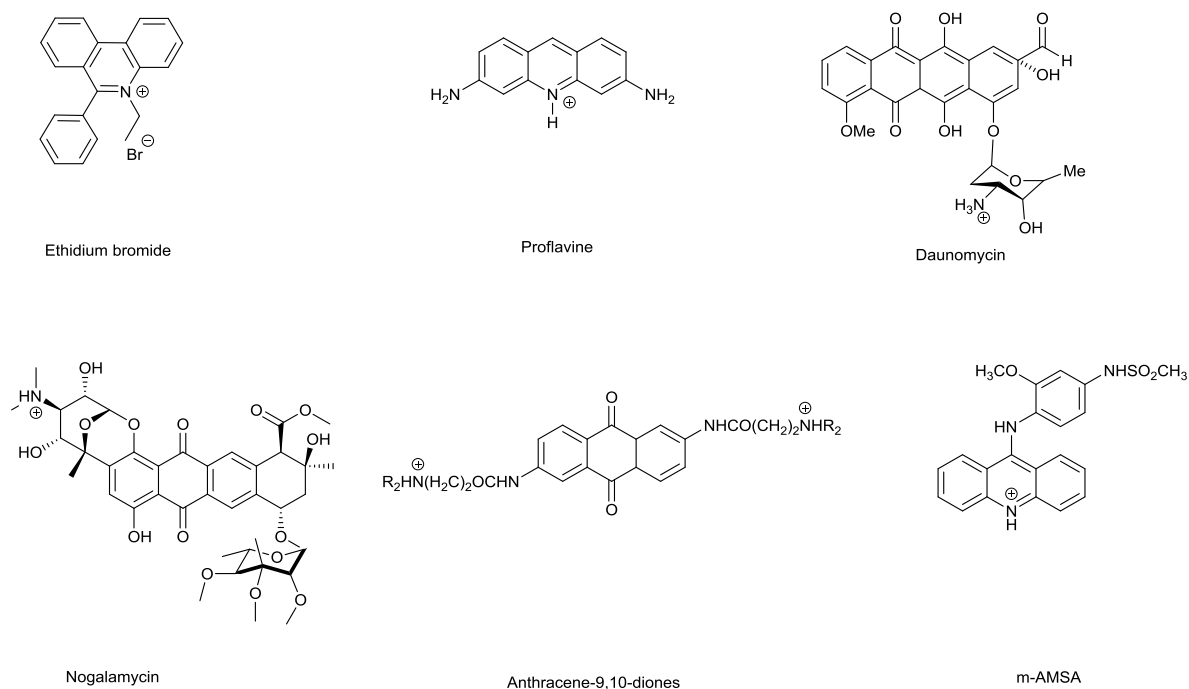
Figure 16. Some common DNA intercalators.

Ethidium Bromide, is an intercalating agent commonly used as a fluorescent tag (nucleic acid stain) in molecular biology laboratories for techniques such as agarose gel electrophoresis. When exposed to ultraviolet light, it will fluoresce with an orange colour which a 20-fold increase after binding to DNA. In addition, ethidium bromide may be a mutagen, a carcinogen, or a teratogen, although this depends on the organism exposed and the circumstances of exposure.[82]

Proflavine, can intercalate between the bases of DNA and it also has a mutagenic effect on DNA. It differs from most other mutagenic components by causing base-pair deletions or base-pair insertions but not substitutions. Proflavine is a disinfectant bacteriostatic against many gram-positive bacteria.[83, 84]

Daunorubicin, inhibits DNA and RNA synthesis as sequence specific ds-DNA intercalating agent. On binding to DNA, daunomycin intercalates with its daunosamine residue directed toward the minor groove. Daunomycin effectively binds to every 3 base pairs which causes unwinding.[85]

Noglamycin, is a threading intercalator which intercalates with an uncharged sugar in the minor groove and a positively charged amino sugar in the major groove. The noglamycin-DNA contacts occur mainly in the major groove.[86]

m-AMSA or amsacrine, from its planar acridinum ring system can intercalate into the DNA of tumor cells, thereby altering the major and minor groove proportions. This compound inhibits both DNA replication and transcription by reducing association between the affected DNA and DNA polymerase, RNA polymerase and transcription factors. Amsacrine also expresses topoisomerase inhibitor activity, specifically inhibiting topoisomerase II.[87]

According to the neighbour exclusion principle,[86, 88-90] the binding of one intercalator between two base pairs hinders the access of another intercalator to the binding site adjacent to the intercalator. Therefore, the assembly of material along the DNA helix can be controlled by altering the intercalator/DNA nucleobase ratio.

Recently, DNA intercalators have been applied in nano-fabrication. Intercalation of dyes has been used to construct multichromophoric arrays.[91] Armitage *et al.* have mimicked phycobiliproteins found in light-harvesting complexes of plants, bacteria and algea. The protein was replaced by a branched double-helical DNA nanostructure which serves as a template for non-covalent binding of the chromophores by intercalation between adjacent base pairs.[91]

Another effort regarding DNA assembly by intercalation was presented by Howell. He constructed a new 9-aminoacridine-3-carboxamide derivative which has potential for promoting the intermolecular assembly of oligonucleotide sequences and forming the X-stacked form of DNA known as the Holliday junction (HJ).[92]

However the full potential to exploit intercalators as reagents for the assembly of material along DNA has yet to be realised. This following section is an outline this thesis describing some initial steps to develop intercalation as a method for nanomaterial fabrication.

1.5 Aims of project

In light of the research reviewed in this chapter, one dimensional (1-D) functional materials and in particular using DNA for their fabrication is a research topic worth pursuing. The two common approaches reviewed, scaffolding and templating, have advantages and disadvantages.

DNA templating is easily carried out in a short time with high yield, but a lack of reproducibility and control in the direction of assembly is observed.

In the scaffolding approach the assembly of nanomaterial is carried out with precise control and reproducibility is a positive attribute to this method. However it requires more time, often difficult organic synthesis and yields are not high.

Therefore a new approach would be an attractive addition to the chemist's toolbox and this research project is based on the modification of DNA by exploiting intercalators as a route to nanomaterial assembly. This is achieved in two steps; the first step is the assembly of azido intercalators into the DNA helix. In the second step; the azido groups are functionalised via click chemistry. A range of alkyne-bearing functional groups can then be assembled along the DNA strand to give a 1-D nanomaterial.

Specifically, acridine derivatives containing two azide groups were synthesized from proflavine, **Pf**; namely proflavine diazide, **PD,** and its methylated derivative, **PDMe**$^+$.After intercalation, integration of alkyne-bearing conductive polymer units, redox groups and fluorescent tags were assembled along the DNA⊃intercalator complex. Chapter 2 describes the synthesis and characterization of the diazido derivatives of **Pf**, **PD** and **PDMe**$^+$, and the binding of these intercalators into DNA. Chapter 3 discusses the molecular coupling of **PD** and **PDMe**$^+$ with different alkynes via click chemistry. Chapter 4 examines the *in-situ* click-coupling of the DNA intercalated complexes of **PD** and **PDMe**$^+$ with the functional alkynes tested in Chapter 3. Finally, chapter 5 draws some conclusions and identifies future possibilities of this new approach to nanomaterial fabrication.

References

1.	B. Datta and G. B. Schuster, *Journal of the American Chemical Society*, 2008, **130**, 2965-2973.
2.	O. I. Wilner, A. Henning, B. Shlyahovsky and I. Willner, *Nano Letters*, **10**, 1458-1465.
3.	N. V. Voigt, T. Torring, A. Rotaru, M. F. Jacobsen, J. B. Ravnsbaek, R. Subramani, W. Mamdouh, J. Kjems, A. Mokhir, F. Besenbacher and K. V. Gothelf, *Nat Nano*, 2010, **5**, 200-203.
4.	M. Knez, A. M. Bittner, F. Boes, C. Wege, H. Jeske, E. Maiβ and K. Kern, *Nano Letters*, 2003, **3**, 1079-1082.
5.	N. C. Seeman and A. M. Belcher, *Proceedings of the National Academy of Sciences of the United States of America*, 2002, **99**, 6451-6455.
6.	J. Weber, R. Singhal, S. Zekri and A. Kumar, *International Materials Reviews*, 2008, **53**, 235-255.
7.	R. Mas-Balleste, J. Gomez-Herrero and F. Zamora, *Chemical Society Reviews*, 2010, **39**, 4220-4233.
8.	S. Barth, F. Hernandez-Ramirez, J. D. Holmes and A. Romano-Rodriguez, *Progress in Materials Science*, 2010, **55**, 563-627.
9.	E. Lahiff, C. Lynam, N. Gilmartin, R. O'Kennedy and D. Diamond, *Anal Bioanal Chem*, 2010, **398**, 1575-1589.
10.	N. C. Seeman and A. M. Belcher, *Proceedings of the National Academy of Sciences of the United States of America*, 2002, **99**, 6451-6455.
11.	S. M. Douglas, H. Dietz, T. Liedl, B. Hogberg, F. Graf and W. M. Shih, *Nature*, 2009, **459**, 414-418.
12.	C. S. Friedrich *Angewandte Chemie International Edition*, 2008, **47**, 5884-5887.
13.	H. Z. Gu, J. Chao, S. J. Mao and N. C. Seeman, *Journal of Biomolecular Structure & Dynamics*, 2009, **26**, 15.
14.	P. W. K. Rothemund, A. Ekani-Nkodo, N. Papadakis, A. Kumar, D. K. Fygenson and E. Winfree, *Journal of the American Chemical Society*, 2004, **126**, 16344-16352.
15.	I. Willner and B. Willner, *Nano Letters*, 2010, **10**, 3805-3815.
16.	O. Obonyo, E. Fisher, M. Edwards and D. Douroumis, *Critical Reviews in Biotechnology*, 2010, **30**, 283-301.
17.	S. V. Tkachev, E. Y. Buslaeva and S. P. Gubin, *Inorg Mater*, 2011, **47**, 1-10.
18.	R. Hassanien, M. Al-Hinai, S. A. Farha Al-Said, R. Little, L. Šiller, N. G. Wright, A. Houlton and B. R. Horrocks, *ACS Nano*, 2010, **4**, 2149-2159.
19.	Y. Xia, P. Yang, Y. Sun, Y. Wu, B. Mayers, B. Gates, Y. Yin, F. Kim and H. Yan, *Advanced Materials*, 2003, **15**, 353-389.
20.	F. S. Kim, G. Ren and S. A. Jenekhe, *Chemistry of Materials*, 2010, **23**, 682-732.
21.	P. Yan, Y. Xie, Y. Qian and X. Liu, *Chemical Communications*, 1999, **0**, 1293-1294.
22.	D. Al-Mawlawi, C. Z. Liu and M. Moskovits, *Journal of Materials Research*, 1994, **9**, 1014-1018.
23.	K. Trivedi, H. Yuk, H. C. Floresca, M. J. Kim and W. Hu, *Nano Letters*, 2011, **11**, 1412-1417.
24.	J. Goldberger, R. He, Y. Zhang, S. Lee, H. Yan, H.-J. Choi and P. Yang, *Nature*, 2003, **422**, 599-602.
25.	C. Thelander, P. Agarwal, S. Brongersma, J. Eymery, L. F. Feiner, A. Forchel, M. Scheffler, W. Riess, B. J. Ohlsson, U. Gösele and L. Samuelson, *Materials Today*, 2006, **9**, 28-35.
26.	R. Tenne, L. Margulis, M. Genut and G. Hodes, *Nature*, 1992, **360**, 444-446.
27.	C. N. R. Rao, A. Govindaraj, F. L. Deepak, N. A. Gunari and M. Nath, *Applied Physics Letters*, 2001, **78**, 1853-1855.
28.	L. Dloczik, R. Engelhardt, K. Ernst, S. Fiechter, I. Sieber and R. Konenkamp, *Applied Physics Letters*, 2001, **78**, 3687-3689.
29.	J. Hu, Y. Bando, Z. Liu, J. Zhan, D. Golberg and T. Sekiguchi, *Angewandte Chemie International Edition*, 2004, **43**, 63-66.
30.	M. Remškar, *Advanced Materials*, 2004, **16**, 1497-1504.
31.	H.-W. Liang, S. Liu and S.-H. Yu, *Advanced Materials*, 2010, **22**, 3925-3937.

32. G. H. Clever, C. Kaul and T. Carell, *Angewandte Chemie - International Edition*, 2007, **46**, 6226-6236.
33. R. H. Baughman, A. A. Zakhidov and W. A. De Heer, *Science*, 2002, **297**, 787-792.
34. A. Nel, T. Xia, L. Mädler and N. Li, *Science*, 2006, **311**, 622-627.
35. S. Xiao, J. Tang, T. Beetz, X. Guo, N. Tremblay, T. Siegrist, Y. Zhu, M. Steigerwald and C. Nuckolls, *Journal of the American Chemical Society*, 2006, **128**, 10700-10701.
36. N. C. Seeman, *Nature*, 2003, **421**, 427-431.
37. N. C. Seeman, *Annual review of biochemistry*, **79**, 65-87.
38. U. Feldkamp and C. M. Niemeyer, *Angewandte Chemie International Edition*, 2006, **45**, 1856-1876.
39. H. A. Becerril and A. T. Woolley, *Chemical Society Reviews*, 2009, **38**, 329-337.
40. G. Qun, C. Chuanding, G. Ravikanth, S. Shivashankar, A. Sathish, D. Kun and T. H. Donald, *Nanotechnology*, 2006, **17**, R14.
41. N. C. Seeman, *Annu. Rev. Biophys. Biomolec. Struct.*, 1998, **27**, 225-248.
42. N. C. Seeman, *Annual Review of Biochemistry*, 2009.
43. Q. Gu, C. Cheng, R. Gonela, S. Suryanarayanan, S. Anabathula, K. Dai and D. T. Haynie, *Nanotechnology*, 2006, **17**, R14-R25.
44. J. D. Watson and F. H. C. Crick, *Nature*, 1953, **171**, 737-738.
45. J. Richter, R. Seidel, R. Kirsch, M. Mertig, W. Pompe, J. Plaschke and H. K. Schackert, *Advanced Materials*, 2000, **12**, 507-510.
46. A. G. Georgakilas, L. Sakelliou, E. G. Sideris, L. H. Margaritis and V. Sophianopoulou, *Radiation Research*, 1998, **150**, 488-491.
47. A. Tanaka, Y. Matsuo, Y. Hashimoto and K. Ijiro, *Chemical Communications*, 2008, **0**, 4270-4272.
48. A. B. Kotlyar, N. Borovok, T. Molotsky, L. Fadeev and M. Gozin, *Nucleic Acids Research*, 2005, **33**, 525-535.
49. X. Liu, H. Diao and N. Nishi, *Chemical Society Reviews*, 2008, **37**, 2745-2757.
50. D. Porath, A. Bezryadin, S. De Vries and C. Dekker, *Nature*, 2000, **403**, 635-638.
51. G. H. Clever and M. Shionoya, *Coordination Chemistry Reviews*, 2010, **254**, 2391-2402.
52. J. Chen and N. C. Seeman, *Nature*, 1991, **350**, 631-633.
53. N. C. Seeman, *New J. Chem.*, 1993, **17**, 739-755.
54. E. Winfree, F. Liu, L. A. Wenzler and N. C. Seeman, *Nature*, 1998, **394**, 539-544.
55. M. N. Christof, A. Michael, G. Song and C. Lifeng, *Angewandte Chemie*, 2000, **39**, 3055-3059.
56. P. W. K. Rothemund, *Nature*, 2006, **440**, 297-302.
57. G. A. Burley, J. Gierlich, D. M. Hammond, P. M. E. Gramlich and T. Carell, DNA-BASED NANOSCALE INTEGRATION: International Symposium on DNA-Based Nanoscale Integration, Jena (Germany), 2006.
58. H. C. Guido, K. Corinna and C. Thomas, *Angewandte Chemie International Edition*, 2007, **46**, 6226-6236.
59. E. Braun, Y. Eichen, U. Sivan and G. Ben-Yoseph, *Nature*, 1998, **391**, 775-778.
60. C. F. Monson and A. T. Woolley, *Nano Letters*, 2003, **3**, 359-363.
61. M. Mertig, L. Colombi Ciacchi, R. Seidel, W. Pompe and A. De Vita, *Nano Letters*, 2002, **2**, 841-844.
62. J. S. Lee, L. J. P. Latimer and R. S. Reid, *Biochemistry and Cell Biology*, 1993, **71**, 162-168.
63. K. Tanaka and M. Shionoya, *Coordination Chemistry Reviews*, 2007, **251**, 2732-2742.
64. A. Moliton and R. C. Hiorns, *Polymer International*, 2004, **53**, 1397-1412.
65. W. Chen, G. z. Güler, E. Kuruvilla, G. B. Schuster, H.-C. Chiu and E. Riedo, *Macromolecules*, 2010, **43**, 4032-4040.
66. S. Pruneanu, L. Dong, T. A. Hollis, N. G. Wright, M. A. Galindo, A. R. Pike, B. A. Connolly, B. R. Horrocks and A. Houlton, AIP Conference Proceedings, 2008.
67. S. Pruneanu, S. A. F. Al-Said, L. Dong, T. A. Hollis, M. A. Galindo, N. G. Wright, A. Houlton and B. R. Horrocks, *Advanced Functional Materials*, 2008, **18**, 2444-2454.
68. P. Nickels, W. U. Dittmer, S. Beyer, J. P. Kotthaus and F. C. Simmel, *Nanotechnology*, 2004, **15**, 1524-1529.

69. Y. Bardavid, J. Ghabboun, D. Porath, A. B. Kotylar and S. Yitzchaik, *Polymer*, 2008, **49**, 2217-2222.
70. Y. Ma, J. Zhang, G. Zhang and H. He, *Journal of the American Chemical Society*, 2004, **126**, 7097-7101.
71. F. Seela, E. Feiling, J. Gross, F. Hillenkamp, N. Ramzaeva, H. Rosemeyer and M. Zulauf, *Journal of Biotechnology*, 2001, **86**, 269-279.
72. A. R. Pike, L. C. Ryder, B. R. Horrocks, W. Clegg, B. A. Connolly and A. Houlton, *Chemistry – A European Journal*, 2005, **11**, 344-353.
73. S. Obeid, A. Baccaro, W. Welte, K. Diederichs and A. Marx, *Proceedings of the National Academy of Sciences*, 2010, **107**, 21327-21331.
74. P. M. E. Gramlich, S. Warncke, J. Gierlich and T. Carell, *Angewandte Chemie International Edition*, 2008, **47**, 3442-3444.
75. J. Gierlich, K. Gutsmiedl, P. M. E. Gramlich, A. Schmidt, G. A. Burley and T. Carell, *Chemistry - A European Journal*, 2007, **13**, 9486-9494.
76. J. Gierlich, G. A. Burley, P. M. E. Gramlich, D. M. Hammond and T. Carell, *Organic Letters*, 2006, **8**, 3639-3642.
77. M. Fischler, U. Simon, H. Nir, Y. Eichen, G. A. Burley, J. Gierlich, P. M. E. Gramlich and T. Carell, *Small*, 2007, **3**, 1049-1055.
78. G. A. Burley, J. Gierlich, D. M. Hammond, M. E. Phillipp, Gramlich and T. Carell, AIP Conference Proceedings, 2006.
79. A. R. Peacocke and J. N. H. Skerrett, *Transactions of the Faraday Society*, 1956, **52**, 261-279.
80. S. Imoto, T. Hirohama and F. Nagatsugi, *Bioorganic & Medicinal Chemistry Letters*, 2008, **18**, 5660-5663.
81. H. Stephan, B. D. William, A. V. Alexander, R. Notker, E. M.-B. Maria, P. E. Nikolaus, A. K. Sergeij and J. L. P. Lustres, *ChemPhysChem*, 2002, **3**, 452-455.
82. J. B. Lepecq and C. Paoletti, *Journal of Molecular Biology*, 1967, **27**, 87-106.
83. B. Baldeyrou, C. Tardy, C. Bailly, P. Colson, C. Houssier, F. Charmantray and M. Demeunynck, *European Journal of Medicinal Chemistry*, 2002, **37**, 315-322.
84. M. Aslanoglu, *Analytical Sciences*, 2006, **22**, 439-443.
85. J. Bernard, M. Weil, M. Boiron, C. Jacquillat, G. Flandrin and M. F. Gemon, *Blood*, 1973, **41**, 489-496.
86. M. J. G. G Michael Blackburn, David Loakes and David M Williams, *Nucleic Acids in Chemistry and Biology*, 2006.
87. P. R. Walker, C. Smith, T. Youdale, J. Leblanc, J. F. Whitfield and M. Sikorska, *Cancer Research*, 1991, **51**, 1078-1085.
88. H. Ihmels and D. Otto, Editon edn., 2005, vol. 258, pp. 161-204.
89. H. Ihmels, K. Faulhaber, G. Viola and C. Schmuck, in *Highlights in Bioorganic Chemistry*, Wiley-VCH Verlag GmbH & Co. KGaA, Editon edn., 2005, pp. 172-190.
90. H. Ihmels, K. Faulhaber, D. Vedaldi, F. Dall'Acqua and G. Viola, *Photochemistry and Photobiology*, 2005, **81**, 1107-1115.
91. A. L. Benvin, Y. Creeger, G. W. Fisher, B. Ballou, A. S. Waggoner and B. A. Armitage, *Journal of the American Chemical Society*, 2007, **129**, 2025-2034.
92. L. A. Howell, Z. A. E. Waller, R. Bowater, M. O'Connell and M. Searcey, *Chemical Communications*, 2011, **47**, 8262-8264.

Chapter 2 - *Synthesis, characterisation and binding of diazido proflavine derivatives to DNA*

Chapter 2 - Synthesis, characterisation and binding of diazido proflavine derivatives to DNA

2.1 Introduction

In the previous chapter, whilst the majority of the reviewed challenges for growing 1D material are based on inorganic frameworks,[1-6] a number are based on organic materials. A range of organic molecules are able to bind to DNA in a variety of ways according to supramolecular chemistry principles such as major and minor groove association, sugar-phosphate backbone binding, intercalation between base-pairs and hydrogen-bonding with base-pairs.[7, 8]

Intercalators are polycyclic heteroaromatic compounds which can non-covalently insert between adjacent DNA basepairs.[7, 8] DNA intercalators can target non-canonical DNA structures such as the quadruplex,[9, 10] Z-DNA[11, 12] and branched DNA.[13-15] Such compounds are of special interest as both therapeutic agents and new tools in nucleic acid biochemistry. Recently, the modification of intercalators has been achieved with azides or alkynes to provide specific functionality and the ability to perform click chemistry type Huisgen 1, 3-dipolar cycloaddition reaction.[16, 17]

2.1.1 Acridines

Acridines are mainly known to interact with DNA by intercalation.[18, 19] These compounds have anticancer, antimalarial and antibacterial features which are due to their ability to intercalate to DNA.[19-21]
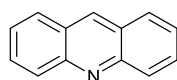
Figure 1. Acridine molecular structure

2.1.2 Acridine derivatives

One class of acridine intercalators is based on proflavine, 3,6-diaminoacridine. The proflavine structure is shown below in Figure 2.
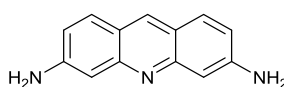
Figure 2. Proflavine (**Pf**) molecular structure

Some recent developments on the application of proflavine based systems are described below. Proflavine binds to DNA through two mechanisms, the stronger of which is intercalation. In this binding mode the planar aromatic dye lies between two adjacent bases and π-π interactions between the dye and base pairs act as a stabilizing force. The ratio of dye molecules to nucleotides at saturation is one to four due to the neighbour exclusion principle.[7, 8] Weaker binding involves electrostatic interaction between the positive charge on the dyes and the negatively charged phosphate groups of the DNA backbone. In this case the ratio of proflavine to nucleotide at saturation is now one to one.[18, 19, 22, 23]

One example of a proflavine derivative is shown in Figure 3, where the acridine bears two symmetrical imidazolidinone rings.[24]

R = ethyl, n-propyl, n-butyl, n-pentyl
and n-hexil
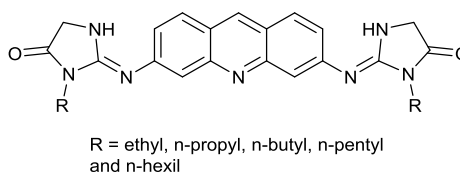
Figure 3. Molecular structure of an imidazole modified acridine dye, 3,6-bis((1-alkyl-5-oxo-imidazolidin-2-yliden)imino)acridine.[24]

These compounds inhibit topoisomerase I, and those with longer alkyl chains are able to penetrate membranes and efficiently suppress cell proliferation. The highest activity was found for 3,6-bis((1-n-hexyl-5-oxoimidazolidin-2-yliden)imino)acridine hydrochloride with $IC_{50} = 2.12$ μM (HL60 cells, Human promyelocytic leukemia cells, cell line has been used for laboratory research on how certain kinds of blood cells are formed) and 5.28 μML1210 cells (L1210 are mouse lymphocytic leukemia cells which are derived from the ascitic fluid of 8 month old female mice) after 72 h incubation.

Benchabane and co-workers reported the conversion of the amine groups on proflavine (**Pf**) to acetamide groups and showed that the presence of the acetamide groups was responsible for a strong nonclastogenic cytotoxicity. on both tumour CHO (Chinese hamster ovary) cells and human normal keratinocytes.[25] Two derivatives shown in Figure 4 displayed specific cytotoxicity to CHO cells. These results suggested that the two derivatives could be considered as interesting candidates for anticancer chemotherapy.
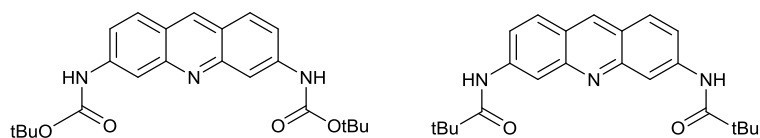
Figure 4. Two proflavine derivatives containing 1,1-dimethylethyl substituents.

In another instance, Searcey and his group synthesised a series of azido-and-alkyno acridine derivatives containing two arms.[16, 26] One arm is a 9-amino substituent which lies in the minor groove, and the other is a carboxamide substituent in either of the 3 or 4 positions which lies in the major groove, see Figure 5. The antitumour activity of these intercalators against HL60 cells depends on the position of the carboxamide substituent.[16, 26]
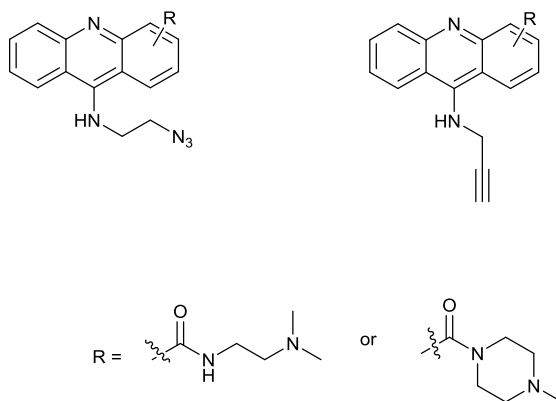
Figure 5. Azido and alkyno acridines derivatived from 9-aminoacridine-3 or 4-carboxamide and suitable for click reaction.[16, 26]

Synthesis of new derivatives by a click reaction with TurboBeads™ Azide (-Ph-CH2-N3) at the 9-propargylamine-substituent was also investigated by this group. Their studies indicated that in the presence of the click product obtained (one of the few 9-aminoacridine-3-carboxamide structures), the formation of DNA Holliday junctions increases by at least 100 fold compared to the addition of divalent metal ions.[16]

In this research project, acridine derivatives containing two azide groups were synthesized from Proflavine, see Figure 2. The interaction between these proflavine derivatives, N,N'-(acridine-3,6-diyl)bis(2-azidoacetamide) (**PD**) and 3,6-bis(2-azidoacetamido)-10-methylacridin-10-ium (**PDMe$^+$**) with DNA was investigated by UV/vis, fluorescence, CD and LD spectroscopies, as well as viscometry and melting temperature measurements. These proflavine diazido derivatives, once intercalated into DNA have potential to assemble a range of molecular functionalities via click chemistry.
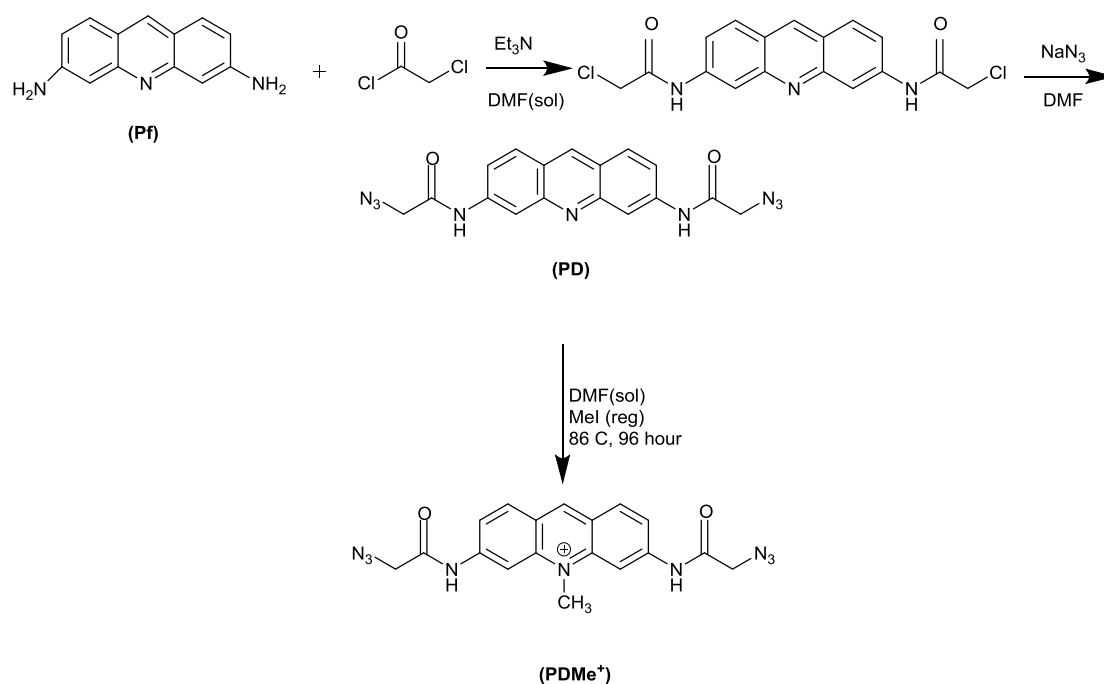
Scheme 1. Synthesis of **PD** and **PDMe⁺**

2.2 Results and Discussion

Acridine derivatives bearing two pendant azido groups were chosen as suitable intercalators for modification by click chemistry. Here the synthesis of **PD** and **PDMe⁺** is described and their binding studies with DNA reported.

2.2.1 Synthesis of PD

This synthetic route to **PD** from proflavine is shown in Scheme 1. The synthesis of the PD derivative is conducted in two steps. Firstly, the primary amine reacts with chloroacetyl chloride to give the amide derivative of proflavine, see Scheme 2.
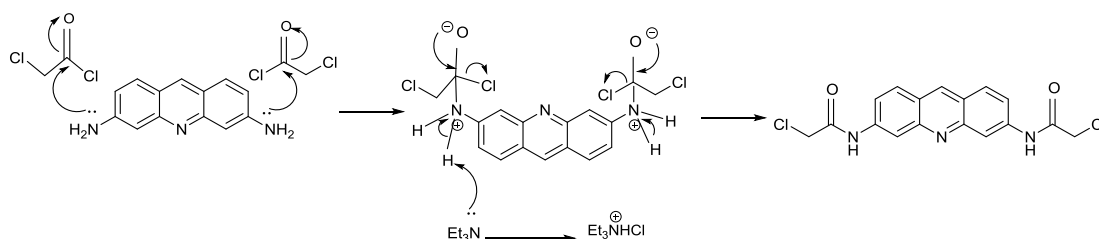
Scheme 2 The mechanism of the S_N2 reaction between proflavine and chloroacetyl chloride

In Scheme 2 the formation of the dichloro proflavine derivative (a substituted amide) is accompanied by the production of two equivalents of HCl, which needs to be neutralized by a suitable base. The use of triethylamine guarantees that there is no reaction between proflavine and HCl.

27

The second step involves the reaction of sodium azide with the dichloro proflavine derivative to generate the target molecule **PD**. The mechanism of this reaction is described below in Scheme 3.
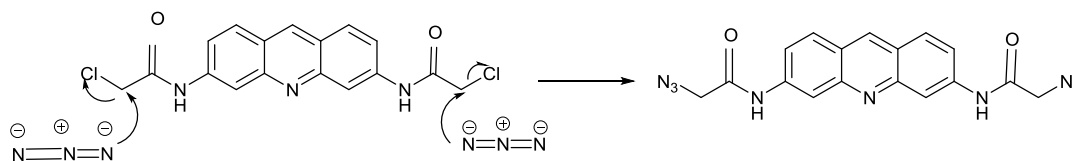
Scheme 3 Synthetic route to **PD**

In the preparation of **PD**, evidence of modification was indicated by ^{1}H NMR and IR spectroscopy and MS spectrometry. For **PD,** a broad peak at δ = 6.58 ppm associated with the NH_2 group of proflavine disappear and new peaks at δ = 10.82 ppm and 4.2 ppm appear which are related to the amide NH and aliphatic CH_2 groups. High resolution mass spectrometry indicated the molecular ion for [**PD** + H$^+$] at 376.1266 which correlates well with the calculated mass of 376.1270. Furthermore, IR spectroscopy showed a peak at 1676 cm^{-1} relative to carbonyl group and a new sharp peak at 2114 cm^{-1} characteristic of an azide group which also confirmed the successful conversion of **Pf** to **PD**.

2.2.2 Synthesis of PDMe$^+$

PD is a neutral compound and its solubility in aqueous solution is very low. Therefore, the introduction of a positive charge increases its solubility and also provides the opportunity for binding to the DNA backbone by electrostatic association. Therefore, it was attempted to methylate **PD** at the pyridinum nitrogen to give **PDMe$^+$**.

PD undergoes reaction with methyl iodide via a S_N2 reaction mechanism in the presence of nitrogen existed in its hetercycle ring to give the methylated derivative **PDMe$^+$**. In the reaction, CH_3^+ and nitrogen act as an electrophile and nucleophile respectively, see Scheme 4.
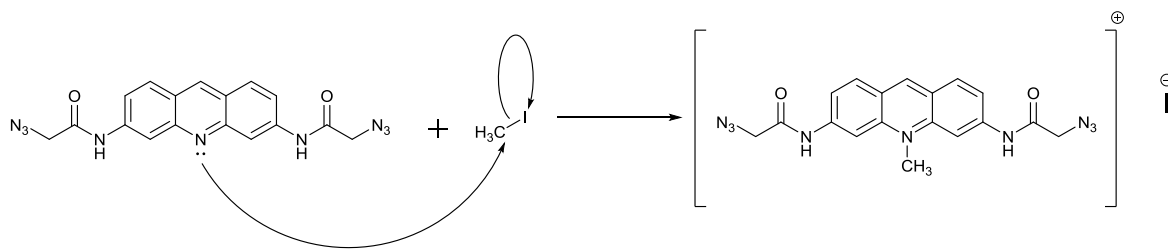
Scheme 4. Synthetic scheme of S_N2 reaction between **PD** and methyl iodide.

In the ^{1}H NMR of **PDMe**[+], a new peak appears at $\delta = 4.49$ ppm which is due to the methyl group attached to the pyridinium nitrogen, confirming successful methylation of **PD**. High resolution mass spectrometry showed a molecular ion of mass 390.1437 and correlates well to the calculated mass of 390.1427 for **PDMe**[+], confirming the successful methylation of **PD**.

IR spectroscopy showed the peak changes to 1695 cm^{-1} relative to carbonyl group and the sharp peak to 2099 cm^{-1} characteristic of the azide group.

Both target compounds, **PD** and **PDMe**[+], were characterised by IR and UV/vis spectroscopy. Both these techniques provide characteristic spectroscopic features which are key to the future analysis of their binding with DNA and their subsequent click modification. Therefore the following two sections discuss this analytical data in more detail.

2.2.3 Infrared characterisation of PD and PDMe[+]

IR was performed primarily to identify the azido group of **PD** and **PDMe**[+] as this vibrational mode will be used to confirm successful modification of the intercalators via click chemistry in later investigations.

Assignment of the vibrational bands was achieved using literature references for azide derivatives.[27] The vibrations were observed at 2114 cm^{-1} for **PD** and 2099 cm^{-1} for **PDMe**[+] confirming the presence of the azide group in the synthesised diazido proflavine derivatives as shown in Figure 6 and in Table 1.
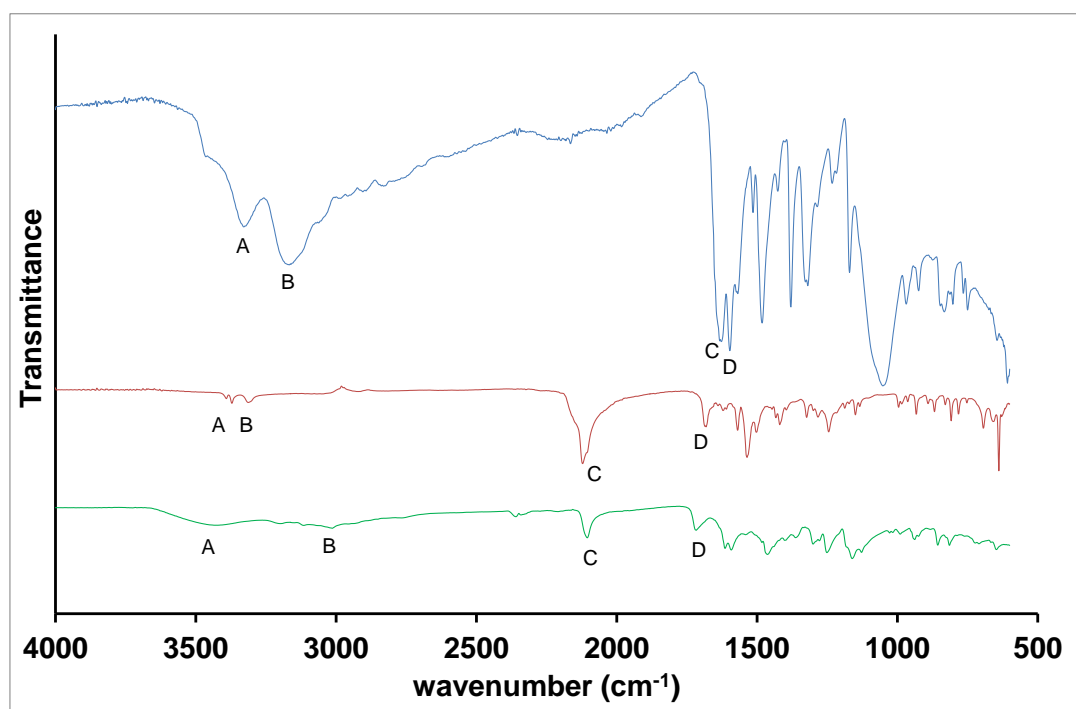
Figure 6. IR spectra of **Pf** (blue), **PD** (red) and **PDMe$^+$** (green).

Compounds	A	B	C	D
Pf	3308 cm^{-1} N-H stretching related NH$_2$	3142 cm^{-1} N-H stretching related NH$_2$	1620 cm^{-1} aromatic and poly cyclic rings	1593 cm^{-1} aromatic and poly cyclic rings
PD	3362-3380 cm^{-1} Secondary amide N-H	3296 cm^{-1} Secondary amide N-H	2114 cm^{-1} N$_3$ group	1676 cm^{-1} secondary amide C=O
PDMe$^+$	3408 cm^{-1} Secondary amide N-H	2984 cm^{-1} N-CH$_3$ C-H stretch	2099 cm^{-1} N$_3$ group	1695 cm^{-1} secondary amide C=O

Table 1. Related IR peaks signed for Pf, PD and PDMe$^+$ resulted from Figure 8.

2.2.4 UV/vis characterisation of PD and PDMe$^+$

Proflavine derivatives are strongly coloured compounds. The UV absorption spectra of **Pf** and its synthesised derivatives, **PD** and **PDMe$^+$** were recorded at different pH values in aqueous solutions (1% DMSO to aid solubility). In all cases, the maximum absorption was observed between 300-500 nm, see Figure 7.
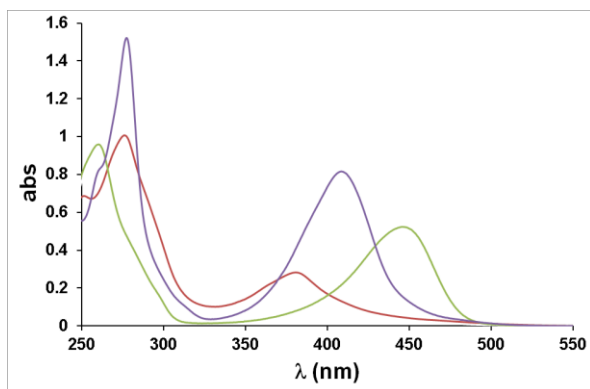
Figure 7. Absorption spectra of 18 μM **Pf** (green),48 **PD** μM (red) and 80 μM **PDMe**$^+$ (purple) in aqueous solution with 1% DMSO (pH 7).

The $S_0 \rightarrow S_1$ transition for the acridine derivatives, **PD** and **PDMe**$^+$ are at higher energy, and exhibit smaller extinction coefficients than **Pf**, see Table 2. The λ_{max} and extinction coefficients of **Pf**, **PDMe**$^+$ and **PD** were 445 nm and 19,000 M^{-1} cm^{-1}, 409 nm and 9,200 M^{-1} cm^{-1} and 381 nm and 5,800 M^{-1} cm^{-1} respectively. Furthermore, similar results for other derivatives of proflavine have been presented by Yamaoka and co-workers when they examined the UV absorption of a *N*-methyl-proflavine labelled with diacetamido substituents.[28] It is also noteworthy that all acridine compounds have considerable absorption in the 255-280 nm region where DNA also absorbs. The maximum absorption observed between 300-500 nm is therefore important for studying and obtaining the binding constants of these intercalators.

	pH	λ_{max} / nm	ε_{max}/M^{-1}cm^{-1}	**HOMO eV**	**LUMO eV**	$\Delta E/eV$
Pf	12	393	19,000	4.83	1.32	3.51
PfH$^+$	7	445	41,000	8.95	5.66	3.29
PD	7	381	5,800	6.02	2.40	3.62
PDH$^+$	3	403	13,200	9.46	6.19	3.27
MePD$^+$	7	409	9,200	9.44	6.09	3.35

Table 2 Maximum wavelengths and extinction coefficients for absorption of the acridine dyes (solution), and comparison of calculated HOMO-LUMO energy gaps by density functional theory method with 6-31G* basis set by Spartan programme.

A further aspect for consideration is the possibility of protonation of the pyridyl nitrogen of the azido intercalators. This is especially important as a positively charged intercalator like **MePD**$^+$ would be expected to bind more strongly to DNA. At pH 7, **Pf** is expected to be protonated to PfH$^+$.[29] However, **PD** is likely to be protonated only at lower pH. The observed spectra, see Figure 8, showed a lower energy absorption maxima at longer wavelengths consistent with this prediction, see Table 2 for details.
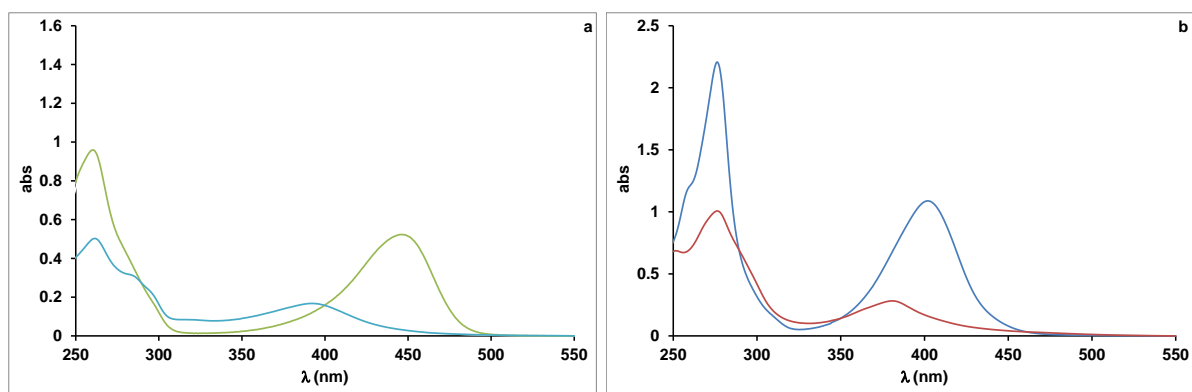
Figure 8. Absorption spectra of **a)** 18 μM **Pf** (green) in pH 7 and (light blue) in pH 12 **b)** 48 μM **PD** (red) in pH 7 and (dark blue) in pH 3 in aqueous solution with 1% DMSO pH 7.

For **Pf** and **PfH**[+] the solution pH for two forms was pH 12 and pH 7 respectively. However, for **PD** and **PDH**[+] the pH values resulted from pH titration were 7 and 3 respectively. These differences prompted a more detailed study into the pKa values of these modified acridines.

2.2.5 pKa determination

Protonation of the acridine dyes was investigated by determining their pKa values using UV/vis spectroscopy. For each dye, spectral changes were monitored at several wavelengths where significant absorption changes occurred. In the figures that follow, two representative wavelength data are shown for each dye; chosen as those that show the clearest changes.

Schulman et al. reported three pK_a values for **Pf** in aqueous solutions at -2.7, 0.3 and 9.5.[29] The pH titration is shown in Figure 11a, **Pf** at pH 7 exists in its monocationic form and the UV absorption at 445 nm is associated with the $S_0 \rightarrow S_1$ transition with an extinction coefficient of 41,000 M^{-1} cm^{-1}.[30, 31] At pH 12, the ring nitrogen is deprotonated and the neutral form has a higher energy absorption maximum at 393 nm with a smaller extinction coefficient. The spectra of the di- and tri-cationic forms (pH < 0), where the exocyclic nitrogens are protonated, show absorption bands between 350-360 nm and extinction coefficients comparable to the neutral species.[29, 32]
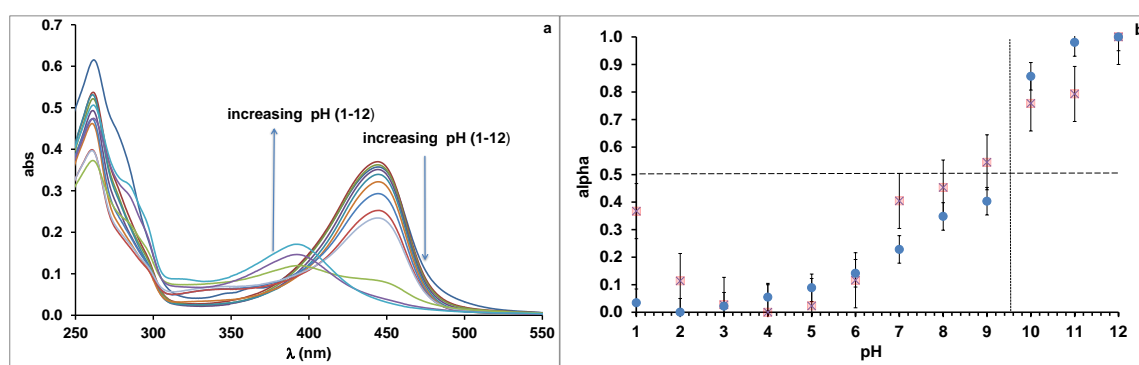
Figure .9.Variation in the absorption spectra of **Pf** with pH (a). Alpha represents the proportion of profavine species that is prevelant at high pH (b); blue circle (448 nm) and pink square (317 nm) (14.7 μM **Pf**, 5 mM phosphate, 1% DMSO; pH adjusted with NaOH or H_3PO_4 at 21 °C.

MePD$^+$ is also monocationic at pH 7. A pK$_a$ of 9.6 observed (**Figure 10a**), indicating deprotonation which is expected to occur from the N-H of the side chain. Isobestic points are observed at 290nm and 350 nm, indicating the presence of only two species in this pH range. Above pH 10, new spectral features are observed, indicating the appearance of a new species, probably for deprotonation of the other side chain.
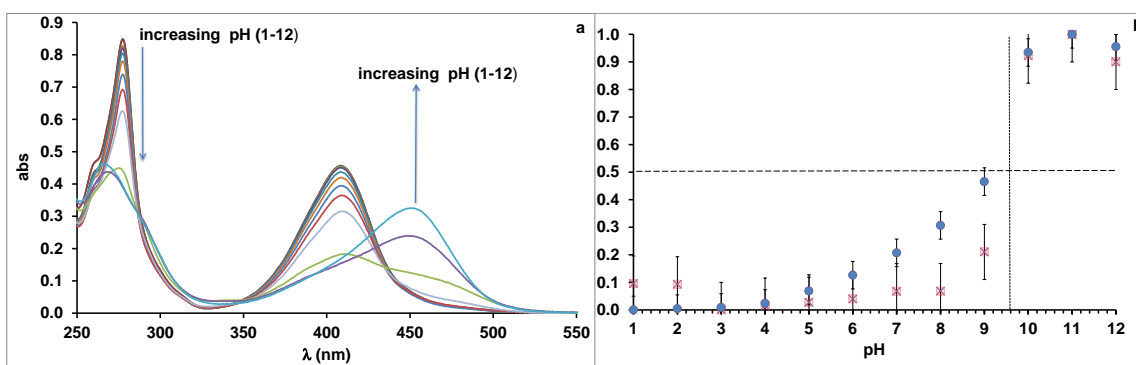
Figure 10. Variation of the absorption spectra of **MePD$^+$**.with pH. (a) alpha represents the proportion of species that is prevelant at high pH. (b); blue circle (407 nm) and pink square (323 nm) PD (43 μM); 5 mM phosphate (pH 6.9)/1% DMSO; pH adjusted with NaOH or H$_3$PO$_4$; 21 ℃.

Considerable change of the **PD** spectrum occurs as the pH drops from 9 to 1. A pKa is observed at ~ 4.2 that this was assigned to protonation of the neutral form which is the prevalent, poorly soluble, form at pH 7.
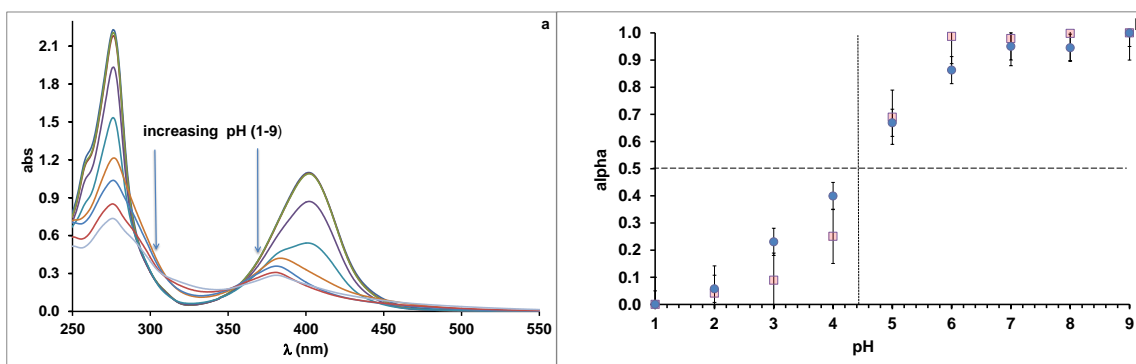
Figure 11. Variation of the absorption spectra of **PD**.with pH (a) alpha represents the proportion of species that is prevelant at high pH. (b) (blue circle) 406 nm; (pink square) 331 nm. PD (54 μM); 5 mM phosphate (pH 6.9)/1% DMSO; pH adjusted with NaOH or H$_3$PO$_4$; 21 ℃.

To explore the spectral changes with pH in greater detail, the frontier molecular orbitals were calculated for the unsolvated minimized structures of **Pf**, **PfH$^+$, PD**, **PDH$^+$** and **MePD$^+$**, see Figure 12 and also the energy data in Table 2.
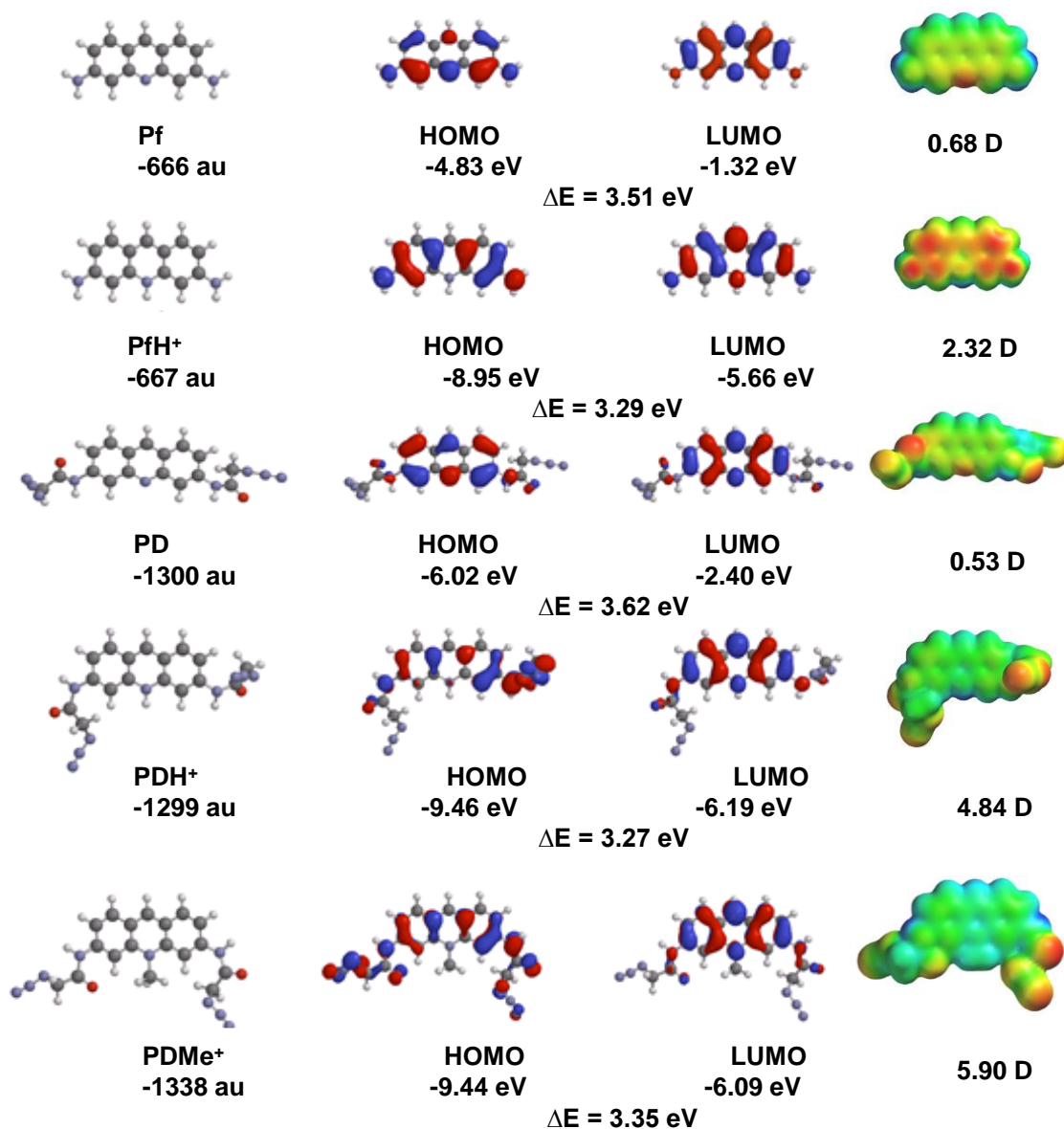
Figure 12. Frontier molecular orbitals calculated and partial charges for the minimised structures for **Pf**, **PfH⁺, PD, PDH⁺** and **MePD**. Semi-empirical structure minimization (PM3) was followed by DFT calculations (B3LYP/6-31G*) of energies and molecular orbitals. Partial charge distributions. Positive and negative partial charges are represented, respectively, by blue and red.

Partial charges calculated for the neutral and monocationic form of **Pf**, **PD** and **MePD**$^+$ are represented in Figure 12. For neutral **Pf** the ring nitrogen carries a high negative partial charge (red) and the exocyclic amino hydrogens carry a partial positive charge (blue). With protonation of the ring nitrogen the negative charge is spread over the ring system and the exocyclic nitrogens and the N-10 proton carries a high positive charge. **PD** is neutral at pH 7 and the negative charge on the ring nitrogen is smaller than **Pf** (-0.608e compared to -0.638e) due to distribution of the significant negative charge residing on the amide linker and the azide nitrogens. However, after protonation of the ring nitrogen, the negative charges are localized on the amido-azido substituents rather than ring system. This explains the origin of a lower pK_a of the central nitrogen of the acridinium ring of **PD** in comparison with **Pf**.

MePD$^+$ indicates partial charge distributions similar to the **PD** in the monocationic form.

In the next sections the focus turns to investigations of the binding of **Pf**, **PD** and **PDMe**$^+$ to DNA, by UV/vis, fluorescence, CD and LD spectroscopy, melting and viscosity measurements.

2.3 The effect of organic solvents on the formation of diazido proflavine derivative -DNA complex

The investigations achieved by Lober *et al.* regarding the effect of organic solvents on the binding of proflavine and some similar compounds with DNA indicate a decrease in the binding capability of proflavine in the presence of organic solvents,[33] is probably due to changes in the properties of **Pf**.[23, 34]

Organic solvent molecules can compete with DNA molecules to interact with the hydrophobic dye molecules. The tendency of dye to bind with DNA decreases with the increase of the hydrocarbon content of the solvent. In addition, certain concentrations of organic solvents can block the formation of dye-DNA complex without any denaturation. These demonstrate the importance of hydrophobic forces in the formation of dye-DNA complexes.

Pf hemisulfate salt, **PD** and **PDMe**$^+$**I**$^-$ were poorly soluble in aqueous solutions and therefore organic solvents were required to dissolve them. However, the organic solvents, as already discussed, can decrease the binding capability of the dye with DNA. In addition, DNA is poorly soluble in organic solvents. It is necessary to first dissolve it

in aqueous solutions, and then add small amounts of organic solvent. Therefore, the choice of an appropriate solvent is extremely important in dye–DNA titrations.

Methanol and DMSO were both selected as candidates for titration. First, it was essential to determine the volume percentages of methanol or DMSO which could be added to buffer to dissolve **Pf** and **PD** without any aggregation. Therefore, **Pf** and **PD** solutions with methanol/buffer ratios of 1:9, 2:8, 3:7 and 4:6 were prepared and the UV/vis spectra (see Figure 13 and Figure 14) showed maximum absorption at a ratio of 4:6 methanol to phosphate buffer. Thus, this ratio of solvents was employed for titration. Also, due to the ease of dissolution of **Pf** and **PD** in DMSO, phosphate buffer containing 1% DMSO was utilized as solvent.
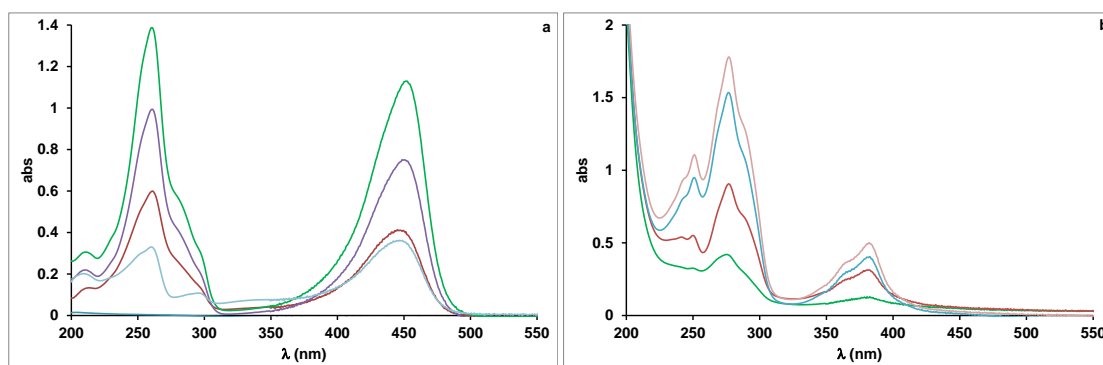
Figure 13 a) 24 μM **Pf** in variant ratios of 1:9 (blue), 2:8 (red), 3:7 (purple) and 4:6 (green) b) 96 μM **PD** in variant ratios of 1:9 (green), 2:8 (red), 3:7 (blue) and 4:6 (pink) of methanol:buffer respectively.

Then the following titrations were carried out:

I) Titration of **Pf** and **PD** with calf thymus DNA in 5 mM phosphate buffer (pH 6.9) containing 40% methanol.
II) Titration of **Pf** and **PD** with calf thymus DNA in 5 mM phosphate buffer (pH 6.9) containing 1% DMSO.

2.4 Titration of Pf, PD with calf thymus DNA in 5 mM phosphate buffer (pH=6.9) and 40% methanol

In 40% methanol, **Pf** can bind to DNA, but the final spectrum at P/D = 2 is less red-shifted than the spectrum reported for binding without methanol,[23] see Figure 14a.
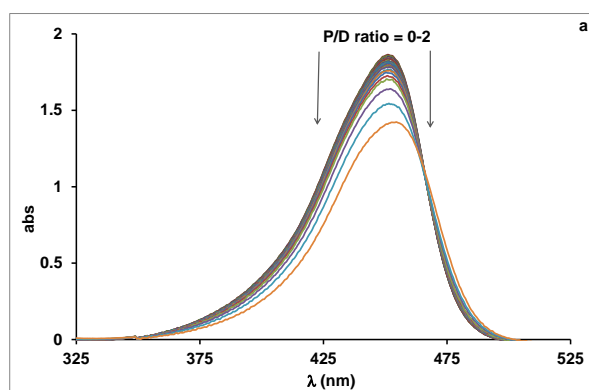
Figure 14a. The titration of 24 μM **Pf** with a solution of (24 μM Pf + 1 mM DNA). Condition, 5 mM phosphate buffer (pH= 6.9) with 40% methanol.

Changes of the **PD** spectrum on addition of DNA in 40% methanol suggest that some binding occurs. **PD** absorbance at $\lambda_{max} \sim 380$ nm decreases with increasing DNA concentration and a new band emerges at ~ 420 nm, see Figure 14b.

The comparison of the final spectrum in the methanol titration with the spectrum of DNA-bound **PD** in buffer with 1% DMSO (Figure 18a) shows that the 420 nm band represents bound **PD.** However, the absorption change in Figure 14b is very small compared to that observed in Figure 18a, indicating that is weak in 40% methanol.
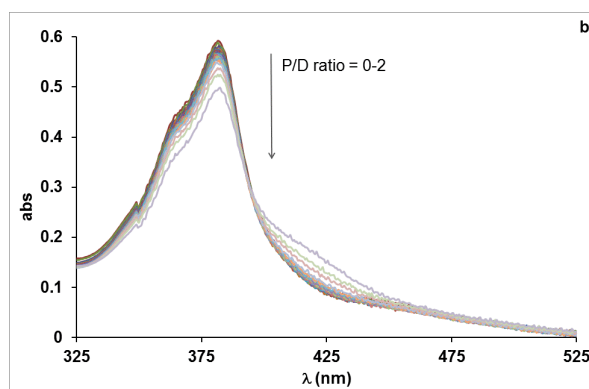
Figure 14b. The titration of 96 μM **PD** with a solution of (96 **PD** μM PD + 3.4 mM DNA) with DNA. Condition, 5 mM phosphate buffer (pH= 6.9) with 40% methanol.

2.5 Absorption titration of Pf, PD and PDMe[+] with CT-DNA and polynucleotide in 5 mM phosphate buffer and 1% DMSO

Subsequantly, the binding of **Pf**, **PD** and **PDMe**[+] to DNA was readily observed by monitoring changes of absorbance in the visible spectrum in the presence of a small amount (1%) of DMSO.[23] **Pf** (Figure 15 and Figure 16) and **PDMe**[+] (Figure 17) have similar behaviors on addition of DNA during titration. Both show red shifts of approximately 15 nm with hypochromicity, and this is what is expected when dyes stack with the DNA base pairs on intercalation.
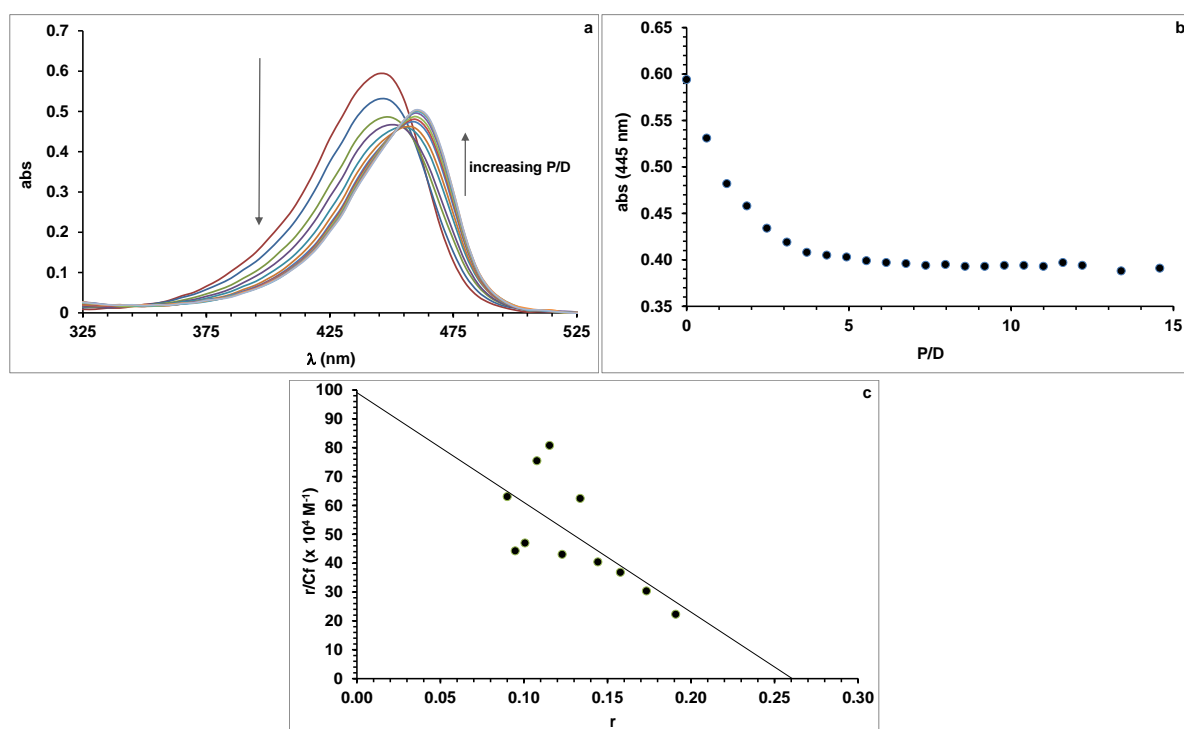
Figure 15. Absorption titrations of 14.5 μM **Pf** with CT-DNA at low salt (a) absorption spectra (b) abs versus P / D (c) Scatchard plot, in 99% 5 mM phosphate buffer and 1% DMSO. $K \geq 3.8 \times 10^6$ M[-1]; n = 0.26
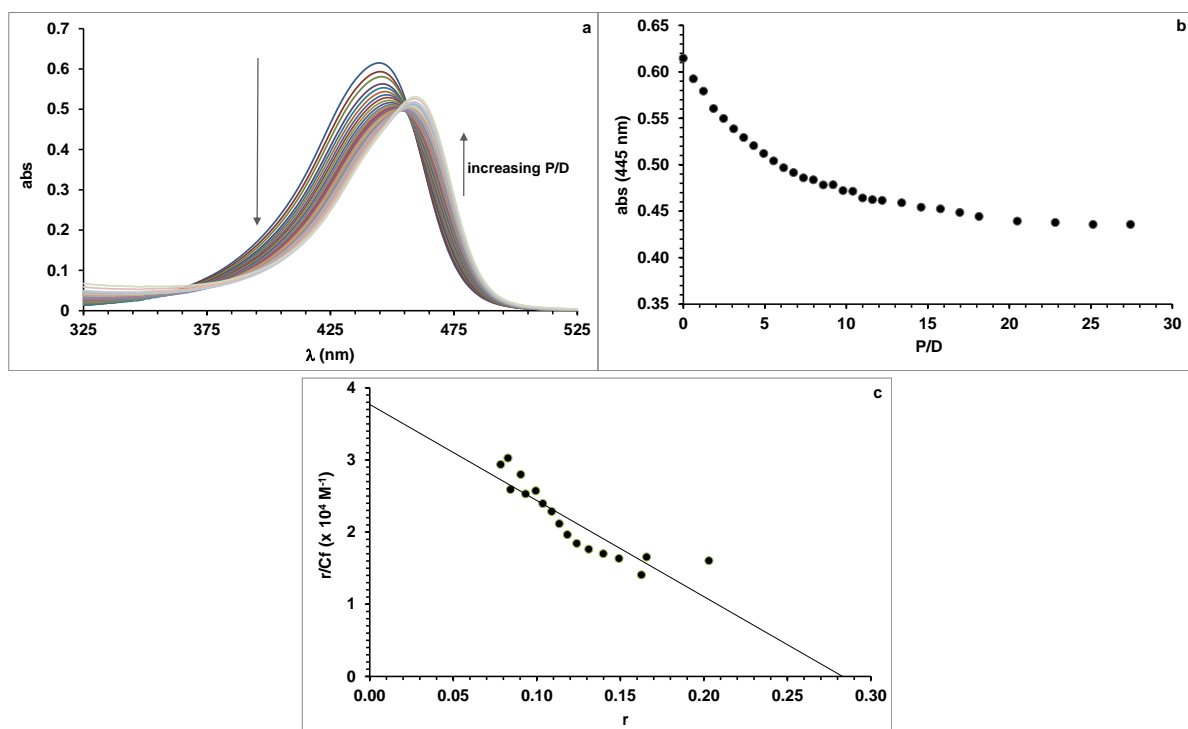
Figure 16. Absorption titration of 15 μM **Pf** with CT-DNA at high salt (a) absorption spectra (b) abs versus P / D (c) Scatchard plot, in 5 mM phosphate buffer/0.5 M NaCl/ 1% DMSO. K $= 1.4 \times 10^5$ M^{-1}; n $= 0.28$.
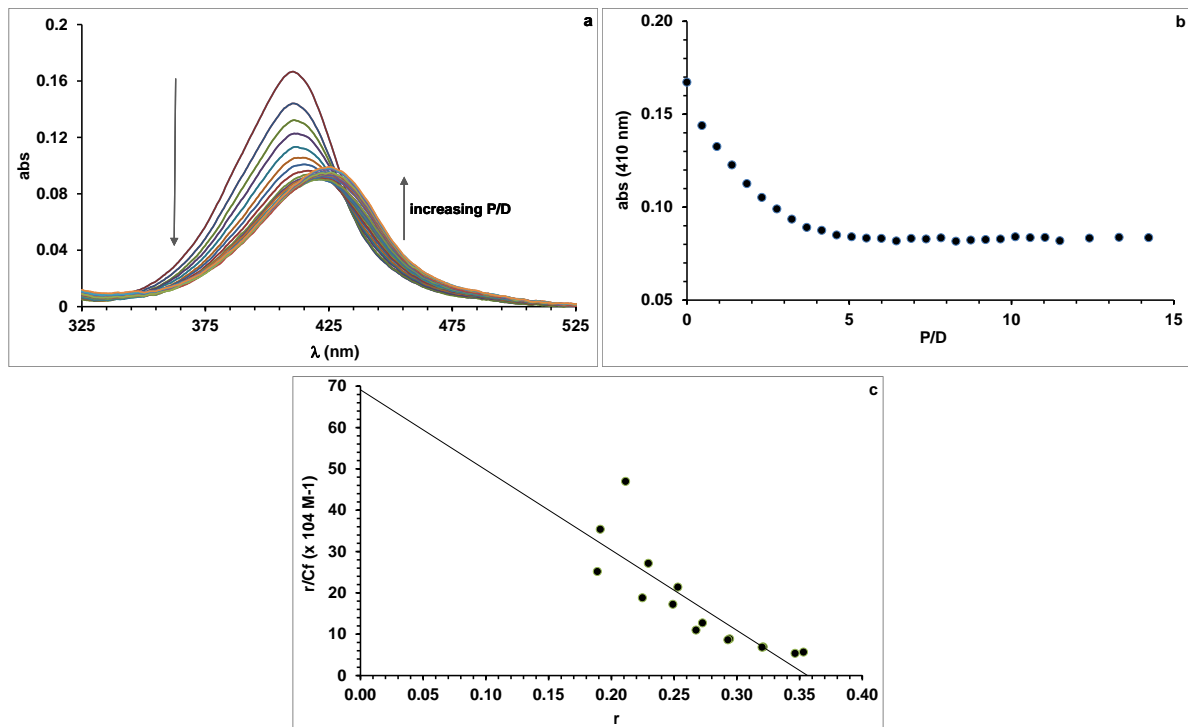
Figure 17. Absorption titration of 18 μM **PDMe**$^+$ with CT-DNA at low salt (a) absorption spectra (b) abs versus P / D (c) Scatchard plot, in 99% 5 mM phosphate buffer and 1% DMSO. K $= 2.0 \times 10^6$ M^{-1}; n $= 0.36$

However, **PD** (Figure 18) indicates red shift about 35 nm and differently hyperchromicity. This is can be interpreted as an unusual phenomenon for binding in DNA. The maximum peak of PD bound into DNA is appeared in 416 nm and represents a shift of 13 nm from the maximum seen for PDH^+ (403 nm). In addition, large amount of increased absorption along with DNA titration compared to the free PD represents a hypochromic changes compared to the spectrum of PDH^+. This can be interpreted as being due to the compound being in the monocationic form, PDH^+, when bound into DNA.
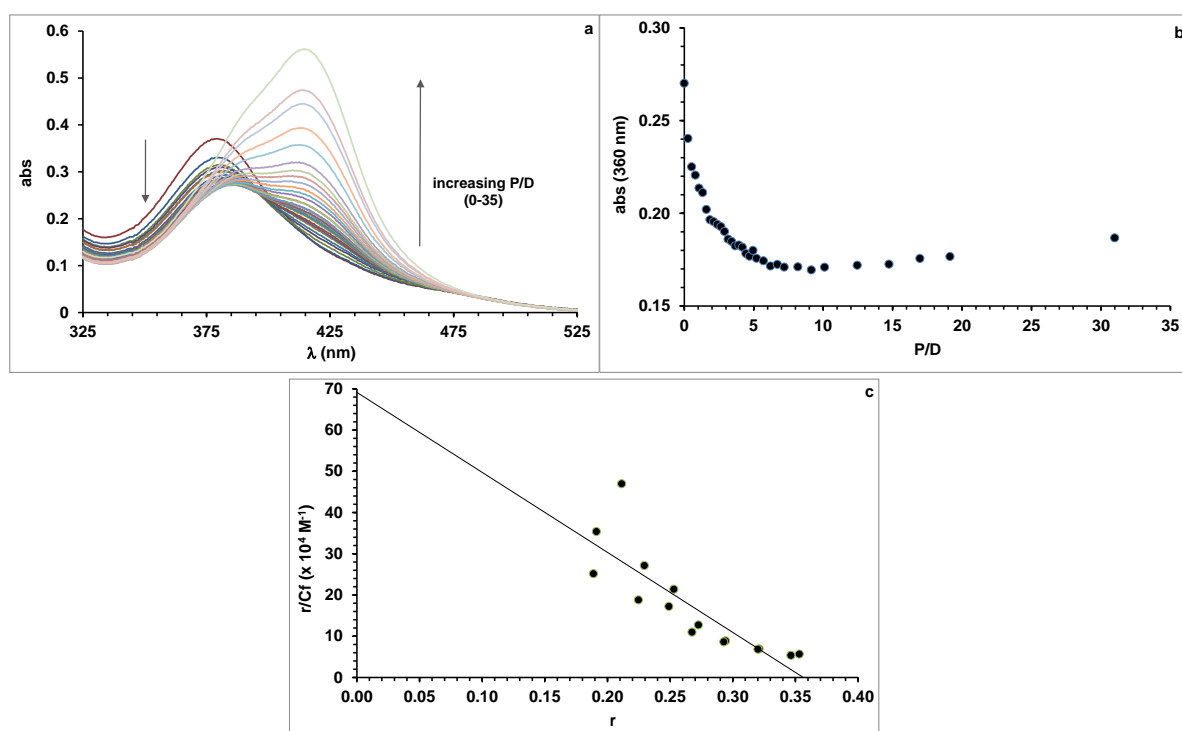
Figure 18. Absorption titrations of 56 µM **PD** with CT-DNA, at low salt. (a) Absorption spectra; (b) abs versus P/D; (c) Scatchard plot. 99% 5 mM phosphate buffer and 1% DMSO. K = 5.3×10^5 M^{-1}; n = 0.33

Binding constants and apparent site sizes as shown in **Table 3** were obtained by analysing the absorption changes using the Scatchard method. **Pf** binds very strongly to CT-DNA and only a lower limit for the association constant could be determined at low ionic strength.

Pf binds quantitatively to DNA under these low salt conditions at 10^{-5} M concentration. Therefore, it could be stated that K $\geq 10^5$M^{-1} and to obtain an exact binding constant, the titration should be carried out at submicromolar concentrations of **Pf**. This cannot readily be accomplished with only an absorption titration because the absorbances would be very low and S/N very high. Instead the titration was carried out at high salt concentration since this reduces the binding constant of a cationic dye to DNA.

As the salt concentration was raised, binding became weaker, as previously observed,[22, 23, 35] and an association constant was readily determined with 500 mM NaCl added to buffer. An estimate of K at 7.5 mM Na^+ (for 5 mM phosphate) could then be made using Record/Manning theory, which states that the binding constant of a monocationic intercalator varies with concentration of added inert monocation according to Equation (1), with B = 0.24, Z = 1, and either $\Psi = 0.82$[36-38] or $\Psi = 1$.[36, 39]

$$\frac{d(lnK_{obs})}{d(ln[Na^+])} = \check{S}(B+Z\Psi) \qquad (1)$$

From this, a binding constant of $K \approx 1.5 \times 10^7$ M^{-1} is predicted at 7.5 mM Na^+, which is higher than the experimental value, and represents an upper limit at low ionic strength. The binding constants measured for **Pf** have similar magnitudes to previously reported values.[22, 23, 34-36, 39]

Dye	[Na^+] / mM	K / M^{-1}	n
Pf	7.5	$\geq 3.8 \times 10^6$	0.26
Pf	507.5	1.4×10^5	0.28
PD	7.5	5.3×10^5	0.33
PDMe	7.5	2.0×10^6	0.36

Table 3. Association constants (K) and apparent binding site sizes (n) determined from absorption titration for the modified proflavine dyes with CT-DNA, using the Schatchard method.

PD and **PDMe**$^+$ also show good affinities for DNA, with site sizes that are close to nearest-neighbor (according to the neighbour exclusion principle, [7, 8] the binding of one intercalator between two base pairs hinders the access of another intercalator to the base pair site adjacent to the intercalator), although their binding constants are somewhat lower than that for **Pf**. Nonetheless, at low ionic strength, both **PD** and **PDMe**$^+$ are quantitatively bound to DNA at high P/D, see experimental section.

2.6 Flow Linear Dichroism and and reduced Linear Dichroisom (LD^r)

Determination of the binding mode between DNA and small molecules can made using linear dichroism spectroscopy.[40, 41] In this process, DNA molecules are oriented under an external electric field (ELD) or hydrodynamic field (flow linear dichroism).

In LD experiments, DNA in the solution is oriented using a shear graqdient in a Covette cell (Figure 19) to produce a hydrodynamic flow field.
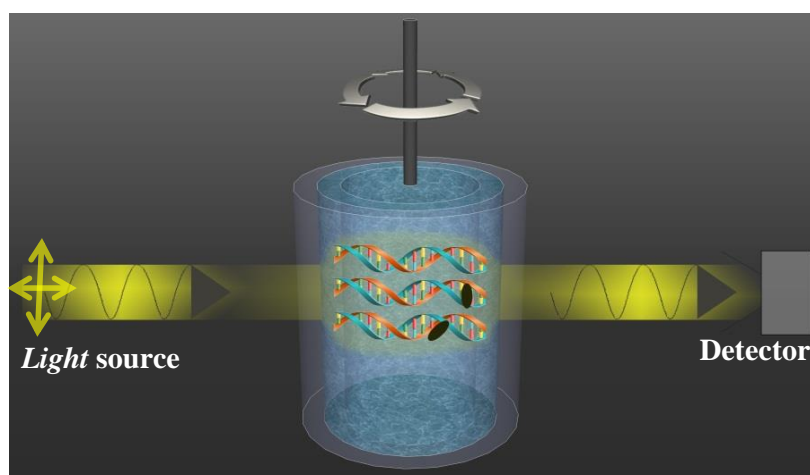
Linear polarisations of light

Figure 19. Schematic diagram of Linear Dichroisom operation.

Macromolecules become oriented in the shear gradient. For DNA , therefore, the helical axis is the orientation axis and lies the flow direction, as shown schematically in Figure 19.

Linear dichroism results from differential absorption of light that is plane polarized parallel and perpendicular than reference axis

$$(LD = A_{||} - A_{\perp}) \qquad (2)$$

The magnitude of the LD signal depends on the degree of orientation of the sample as well as the molar absorptivity and concentration of the sample.

The reduced dichroism is defined as:

$$LD^r(\lambda) = LD\ (\lambda)/A_{iso}(\lambda) \qquad (3)$$

Where A_{iso} is the absorption of the sample without orientation. It is related to the orientation of the chromophore as:

$$LD^r(\lambda)\ = 1.5S\ (3\ \langle\cos^2\alpha\rangle - 1) \qquad (4)$$

Where α represents the angle between the absorbing transition moment and DNA helix axis. S is an orientation function describing the degree of orientation of the DNA helix such that S = 1 is equivalent to perfect orientation and S = 0 to random orientation. $\langle\cos^2\alpha\rangle$ represents an average over the angular didtribution. S depends on the DNA stiffness and length, the flow rate, and the viscosity of the medium. S can be determined from the negative dichroism of DNA at 260 nm, where the π-π* transitions are polarized in the plane of the bases; previous studies have inferred an effective value of α = 80-86° for the orientation of the base pairs to the helix axis.[42, 43]

By comparing the LD^r signals for the DNA bases and a bound molecule, information about the geometry of the bound molecule can be deduced, if the transition moment (TM) directions of the bound molecule are known. For heteroaromatic molecules such as **Pf**, the strong visible absorption arises from $\pi-\pi^*$ transitions and the TMs lie in the aromatic plane (out-of-plane forbidden $n\rightarrow\pi^*$ transitions are generally very weak to be observed).

LD < 0 basepair

LD < 0 Intercalation

LD > 0 Minor groove binder
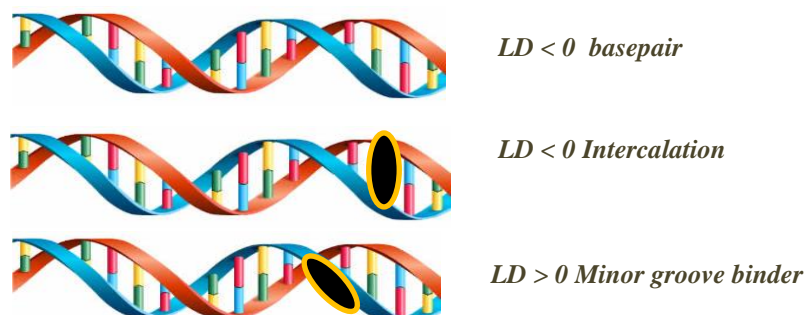
Figure 20. The different LD possibility for DNA with molecules overlaid

If a molecule is not bound to DNA, it is not oriented in the flow field used, so LD = 0. Also, if a bound molecule is oriented so that its TM LIES AT $54°$ to the helix axis, LD = 0. Finally, if a molecule is bound with random orientation, LD = 0. To distinguish between these possibilities, other techniques must be employed, e.g. circular dichroism will show if the molecule is bound in a chiral environment, see CD section.

The minor groove is oriented at ~ $45°$ to the helix axis. Therefore, minor groove bound molecules typically show positive LD signals. If a molecule intercalates, it has an orientation similar to the surrounding basepairs and thus has a negative LD signal.

If a molecule is fully bound to DNA, There is correspondence between its LD and absorption spectra. In such case, the LD^r can be calculated (LD/A_{iso}) and from it orientation angles can be deduced by comparison with a standard, which is generally the LD^r of the base pairs.

 This eliminates the need to quantify the orientation factor (S). Usually α_{DNA} is set at $86°$, see above.

$$\frac{LD^r(dye)}{LD^r(DNA)} = \frac{1.5\ S\ (3<cos^2\alpha_{dye}> -1)}{1.5\ S\ (3<cos^2\alpha_{DNA}> -1)} \qquad (5)$$

LD measurments were performed to establish the binding modes of the **Pf** dyes. Negative LD (Figure 19) and LD^r (Figure 20) values in the UV of the same order for Calf thymus DNA are seen for every dye (**Pf**, **PD**, **PDMe$^+$**). In addition, negative LD and LD^r values in the visible region for dyes bound to DNA strongly suggest dye

intercalation. The LD^r magnitudes of dye bound into DNA in the visible region and UV regions are approximately the same order for **PD**, while the LD^r magnitude of **Pf** in the visible region is larger than its value in UV region, and for **PDMe$^+$** the magnitude is lower in the visible than the UV. Higher visible LD^r is often observed for strong intercalators and suggests either a high local orientation around the bound dye compared to the rest of the DNA or that the dye (**Pf**) only binds strongly to DNA that is highly oriented.

Dye	LD^r (dye) / LD^r (DNA$_{260}$)	λ_{dye} (nm)	α_{dye}
Pf	1.1392	445	~90°
PDMe$^+$	0.7930	425	75°
PD	0.9139	420	80°

Table 4. Calculated orientation angle factors of **Pf**, **PD** and **PDMe$^+$**if $\alpha_{DNA} = 90^\circ$.

For structural interpretation of LD, reduced linear dichroism (LD^r) spectra were computed (Figure 22) using Equation (4) and tabulated in Table 4. In general, the LD^r signals at 260 nm for DNA with and without dye report on changes in base orientation induced by dye binding, although overlap of strong dye absorption with DNA at 260 nm precludes quantitative analysis. The ratio of LD^r signals in the visible and UV regions allows calculation of the angle between the dye and base pair planes. An important caveat is that the latter comparison is valid only if all the dye absorption arises from bound material, since free dye contributes to isotropic absorption but not to LD. Therefore, spectra were measured under conditions (low salt and high P/D) that favour complete binding. For our samples, there was good correspondence between the isotropic absorption and LD spectra, and close to 100% of dye is bound.

Negative LD^r signals in the dye visible absorption bands (Figure 22) are consistent with the chromophore long axes lying approximately parallel to the base pair planes. For **Pf**, this agrees with previous electric LD results which showed the ring system was parallel to the base planes for DNA with various base compositions.[44] **Pf** shows greater magnitude LD^r in the visible than in the UV. For **PD** and **PDMe$^+$**, the visible LD^r magnitude is lower than that in the UV. Previous studies have inferred an effective value of 80-86° for the orientation of the base pairs to the helix axis.[34, 43] Nevertheless, significantly more negative LD^r in the dye than the DNA band, as observed for **Pf**, has been reported previously for other intercalators such as methylene blue.[45] Previous spectral analysis[46] of **Pf** and related dyes assigned the 465 nm absorption solely to a long-axis polarized transition, and 263 nm absorption predominantly to long-axis

polarized transitions with a small contribution from a short-axis polarized transition. Similar assignments are likely for **PD** and **PDMe$^+$**. Thus different values of LD^r(vis)/LD^r(UV) suggest that **PD** and **PDMe$^+$** adopt slightly different intercalation geometries than does **Pf**, as also inferred from CD spectra. Wedging intercalation from the major groove, due to the bulky substituents impeding full insertion between the base pairs, would result in smaller LD^r for the dye since the chromophore would sample a range of orientation, as observed for piperazinecarbonyloxyalkyl derivatives of anthracene and pyrene.[47]
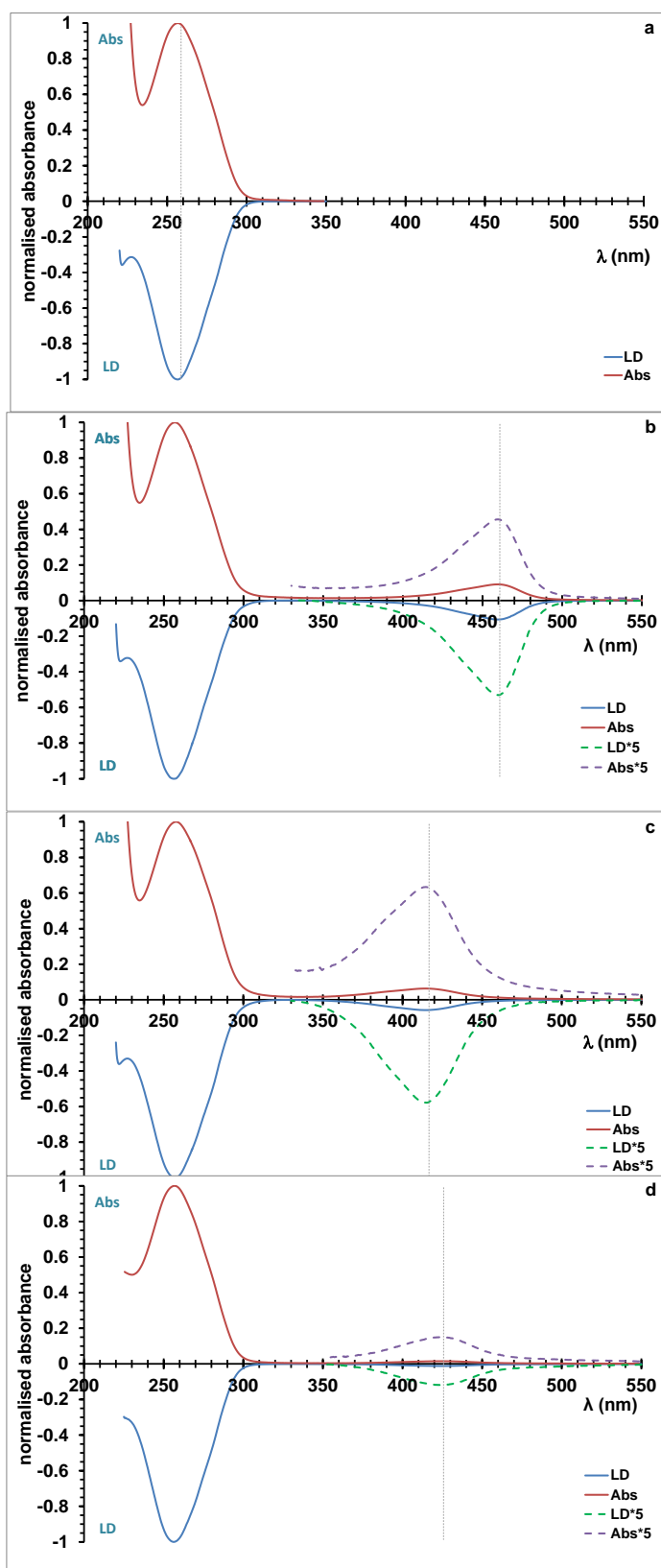
Figure 21. Linear dichroism (LD) and isobestic absorption (abs) spectra of (a) DNA; (b) DNA + **Pf**; (c) DNA + PD; (d) DNA + PDMe$^+$. All measurements recorded for the solutions of 20 μM **Pf**, 20 μM **PD** and 20 μM **PDMe**$^+$ with and without 1mM CT DNA. Data are normalised to 1 at 258 nm. [**Pf**] = 16 μM; [**PD**] = 28 μm; [**PDMe**$^+$] = 20 μM; [DNA] = 1mM; 5 mM phosphate (pH 6.9)/1% DMSO. Rotation speed = 600 rpm.
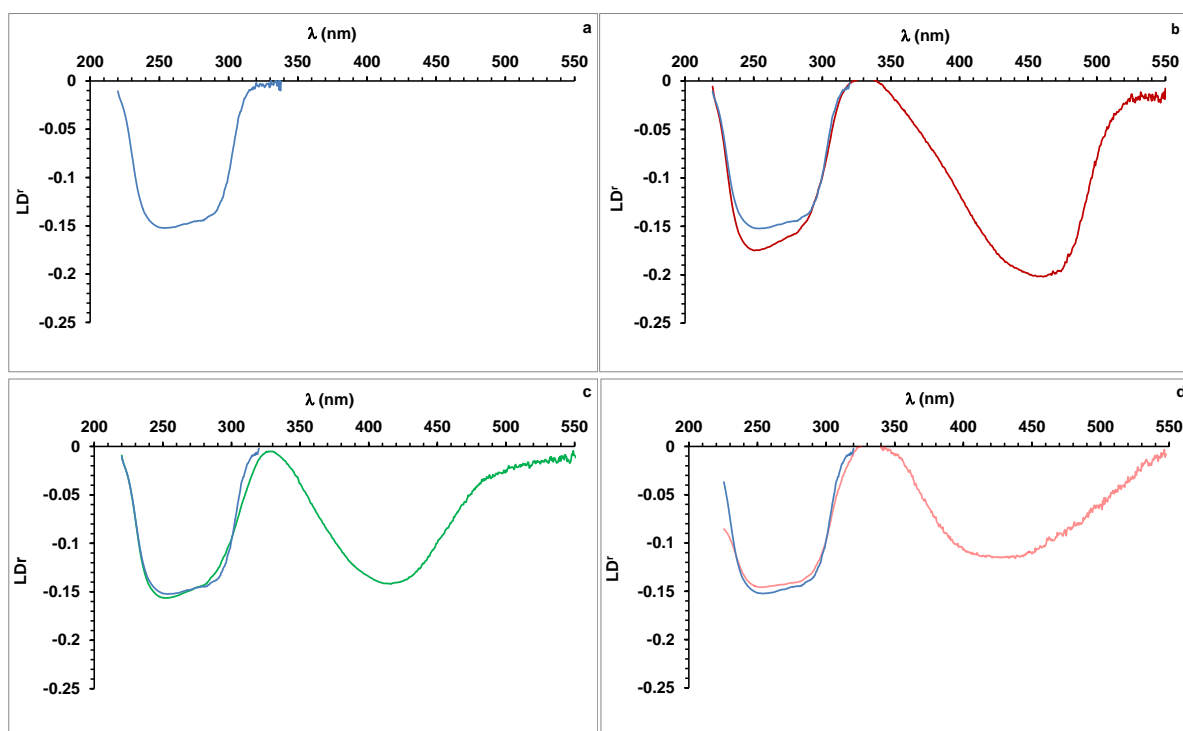
Figure 22. Reduced linear dichroism (LD^r) spectra of (a) DNA; (b) DNA + **Pf**; (c) DNA + **PD**; (d) DNA + **PDMe$^+$**. P/D = 50; [DNA] = 1mM. Shear gradient = 1900 s^{-1} (600 rpm). All measurements recorded for the solutions of 20 μM **Pf**, 20 μM **PD** and 20 μM **PDMe$^+$** with and without 1mM CT DNA.

2.7 Circular Dichroism

CD measuraments were also performed to elucidate the dye (intercalator) binding mode (at a DNA/dye ratio of 100), see Figure 23. CD is an excellent spectroscopic technique for demonstrating interaction of a small molecule with DNA. Even though a non-chiral molecule has no intrinsic CD, binding to a chiral medium such as the right-handed B-DNA duplex confers a CD signal in its absorption band (called induced CD, ICD). Any changes in the DNA CD spectrum on binding of a small molecule indicate an alternation of the DNA structure.

Pf, **PD** and **PDMe$^+$** are achiral in aqueous solution. On binding to DNA, all three dye exhibit induced circular dichroism (ICD) signals in their visible absorption bands (Figure 23b). The ICD for **Pf** resembles that reported previously at similar binding ratios at low ionic strength.[48-50] The ICD signals are weak, which is consistent with predominantly intercalative binding.[51] The magnitude of the induced CD for intercalated molecules is predicted to be quite small ($\Delta\varepsilon/\varepsilon <$ ca. 1×10^{-5}) and may be positive or negative depending on the orientation of dye to DNA base pair. The ICD for Pf resembles that reported previously at similar binding ratios at low ionic strength.[48-50] The non-conservative splitting pattern

has been attributed to degenerate vibronic exciton coupling between intercalated and externally bound dyes.[22, 50]

External binding is found to be minimal at high concentration of salt but more important at low salt concentrations even at the high P/D ratios used in the CD experiments for, **Pf**, **PD** and **PDMe**$^+$.[49, 50]

The deconvoluted CD spectrum of pure intercalated **Pf** is reported to be positive but that of acridine orange, which is tetramethylated on the exocyclic nitrogens, is negative.[50] This was attributed to different intercalation geometries of the two dyes, since the transition moment involved is the same long-axis polarized π-π^* transition for each.[19, 49, 50] It was suggested that H-bonds between **Pf** and the DNA backbone, as observed in crystal structures,[19, 49, 50] are ponsible for that difference since the magnitude of the **Pf** ICD was sensitive to increasing ionic strength.

Negative ICD spectra for **PD** and **PDMe**$^+$ suggest that these dyes might have different intercalation orientations more similar to acridine orange than **Pf**, although in natural DNA it could also indicate different sequence preferences.[19, 45, 49, 50, 52, 53] However, the recently reported ICD spectra[45] for **Pf** bound to [poly(dA-dT)]$_2$ and [poly(dG-dC)]$_2$ are similar and both show splitting, so sequence is unlikely to be the source of the differences. The absence of splitting in the ICD spectra of **PD** and **PDMe**$^+$ suggests that external binding is not as important for these dyes as for **Pf**, perhaps due to the increased bulk of the side chains that could hinder association of extra dyes in the major groove. This is consistent with the report that external binding was blocked by glycosylation of the major groove in T2 DNA.[49]
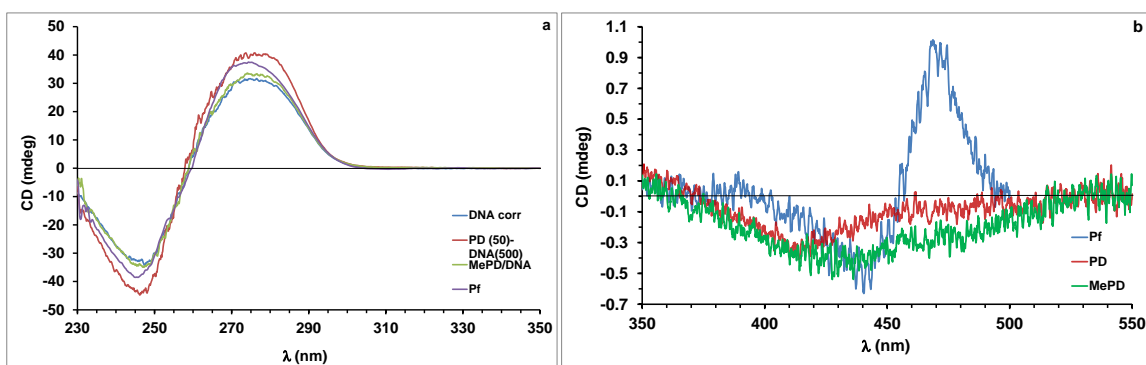
Figure 23. Circular dichroism (CD) spectra of **Pf**, **PD** and **MePD**$^+$ (a) in the UV and (b) in the Vis in the presence of CT –DNA . [**Pf**] = 10 μM/[DNA] = 500 μM; [**PD**] = 50 μM/[DNA] = 1000 μM; [**PDMe**$^+$] = 50 μM/[**DNA**] = 500 μM; 5 mM phosphate (pH 6.9)/1% DMSO.

2.8 Emission with CT-DNA and Polynucleotides

Light of the correct energy stimulates molecules of a substance from its ground state to a higher energy level (excited state). The molecules can return to ground state by losing energy, mainly heat to its surroundings. In some cases a fraction of absorbed energy is emitted as radiation, but generally at a longer wavelength relative to the exciting light stokes shift. This process is known as fluorescence and such molecules are fluorescent.

The interaction of DNA with a fluorescent molecule usually gives rise to a shift of emission maximum and a increasing or decreasing change in fluorescent quantum yield.[54, 55] Dyes with enhanced fluorescence are often used as DNA stains. In the absence of DNA, the fluorescence quantum yield of these dyes decreases due to e.g. conformational changes or protonation processor with solvent. On the other hand, binding of these dyes to DNA provides a shielding environment from solvent molecules and also reduced conformational flexibility of dyes. As a result the emission intensity increases.

The fluorescence intensity of other types of fluorescent compounds decreases on the association with DNA. An electron- or energy transfer between the excited dye and DNA could be the reason for this quenching.[56] The absorbance maxima of organic dyes appear at longer wavelengths than DNA absorbance. Therefore, the energy transfer between excited dye and DNA is disfavoured. Most often, an electron-transfer reaction between excited dye and the DNA bases occurs, with guanine being the base with the highest tendency to be oxidized.

The emission of **Pf**, **PD** and **PDMe**$^+$ is on binding to calf-thymus DNA**,** [poly(dG-dC)]$_2$ and [poly(dA-dT)]$_2$, as shown in following sections.

2.8.1 Proflavine Emission with Different DNA Sequences

The emission of **Pf** is decreased during titration of the dye with DNA. This is attributed to electron transfer from guanine to the singlet state of the dye.[35, 57] The emission intensity of **Pf** bound to CT-DNA decreases in the range P/D = 0-20 and thereafter slowly rises as shown in Figure 24c and 24d, mirroring previous reports.[57] **Pf** fluorescence is quenched by guanine (Figure 24a) but enhanced by adenine (Figure 24b), from comparison of emission in the presence of [poly(dA-dT)]$_2$ and [poly(dG-dC)]$_2$.

The quenching observed at low P/D with [poly(dA-dT)]$_2$ is attributed to self-quenching by externally attacked dyes, a known binding mode for **PfH**$^+$,[22, 23, 49] and at high binding ratios the intensity increase reflects the increase in reported lifetime.[57]
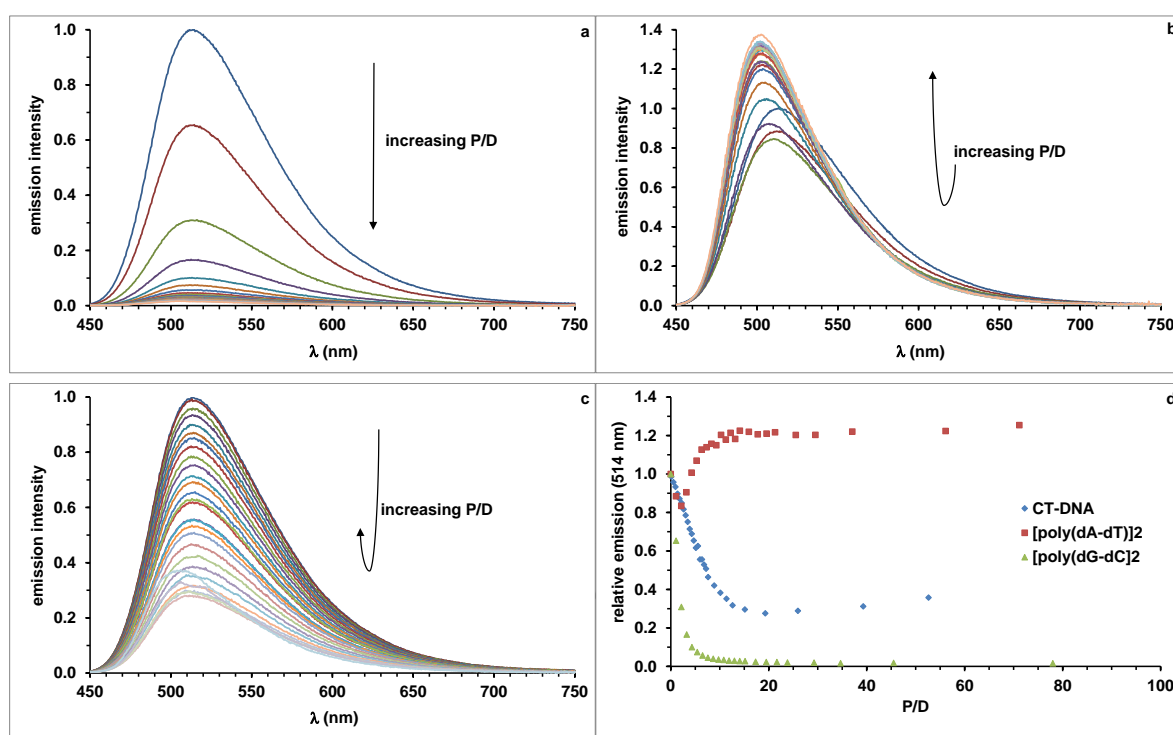
Figure 24. Emission spectra for titration of **Pf**$^+$ with added (a) [poly(dG-dC)]$_2$, (b) [poly(dA-dT)]$_2$ and (c) CT- DNA; **d**) comparative relative emission intensities. [**Pf**] = 5 μM; 5 mM phosphate buffer (pH 6.9)/1%DMSO; 21 °C. Excitation wavelength: **Pf** (415 nm).

2.8.2. PD emission with different DNA sequences

PD is quenched by adenine as well as guanine in polynucleotides (Figure 25b and 25a), indicating that its singlet state is more readily reduced than that of **Pf**. This can rationalized by considering the computational and spectroscopic data presented previously. Ground state reduction is predicted to occur more readily than for **Pf** due to the lower electron densities on the aromatic ring system of **PD**.

Additionally, the **PD** $S_0 \rightarrow S_1$ transition is at higher energy than that of **Pf**. As a result, the excited singlet state of **PD** are significantely more oxidizing than that of **Pf**.
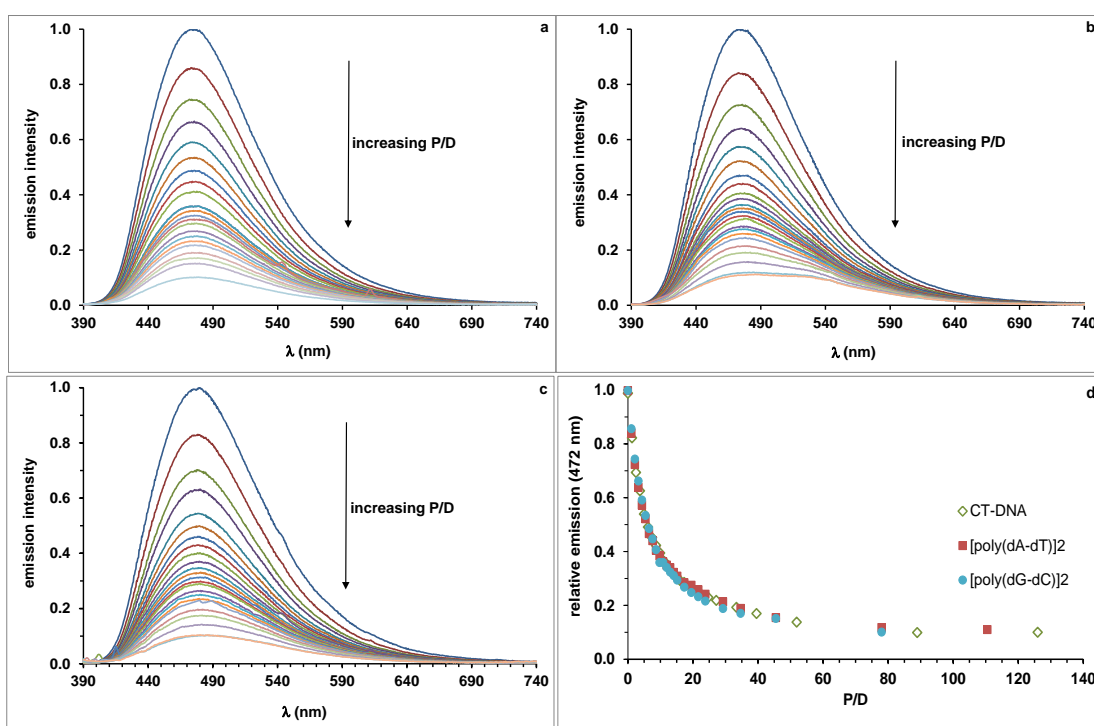
Figure 25. Emission spectra for titration of **PD** with added (a) [poly(dG-dC)]$_2$, (b) [poly(dA-dT)]$_2$ and (c) CT- DNA; (d) comparative relative emission intensities. [**PD**] = 5 μM; 5 mM phosphate buffer (pH 6.9)/1% DMSO; 21 °C. Excitation wavelength: **PD** (380 nm).

2.8.3 PDMe$^+$ emission with different DNA sequences

PDMe$^+$ behaviour is similar to **PD** and is quenched by adenine as well as guanine in polynucleotides (Figure 26b and 26a), indicating that its singlet states are also more readily reduced than **Pf**.

This can rationalized by considering some computational and spectroscopic data discussed for **PD**.
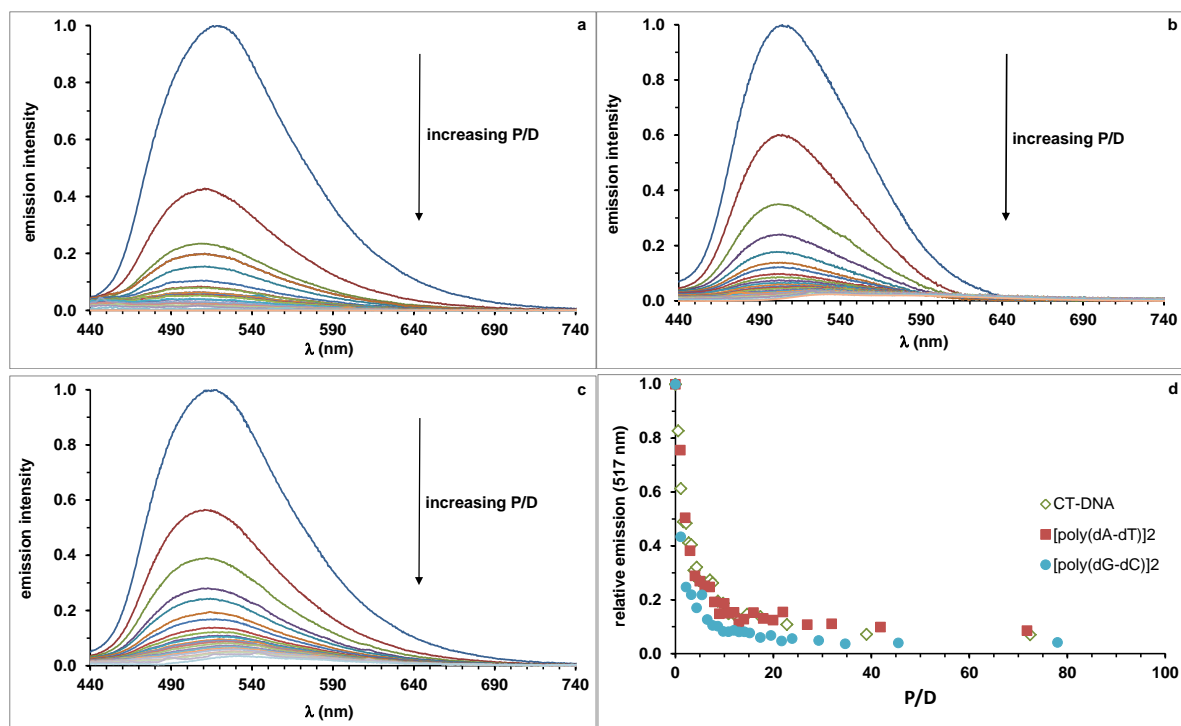
Figure 26. Emission spectra for titration of **PDMe$^+$** with added (a) [poly(dG-dC)]$_2$, (b) [poly(dA-dT)]$_2$ and (c) CT- DNA; (d) comparative relative emission intensities. [**PDMe$^+$**] = 5 μM; 5 mM phosphate buffer (pH 6.9)/1%DMSO; 21 ℃. Excitation wavelength: **PDMe$^+$** (415 nm).

2.8.4 The comparative conclusion of Pf, PD and PDMe$^+$ emission

The emission titrations indicate that **PD** and **PDMe$^+$** show little selectivity in binding to [poly(dA-dT)]$_2$, [poly(dG-dC)]$_2$ or mixed sequence CT-DNA. **Pf** appears to bind more strongly to [poly(dG-dC)]$_2$ than to [poly(dA-dT)]$_2$ and CT-DNA under our low ionic strength conditions, although other studies report little selectivity at higher ionic strength.[34] However, recent molecular modelling[58] suggests that **Pf** should bind more strongly to [poly(dG-dC)]$_2$ than [poly(dA-dT)]$_2$ due to greater $\pi - \pi$ stacking in the former case. The observations for **Pf** can be interpreted due to the smaller substituents on **Pf** allowing it to intercalate deeply into base pair pockets, thus benefiting from enhanced $\pi-\pi$ stacking in the GC pockets. By contrast, **PD** and **PDMe$^+$** can not

intercalate as deeply as **Pf** from the major groove due to their bulky substituents, so they experience similar stacking interactions in all type of base pair pockets.

2.9 Thermal denaturation

One powerful and rapid approach for determination of the stabilizing effect of the bound dyes on the DNA helix is defined in the term of thermal denaturation.[59] The melting experiment is performed on samples of DNA which are heated in a buffer solution with different ionic strengths in the presence or in the absence of intercalators. The UV absorbance is monitored at a wavelength where the nucleic bases absorb strongly (usually 260 nm). The plots of normalized absorbance versus temperature are known as melting curves. The denaturation (duplex-to-random coil transition) of DNA is accompanied by a sharp increase of UV absorption, and the mid-point of this transition, (when one-half of DNA is in the double-helical state) is defined as the melting temperature of the DNA sample, T_m. Intercalation of small molecules stabilises the ds-DNA against thermal denaturation and as a result increases the T_m. The differential between the melting temperatures of intercalator-bound DNA and naked DNA (ΔT_m) can be interpreted in terms of the strength of binding.
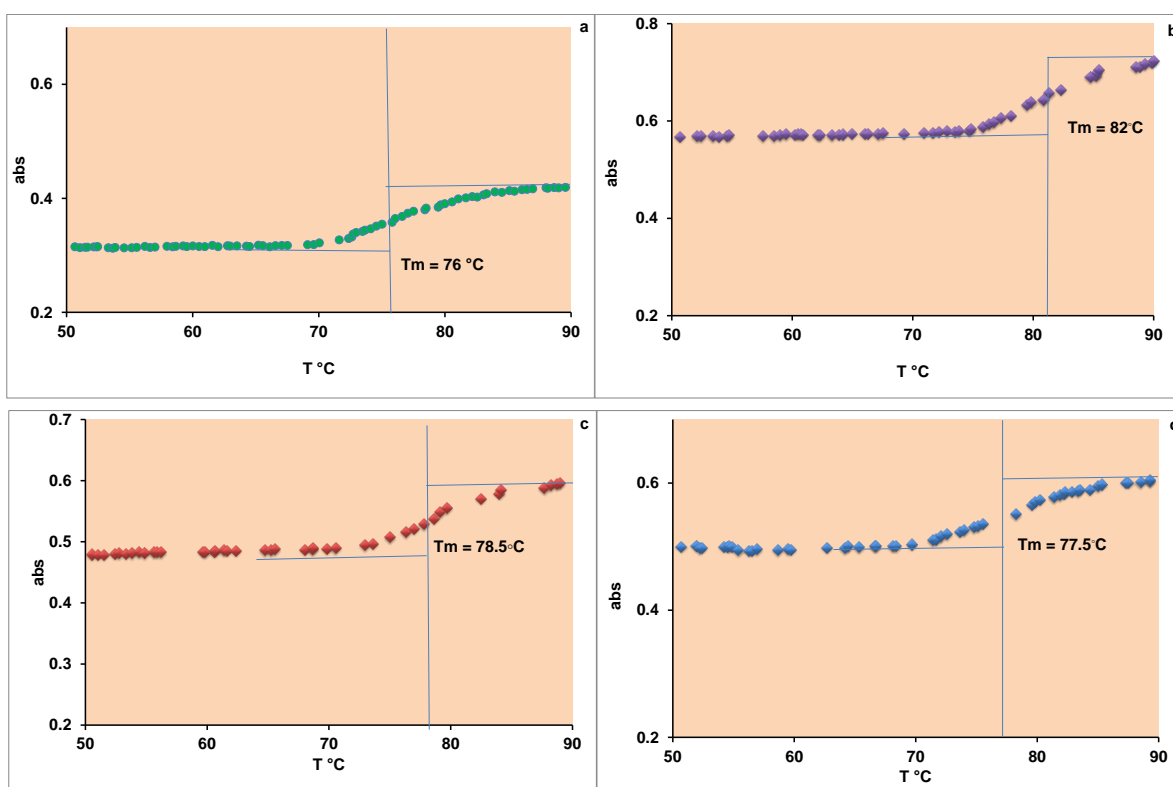
Figure 27. Schematic representation of a thermal denaturation experiment of (a) CT – DNA (b) CT-DNA + **Pf** (c) CT-DNA + **PDMe$^+$** d) CT-DNA + **PD**. [DNA] = 49 µM , [dye] = 5 µM, $\lambda_{measured}$ = 260 nm, solvents: 1% DMSO and 50 mM phosphate buffer.

Representative melting curves are shown in Figure 27 for DNA with the different dyes. After adding intercalators into DNA the melting temperature of ds-DNA increases from 76 ºC to 77.5 ºC ,78.5 ºC and 82 ºC for **PD**, **PDMe**[+] and **Pf** respectively. This trend reflects the association constants of the dyes for CT-DNA, see Table 3.

2.10 Viscosity

Proflavine, **Pf**, is a classical intercalator that increases sonicating DNA viscosity due to lengthening of the duplex as previously has been reported.[34, 44, 60] Studies with different DNAs found that elongation was greater for AT-rich than GC-rich DNA.[44] It was argued from this and T-jump measurments that **Pf** has a greater tendency to bind externally with GC-rich DNA.

Figure 28 shows that **PD** and **PDMe**[+] also increase the viscosity of long CT-DNA, but to a lesser extent than **Pf**. **Pf** is quantitatively bound under the conditions used, and the initial slope of 1.40 (up to r = 0.1) is consistent with monointercalation (for simple intercalators, containing only intercalating chromophore) into high molecular weight DNA with no significant change of persistence length (Figure 28). It was recently reported that no change in persistence length occurs on bis-intercalation (for bifunctional molecules that possess two planer intercalating aromatic ring systems covalently linked by chains of varying length) of YOYO-1, although other experiments have indicated that intercalators might either increase or decrease persistence length.[61]
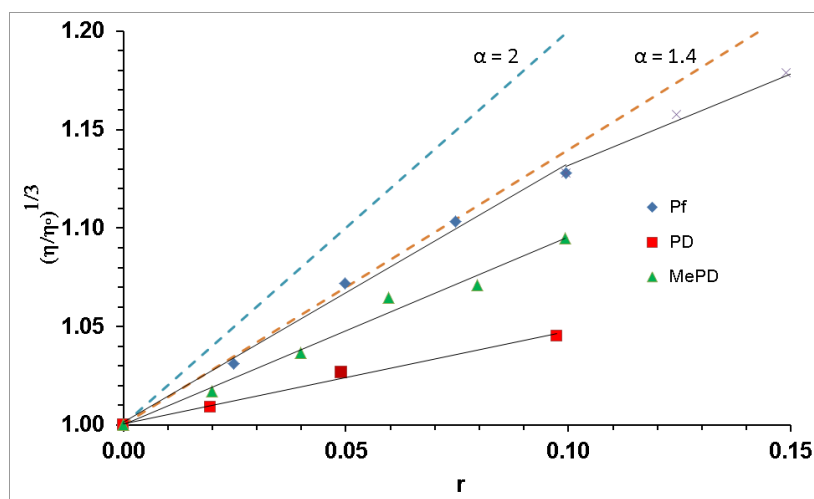
Figure 28. Viscosity of CT-DNA on addition of **Pf**, **PD**, and **PDMe**[+]. 5 mM phosphate/1% DMSO; [DNA] = 300 μM; 25 °C. The dashed line represents a slope of 2 as predicted for monointercalation with rod-like DNA. The dotted line represents a slope of 1.4 as predicted for monointercalation with random coil DNA.

PD and **PDMe**[+] are also quantitatively bound and, although their slope of (0.5 and 0.99, respectively) are lower than for **Pf**, they are still consistent with intercalation. The slope

for **PD** is substantially lower than for **Pf** or **PDMe⁺,** and its low value implies either that **PD** is not fully intercalated and some dye is externally bound, or that binding causes a reduction in persistence length that counteracts the increase in contour length due to intercalation. The lack of splitting in CD spectroscopy suggests that external binding is not important for **PD** and **PDMe⁺**, so that possibility is discard. Minor groove binders cause little change in viscosity[62] but partial intercalators are known to decrease the viscosity of DNA by bending through wedging,[63, 64] as covalent binding of cisplatin that statically bends DNA.[65] These bending interactions decrease the viscosity of rod-like DNA by shortening the axial length. In long DNA, the effect can be equated with a decrease of persistence length which reduces the relative viscosity according to Equation. Since **PD** and **PDMe⁺** increase viscosity but less so than **Pf**, they seem to have features of both, classical and wedging intercalators and the results suggest they have an interaction geometry that reduces the DNA persistence length.

2.11 Intercalative binding of modified proflavines

Proflavine was chosen as the framework molecule for functional intercalators since its intercalative binding is strong and well-characterised the exocyclic amino groups are both located in the major groove and have H – bonds to the phosphate and sugar groups of the backbone as this crystal structure was confirmed by the NMR structure with a tetramer [d(CCGG)]$_2$[66]and crystal structures with RNA[67] and DNA[68] CG dinucleotide minihelices. The wide major groove should be able to accommodate the substituents on the exocyclic amines when the modified dyes are intercalated. **PD** and **PDMe⁺** are likely to bind in a similar manner as **Pf** thus placing the azide groups of in the major groove. Linear dichroism results indicate that **Pf**, **PD** and **PDMe⁺**, all, intercalated between DNA base pairs. The small induced CD signals are consistent with intercalative binding. Other spectroscopic methods indicate relative binding affinities of three compounds. In addition, the LD^r signals for these compounds, **PD** and **PDMe⁺** are strongly negative but smaller than **Pf**. These observations suggest that **PD** and **PDMe⁺** bind to DNA by intercalation but different geometries and dynamics than **Pf** because of bulky substituents which probably prevent them from being deeply embedded in the interaction pocket.

It seems that the acridine moiety of **PD** and **Pf** cannot intercalate deeply with DNA base pairs and instead intercalates at the edges of the base pairs closest to the major groove. For example [Ru(phen)$_3$]$^{2+}$[64, 69, 70] partially intercalates from the minor groove in this manner. For **PD** and **PDMe⁺** with smaller LD^r signals that are suggestive of

partial/wedging intercalation, it is likely that these dyes experience a range of orientation angles other than perpendicular to the helix axis.[47] Against **Pf** which has preference to GC-rich sequence, **PD** and **PDMe**[+] have little sequence selectivity. Therefore, this is an advantages for these intercalators to be as non-sequence specific anchors for directed self-assembly on DNA scaffold.

2.12 Protonation-Coupled intercalation of PD

When the phenomenon of intercalation and external binding occur, the spectra usually show a shift to longer wavelength with a decrease in the absorption. The behaviour of **PD** during titration was different from what was expected for intercalation. The absorbance λ_{max} for free **PD** and **PD** bound to DNA appeared at 378.5 nm and 414 nm, respectively see Figure 29. Although this spectrum shows a strong red shift to 414 nm, it also indicates the increase of absorption, usually $\pi-\pi$ stacking for intercalator leads to a decrease of absorbance. Thus, it is difficult to interpret what interaction occurs between **PD** and DNA. Therefore, a hypothesise was assumed that **PD** at pH 7 does not have a strong attraction to DNA. However, as **PD** approaches DNA, it becomes protonated and then intercalates as a monocation. Several compounds have been reported to behave in this manner. [71-73]

Coupled protonation and DNA binding has been reported previously for neutral dibenzoacridine[71] as well as other intercalators,[72] minor groove binders[73] and proteins.[74] It is also known that the apparent pK_a of cytosine is raised significantly from ~4.5 when it protonates on formation of CGC-triplexes, with a 3-5 unit increase reported for internal positions.[75] Moreover theory predicts that the DNA minor groove is more acidic than the surrounding solvent,[76] with experiments indicating a drop of up to 2 units.[77] This is likely a result of the high negative potential in the minor groove caused by electrostatic focussing.[78] Thus, the increase of apparent pK_a of **PD** on binding to DNA is not without precedent. Since the local pH in the DNA grooves is apparently much lower than bulk solution.[79]
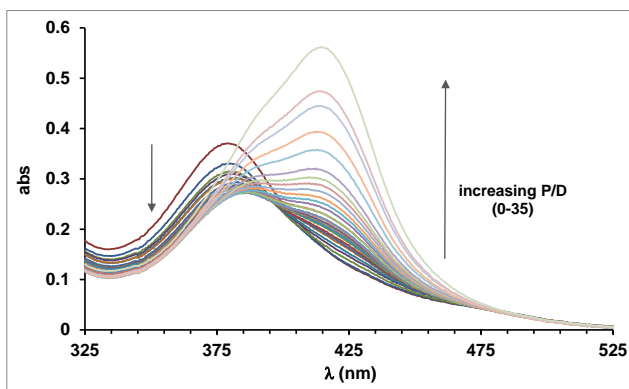
Figure 29. The titration curve of 96 uM **PD** with calf thymus DNA in phosphate buffer (pH=6.9) and 1% DMSO.

To prove this hypothesis, what is needed to know is what the spectrum of protonated monomer **PD** looks like. To obtain the spectrum of protonated **PD**, samples of **PD** at various pH (1-9) were prepared. The Figure 30 shows the associated spectra.
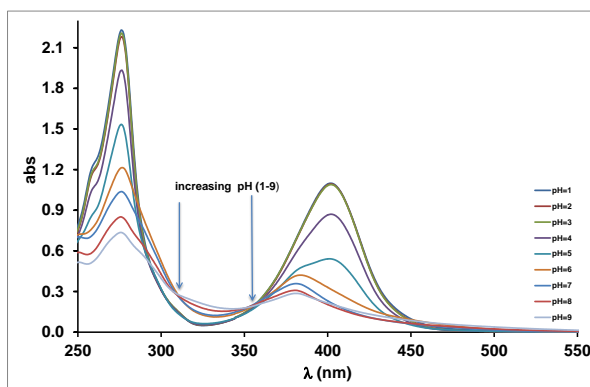
Figure 30. Variation of the absorption spectra of **PD**.with pH. (a) PD (54 μM); 5 mM phosphate (pH 6.9)/1% DMSO; pH adjusted with NaOH or H_3PO_4; 21 ℃

Figure 30 indicates that decreasing pH results in a shift of λ_{max} to longer wavelength accompanied by a strong increase in absorption. The manner in which the spectra change is the same as observed by Schulman *et al.* for 3-aminoacridine and several 3,6-diaminoacridines such as **Pf** in various states of protonation, although the pH ranges over which the changes were observed are different.[80] It is clear from comparison of spectra in Figures 29 and 30 and the extinction coefficients in Table 2 that the final spectrum with DNA represents a hypochromic shift with respect to the spectrum of **PDH**[+].

2. 13 Conclusions

Proflavine, **Pf**, can readily be modified with azide groups on its exocyclic amines via a amide linker. The resultant compound, **PD**, is neutral and binds weakly to DNA but methylation on the ring nitrogen gives a strongly binding dye, **PDMe$^+$**. Like **Pf, PDMe$^+$** and **PD** intercalate at high P/D values as evidenced by linear dichroism studies. **PD** is poorly soluble in water, but becomes protonated on binding to DNA, resulting in an apparent **pK$_a$** shift of >3 units. A recently deposited structure of **Pf** intercalated with an oligonucleotide places the amines in the major groove of DNA, and it is likely that modified dyes adopt a similar binding geometry. On the other hand, their bulky substituents appear to hinder deep intercalation, and therefore they lodge towards the edge of major groove. **PD** and **PDMe$^+$** are good candidates for applicaton as an intercalative anchor for assembly of supramolecular structure on a DNA acaffold since they bind strongly with little sequence selectivity.

2.14 Experimental

Material and Methods

Reagents and solvents were purchased from Sigma Aldrich. Proflavine hemisulfate salt hydrate as used as received. Polynucleotides [poly(dG-dC)]$_2$, [poly(dA-dT)]$_2$ and calf-thymus DNA were purched from Sigma. All nucleic acids were dialyzed extensively against pure water before use to remove excess salts, and stored in 5 mM phosphate buffer (pH 6.9).**PD**[81] and **PDMe$^+$**[82]were synthesised as new compounds. NMR was performed on a 300 MHz Bruker spectrospin WM 300 WB spectrometer and UV-spectra were measured on a Cary 100 Bio spectrometer. IR spectra on a Rad FTS-7, spectrometer and Mass spectra were recorded a Waters Micromass LCT premier mass spectrometer.

The following sections describe the synthetic experimental details and characterisation.

Synthesis of PD: N,N'-(acridine-3,6-diyl)bis(2-azidoacetamide).

(Pf)

intermidiate

(PD)
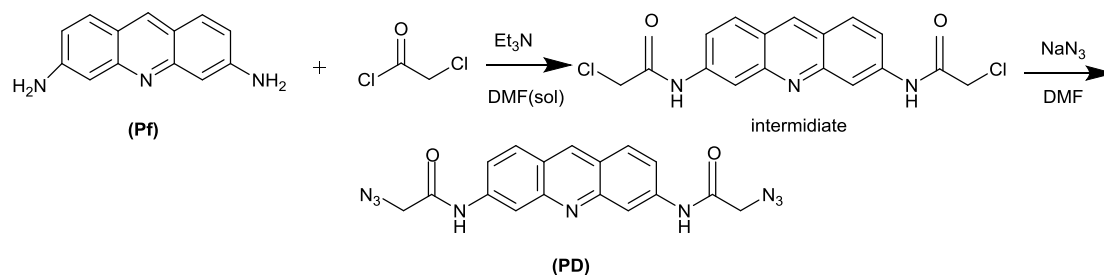
Anhydrous DMF (400 mL) and triethyl amine (2 mL, 14.4 mmole) were added to **Pf** (1 g, 3.87 mmole). This solution was stirred vigorously for half an hour at room temperature and then chloroacethyl chloride (6 mL, 75.3 mmole) was added drop wise at 0°C temperature. The solution was allowed to stir for 3 hours. TLC was performed in chloroform/methanol (90:10) to show that the reaction had gone to completion.

Water (100 mL) was added to quench the reaction. The solvent was then removed in vacuo and the residue was filtered. The precipitate on filter paper was washed with water (3 × 50 mL) and chloroform and then dried in vacuum-oven at 60°C to afford an orange solid (intermediate) in yield of 1.12 g, 79.7%. In the further step, DMF (375 mL) was added to the orange solid (500 mg, 1.38 mmole). Sodium azide (0.55 g, 9.1 mmole) was then added and the reaction solution was stirred and heated at reflux at 80°C overnight. TLC was performed in chloroform/methanol (95:5) that the reaction had gone to completion. The reaction mixture at room temperature was cooled and solvent was then removed in vacuo. ^{1}H NMR spectrum of residue confirmed the successful synthesis of intermediate. ^{1}H NMR (300 MHz, DMSO-d6, 25°C) intermediate: δ 11.47(s, 2 H, NH), 9.65 (s, 1 H, CH) 8.86 (s, 2 H, CH) 8.41 (d, 2 H, CH, J = 9.21) 7.8 (dd, 2 H, CH, J = 1.61, 9.10) 4.48 (S, 4 H, CH$_2$)

^{1}H NMR (300 MHz, DMSO-d6, 25°C) of **PD** δ (300 MHz, DMSO, 25 °C) 10.82 (s, 2 H, NH) 8.90 (s, 1 H, CH) 8.50 (s, 2 H, CH) 8.1 (d, 2 H,CH J = 9.05) 7.7 (dd, 2 H, CH, J = 1.99, 9.05) 4.2 (s, 4 H, CH2).

^{13}C NMR (400MHz, DMSO-d6), δ167.24, 149.70, 140.07, 135.32, 129.24, 122.65, 120.01, 114.47, 51.50).

HRMS (ESI, m/z): **[M +H]**$^+$ calculated for C$_{17}$H$_{14}$N$_9$O$_2$, 376.1270; found, 376.1266.

IR spectroscopy showed a peak at 1675 cm^{-1} relative to carbonyl group and a new sharp peak at 2114 cm^{-1} characteristic of an azide group which also confirmed the successful conversion of **Pf** to **PD**.

Synthesis of PDMe[+]: 3,6-bis(2-azidoacetamido)-10-methylacridin-10-ium
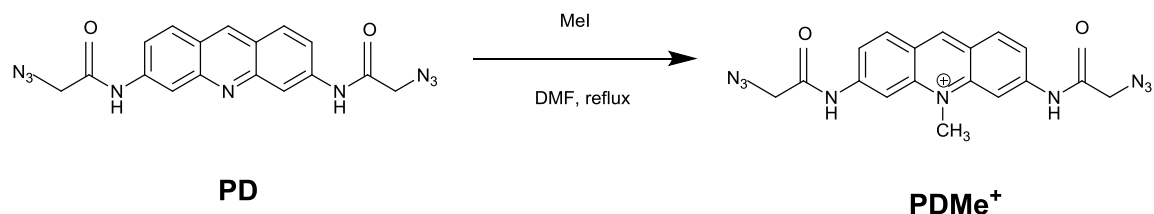
PD (200 mg, 0.53 mmole) was placed under vacuum and after an hour, 50 ml anhydrous DMF was added. The solution was stirred vigorously for 30 min then methyl iodide (100 µL, 1.6 mmole) was added. The solution then was stirred under N_2 with reflux (86°C) for 48 hours. TLC was performed in chloroform/methanol (95:5) to show that the reaction had gone to completion. Solvent was removed in vacuo and the residue was extracted with ethyl acetate. The organic layer was dried with $MgSO_4$ and evaporated to afford a orange-red solid which was purified by column chromatography using DCM/methanol (95:5) This gave a dark red solid with a yield of 10%.

^{1}H NMR (300 MHz, DMSO d6, 25°C). δ 11.296 (s, 2 H, NH), 9.742 (s, 1 H, CH), 8.994 (s, 2 H, CH), 8.505 (d, 2 H, CH), 7.885 (dd, 2 H, CH), 4.49 (s, 3 H, CH3), 4.31 (s, 4 H, CH_2).

13C NMR (400 MHz, DMSO d6) δ 169.36, 147.84, 143.29, 133.91, 122.90, 120.92, 103.92, 55.45, 52.33, 49.13, 38.13.

HRMS (ESI, m/z): [M][+] calculated for C18H16N9O2, 390.1427; found, 390.1437.

IR spectroscopy showed the peak changes to 1695 cm^{-1} relative to carbonyl group and the sharp peak to 2099 cm^{-1} characteristic of the azide group.

Instruments and measurments

Spectroscopic experiments were carried out in 5 mM phosphate buffer 1% DMSO at 21 ℃, unless otherwise stated.

UV/vis absorption

UV/Vis measurements were carried out on a Cary 100 Bio UV/visible spectrophotometer and all data are normalized to a 1 cm pathlength. Titrations with calf thymus DNA solution were performed by adding aliquots of concentrated DNA to a constant concentration of ligand. The concentration of all materials were determined by UV/vis absorption spectroscopy using the following extinction coefficients, determined

analytically for **PD** and **PDMe**[+] and obtained from literature for other materials. **Pf** (445 nm) 41,000 M^{-1} cm^{-1} [32,33]; **PD** (381 nm) 6,600 M^{-1} cm^{-1}; **PDMe**[+] (409 nm) 9,200 M^{-1} cm^{-1}; CT-DNA (260 nm) 6,600 $M^{-1}cm^{-1}$; [poly (dA - dT)]$_2$ (262 nm) 6,700 M^{-1} cm^{-1}; [poly (dG-dC)]$_2$ (254 nm) 8,400 M^{-1} cm^{-1}.

DNA binding analysis

Self-assembly of nanostructures through DNA intercalation requires evidence that selective intercalators bind strongly enough to DNA to assemble for assembly of stable nanomaterials. The following data analysis allows calculation of the association constant of an intercalators as well as determination of binding site size. This information is important to establish whether the new modified intercalators follow the neighbour exclusion principle and are stable enough with DNA to accommodate other materials containing new functionalities.

DNA molecules simultaneously can bind a number of dye intercalator molecules such as proflavine in a number of ways. The association constant of a DNA intercalator can be obtained by the titration of a solution of intercalator with a increasing concentration of DNA. The maximum absorbance peak in visible area during titration is used to obtain the fraction of intercalators which bind to DNA or remain free in solution.

$$[DNA] + [Intercalator] \xrightleftharpoons{K} [DNA\text{-}Intercalator] \qquad (6)$$
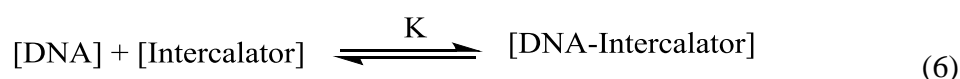
It is common to present binding data as a Scatchard plot that is r/C_f versus r, where $r = C_b/P$ which is superlative in its ability to enhance nonlinearities due to binding site overlap and multiple binding sites.

In general, the notations that *r is* the number of bound intercalator molecules per DNA unit ($r = C_b/P$, where C_b is the concentration of bound intercalator molecules and P is DNA concentration), n, the number of binding sites per DNA base unit and C_f the concentration of free dye.
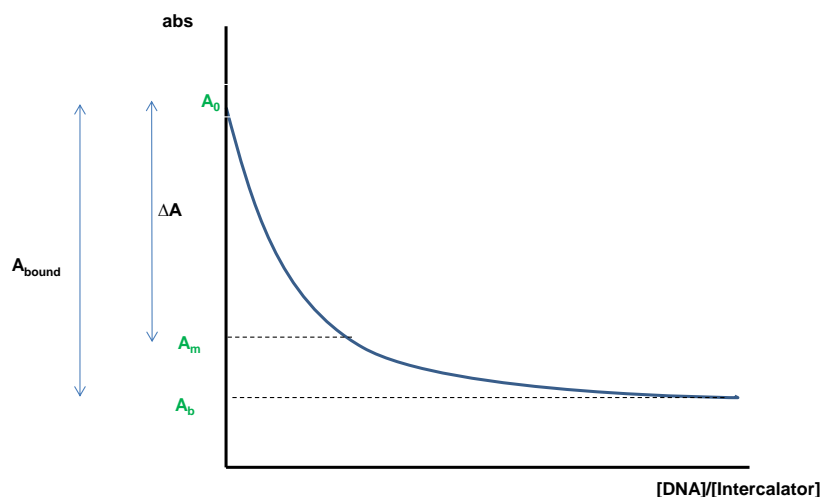
Figure 34. Schematic plot of absorption variation with increasing binding ratio ([DNA]/[intercalator]). A_0 is the absorption of intercalator in the absence of DNA, A_b is the absorption of fully bound intercalator, and A_m is the measured absorption at any binding ratio.

Figure 34. illustrates how the absorbance of a chromophore at a fixed wavelength changes when DNA is added, causing the absorbance to decrease. Under suitable conditions, a plateau value is reached when 100% of the chromophore is bound. To achieve these conditions, the concentrations of chromophore and DNA must be higher than the reciprocal association constant. According to Figure 15, the fraction of bound dye (α) at any binding ratio can then be calculated according to the following equation:

$$\alpha = \frac{(A0 - A_m)}{(A0 - A_b)} \tag{7}$$

And:

$$C_b = \alpha \times [C_{total}] \tag{8}$$

$$C_f = (1 - \alpha) \times [C_{total}] \tag{9}$$

Where C_{total} is total concentration of intercalator.

The basic binding model of Scatchard derives from a simple consideration of the law of mass action, where B_{app} represents the apparent number of binding sites per P (P is defined as a base concentration of DNA) and K_{app} is the apparent binding constant as shown in Figure 35.
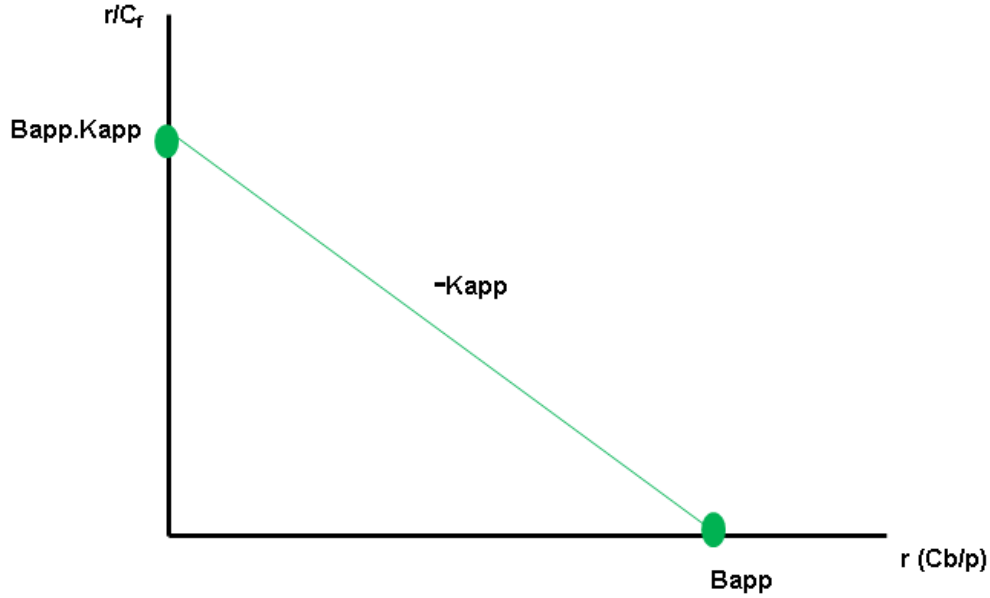
Figure 35: Scatchard plot of r/C_f versus r.

$$Kapp = \frac{[\,intercalator/DNA\ complex]}{[free\ intercalator][free\ binding\ sites\ of\ DNA]} \qquad (10)$$

$$= \frac{C_b}{(C_t - C_b)(B_{app}\ P - C_b)} = \frac{C_b}{C_f(B_{app}\ P - C_b)} \qquad (11)$$

$$\frac{r}{C_f} = K_{app}\ (B_{app} - r) \qquad (12)$$

Therefore: slope $= -K_{app}$

From the x-intercept (when y = 0): $0 = K_{APP}\ (B_{APP} - r) \Rightarrow K_{app}.B_{app} = K_{app}.r$ \qquad (13)

$r = B_{app}$ or $B_{app} = \dfrac{-intercept}{slope}$ = the number of binding sites per base of DNA. \qquad (14)

Nonlinearity of the binding plot may arise from several effects which are difficult to distinguish: overlap of binding sites, cooperative effects, existence of two binding sites, or intercalator aggregation in solution as shown in Figure 36.
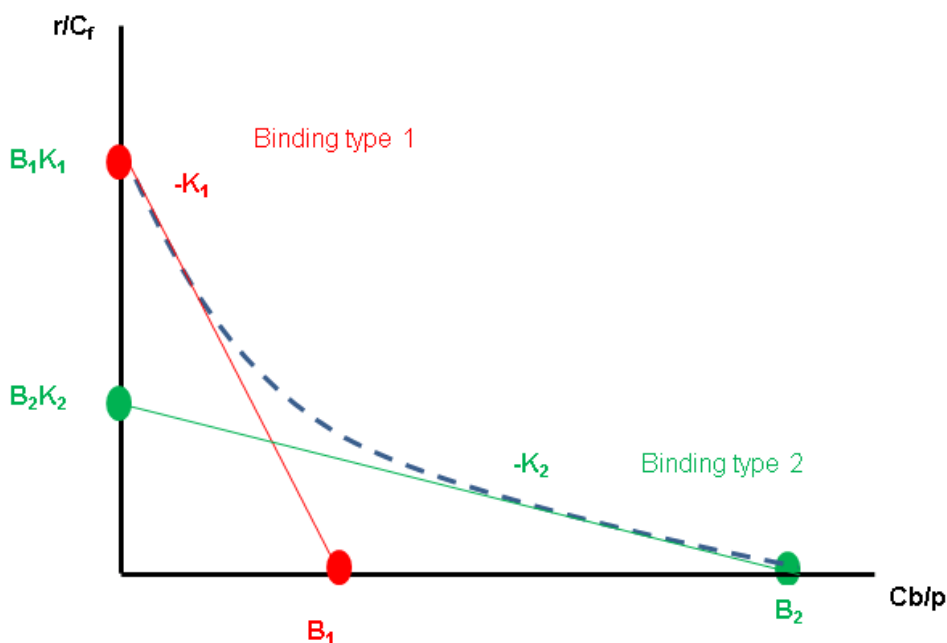
Figure 36. Scatchard plot of r/C_f versus r for two binding sites.

The Scatchard Equation is valid for equivalent and independent binding sites. In DNA, this is not always the case because of overlap of potential binding sites. This can cause the plot to deviate from linear behaviour at high binding ratio. This shape of plot can be filled using the McGhee and Von Hippel binding model as have been shown. Considering DNA as a linear lattice-like macromolecule with N independent binding, the McGhee/von Hippel model for noncooperative binding using the Scatchard representation is written as follows.[83-85]

$$\frac{v}{L} = K(1 - nv)[\frac{1-nv}{1-(n-1)\,v}]^{n-1} \qquad (15)$$

v = The number of ligand molecules bound per macromolecule.

vK = microscopic dissociation constant of each binding sites.

n = the number of repeating units occupied by the ligand ($= B_{app}^{-1}$).

For cooperative binding, the equation becomes:

$$\frac{v}{L} = K(1 - nv)[\frac{(2\omega-1)(1-nv)+v-R}{2\,(\omega-1)(1-nv)}]^{n-1}[\frac{1-(n+1)v+R^2}{2\,(1-nv)}]^2 \qquad (16)$$

where $\boldsymbol{R} = [1 - (n+1)v]^2 + 4\omega v\,(1-nv)^{1/2}$ and ω is the cooperativity factor which represents the interation between ligands bound contiguously ($\omega > 1$ for cooperative interactions; $\omega < 1$ for anticooperativity; $\omega = 1$ for noncooperative binding).

Estimation of bound ligand concentration

For binding of a ligand, L, to a site, S, in a biopolymer, we can write the following equilibrium:

$$L + S \underset{}{\overset{K}{\rightleftharpoons}} L{:}S \qquad\qquad (17)$$

We use the following nomenclature when considering the equilibrium quantitatively:

C_t = total ligand concentration

C_b = bound ligand concentration

C_f = free ligand concentration

S_t = total site concentration

S_b = bound site concentration

S_f = free site concentration

P = concentration of polymer units

B = number of sites per polymer unit = S/P ; $\therefore$ S = BP

X = concentration of bound sites = [L:S] = C_b

$$K = \frac{X}{C_f \cdot S_f} = \frac{C_b}{C_f \cdot S_f} \qquad\qquad (18)$$

$$K = \frac{C_b}{\left(C_t - C_b\right)\left(S_t - C_b\right)} = \frac{C_b}{C_t S_t - C_t C_b - C_b S_t - C_b^2} \qquad (19)$$

$$K\left(C_t S_t - C_t C_b - C_b S_t + C_b^2\right) - C_b = 0 \qquad\qquad (20)$$

$$KC_b^2 - \left(KC_t + KS_t + 1\right)C_b + KC_t S_t = KC_b^2 - \left(KC_t + KBP + 1\right)C_b + KC_t BP = 0 \qquad\qquad (21)$$

$$C_b = \frac{\left(KC_t + KBP + 1\right)\pm\sqrt{\left(KC_t + KBP + 1\right)^2 - 4K^2 C_t BP}}{2K} \qquad\qquad (22)$$

For C_t = 0.100 mM, P = 0.600 mM, K = 5.3×10^5 M^{-1}, B = 0.33

$$C_b = \frac{(158.94) \pm \sqrt{(158.94)^2 - 22247.28}}{1.06 \times 10^6} = \frac{158.94 \pm \sqrt{25261.9236 - 22247.28}}{1.06 \times 10^6} \quad (23)$$

$$C_b = \frac{158.94 \pm \sqrt{3014.6436}}{1.06 \times 10^6} = \frac{158.94 \pm 54.90577}{1.06 \times 10^6} = \frac{104.03}{1.06 \times 10^6} \text{ or } \frac{213.85}{1.06 \times 10^6} \quad (24)$$

$$C_b = 98 \times 10^{-6} \text{ M or } 202 \times 10^{-6} \text{ M}$$

$$\frac{C_b}{C_t} = \frac{0.098\,\text{mM}}{0.100\,\text{mM}} = 98\% \quad (25)$$

The calcalation above is the case for **PD** in the samples for AFM, SCM, and fluorescence microscopy.

The binding constant for **PDMe** is higher, with a similar site size (K = 2 ×10^6 M^{-1}; B = 0.36), so 99.7% is calculated to be bound.

Fluorescence spectroscopy

All emission measurements were carried out on a SPEX FluoroMax spectrophotometer. The fluorescence measurements were performed using 5 μM solutions of **Pf**, **PD** and **PDMe⁺** without and with 20 μM and 500 μM CT-DNA.

Emission spectra of **Pf** were recorded in the region 440-750 nm using an excitation wavelength of 430 nm with a 1.75 slit width for emission beam. Excitation spectra of **Pf** were recorded in the region 250-520 nm using an emission wavelength of 512 nm. The slit width for excitation beams was 2 nm.

Emission spectra of **PD** were recorded in the region 390-750 nm using an excitation wavelength of 380 nm with a 3.25 nm slit width for emission beam. Excitation spectra of **PD** were recorded in the region 250-550 nm using an emission wavelength of 472 nm and a 4 nm slit width for excitation beam.

Emission spectra of **PDMe⁺** were recorded in the region 400-750 nm using an excitation wavelength of 415 nm with a 4 nm slit width for emission beam. Excitation spectra of **PDMe⁺** were recorded in the region 250-540 nm using an emission wavelength of 523 nm with a 3 nm slit width for excitation beam.

For all measurments, the step increment and the integration time were 0.5 nm and 0.5 s⁻¹, crespectively.

The interaction of **Pf**, **PD** and **PDMe⁺** with DNA is evidenced through changes in the fluorescence spectra that occur when the amount of DNA added to dye solution. increases. According to fluorescence measurements, increasing DNA concentration to a high ratio of DNA to dye concentration (DNA conc/dye conc = 100) gives rise to complete intercalation into DNA.

CD experiments

CD spectra were measured on a Jasco J-810 spectropolarimeter, and data were normalized to a 1 cm path length. The data are presented, as collected, in mdeg; these data can be converted to absorbance units through division by factor 32980 mdeg. Although **Pf** and its derivatives are achiral, they show induced CD signals when bound to nucleic acids as a result of coupling of their electric-dipole-allowed transition with the transitions of the chirality organised nucleobases. All measurements were recorded for the solutions of **Pf** and **PDMe⁺** with 10 μM concentration with and without 500 μM CT DNA, and, for **PD**, 50 μM.

LD experiments

LD spectra were measured on an Applied Photophysics Chirascan CD spectropolarimeter, adapted to produce linearly polarized light. Orientation of the intercalator nucleic acid samples was achieved in a flow Couette cell with an outer rotating cylinder and an inner cylinder of 3 cm diameter. The experimental path length was 1 mm, and data were normalized to a 1 cm path length.

Linear dichroism (LD) results from differential absorption of light that is plane polarized parallel and perpendicular than reference axis.

The magnitude of the LD signal depends on the degree of orientation of the sample as well as the molar absorptivity and concentration of the sample.

The reduced dichroism is defined as:

$$LD^r(\lambda) = LD(\lambda)/A_{iso}(\lambda) \qquad (26)$$

Where A_{iso} is the absorption of the sample without orientation. It is related to the orientation of the chromophore as:

$$LD^r(\lambda) = 1.5S (3 \langle\cos^2\alpha\rangle - 1) \qquad (27)$$

where α represents the angle between the absorbing transition moment and DNA helix axis. S is an orientation function describing the degree of orientation of the DNA helix such that S = 1 is equivalent to perfect orientation and S = 0 to random orientation. $\langle\cos^2\alpha\rangle$ represents an average over the angular distribution. All measurements were recorded for the solutions of 20 μM **Pf**, 20 μM **PD** and 20 μM **PDMe**$^+$ with and without 1mM CT DNA.

Thermal denaturation

Thermal denaturation experiments were performed by monitoring the absorbance at 260 nm versus temperature. Nucleic acid concentrations were typically 49 μM for these experiments.

pH Titrations

Buffer of required pH was prepared by adjusting the pH of a 5 mM phosphate (pH 6.9) solution using small aliquots of concentrated phosphoric acid or sodium hydroxide.

To ensure complete dissolution of dyes, solids were initially dissolved in 100% DMSO, and diluted with 5 mM phosphate buffer with the required pH to give samples in 99% 5 mM phosphate/1% DMSO. Samples typically contained 14.7 μM **Pf**, 18.9 μM **PDMe**$^+$ and 48.6 μM **PD**.

Dilute solution viscosimetry

A Cannon-Manning extra low charge size 75 semi-micro viscometer, immersed in a water bath thermostated at 25 °C, was used to measure the relative intrinsic viscosity[86] of dilute solutions of CT-DNA. The DNA concentration and the viscometer volume (300 mL) were kept constant for a series of added dye concentrations. The flow time for water was 177 s, and for solutions containing DNA was >245 s. Measurements were carried out in triplicate and gave standard deviations of $<\pm1$ s. The flow times are related to the relative intrinsic viscosity according to Equation (28), where $[\eta]$ is the intrinsic viscosity in the presence of dye, $[\eta]_0$ is the intrinsic viscosity of free DNA. t_0, t_d, and t represent the flow times for buffer only, naked DNA, and dye-bound DNA, respectively.

$$\frac{[\eta]}{[\eta]_0} = \frac{t - t_0}{t_d - t_0} \qquad (28)$$

For rigid rod DNA, the relative contour length, L, is related to the relative intrinsic viscosity and the binding ratio according to Equation (29), where r is bound dye per base.[60] L is the contour length in the presence of dye and L_0 is the contour length of free DNA. For monointercalation, every bound dye extends DNA by the equivalent of two bases (or one base pair). Thus, a plot of the cube root of the relative intrinsic viscosity against binding ratio yields a slope of $\alpha = 2$.

$$\sqrt[3]{\frac{[\eta]}{[\eta]_0}} = \frac{L}{L_0} = 1 + \alpha r \qquad (29)$$

Experiments with sonicated DNA from Sigma gave no significant difference in viscosity from that of water up to a concentration of 900 µM. Experiments were therefore carried out with high molecular weight CT-DNA, which means that changes in contour length and changes in flexibility cannot be readily distinguished. Nevertheless, this method is useful for comparing the effects of different dyes on the hydrodynamics of DNA. Applying the wormlike chain model for a random coil, the intrinsic viscosity of DNA, is[87]:

$$[\eta] \propto L^{3/2} \times l_P^3 \qquad (30)$$

where l_P is persistence length (50 nm for DNA). Thus, if the persistence length does not change on intercalation, a plot of the cube root of the relative intrinsic viscosity against

binding ratio yields a slope of 1.4. If the persistence length changes on intercalation, the slope will additionally reflect that change.

$$\sqrt[3]{\frac{[\eta]}{[\eta]_0}} = \sqrt{\frac{L}{L_0}} g \frac{l_P}{l_P^0} = 1 + \sqrt{2} \frac{l_P}{l_P^0} r \tag{31}$$

Molecular modelling

Molecular modelling was performed with Spartan 04 (Spartan, 2004) using the semi-empirical method basis set including ZIndo for excited states and density functional theory method (B3LYP) with basis set 6-31G* to calculate potential densities and HOMO and LUMO energies of Pf, PD, MePD and their protonated forms.

References

1. R. Tenne, L. Margulis, M. Genut and G. Hodes, *Nature*, 1992, **360**, 444-446.
2. M. Remškar, *Advanced Materials*, 2004, **16**, 1497-1504.
3. C. N. R. Rao, A. Govindaraj, F. L. Deepak, N. A. Gunari and M. Nath, *Applied Physics Letters*, 2001, **78**, 1853-1855.
4. H.-W. Liang, S. Liu and S.-H. Yu, *Advanced Materials*, 2010, **22**, 3925-3937.
5. J. Hu, Y. Bando, Z. Liu, J. Zhan, D. Golberg and T. Sekiguchi, *Angewandte Chemie International Edition*, 2004, **43**, 63-66.
6. L. Dloczik, R. Engelhardt, K. Ernst, S. Fiechter, I. Sieber and R. Konenkamp, *Applied Physics Letters*, 2001, **78**, 3687-3689.
7. H. Ihmels and D. Otto, Editon edn., 2005, 258, 161-204.
8. M. J. G. G Michael Blackburn, David Loakes and David M Williams, *Nucleic Acids in Chemistry and Biology*, 2006.
9. J. Richter, M. Mertig, W. Pompe, I. MoÌ^nch and H. K. Schackert, *Applied Physics Letters*, 2001, **78**, 536-538.
10. K. Shin-ya, K. Wierzba, K. Matsuo, T. Ohtani, Y. Yamada, K. Furihata, Y. Hayakawa and H. Seto, *Journal of the American Chemical Society*, 2001, **123**, 1262-1263.
11. J. K. Barton, *Science*, 1986, **233**, 727-734.
12. Y. Xu, Y. X. Zhang, H. Sugiyama, T. Umano, H. Osuga and K. Tanaka, *Journal of the American Chemical Society*, 2004, **126**, 6566-6567.
13. M. Tanada, S. Tsujita and S. Sasaki, *Journal of Organic Chemistry*, 2006, **71**, 125-134.
14. A. Oleksi, A. G. Blanco, R. Boer, I. Usón, J. Aymamí, A. Rodger, M. J. Hannon and M. Coll, *Angewandte Chemie International Edition*, 2006, **45**, 1227-1231.
15. M. L. Carpenter, G. Lowe and P. R. Cook, *Nucleic Acids Research*, 1996, **24**, 1594-1601.
16. L. A. Howell, Z. A. E. Waller, R. Bowater, M. O'Connell and M. Searcey, *Chemical Communications*, 2011, **47**, 8262-8264.
17. L. A. Howell, A. Howman, M. A. O'Connell, A. Mueller and M. Searcey, *Bioorganic & Medicinal Chemistry Letters*, 2009, **19**, 5880-5883.
18. L. S. Lerman, *Journal of Molecular Biology*, 1961, **3**, 18-IN14.
19. M. Aslanoglu, *Analytical Sciences*, 2006, **22**, 439-443.
20. S. Neidle, Editon edn., 1979, 16, 151-221.
21. H. M. Berman and P. R. Young, *Annual review of biophysics and bioengineering*, 1981, **10**, 87-114.
22. R. W. Armstrong, T. Kurucsev and U. P. Strauss, *Journal of the American Chemical Society*, 1970, **92**, 3174-3181.
23. A. R. Peacocke and J. N. H. Skerrett, *Transactions of the Faraday Society*, 1956, **52**, 261-279.
24. L. Janovec, M. Kozurková, D. Sabolová, J. Ungvarský, H. Paulíková, J. Plsíková, Z. Vantová and J. Imrich, *Bioorganic & Medicinal Chemistry*, 2011, **19**, 1790-1801.
25. Y. Benchabane, C. Di Giorgio, G. Boyer, A. S. Sabatier, D. Allegro, V. Peyrot and M. De Méo, *European Journal of Medicinal Chemistry*, 2009, **44**, 2459-2467.
26. L. A. Howell, A. Howman, M. A. O'Connell, A. Mueller and M. Searcey, *Bioorganic & Medicinal Chemistry Letters*, 2009, **19**, 5880-5883.
27. F. F. Chen and F. Wang, *Molecules*, 2009, **14**, 2656-2668.

28. K. Yamaoka, S. Noji and M. Yoshida, *Bulletin of the Chemical Society of Japan*, 1981, **54**, 31-34.
29. S. G. Schulman, D. V. Naik, A. C. Capomacchia and T. Roy, *Journal of Pharmaceutical Sciences*, 1975, **64**, 982-986.
30. N. F. Gersch and D. O. Jordan, *Journal of Molecular Biology*, 1965, **13**, 138-IN121.
31. G. R. Haugen and W. H. Melhuish, *Transactions of the Faraday Society*, 1964, **60**, 386-394.
32. N. Mataga, Y. Kaifu and M. Koizumi, *Bulletin of the Chemical Society of Japan*, 1956, **29**, 373-379.
33. G. Löber, H. Schütz and V. Kleinwächter, *Biopolymers*, 1972, **11**, 2439-2459.
34. B. a. García, J. M. Leal, R. Ruiz, T. Biver, F. Secco and M. Venturini, *The Journal of Physical Chemistry B*, 2010, **114**, 8555-8564.
35. J. C. Thomes, G. Weill and M. Daune, *Biopolymers*, 1969, **8**, 647-659.
36. R. A. G. Friedman and G. S. Manning, *Biopolymers*, 1984, **23**, 2671-2714.
37. M. T. Record, C. F. Anderson and T. M. Lohman, *Quarterly Reviews of Biophysics*, 1978, **11**, 103-178.
38. W. D. Wilson and I. G. Lopp, *Biopolymers*, 1979, **18**, 3025-3041.
39. G. S. Manning, *Quarterly Reviews of Biophysics*, 1978, **11**, 179-246.
40. B. Norden, M. Kubista and T. Kurucsev, *Quarterly Reviews of Biophysics*, 1992, **25**, 51-170.
41. B. Norden and T. Kurucsev, *Journal of Molecular Recognition*, 1994, **7**, 141-156.
42. P.-J. Chou and W. C. Johnson, *Journal of the American Chemical Society*, 1993, **115**, 1205-1214.
43. Y. Matsuoka and B. Nordén, *Biopolymers*, 1982, **21**, 2433-2452.
44. J. Ramstein, M. Dourlent and M. Leng, *Biochemical and Biophysical Research Communications*, 1972, **47**, 874-882.
45. E. Tuite and B. Norden, *Journal of the American Chemical Society*, 1994, **116**, 7548-7556.
46. Y. Matsuoka and K. Yamaoka, *Bulletin of the Chemical Society of Japan*, 1979, **52**, 3163-3170.
47. H.-C. Becker and B. Nordén, *Journal of the American Chemical Society*, 2000, **122**, 8344-8349.
48. M. Kamiya, *Biochimica et Biophysica Acta (BBA) - Nucleic Acids and Protein Synthesis*, 1979, **562**, 70-79.
49. H. J. Li and D. M. Crothers, *Biopolymers*, 1969, **8**, 217-235.
50. D. Fornasiero and T. Kurucsev, *The Journal of Physical Chemistry*, 1981, **85**, 613-618.
51. R. Lyng, T. Härd and B. Norden, *Biopolymers*, 1987, **26**, 1327-1345.
52. R. Lyng, A. Rodger and B. Norden, *Biopolymers*, 1991, **31**, 1709-1720.
53. R. Lyng, A. Rodger and B. Norden, *Biopolymers*, 1992, **32**, 1201-1214.
54. D. E. Graves, *Methods in molecular biology (Clifton, N.J.)*, 2001, **95**, 161-169.
55. H. Ihmels, K. Faulhaber, G. Viola and C. Schmuck, in *Highlights in Bioorganic Chemistry*, Wiley-VCH Verlag GmbH & Co. KGaA, Editon edn., 2005, pp. 172-190.
56. G. Löber, *Journal of Luminescence*, 1981, **22**, 221-265.
57. Y. Kubota and R. F. Steiner, *Biophysical Chemistry*, 1977, **6**, 279-289.
58. R. Ruiz, B. García, G. Ruisi, A. Silvestri and G. Barone, *Journal of Molecular Structure: THEOCHEM 915*, 2009, **915**, 86-92.
59. J. L. Mergny and L. Lacroix, *Oligonucleotides*, 2003, **13**, 515-537.
60. G. Cohen and H. Eisenberg, *Biopolymers*, 1969, **8**, 45-55.

61.   K. Günther, M. Mertig and R. Seidel, *Nucleic Acids Research*, 2010, **38**, 6526-6532.
62.   D. Suh and J. B. Chaires, *Bioorganic & Medicinal Chemistry*, 1995, **3**, 723-728.
63.   L. Kapicak and E. J. Gabbay, *Journal of the American Chemical Society*, 1975, **97**, 403-408.
64.   S. Satyanarayana, J. C. Dabrowiak and J. B. Chaires, *Biochemistry*, 1992, **31**, 9319-9324.
65.   J. L. Butour and J. P. Macquet, *Biochimica et Biophysica Acta*, 1981, **653**, 305-315.
66.   D. J. Patel and L. L. Canuel, *Proceedings of the National Academy of Sciences*, 1977, **74**, 5207-5211.
67.   S. Neidle, A. Achari, G. L. Taylor, H. M. Berman, H. L. Carrell, J. P. Glusker and W. C. Stallings, *Nature*, 1977, **269**, 304-307.
68.   H.-S. Shieh, H. M. Berman, M. Dabrow and S. Neidle, *Nucleic Acids Research*, 1980, **8**, 85-98.
69.   P. Lincoln and B. Nordén, *Journal of Physical Chemistry B*, 1998, **102**, 9583-9594.
70.   A. Reymer and B. Norden, *Chemical Communications*, 2012, **48**, 4941-4943.
71.   J. Booth and E. Boyland, *Biochimica et Biophysica Acta*, 1953, **12**, 75-87.
72.   F. Pierard, A. D. Guerzo, A. K.-D. Mesmaeker, M. Demeunynck and J. Lhomme, *Physical Chemistry Chemical Physics*, 2001, **3**, 2911-2920.
73.   K. Nguyen, M. Monteverde, S. Lyonnais, S. Campidelli, J. P. Bourgoin and A. Filoramo, AIP Conference Proceedings, 2008.
74.   F. Dullweber, M. T. Stubbs, Đ. Musil, J. Stürzebecher and G. Klebe, *Journal of Molecular Biology*, 2001, **313**, 593-614.
75.   W. D. Wilson, H. P. Hopkins, S. Mizan, D. D. Hamilton and G. Zon, *Journal of the American Chemical Society*, 1994, **116**, 3607-3608.
76.   G. Lamm and G. R. Pack, *Proceedings of the National Academy of Sciences*, 1990, **87**, 9033-9036.
77.   S. Hanlon, L. Wong and G. R. Pack, *Biophysical Journal*, 1997, **72**, 291-300.
78.   R. Rohs, S. M. West, A. Sosinsky, P. Liu, R. S. Mann and B. Honig, *Nature*, 2009, **461**, 1248-1253.
79.   S. Suzuki, T. Yamanashi, S. Tazawa, O. Kurosawa and M. Washizu, *Industry Applications, IEEE Transactions on*, 1998, **34**, 75-83.
80.   K. M. Abu-Salah, A. A. Ansari and S. A. Alrokayan, *Journal of Biomedicine and Biotechnology*, **2010**.
81.   W. Zhou, J. Xu, H. Zheng, H. Liu, Y. Li and D. Zhu, *The Journal of Organic Chemistry*, 2008, **73**, 7702-7709.
82.   H. Suzuki and Y. Tanaka, *The Journal of Organic Chemistry*, 2001, **66**, 2227-2231.
83.   J. D. McGhee and P. H. von Hippel, *Journal of Molecular Biology*, 1974, **86**, 469-489.
84.   S. C. Kowalczykowski, L. S. Paul, N. Lonberg, J. W. Newport, J. A. McSwiggen and P. H. Von Hippel, *Biochemistry*, 1986, **25**, 1226-1240.
85.   C. Auclair, B. Dugue, B. Meunier and C. Paoletti, *Biochemistry*, 1986, **25**, 1240-1245.
86.   E. L. Gilroy, M. R. Hicks, D. J. Smith and A. Rodger, *Analyst*, 2011, **136**, 4159-4163.
87.   H. Yamakawa and M. Fujii, *Macromolecules*, 1974, **7**, 128-135.

Chapter 3 - *Functionalisation of PD and PDMe⁺ via click chemistry*

Chapter 3 - Functionalisation of PD and PDMe[+] via click chemistry

3.1 Introduction

In the previous chapter, the binding of **PD** and **PDMe**[+] into the DNA duplex was investigated. These investigations proved that **PD** and **PDMe**[+] intercalated into the DNA framework and remained stable suggesting that the azido groups would be available for further modification via click chemistry. If so, the controlled functionalization of [DNA ⊃ **PD**] and [DNA ⊃ **PDMe**[+]] to give decorated DNA via a two-step approach intercalation followed by click-coupling should be possible. Therefore, this chapter investigates the modification of **PD** and **PDMe**[+] with a range of different alkyne groups via click chemistry in order to provide a synthetic protocol suitable for the functionalization of [DNA ⊃ **PD**] and [DNA ⊃ **PDMe**[+]] to produce highly controlled nanoscale materials, discussed later in Chapter 4.

The term "click chemistry" was established in 2001 by Sharpless[1] and co-workers, and was used to describe a series of powerful, reliable and regioselective reactions for the rapid synthesis of novel compounds.[1-10] Click reactions are typically high yielding, wide in scope and often stereospecific, leading to the generation of only innocuous by-products that can be removed from the click product easily without applying chromatographic techniques.[11, 12]

In particular, click chemistry often refers to the Cu (I)-catalysed 1,3-dipolar azide-alkyne cycloaddition[13] which has widely been applied in the synthesis of classical and combinatorial organic compounds, in drug discovery and polymer/material science.[14]

The first set of experiments describes the click functionalization of the diazido intercalators, **PD** and **PDMe**[+] with different alkyne groups, phenylacetylene, ethynylferrocene, **EFc** and N-(pent-4-ynyl)-2-(2-thienyl)pyrrole, **pent-TP**. These reactions were used to assess the conditions required to decorate the [DNA ⊃ **PD**] and [DNA ⊃ **PDMe**[+]] complexes in a second set of reactions described in Chapter 4. The polymerisation of **pent-TP** monomers after the click reaction with **PD** and **PDMe**[+] is discussed in detail.

The structures and properties of the resulting click products were provided by means of ^{1}H NMR, MS spectra, FT-IR and cyclic voltammetry (CV).

3.1.1 Huisgen 1, 3-dipolar cycloaddition reaction

Cycloaddition of azides and terminal alkynes to give triazoles is a known reaction often called 'click chemistry'. It is used in the synthesis of large organic molecules and was first introduced by Sharpless et.al.[5] The reaction is catalysed by copper (I) formed by the reduction of Cu(II) ions by sodium ascorbate to yield 1,4-disubstituted 1,2,3-triazloes. Commonly used solvents are various polar and non-polar aprotic organic solvents and also water. However, click reactions often occur better in water than organic solvent.[5, 15-18]

The proposed mechanism for the Cu (I) catalysed ligation is shown in the scheme below.
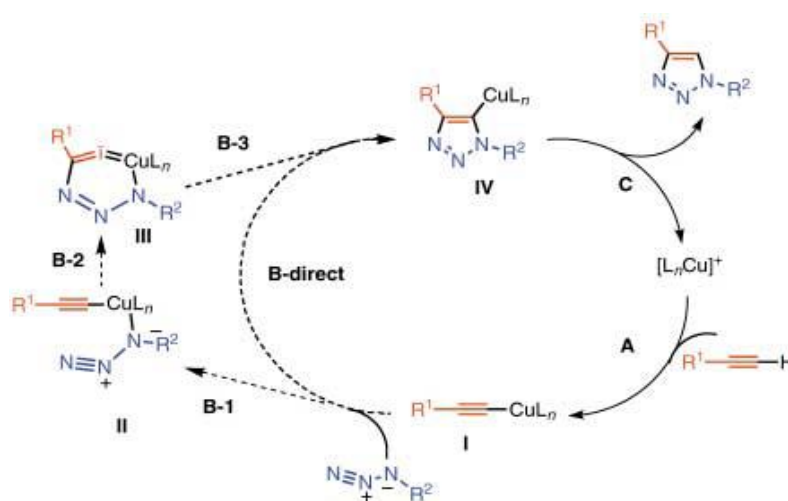
Scheme 1 Catalytic cycle of Hussgien 1,3-dipolar cycloaddition.[19]

As Scheme 1 shows, the formation of the triazole ring can be thought to proceed through one of two possible routes, a direct mechanism or a three step approach. First, the reaction between the copper (II) salt and the ligand in the presence of the reducing agent sodium ascorbate gives the protected copper (I) complex which can then insert into the alkyne group. The resulting copper (I) acetylide then reacts with the azide ion directly or indirectly giving the desired triazole ring as the "click" connectivity of the reaction.

3.1.2 Chapter outline

Click reactions were performed between the azido **Pf** derivatives and three different alkynes, phenylacetylene, **EFc** and **pent-TP** in the presence of copper sulphate, sodium ascorbate and TBTA (tris(benzyltriazolylmethyl)amine as the stabilising ligand for the Cu(I) catalyst. The reaction conditions of the click reactions were trialled and optimised with the ultimate goal of click modification of the intercalated [DNA ⊃ **PD**] and

76

[DNA ⊃ **PDMe**$^+$] complexes. Due to the presence of DNA, the reaction must be carried out in an aqueous environment. However the solubility of **PD** and **PDMe**$^+$ in water is limited and therefore mixed solvent systems were investigated.

3.2 Results and discussion

PD and **PDMe**$^+$ were used as synthesised in Chapter 2, phenylactetylene and **EFc** were commercially available whereas **pent-TP** required to be synthesised. This was reproduced according to the procedure developed in the literature.[20-22]

3.2.1 Synthesis of N-pentynyl-2-(2-thienyl)-pyrrole (pent-TP)

Pent-TP was produced in a four step synthetic pathway as shown in Scheme 2. Firstly, the reaction between thiophene carbonyl chloride and allylamine proceed via an SN$_2$ mechanism to produce the thiophene allylcarboxamide (i) in yield of up to 87%. After purification, product (i) reacts with thionyl chloride in toluene. Simple solvent removal without any purification yielded the thiophene imidoyl chloride (ii) in a yield of up to 86%. In the third step, an elimination reaction resulted in ring closure and the formation of the desired product, 2-(2-thienyl)pyrrole,[23](**TP**) (iii) and finally in fourth step (d) **TP** is modified with a C5 terminal alkyne, initially by deprotonatation with sodium hybride and subsequent alkylation with 5-chloro-1-pentyne to produce **pent-TP**.[20-22]
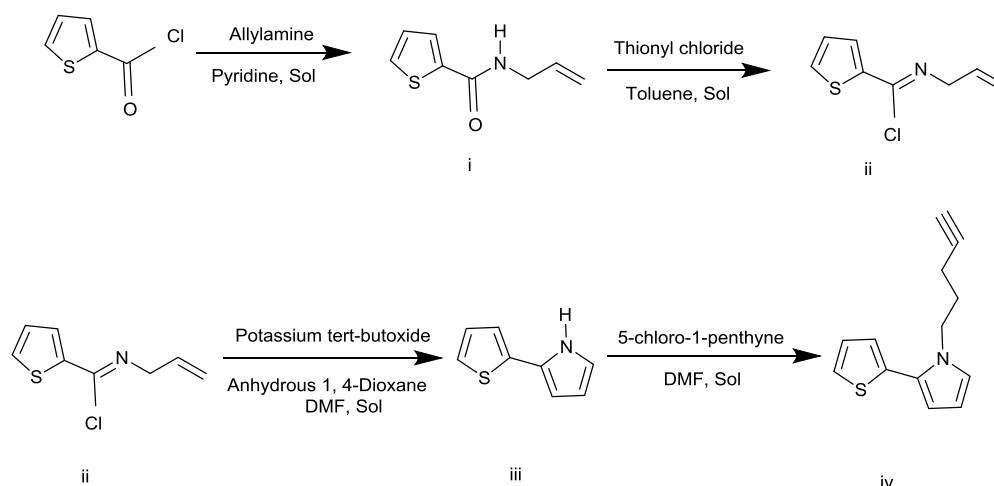
Scheme 2. the synthetic steps to produce pent-TP from thiophene carbonyl chloride.

After preparing **pent-TP**, the Cu (I) catalysed reaction between the diazidointercalators **PD** and **PDMe**$^+$ with the three alkyne bearing moieties was investigated and is discussed in the following sections.

3.2.2 Click modification of PD

PD underwent the click reaction with phenylacetylene, **EFc** and **pent-TP**. The solvent system used was 62.5% water, 6.2% methanol and 31.3% t-BuOH. The reaction proceeded at room temperature and for 48 hours.

3.2.2.1 Click reaction of PD with phenylacetylene to produce PD + phenylacetylene

In order to test whether **PD** can be easily click modified, initial experiments with phenylacetylene were carried out because it is a cheap and readily available starting material. The possibility of monitoring the click reaction by FTIR spectroscopy was investigated.
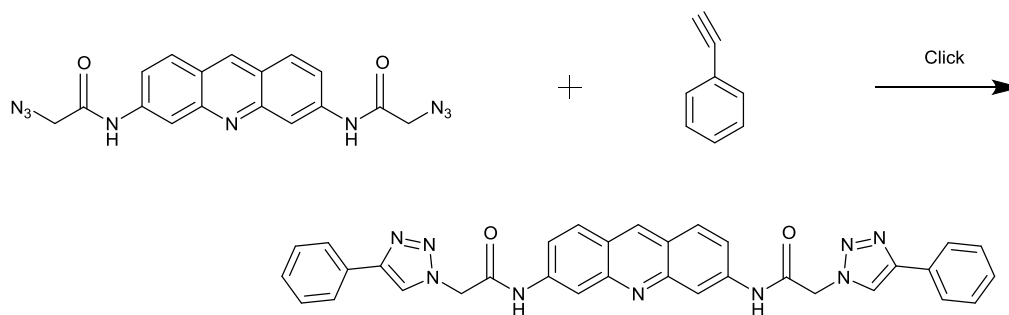
Scheme 3. Synthetic scheme of the click modification of **PD** with phenyl acetylene to produce the click product **PD + phenyl acetylene.**

In the preparation of click product (**PD + phenylacetylene)**, evidence of modification was indicated by ^{1}H NMR and IR spectroscopy and MS spectrometry. Evidence for the formation of the desired product was judged by the appearance of peaks at $\delta = 8.46$ ppm associated with the CH group of triazole rings and disappearance of the peak at $\delta = 3.01$ ppm related to acetylide CH of phenyl acetylene. Furthermore, the IR characteristics of **PD**, **phenylacetylene** and the click product (**PD + phenylacetylene**) were recorded and showed a peak at 2114 cm^{-1} (C) relating to the azide group of **PD**, see spectrum (i) in Figure 1. The spectrum of **phenylacetylene** indicated two peaks at 2104 cm^{-1} (B) and 3300 cm^{-1} (A) regarding to stretching of C≡C and C≡*C*-H respectively, see Figure 1(ii). The spectrum of the product after the click reaction, Figure 1 (iii) implied the successful performance of click chemistry due to the disappearance of the peaks associated with both the alkyne and azide groups. High resolution mass spectrometry indicated the molecular ion for [(**PD + phenylacetylene**) + H$^+$] at 580.2210 which correlates well with the calculated mass of 580.2209. The yield of reaction was 60%.
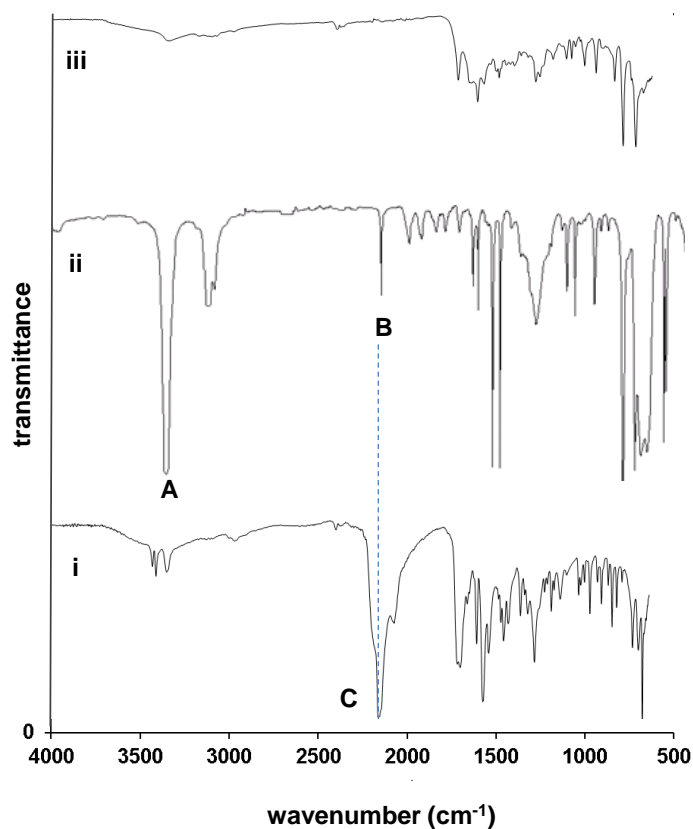
Figure 1. FTIR spectra of (i) **PD**, (ii) phenylacetylene and (iii) **PD** + **phenylacetylene**. The peaks labelled A, B and C are the C-H of C≡ C-H, C≡C and N_3 stretches respectively.

3.2.2.2 Click reaction of PD with EFc to produce PD + EFc

After testing the ability of **PD** to undergo click chemistry with the simple alkyne, phenylacetylene, a second click modification was performed using the redox active tag, ethynylferrocene, **EFc**. **EFc** is a one electron redox group that provides for further characterisation via electrochemistry.
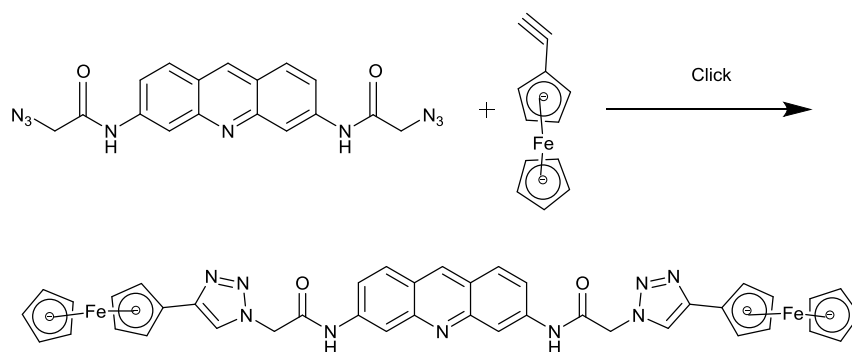
Scheme 4. Synthetic scheme of the click modification of **PD** with **EFc** to produce the click product **PD** + **EFc.**

In the preparation of click product (**PD** + **EFc**), evidence of modification was indicated by ^{1}H NMR and IR spectroscopy and MS spectrometry. Evidence for the formation of the desired product was judged by the appearance of peaks at $\delta = 8.26$ ppm associated with

79

the CH group of triazole rings and disappeared peak at $\delta = 2.67$ ppm related to acetylide CH of **EFc** are good proof for click modification of **PD** by **EFc**. The IR characteristics of **PD**, **EFc** and click product (**PD** + **EFc**) were recorded and showed a peak at 2114 cm^{-1} (C) relating to the azide group of **PD**, see spectrum (i) in Figure 2. The spectrum of **EFc** indicated two peaks at 2103 cm^{-1}(B) and 3279 cm^{-1}(A) regarding to stretching of C≡C and C≡C-H respectively, see Figure 2 (ii). The spectrum of the product (**PD** + **EFc**) after the click reaction, Figure 2 (iii) implied the successful performance of click chemistry due to the disappearance of the peaks associated with both the alkyne and azide groups.

High resolution mass spectrometry indicated the molecular ion for [(**PD** + **EFc**) + Na$^+$] at 818.1337 which correlates well with the calculated mass of 818.1354. The yield of reaction was 50%.
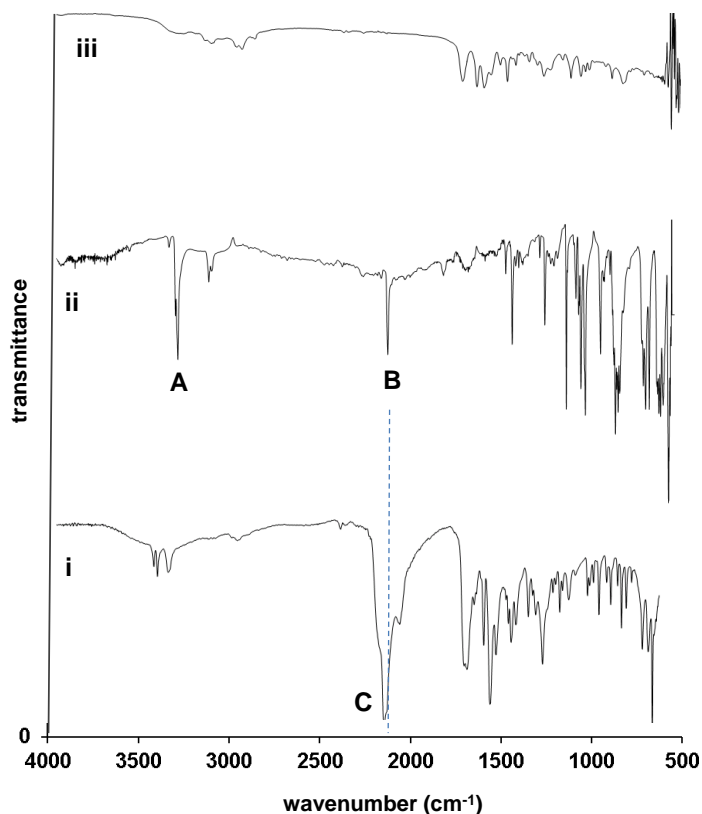
Figure 2. FTIR spectroscopy of (i) **PD** and (ii) **EFc** and (iii) click product **PD** + **EFc**. The peaks labelled A, B and C are the C-H of C≡ C-H, C≡C and N$_3$ stretches respectively.

Ethynylferrocene was clicked to **PD** and the cyclic voltammograms of **EFc** (a), **PD** (b) and **PD** +**EFc** (c) are shown in Figure 3. Figure 3 (a) shows a reversible redox wave of **EFc** in which ethynylferrocene, is oxidised at a potential of 0.474 V, and reduced at 0.408 V. Figure 3 (b), **PD** shows a possible oxidation peak (i) at 1.098 V but no clear

corresponding reduction peak as would be expected for the unmodified intercalator. Figure 3 (c), the cyclic voltammogram of the click product, **PD +EFc**, is similar to that of **EFc** and shows a clear reversible redox wave in which the product **PD +EFc** is oxidised at a potential of 0.382 V and reduced at 0.310 V.
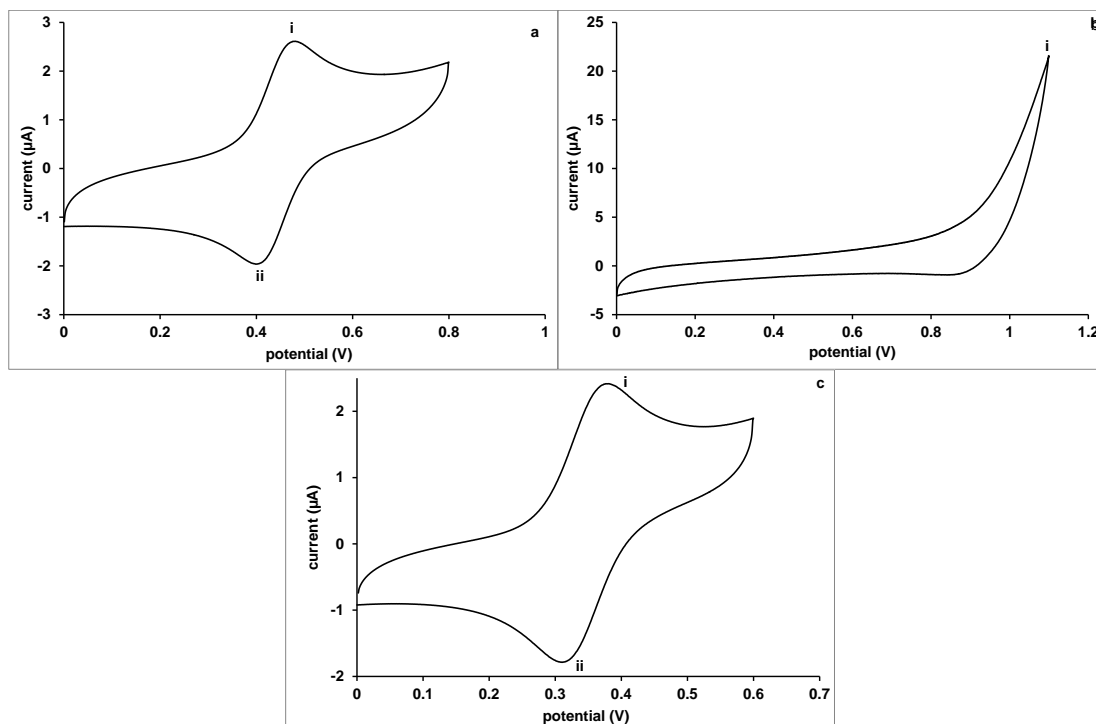
Figure 3. Cyclic voltammograms of (a) **EFc** (b) **PD** and (c) **PD + EFc**. Voltammograms were recorded at 0.6 mM concentration of **PD** and other 2.4 μM in 100 mM LiClO$_4$ in MeCN at room temperature. The working electrode was a gold microelectrode (2 mm diameter), a tungsten wire as a counter electrode and a silver wire as a quasi-reference electrode. Scan rate 0.1 V/s.

The cyclic voltammograms of the two ferrocenyl compounds, **EFc** and **PD + EFc,** indicated that upon modification of **PD** the formal standard redox potential of **EFc** at 0.441 V is shifted negatively to 0.346 V. It is clear that this is as a result of the successful click reaction and the creation of **PD + EFc**. The negative shift of nearly 100 mV is explained by the electron donating affect of the triazole ring. It is also noted that there is a small increase in peak separation after the click reaction, which is attributed to the increased ohmic drop due to the larger solution resistance of the more hydrophobic species **PD + EFc** . The cyclic voltammogram of **PD +EFc** does not show any apparent communication between the two ferrocene units, there is only one oxidation and reduction peak, and suggests that both redox groups are simultaneously oxidised and reduced.

Compounds	E anodic (V)	E cathodic (V)	ΔE (V)	E° (V)
Ethynyl ferrocene, EFc	0.408	0.474	0.066	0.441
Synthetic click, PD + EFc	0.310	0.382	0.072	0.346

Table 1. Electrochemical data from cyclic voltammetry experiments of **EFc** and **PD** + **EFc**.

3.2.2.3 Click reaction of PD with pent-TP to produce PD + pent-TP

The click reaction between **PD** and **pent-TP** was performed in order to assess the modification of **PD** with monomers which could be polymerised to form conductive nanostructures along a DNA guide pre-loaded with the azido intercalator. This two-step approach, intercalation of **PD** into DNA followed by the click modification by **pent-TP** is explored in Chapter 4.
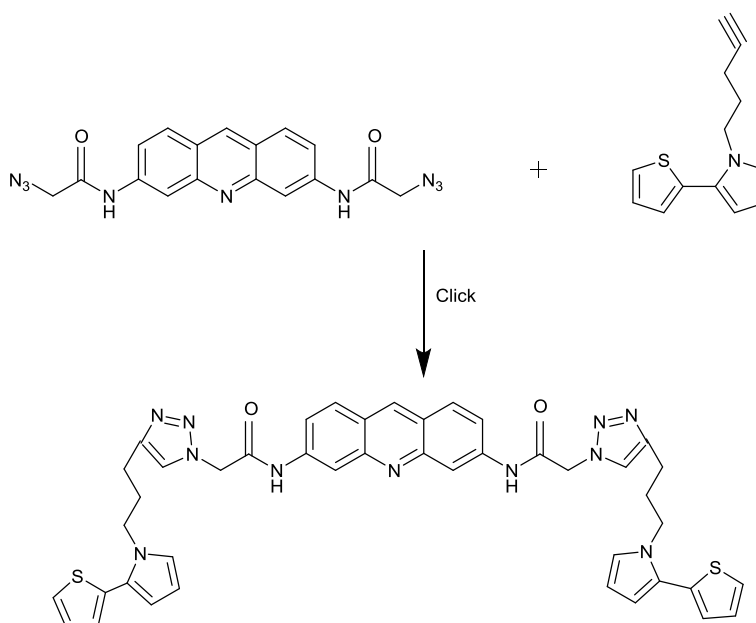
Scheme 5. Synthetic scheme of click modification of **PD** with **pent-TP** to produce **PD + pent-TP**.

In the preparation of click product (**PD + pent-TP**), evidence of modification was indicated by ^{1}H NMR and IR spectroscopy and MS spectrometry. Evidence for the formation of the desired product was judged by the appearance of peaks at $\delta = 8.45$ ppm associated with the CH group of triazole rings and disappeared peak at $\delta = 1.22$ ppm related to acetylide CH of of **PD** by **pent-TP**.

The IR characteristics of **PD**, **pent-TP** and click products were recorded. The IR **pent-TP** are good proof for click modification spectrum of **PD** showed a peak at 2114 cm^{-1} (C) relating to the azide group, see spectrum (i) in Figure 4. The spectrum of **pent-TP** indicated two peaks at 2112 cm^{-1} (B) and 3283 cm^{-1} (A) regarding to stretching

of C≡C and C≡*C*-H respectively, see Figure 4 (ii). The spectrum of the product after the click reaction, Figure 4 (iii) implied the successful performance of click chemistry due to the disappearance of the peaks associated with both the alkyne and azide groups.

High resolution mass spectrometry indicated the molecular ion for [(**PD** + **pent- TP**) + Na$^+$] at 828.2629 which correlates well with the calculated mass of 828.2627. The yield of reaction was 79%.
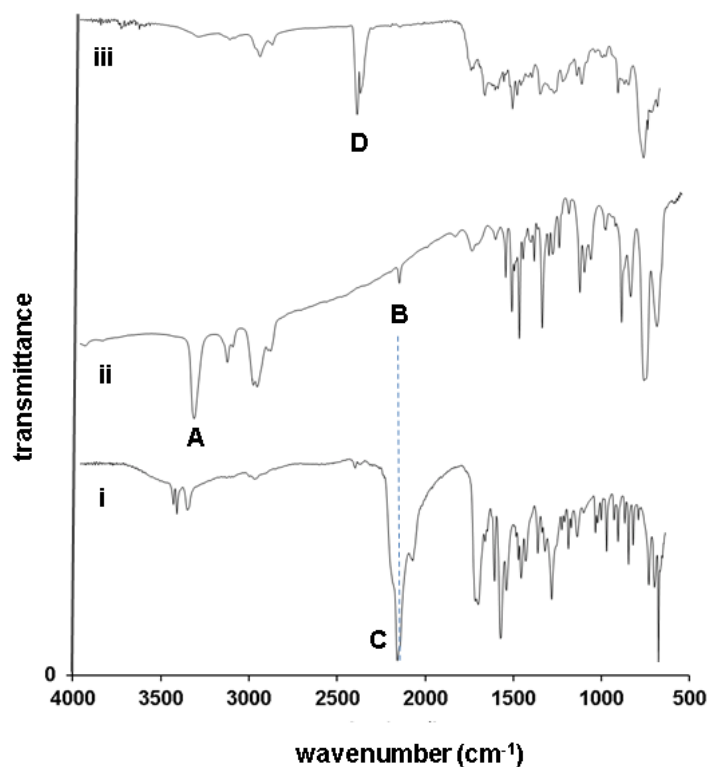
Figure 4. FTIR spectroscopy of (i) **PD** and (ii) **pent-TP** and (iii) click product, **PD** + **pent- TP**. The peaks labelled A, B, C and D are the C-H of C≡ C-H, C≡C, N$_3$ and CO$_2$ stretches respectively.

The click modification of **PD** with **phenylaceylene**, **EFc** and **pent-TP** were all successfully performed and the respective products characterised by FTIR and CV where appropriate. Due to the enhanced binding properties of **PDMe**$^+$ to DNA, the click modification of **PDMe**$^+$ with **pent-TP** was also investigated.

3.2.3 Click reaction of PDMe$^+$with pent-TP to produce click product (PDMe$^+$+ pent-TP)

With the ultimate goal of using **PDMe**$^+$ to assemble the **pent-TP** monomer units along DNA for the formation of conductive polymers the click reaction between **PDMe**$^+$ and **pent-TP** was also performed. **PDMe**$^+$ is more soluble than **PD** in aqueous systems and so is favoured as a possible reagent in the proposed two-step approach for the DNA guided assembly of nanomaterial, intercalation followed by click modification. **PD** underwent the click reaction with phenylacetylene, **EFc** and **pent-TP**. The solvent

system used was 21.1% DMF, 52.6% water, 10.5% methanol and 15.8% t-BuOH. The reaction proceeded at room temperature for 24 hours.
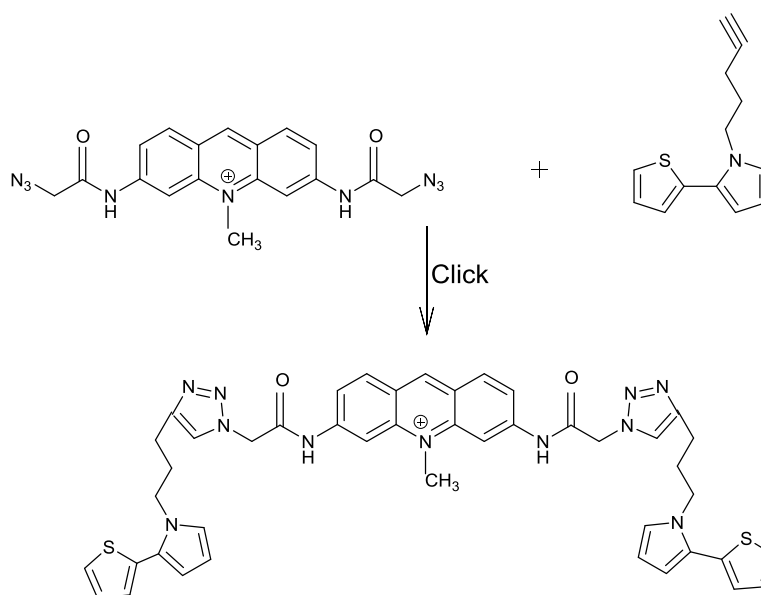
Scheme 6. Synthetic scheme of modification of **PDMe⁺** with **pent-TP** to produce **PDMe⁺+ pent-TP**.

3.2.3.1 IR characterisation of click product PDMe⁺ + pent-TP

In the preparation of click product (**PDMe⁺ + pent-TP**), evidence of modification was indicated by ¹H NMR and IR spectroscopy and MS spectrometry. Evidence for the formation of the desired product was judged by the appearance of peaks at $\delta = 7.94$ ppm associated with the CH group of triazole rings and disappeared peak at $\delta = 1.22$ ppm related to acetylide CH of of **PDMe⁺** by **pent-TP**.

The IR characteristics of **PDMe⁺**, **pent-TP** and click products were recorded. The IR spectrum of **PDMe⁺** showed a peak at 2099 cm⁻¹ (C) relating to the azide group, see spectrum (i) in Figure 5. The spectrum of **pent-TP** indicated two peaks at 2112 cm⁻¹ (B) and 3283 cm⁻¹ (A) regarding to stretching of C≡C and C≡*C-H* respectively, see Figure 5 (ii). The spectrum of the product after the click reaction, Figure 5 (iii) implied the successful performance of click chemistry due to the disappearance of the peaks associated with both the alkyne and azide groups.

High resolution mass spectrometry indicated the molecular ion for (**PDMe⁺ + pent- TP**) at 820.2932 which correlates well with the calculated mass of 820.2964. The yield of reaction was 70%.
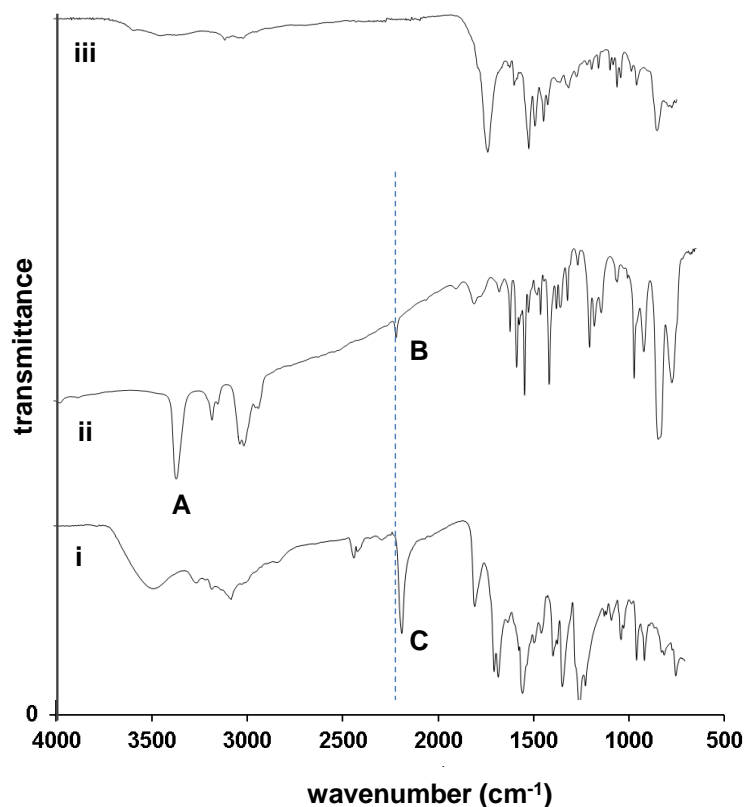
Figure 5. FTIR spectroscopy of (i) **PDMe⁺** and (ii) **pent-TP** and (iii) click product, **PDMe⁺** + **pent-TP**. The peaks labelled A, B and C are the C-H of $C \equiv$ C-H, $C \equiv C$ and N_3 stretches, respectively.

3.3 Electrochemistry of PDMe⁺

The cyclic voltammogram of **PDMe⁺** is shown in Figure 6. **PDMe⁺** undergoes oxidation at 1.03 V, peak (i), but the process is irreversible, possibly due to the instability of the radical cation. The reported oxidation peak of proflavine itself is reported to be 0.94 V,[24] in good agreement with the value here for **PDMe⁺**.

A much smaller reduction peak (ii) is seen at about 0.400 V, which in some reports on the electrochemistry of proflavine has been assigned to the reduction of oxidation products at the exocyclic amine groups.[13] Here, **PDMe⁺** may also have some oxidation products which in turn could be reduced and hence the small peak observed.
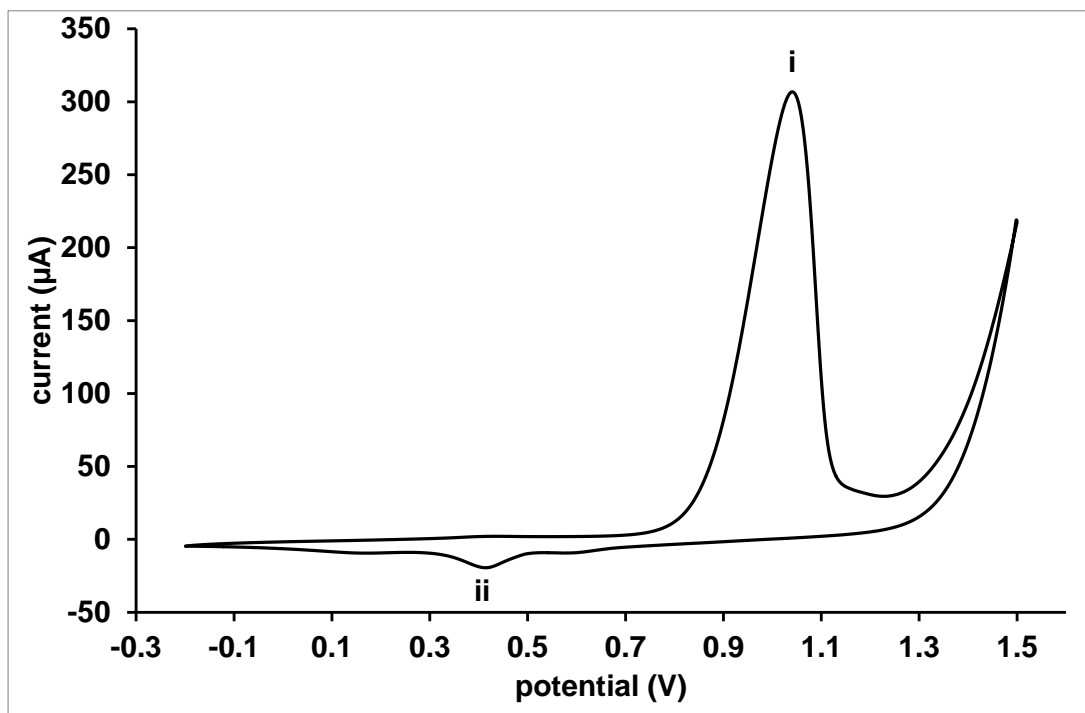
Figure 6. Cyclic voltammogram of **PDMe⁺**, voltammogram was recorded at 0.6 mM concentration in 100 mM LiClO$_4$ in MeCN at room temperature. The working electrode was a gold microelectrode (2 mm diameter), a tungsten wire as a counter electrode and a silver wire as a quasi-reference electrode. Scan rate 0.1 V/s.

3.4 Electrochemical polymerisation of pent-TP

Films of polypyrrole exhibit conductivities of up to 100 S cm^{-1}, but when combined with a low oxidation potential monomer such as thiophene, as in **pent-TP**, a system that can be polymerized easily to give high conductivities is accessible.[25]

The cyclic voltammogram of **pent-TP** is shown in Figure 7. In an acetonitrile solution of the monomer, the oxidation peak of **pent-TP** is observed at a potential of 1.40 V (i). The oxidised monomer can then form oligomers and subsequently a conductive polymer film **poly-pent-TP** at the surface of the working electrode. This polymer is reduced on the reverse sweep at around 1.11 V (iii) and 0.97 V (iv). Upon repeated cycles, the current of the reduction peak of the polymer tends to increase as the polymer length becomes longer.[21] As expected, the oxidation potential (ii) of the polymer (1.12 V) is observed after more than one cycle and is at a lower potential than the oxidation of the monomer. This is explained by the increased conjugation of the polymer, stabilizing the radical formed on oxidation throughout the polymer. On the electrode, black precipitate was seen due to the formation of polymer of **pent-TP**.
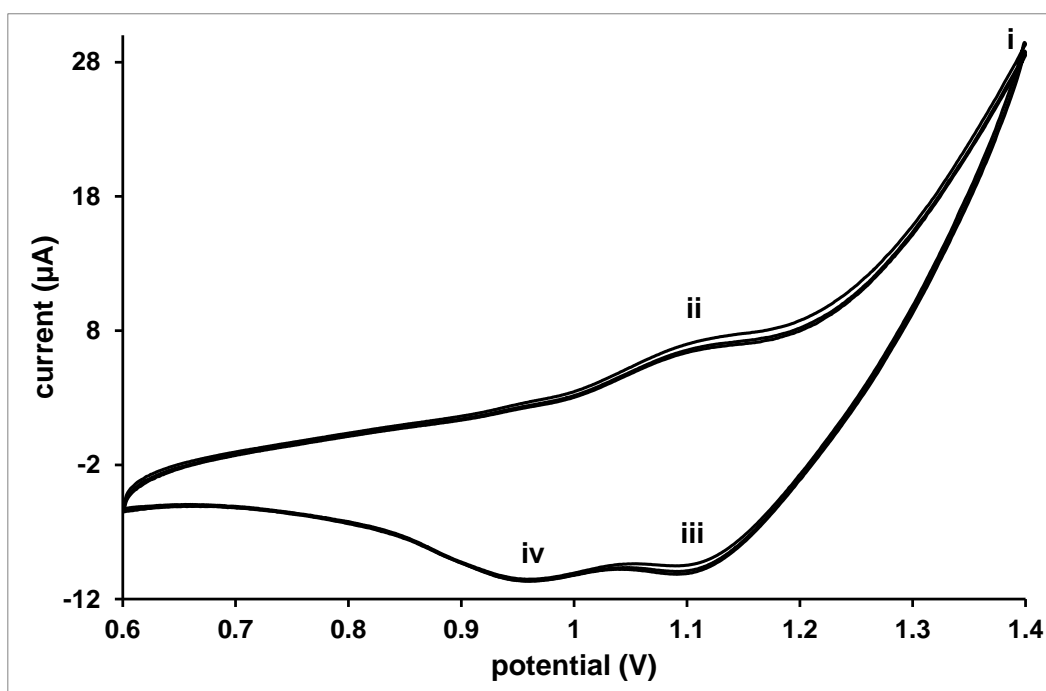
Figure 7. Cyclic voltammograms of **pent-TP** voltammogram was recorded at 1 mM concentration in 100 mM LiClO$_4$ in MeCN at room temperature. The working electrode was a gold microelectrode (2 mm diameter), a tungsten wire as a counter electrode and a silver wire as a quasi-reference electrode. Scan rate 0.1 V/s.

3.5 Electrochemistry of click product, PDMe$^+$ + pent-TP

The cyclic voltammogram of **PDMe$^+$+pent-TP** is shown in Figure 8. The oxidation peak (i) at 1.7 V is the oxidation of the monomer into the polymer, which is not a reversible process and so no reduction peak is observed. However there is a quasi-reversible redox wave due to the oxidation and reduction of the polymer, centred on 1.1 V. The reduction peak (iii) is observed at 0.99 V and the oxidation peak (ii) at 1.2 V. As the polymeric film grows on the working electrode with continued cycling an increase in the currents of these two peaks is observed.

Compounds	Oxidation of monomer	Oxidation of polymer	Reduction of polymer
pent-TP	1.4 V	1.12 V	1.11 V , 0.97 V
PDMe$^+$ + pent-TP	1.7 V	1.2 V	0.99 V

Table 2. Electrochemical data from cyclic voltammetry experiments of **pent-TP** and **PDMe$^+$ + pent – TP.**

After click modification of **PDMe⁺**, the oxidation of the **pent-TP** groups becomes noticeably more positive, a shift from 1.4 to 1.7 V, which is opposite to the shift observed in the case of the ferrocene modified intercalator. However a previous study has reported that the oxidation potential of pyrrole based systems is increased when alkylation at the N-position imparts an increased steric constraint on the ring system.[21] It is therefore conceivable that after modification of the simple alkyne unit with the bulky intercalator, **PDMe⁺**, that the oxidation potential will increase due to steric reasons.
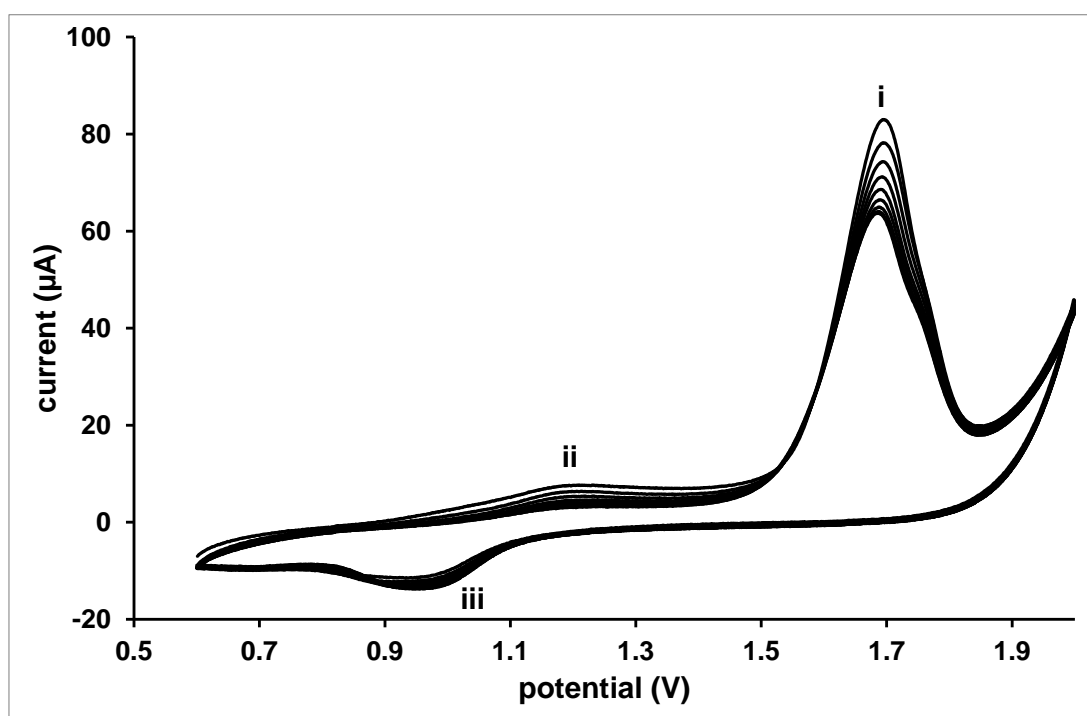
Figure 8. Cyclic voltammograms of **PDMe⁺**+ **pent-TP**, recorded at 2.6 mM concentration in 100 mM LiClO₄ in MeCN at room temperature. The working electrode was a gold microelectrode (2 mm diameter), a tungsten wire as a counter electrode and a silver wire as a quasi-reference electrode. Scan rate 0.1 V/s.

3.6 Conclusion

The feasability of **PD** and **PDMe⁺** being modified by the click reaction was examined using a range of alkyne bearing groups. Alkyne moieties with different properties such as the redox active group **EFc** or the monomer unit **pent-TP** for the fabrication of conductive polymers were chosen. The synthetic click products, [**PD** + **phenylacetylene**], [**PD** + **EFc**], [**PD** + **pent- TP**] and [**PDMe⁺** + **pent-TP**], were characterized by ¹H-NMR ¹³C-NMR, FT-IR and mass spectrometry.

Ethynylferrocene, **EFc** has a standard potential of 441 mV which on reaction with **PD** shifts to 346 mV for the click product, **PD + EFc**, which was noticeably more negative.

The observed negative shift of 93 mV is expected due to the electron donating effects of the triazole ring.[26]

The electrochemical polymerisation of **PDMe$^+$ + pent-TP** indicated that click product forms a polymer film at the working electrode during electrochemical polymerisation. This is an interesting material for the possible binding of DNA to the modified surface through intercalation and may have applications in the detection of DNA.

3.7 Experimental

Material and methods

Reagents were purchased from Sigma Aldrich. Lambda DNA was purched from New England Biolabs. N-pentynyl-2-(2-thienyl)-pyrrole, **pent TP,** was synthesised in the lab by Cava *et al.*[21] NMR was performed on a 300MHz Bruker spectrospin WM 300 WB spectrometer and UV-spectra were measured on a Cary 100, IR and mass spectra were recorded on a Bio-Rad FTS-7 FT-IR Spectrometer and a Waters Micromass LCT premier mass spectrometer respectively. Fluorescence images were collected on an Axioplan 2 microscope (Zeiss) using Axiovision Viewer 3 software (Zeiss). CV analyses were carried out on the analytical workstation which was an electrochemical analyser/Workstation CH1760B, Model 700B Series by CH Instruments, Inc., USA with sensitivity of up to picoamperes.

Preparation chips of N doped Si <100> for FTIR

A wafer of n-type (100) silicon was diced into chips approximately 1 cm^2 which were sequentially cleaned using a cotton bud soacked in acetone, propanol and finally water before being dry using a nitrogen stream and placed in an oven for half an hour .

Thiophene N-allylcarboxamide
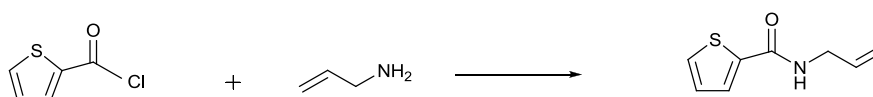
Molecular weight = 167 g/mol

Thiophene carbonyl chloride (10.0 g, 68.2 mmol) was added to allylamine (5.12 mL, 68.2 mmol) in pyridine (60.0 mL) and stirred vigorously for 2 hours. TLC was performed in hexane/ethyl acetate (80:20) to show the reaction had gone to completion. The solvent was removed by coevaporating with toluene. The brown oil produced was

dissolved in DCM and washed with water (3×50.0 mL). The solvent was then dried using magnesium sulphate and removed in vacuo to afford an orange solid (9.82 g, 59.0 mmol, 86.5%).[23] ^{1}H-NMR (300 MHz, CDCl$_3$, 25°C) δ = 3.96 (dd, 2H, CH$_2$), 5.13 (m, 2H, CH$_2$), 5.82 (m, 1H, CH), 6.58 (s, 1H, NH), 6.97 (m, 1H, CH), 7.38 (m, 1H, CH), 7.52 (m, 1H, CH).

Thiophene imidoyl chloride
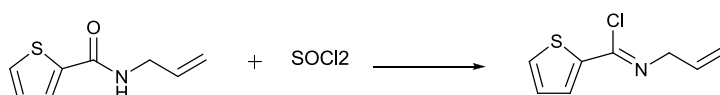
Molecular Weight = 186 g/mol

Thiophene allylamine (9.82 g, 59 mmol), thionyl chloride (44 ml in 176 mL toluene) and DMF (12 drops) was stirred for 18 hours then the solvent was removed in vacuo to afford an orange-brown oil (9.41g, 51mmol, 85.9%).[23]

^{1}H-NMR (300 MHz, CDCl$_3$, 25°C) δ = 4.33 (m, 2H, CH$_2$), 5.26 (m, 2H, CH$_2$), 6.02 (m, 1H, CH), 7.07 (m, 1H, CH), 7.48 (m, 1H, CH), 7.78 (m, 1H, CH).

Preparation 2-(2-thienyl)-pyrole (TP)
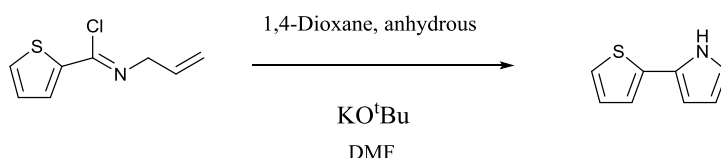
Molecular weight = 149 g/mol

Imidoyl chloride (9.41 g, 50.7 mmol) in anhydrous 1, 4-dioxane (40mL) was added drop wise to a solution of potassium tert-butoxide (17.1 g, 152 mmol) in anhydrous DMF (60 mL) and was allowed to stir under N$_2$ overnight. TLC was carried out in hexan: ethylacetate (95:5) to monitor the progress of the reaction. The solution was then poured over iced water (400mL) and extracted with diethyl ether. The ethereal layers were collected and dried with magnesium sulphate and evaporated to afford a brown oil and then purified by column chromatography in a solvent system hexane/ethyl acetate (80:20). This gave a light brown solid 2.54 g, 17 mmol, 33.6%.[1] H-NMR (300 MHz,

CDCl$_3$, 25 $^\circ$C) δ = 6.18 (m, 1H, CH), 6.34 (m, 1H, CH), 6.71 (m, 1H, CH), 6.93 (m, 2H, 2×CH-thiophene), 7.04 (m, 1H, CH-thiophene), 8.22 (s, 1H, NH).

Alkylation of TP with 5-chloro-1-pentyne
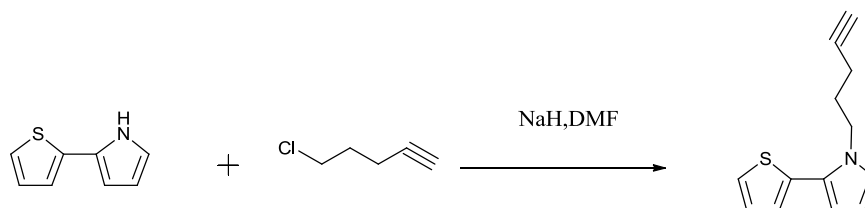
Molecular weight = 215 g/mole

DMF (100mL) was added to 2-(2-thienyl)-pyrole (2.54g, 17 mmol) by cannular under nitrogen. Sodium hydride (60% dispersion in mineral oil) (1.36 g, 34 mmol) was then added under nitrogen and stirred for half an hour at room temperature then the solution mixture was placed in ice bath to reach 0 $^\circ$C to add 5-chloro-1-penthyne (3.80 g, 3.88 mL, 37.4 mmol). The reaction mixture was then stirred overnight. The reaction mixture was filtered to separate unreacted sodium hydride and then the solvent was removed in vacuo and the residue was extracted with ethyl acetate and the solvent again removed in vacuo. ^{1}H-NMR confirmed a brown oil product.[23]

^{1}H-NMR (300MHz , CDCl$_3$, 25 ∘C) δ = 1.80 (m, 2H, CH$_2$), 1.90 (t, 1H, CH), 2.06 (m, 2H, CH$_2$), 4.06 (t, 2H, CH$_2$), 6.10 (dd,1H, CH), 6.22 (dd, 1H, CH), 6.71 (dd, 1H, CH), 6.96 (m, 2H, 2×CH), 7.19 (dd, 1H, CH).

"Click" Reaction Procedures

All click reactions except solvent percentage were carried out according to the method reported by Sharpless *et al.*[4]

[PD + phenyl acetylene] : N,N'-(acridine-3,6-diyl)bis(2-(4-phenyl-1-H-1,2,3,-triazol-1-yl)acetamide)
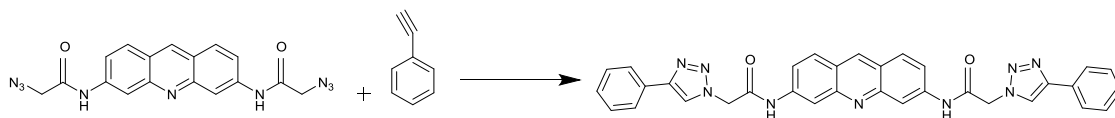
PD (0.50 g, 1.26 mmol), sodium Ascorbate (0.57 g, 2.9 mmol) and copper (II) sulphate (0.18 g, 0.72 mmol) were dissolved in a solvent mixed 50 mL distilled water, 25 mL tBuOH and 10 mL methanol and stirred for half an hour. Phenylacetylene (3 mL, 27.3 mmol) was then added and the mixture stirred vigorously for 48 hours. TLC was carried out in chloroform: methanol (90:10) to monitor the progress of the reaction. The solvent

was removed in vacuo and then the residue was washed with an aqueous solution of EDTA and thus with chloroform:methanol (9:1) is washed and filtered to give the product in 60% yield.

^{1}H-NMR (300 MHz, DMSO-d$_6$, 25°C) δ 10.97 (s, 2 H, NH) 8.94 (s, 1 H, CH) 8.67 (s, 2 H, CH) 8.46 (s, 2 H, CH) 8.13 (d, 2 H, CH, J = 9) 7.90 (d, 4, CH) 7.69 (d, 2 H, CH, J = 9) 7.47 (t , 4, CH) 7.35 (t, 2 H, CH) 5.52 (s, 4 H, CH$_2$).

^{13}C-NMR (400 MHz, DMSO-d$_6$) δ = 165.29, 149.99, 146.67, 140.55, 135.69, 131.37, 130.09, 129.33, 128.30, 125.76, 123.46, 120.40, 115.30, 53.07, 31.10.

HRMS (ESI, m/z): [M +H] calculated for C$_{33}$H$_{26}$N$_9$O$_2$, 580.2209; found 580.2210.

[PD + EFc]: 3,3'-(1,1'-((acridine-3,6-diylbis(azanediyl))bis(2-oxoethane-2,1-diyl))bis(1H-1,2,3-triazole-4,1+diyl))bis(cyclopenta-2,4-dien-1-ylium)dicyclopenta-2,4-dien-1-ylium dimethideyliron
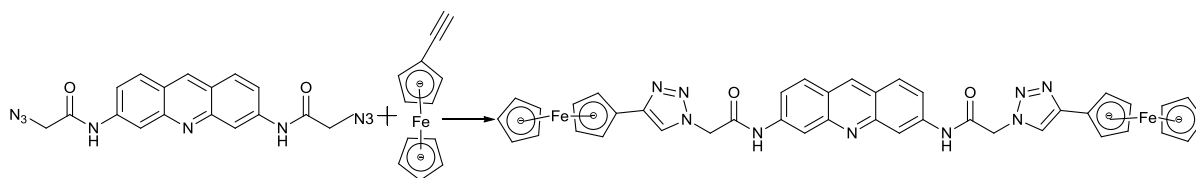
PD (50.0 mg, 0.133 mmol) was added to 1 mL DMF. EFc (56.0 mg , 0.267 mmol) was then added and mixture stirred for 10 minutes. Sodium ascorbate (60.7 mg, 0.3 mmol), copper sulfate (19.0 mg, 0.076 mmole) and TBTA [tris(benzyltriazolylmethyl)amine] (1.40 mg, 2.7×10$^-$3 mmol) were dissolved with the solvent containing 5 mL deionised water, 1.5 mL tBu-OH and 1 mL methanol and then added. The reaction mixture was stirred overnight. TLC was performed in dichloromethane:methanol (95:5) to show the reaction had gone to completion. The solvent was removed in vacuo and then the residue was sequentially washed and filttered using an aqueous solution of EDTA before and column chromatography was performed in DCM:methanol (95:5) to give the product in 50% yield.

^{1}H-NMR (300 MHz, DMSO-d$_6$, 25°C) δ = 4.07 (s, 10 H, CH), 4.32 (s, 4 H, CH), 4.77 (s, 4 H, CH), 5.46 (s, 4 H, CH$_2$), 7.69 (dd, 2 H, CH), 8.12 (d, 2 H, CH), 8.26 (s, 2 H, CH), 8.46 (s, 2 H, CH), 8.93 (s, 1 H, CH), 10.97 (s, 2 H, NH).

^{13}C-NMR (400 MHz, DMSO-d$_6$, 25°C) δ=52.97, 66.91, 68.80, 69.81, 76.74, 115.14, 120.55, 122.92, 123.36, 130.70, 136.02, 140.65, 145.72, 150.12, 165.65.

HRMS (ESI, m/z): **[M +Na]$^+$** calculated for C$_{41}$H$_{33}$N$_9$NaFe$_2$O$_2$, 818.1354; found, 818.1337.

[PD + pent-TP]: N^3, N^6-bis (3-(4-(3-(2-(thiophen-2-yl)-1H-pyrrol-1-yl)propyl)-1-H-1,2,3-triazol-1-yl)prop-1-en-2-yl)acridine-3,6-diamine
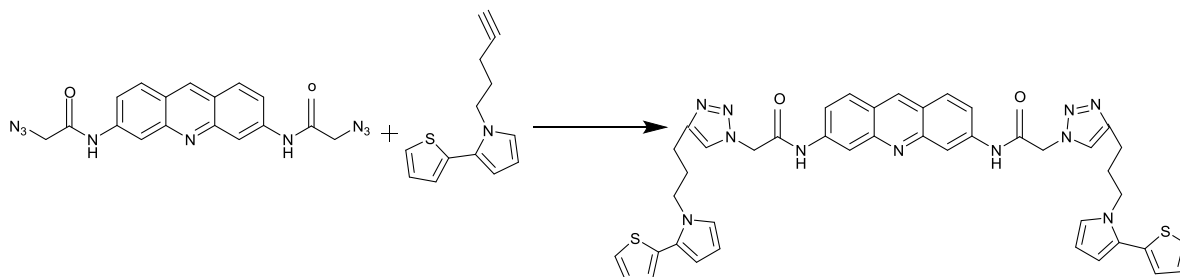
PD (100 mg, 0.26 mmol) was dissolved in 2mL DMF. **Pent-TP** (120 mg, 0.56 mmol) was then added and the mixture stirred for 10 minutes. Sodium ascorbate (121 mg, 0.612 mmol), copper (II) sulphate (37.9 mg, 0.15 mmol) and TBTA (2.82 mg, 5.3×10^{-3} mmol) were dissolved with the solvent containing 5 mL deionised water, 1.5 mL tBu-OH and 1 mL methanol was then added. The reaction mixture was stirred for overnight. TLC was performed in chloroform:methanol (90:10) to monitor the progress of the reaction. The solvent was removed in vacuo and then the residue was sequentially washed with an aqueous solution of EDTA and then chloroform:methanol (9:1) to give the product in 79% yield.

^{1}H-NMR (300 MHz, DMSO-d$_6$, 25°C) δ = 10.88 (s, 2 H, NH) 8.92 (s, 1 H, CH) 8.45 (s, 2 H, CH) 8.11 (dd, 2 H, CH J = 4.03, 9) 7.90 (s, 2 H, CH) 7.65 (d, 2 H, CH J = 8.83) 7.48 (d, 2 H, CH) 7.08 (m, 4 H, CH) 6.97 (s, 2 H, CH) 6.21 (dd, 2 H, CH J=1.51 , 3.18) 6.09 (t, 2 H, CH) 5.39 (s, 4 H, CH2) 4.11 (t, 4 H, CH2) 2.61 (t, 4 H, CH2) 1.98 (m, 4 H, CH2).

^{13}C-NMR (400 MHz, DMSO-d$_6$) δ = 165.54, 150.25, 146.42, 140.55, 135.96, 134.68, 130.098, 128, 126.01, 125.25, 24.23, 122.95, 120.4, 115.05, 110.46, 108.16, 52.56, 46.7, 31.14, 22.22.

HRMS (ESI, m/z): **[M +Na]$^+$** calculated for C$_{43}$H$_{39}$N$_{11}$NaO$_2$S$_2$, 828.2627; found, 828.2629.

[PDMe⁺+pent-TP]: 10-methyl-3,6-bis(2-(4-(3-(2-(thiophen-2-yl)-1H-pyrrol-1-yl)propyl)-1H-1,2,3-triazol-1-yl)acetamido)acridin-10-ium
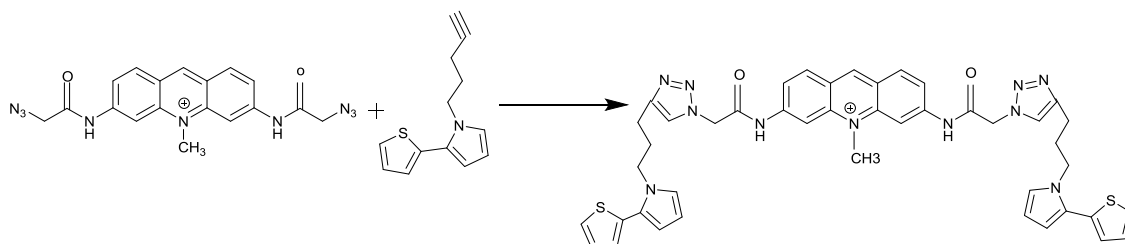
PDMe⁺ (50.0 mg, 0.097 mmol) was dissolved in 2 mL DMF. N-pentynyl-2-(2-thienyl)-pyrrole **pent-TP** (41.7 mg, 0.194 mmol) was then added and the mixture stirred for 10 minutes. Sodium ascorbate (44.2 mg, 0.22 mmol) and copper (II) sulphate (13.8 mg, 0.06 mmol) were dissolved in 5 mL deionised water and TBTA (1.03 mg, 1.04×10^{-3} mmol) was dissolved in 1.5 mL tBu-OH and 1 mL methanol and then added to the reaction and then was stirred overnight. TLC was performed in chloroform/methanol (90:10) to show the reaction had gone to completion. The solvent was removed in vacuo and then the residue was sequentially washed with an aqueous solution of EDTA and then chloroform:methanol (9:1) to give the product in 70% yield.

^{1}H-NMR (300 MHz, DMSO-d$_6$, 25°C) δ = 11.62 (s, 2 H, NH) 9.76 (d, 2 H, CH) 8.95 (s, 2 H, CH), 8.53 (d, 2 H, CH), 7.94 (s, 2 H, CH), 7.87 (dd, 2 H, CH) 7.46 (d, 2 H, CH) 7.08 (m, 4 H, CH) 6.97 (s, 2 H, CH) 6.22 (dd, 2 H, CH) 6.10 (t, 2 H, CH) 5.52 (s, 4 H, CH2) 4.39 (t, 4 H, CH2) 4.10 (t, 4 H, CH2) 2.61 (t, 4 H, CH2)1.96 (m, 4 H, CH2).

^{13}C-NMR (400 MHz, DMSO-d$_6$) δ = 189.76, 174.946, 164.473, 146.441, 134.857, 129.368, 128.908, 128.682, 128.330, 128.099, 126.055, 125.534, 125.312, 124.588, 124.144, 110.422, 108.288, 104.225, 52.852, 46.728, 40.023, 36.322, 31.204, 22.695.

HRMS (ESI, m/z): **[M]⁺** calculated for C$_{44}$H$_{43}$N$_{11}$O$_2$S$_2$, 820.2964; found, 820.2932.

FTIR study of click reactions

A silicon wafer n-type (100) was diced into chips approximately 1 cm^2 which were sequentially cleaned using cotton buds soaked in acetone, propanol and finally water. The chips were then dried using a nitrogen stream and then placed in an oven 80 °C for half an hour. These clean and dry substrates were used to deposit reaction samples for analysis by FTIR.

Cyclic Voltammetry

Details of the cyclic voltammetry experiments of PD, PDMe$^+$, pent TP, click product (PDMe$^+$ + pent-TP), EFc and click product (PD + EFc)

Cyclic voltammetry experiments of PDMe$^+$, pent TP, click product PDMe$^+$ + pent TP

Gold, tungsten and silver wires were used as working, counter and reference electrodes respectively. Cyclic voltammograms were then recorded using the following parameters:

condition: 0.6 mM **PD** and 0.6 mM **PDMe$^+$**, 100 mM LiClO$_4$ in MeCN: r.t,. Scan rate 0.1 V/s. Init E (V) = -0.2, High E (V) = 1.5, Low E (V) = -0.2, Init P/N = P, Scan Rate (V/s) = 0.1, Segment = 4, Sample interval (V) = 0.001, quiet time (sec) = 2, Sensitivity (A/V) = 1e^{-4}

1 mM **pent-TP**, 100 mM LiClO$_4$ in MeCN: r.t, Scan rate 0.1 V/s. Init E (V) = 0.6, High E (V) = 1.4, Low E (V) = 0.6, Init P/N = P, Scan Rat (V/s) = 0.1, Segment = 8, Sample interval (V) = 0.001, quiet time (sec) = 2, Sensitivity (A/V) = 1e^{-4}.

Click product (PDMe$^+$ +pent-TP): 100 mM LiClO$_4$ in MeCN, r.t., Scan rate 0.1 V/s. Init E (V) = 0.4, High E (V) = 1.8, Low E (V) = 0.4, Init P/N = P, Scan Rate (V/s) = 0.1, Segment = 20, Sample interval (V)= 0.001, quiet time (sec) = 2, Sensitivity (A/V) = 1e^{-4}.

And for 2.4 μM **EFc** and 2.4 μM (**PD + EFc**), 100 mM LiClO$_4$ in MeCN: r.t,. Scan rate 0.1 V/s. Init E (V) = -0.2, High E (V) = 2, Low E (V) = -0.2, Init P/N = P, Scan Rate (V/s) = 0.1, Segment = 4, Sample interval (V) = 0.001, quiet time (sec) = 2, Sensitivity (A/V) = 1e^{-4}

Preparation of solutions for elctrochemical analysis:

i) Lithium perchlorate solution (0.1 M):

Lithium perchlorate (217.76 mg) was dissolved in 20 mL of dry acetonitrile to obtain a solution of 0.1 M lithium perchlorate.

ii) Pent TP

10 mM DMSO solutions of **pent-TP** was diluted with 10 mL solution of 0.1 M lithium perchlorate (prepared in acetonitrile as above) to prepare 1 mM solution of **pent-TP**. **pent-TP** for electrochemical polymerisation.

iii) Deoxygenated solutions of PDMe$^+$

A 10 mM DMSO solution of **PDMe$^+$** was diluted with 0.1 M lithium perchlorate (prepared in acetonitrile as above). Dry nitrogen was bubbled through the solution for at least 30 min to deoxygenate the solution, total concentration of **PDMe$^+$** was 0.6 mM.

iv) Click PDMe$^+$ + pent-TP

4 mM DMSO solution of **PDMe$^+$** + **pent-TP** was diluted with 5 mL solution of 0.1 M lithium perchlorate (prepared in acetonitrile as above) to prepare 2.6 mM solution of **PDMe$^+$** + **pent-TP**.

v) 10 mM DMSO solutions of **PD** was diluted with the 0.1 M lithium perchlorate (prepared in acetonitrile as above). Dry nitrogen was bubbled through the solution for at least 30 min to deoxygenate the solution, total concentration of **PD** was 0.6 mM.

vi) Ethynylferrocene, EFc

1 mM aqueous solution of **EFc** was diluted with 10 mL solution of 0.1 M lithium perchlorate (prepared in acetonitrile as above) to prepare 2.4 μM solution of **EFc**.

vii) Click PD + EFc

1 mM aqueous solutions of click was diluted with 10 mL solution of 0.1 M lithium perchlorate (prepared in acetonitrile as above) to prepare 2.4 μM solution of click product (**PD + EFc**).

References

1.	V. V. Rostovtsev, L. G. Green, V. V. Fokin and K. B. Sharpless, *Angewandte Chemie International Edition*, 2002, **41**, 2596-2599.
2.	P. Wu, A. K. Feldman, A. K. Nugent, C. J. Hawker, A. Scheel, B. Voit, J. Pyun, J. M. J. Fréchet, K. B. Sharpless and V. V. Fokin, *Angewandte Chemie International Edition*, 2004, **43**, 3928-3932.
3.	S. Löber, P. Rodriguez-Loaiza and P. Gmeiner, *Organic Letters*, 2003, **5**, 1753-1755.
4.	Z. Li, T. S. Seo and J. Ju, *Tetrahedron Letters*, 2004, **45**, 3143-3146.
5.	H. C. Kolb, M. G. Finn and K. B. Sharpless, *Angewandte Chemie - International Edition*, 2001, **40**, 2005-2021.
6.	B. Helms, J. L. Mynar, C. J. Hawker and J. M. J. Fréchet, *Journal of the American Chemical Society*, 2004, **126**, 15020-15021.
7.	A. Brik, J. Muldoon, Y.-C. Lin, J. H. Elder, D. S. Goodsell, A. J. Olson, V. V. Fokin, K. B. Sharpless and C.-H. Wong, *ChemBioChem*, 2003, **4**, 1246-1248.
8.	C. W. Tornøe, C. Christensen and M. Meldal, *The Journal of Organic Chemistry*, 2002, **67**, 3057-3064.
9.	S. Löber and P. Gmeiner, *Tetrahedron*, 2004, **60**, 8699-8702.
10.	H. C. Kolb, M. G. Finn and K. B. Sharpless, *Angewandte Chemie International Edition*, 2001, **40**, 2004-2021.
11.	H. C. Kolb, M. G. Finn and K. B. Sharpless, *Angewandte Chemie - International Edition*, 2001, **40**, 2004-2021.
12.	K. Nwe and M. W. Brechbiel, *Cancer Biotherapy and Radiopharmaceuticals*, 2009, **24**, 289-302.
13.	W. G. Lewis, L. G. Green, F. Grynszpan, Z. Radić, P. R. Carlier, P. Taylor, M. G. Finn and K. B. Sharpless, *Angewandte Chemie International Edition*, 2002, **41**, 1053-1057.
14.	J. E. Moses and A. D. Moorhouse, *Chemical Society Reviews*, 2007, **36**, 1249-1262.
15.	F. Amblard, J. H. Cho and R. F. Schinazi, *Chemical Reviews*, 2009, **109**, 4207-4220.
16.	C. Beyer and H.-A. Wagenknecht, *Chemical Communications*, 2010, **46**.
17.	W. H. Binder and R. Sachsenhofer, *Macromolecular Rapid Communications*, 2007, **28**, 15-54.
18.	D. M. Kolpashchikov, *Chemical Reviews*, **110**, 4709-4723.
19.	F. Himo, T. Lovell, R. Hilgraf, V. V. Rostovtsev, L. Noodleman, K. B. Sharpless and V. V. Fokin, *Journal of the American Chemical Society*, 2004, **127**, 210-216.
20.	E. S. Yim, M. K. Park and B. H. Han, *Ultrasonics Sonochemistry*, 1997, **4**, 95-98.
21.	M. Vautrin, P. Leriche, A. Gorgues and M. P. Cava, *Electrochemistry Communications*, 1999, **1**, 233-237.
22.	L. I. Belen'kii, G. P. Gromova and V. I. Smirnov, *Chem Heterocycl Comp*, 2008, **44**, 1092-1100.
23.	R. E. Niziurski-Mann and M. P. Cava, *Advanced Materials*, 1993, **5**, 547-551.
24.	S. T. Girousi, D. K. Alexiadou and A. K. Ioannou, *Microchimica Acta*, 2008, **160**, 435-439.
25.	S. Srinivasan and G. B. Schuster, *Organic Letters*, 2008, **10**, 3657-3660.
26.	D. Schweinfurth, R. Pattacini, S. Strobel and B. Sarkar, *Dalton Transactions*, 2009, 9291-9297.

Chapter 4 - *DNA directed assembly of nanomaterials: Intercalation + Click Chemistry*

Chapter 4 - DNA directed assembly of nanomaterials: Intercalation + Click Chemistry

4.1 Introduction

The preceding chapters reported the synthesis and characterisation of the intercalators **PD** and **PDMe⁺**, investigations into their binding to DNA and their suitability to undergo the click reaction. The findings of Chapter 2 showed that **PD** and **PDMe⁺** bind to DNA through intercalation and the DNA complexes have binding constants similar to proflavine, the intercalator from which they are derived. In Chapter 3, the ability of **PD** and **PDMe⁺** to undergo click chemistry was established and the synthesis of click coupled products with ethynyl ferrocene, **EFC**, phenylacetylene and **pent-TP**, **pent -TP** described.

Therefore, this chapter discusses the DNA directed assembly of nanomaterials via a combination of intercalation and click chemistry. This new approach to the assembly of nanomaterials occurs during two steps; firstly, intercalation of the diazido proflavine derivatives, **PD** and **PDMe⁺**, into DNA**,** and secondly, the modification of the diazido intercalator by click chemistry. All modifications are carried out to provide additional functionality to the DNA nanostructure without altering its original composition, i.e. an enhanced template-scaffolding approach for the DNA directed assembly of functional materials.

This chapter focuses on the system which comprises of three components; DNA, an azido modified intercaltor and an alkyne reporter/functional unit. The system is constructed in two steps. First, intercalation into DNA and second, click chemistry after intercalation.

4.2. Intercalators for controlled assembly at DNA

Commercial λ-DNA used in this work, is about 17 μm long and contains precisely 48502 base pairs. DNA, as a biopolymer, due to its nanoscale diameter ∼ 2 nm and shape is a suitable candidate as a nanofabrication template.[1-3] The polymer length and sequence affords control over the template that can be exploited in nanomaterial design.[4, 5]

According to the neighbour exclusion principle,[6, 7] the binding of one intercalator between two base pairs hinders the access of another intercalator to the base pair site adjacent to the intercalator. Therefore, the assembly of material along the DNA helix can be controlled by altering the intercalator / DNA nucleobase ratio. For example in

the case of maximum loading of intercalator into DNA, for every two base pairs one intercalator molecule is located in the helix. At lower loading levels, the ratio of intercalator to DNA nucleobases can be controlled to provide on average larger distances between the intercalators inserted into the DNA. This approach allows for the design of specific material fabrication routes.
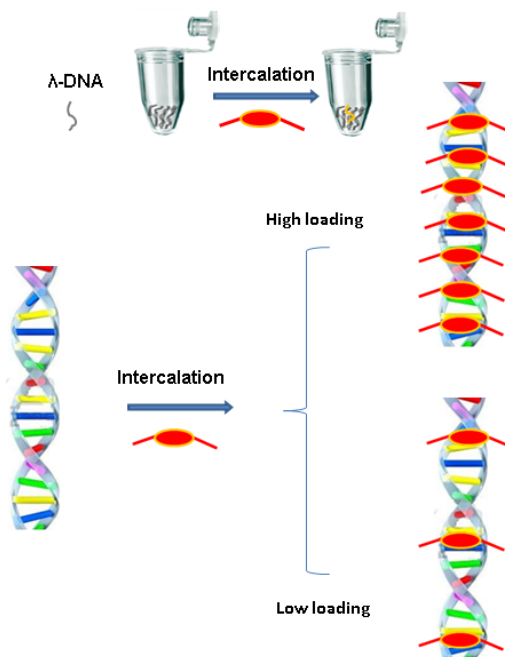
Figure 1. DNA intercalation at a stoichiometry of one intercalator per two base pairs (maximum loading), and at a lower level of loading to increase intercalator separation.

4.3. Assembly at DNA via maximum PD intercalator loading

In the first instance, DNA that had been fully loaded with **PD** was investigated as a platform for the assembly of functional materials via the click reaction. Small aliquots of **PD** were added to a λ-DNA solution, the ratio of DNA base-pairs to intercalator molecule was controlled at 2:1. After stirring for 48 h the fully loaded intercalated complex **[DNA ⊃ PD]** was achieved. In chapter 2, the observed DNA binding constants of **PD** (5.3×10^5) and **PDMe$^+$** (2×10^6) were less than for **Pf** (3.8×10^6), but sufficient that they remain intercalated into the DNA framework and could be used to assemble functional material along the helix. AFM images of the fully loaded intercalated complex **[DNA ⊃ PD]** shown in Figure 2 reveal a mixture of bare DNA molecules (height0.5nm) and complex **[DNA ⊃ PD]** (minimum height 2.8nm) prepared at reaction time (48h). AFM studies indicated that the wire-like structure of the λ-DNA was retained and the images in Figure 2b are similar to those for bare DNA (Figure 2a).
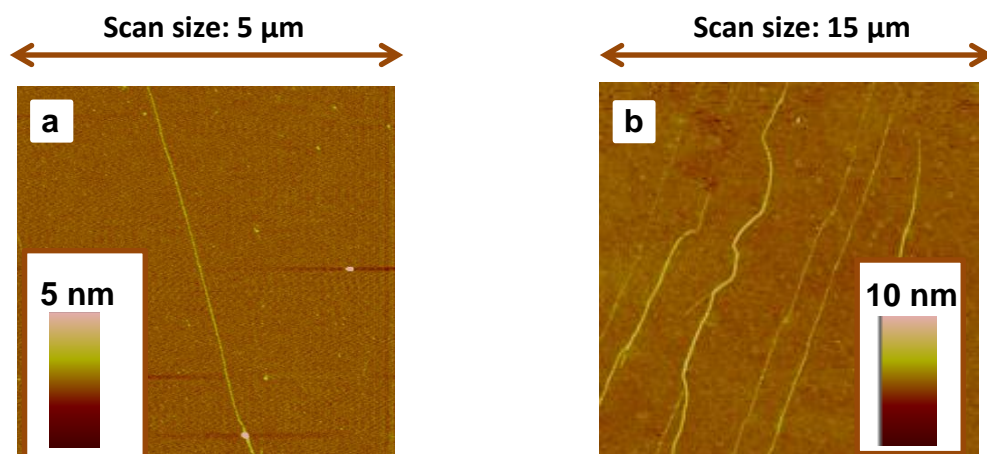
Figure 2. a) AFM image of λ-DNA deposited onto a silicon wafer, scan size: 5 μm, DNA shown has typical height of 1.6 nm; b) typical AFM image of **PD** intercalated into λ-DNA after deposition onto a silicon wafer, scan size: 15 μm, **[DNA ⊃ PD]** strucutres shown have height ranges between 2.8-3.7 nm.

Figure 2a and 2b show DNA wire like structure before and after **PD** intercalation respectively. The AFM image of [DNA ⊃ **PD**] indicates that the linear topology of DNA is not disturbed by the interaction of **PD** even though the minimum observed heights of the intercalated complexes, 2.8 nm, agree with the expectation that intercalation of **PD** increases the DNA bulk. However, there is clearly more than a single helix in many of the observed nanostructures as the height has increased into 3.7 nm, which explains the increased diameters beyond the simple association of the intercalator into the helix. Therefore the intercalation of **PD** in DNA appears to aid the bundling of two or more helices into larger diameter nanostructures, at least under the surface attachment conditions. This phenomenon has been previously reported in the formation of nanoropes from pyrrole templated DNA.[8]

In the following sections the modification of [DNA ⊃ **PD**] at the azido sites of **PD** via the click reaction with different alkynes such as **EFc**, **pent-TP** and acetylene-PEG4-carboxyrhodamine (**APCR)** is described. The modifications were carried out using the same reagents as in Chapter 3, but due to the lack of organo-solubility of DNA the solvent was essentially water. The characterization of the click products was carried out with different techniques depending on the properties of alkyne substituents, for example, **EFc** allows for electrochemical studies, **pent-TP** for UV/Vis, FTIR, mass spectroscopy, AFM and SCM studies and **APCR** for AFM and fluorescence microscopy studies. Therefore, the following sections describe the synthesis and characterisation of the click modified intercalated complexes of **PD** in DNA.

4.3.1 [DNA ⊃ PD] click modification with EFc

As discussed in Chapter 3, the purpose of modifying [DNA ⊃ **PD**] with **EFc** via the click reaction is to assemble a redox compound along the DNA helix so to monitor the reaction electrochemically. Having performed the control experiment in the work described in Chapter 3, here a comparison is made of the performance of the click reaction of the DNA free system **PD** + **EFc** and the intercalated complex [DNA ⊃ **PD**] + **EFc**. The click reaction, [DNA ⊃ **PD**] + **EFc,** *i.e* click modification *in situ* with DNA, was carried out in the solvent system of H$_2$O / tBuOH (90:10).

4.3.1.1 Electrochemistry studies of [DNA ⊃ PD] + EFc

The electrochemical properties of [DNA ⊃ **PD**] + **EFc** were investigated through cyclic voltammetry using a gold working microelectrode, a tungsten wire counter electrode and a silver wire as a reference electrode, Figure 4. Cyclic voltammograms were then recorded using the following parameters: initial potential -0.2 V, high potential 2 V, low potential -0.2, scan rate 0.1 V / sec in an electrolyte solution of 0.1 M lithium perchlorate in acetonitrile.
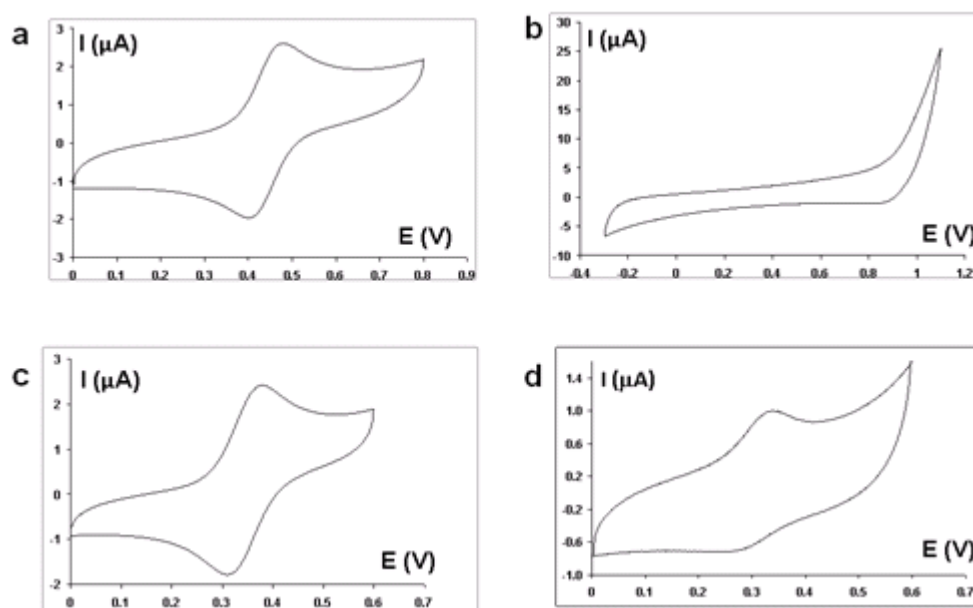
Figure 3: Cyclic voltammograms of (a) **EFc,** (b) **PD,** (c) [**PD** + **EFc**] and (d) [DNA ⊃ **PD**] + **EFc**. Voltammograms were recorded at 0.6 mM **PD** and other 2.4 × 10^{-3} μM concentration in 100 mM LiClO$_4$ in MeCN at room temperature. The working electrode was a gold microelectrode (2 mm diameter), a tungsten wire as a counter electrode and a silver wire as a quasi-reference electrode. Scan rate 0.1 V/s.

The click products [DNA ⊃ **PD**] + **EFc** and **PD** + **EFc** as well as free **EFc** and the intercalated complex [DNA ⊃ **PD**] were characterized electrochemically by cyclic voltammetry and the key parameters are shown in Table 1. The formal redox potential

of **EFc** was 0.441 V (*vs* Ag wire quasi reference electrode, 0.1 M LiClO$_4$ in CH$_3$CN) and was noticeably more positive than the click products [**PD** + **EFc**], 0.346 V and [DNA ⊃ **PD**] + **EFc,** 0.304 V. The formal redox potentials of [**PD** + **EFc**] and [DNA ⊃ **PD**] + **EFc** suggest that both entities are structurally similar *i.e.* ferrocenyl containing products of the click reaction. The observed negative shifts of 0.093 and 0.135 V for [**PD** + **EFc**] and [DNA ⊃ **PD**] + **EFc** respectively are expected due to the electron donating effects of the triazole ring.[9] The cyclic voltammogram of [DNA ⊃ **PD**] + **EFc** shows an anodic peak at 0.267 V and a cathodic peak at 0.341 V. The peak separation for [DNA ⊃ **PD**] + **EFc**, 0.074 V is greater than expected for a reversible two-electron process (ca. 0.030 V), likewise for [**PD** + **EFc**], 0.072 V. This may be due to communication between the two pendant ferrocene groups attached to the central intercalator which affect the electron transfer rate. **EFc** alone does follow the expected Nernstian behaviour of a one electron process with a peak separation of 0.066 V. Nevertheless, the anodic peak is clear evidence for the incorporation of ferrocene groups into the DNA complex because the electrode potentials for the DNA bases are all substantially greater than the anodic peak potential.[10] In the case of [DNA ⊃ **PD**] + **EFc** the ferrocenyl group is also in proximity to the supporting DNA backbone due to intercalation. The negatively charged local environment of the phosphate backbone is known to cause a shift to a more reductive potential,[11] as observed in Table 1. The [**PD** + **EFc**] product (E° = 0.346 V) appears to be in intimate contact with the DNA helix and most likely remains intercalated after the click reaction is performed on the loaded complex [DNA ⊃ **PD**] since there is a substantial lowering of the formal electrode potential to 0.304 V of [DNA ⊃ **PD**] + **EFc**.

Compounds	E anodic (V)	E cathodic (V)	ΔE (V)	E° (V)
Ethynyl ferrocene, EFc	0.408	0.474	0.066	0.441
Synthetic click, PD + EFc	0.310	0.382	0.072	0.346
[DNA ⊃ **PD**] + **EFc**	0.267	0.341	0.074	0.304

Table 1. Formal redox potentials taken from CV studies of **EFc**, molecular click product [**PD** + **EFc**] and intercalated click product [DNA ⊃ **PD** + **EFc**].

4.3.1.2 Atomic Force Microscopy (AFM), [DNA⊃PD] + EFc

The **[DNA⊃PD] + EFc** product was deposited onto a silicon chip surface as prepared before[12] and then examined by tapping mode AFM. Linear features of [DNA ⊃ **PD**] + **EFc** were oberserved and found to have a height range from 4.8 nm to 14.6 nm, (see Figure 4, for a typical image).

Scan size: 5 µm
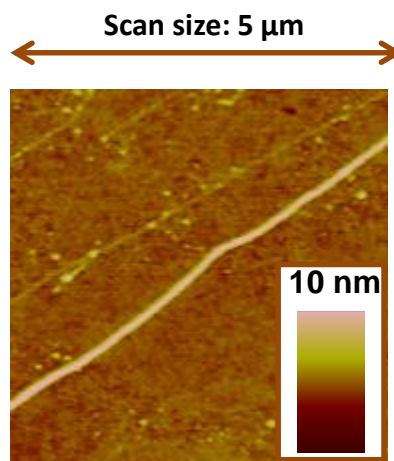
Figure 4. Typical AFM image of [DNA⊃**PD**] + **EFc** showing a height range of 4.8-14.6nm.

However it is not possible to know explicitly that the click product [DNA ⊃ **PD**] + **EFc** remains intercalated, or if it is only a loose association with **DNA** in the solution that causes these observations. Therefore, attention was turned to study the click functionalization of the complex [DNA ⊃ **PD**] with the conductive polymer unit **pent-TP** to give [DNA ⊃ **PD**] + **pent-TP**.

4.3.2. [DNA ⊃ PD] clicked with pent-TP

5-Pentynyl-thienyl-pyrrole, **pent-TP,** has been previously used as a monomeric building block for the fabrication of conductive polymer / DNA based hybrid nanowires.[13, 14] Upon polymerization **pent-TP** forms poly-**pent-TP,** a conductive polymer with exposed terminal alkyne residues exposed for click modification. These materials have promise in future sensing devices as conveniently modifiable transducing elements. It would be advantageous to be able to control the assembly of conductive polymers at the molecular level and the decoration of **pent-TP** along a DNA template pre-loaded with **PD** is an attractive route to achieving this goal, see Figure 5.
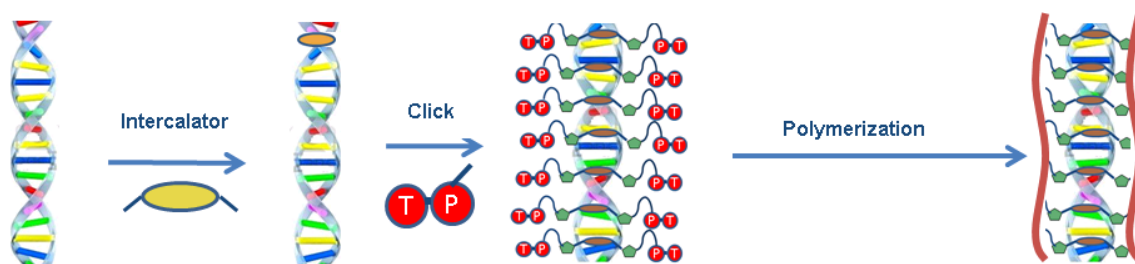
Figure 5. A cartoon model of **PD** intercalated into DNA and then click chemistry with **pent-TP** and finally polymerization.

Therefore, the *in-situ* click reaction of **[DNA ⊃ PD]** with the conductive copolymer unit, **pent-TP**, was performed in order to assemble potentially conductive material along the DNA structure. The click reaction again was performed in a solvent of 90% H_2O and 10% tBuOH. The following section discusses the AFM images from the above system to identify the structural modifications which exist before and after intercalation and also the in-situ click reaction.

4.3.2.1 Atomic Force Microscopy (AFM),[DNA ⊃PD] + pent-TP

Aqueous solutions of [DNA ⊃ **PD**] and [DNA ⊃ **PD**] + **pent-TP** were deposited via molecular combing onto the surface of silanised silicon oxide wafers prepared as previously.[15-17] Tapping mode AFM indicated the formation of wire-like structures aligned on the surface in both cases, see Figure 6a and Figure 6b. The observed 1-D nanostructures of [DNA ⊃ **PD**] and [DNA ⊃ **PD**] + **pent-TP** are comparable in topology to those of bare λ-DNA, see Figure 2a. The mean height as observed by AFM of naked DNA has generally been reported to be 1.6 nm, slightly less than the accepted theoretical 2 nm dimension of the double helix.[18] In Figure 6b the DNA hybrid structure of [DNA ⊃ **PD**] + **pent-TP** appears to contain a junction where two linear structures are linked through an area where the bundled structure has become untwined to form a single extended structure.[8]

The ranges in height of the nanostructures of λ-DNA, [DNA ⊃ PD] and [DNA ⊃ PD] + pent-TP were 0.5 − 2.1 nm, 2.8 − 22.2 nm and 4.1 − 18.8 nm respectively. These findings indicate that PD has more than a simple insertion effect on the observed increase in height, and likewise the click reaction with pent-TP is not solely responsible for the larger diameters observed.
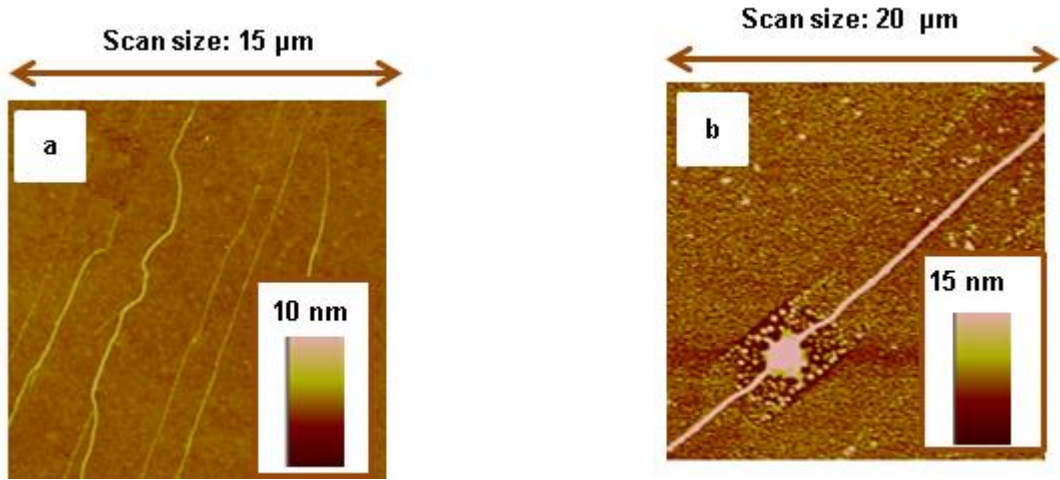
Figure 6 a) [DNA ⊃**PD**]**,** scan size: 15 μm, height ranges between 2.8-3.7 nm b) [DNA ⊃ **PD**] + **pent-TP,** scan size: 20 μm, 16.4 nm height.

To clarify whether the wire like structure of [DNA⊃**PD**] + **pent-TP** is conductive or not, SCM characterization provided valuable information, as is explained below.

4.3.2.2 SCM study of [DNA ⊃ PD] + pent-TP

Scanned conductance microscopy (SCM) is a variant of electrostatic force microscopy (EFM) which can be used to probe the electronic properties of nanostructures. EFM is implemented as a two-pass technique in which the first scan across a line records the topography in tappingTM mode and this information is used to lift the tip a defined height above the sample in the second pass to record the phase response.

To have qualitative analysis, the usual assumption is made that the electrostatic force is negligible compared to the short range forces in the first pass, but that the electrostatic force dominates in the second pass.[19] As shown by previous workers,[20, 21] negative phase shifts (with respect to the background) are only observed when imaging one-dimensional structures that are conductive. The phase shift is proportional to the second derivative of the tip/surface capacitance with respect to the lift height. The capacitance is the series combination of the tip/nanorope and nanorope/surface capacitors. The phase shift, $\Delta\phi$, for an insulating object may be estimated using a model geometry in which the nanorope is represented by the area of a thin dielectric strip directly under the tip, itself modelled as a disc of radius, R_{tip}:[22]

$$\tan(\Phi - \Phi_0) = \frac{Q V_{tip}^2}{2k} \varepsilon_o \pi R_{tip}^2 \left(\frac{1}{(h+t/\varepsilon_{ox})^3} - \frac{1}{(h+t/\varepsilon_{ox}+D/\varepsilon_{nw})^3} \right) \quad (1)$$

where Q is the quality factor, k the cantilever spring constant, t the oxide thickness and d is the thickness of the nanorope. The first term is the background contribution due to

105

the tip/oxide/Si capacitance and the second term is due to the tip/nanorope/Si capacitance. Whilst equation (1) is based on an approximate geometry, it clearly shows that the phase shift is positive for any finite value of the dielectric constant of the nanorope, ε. A negative phase shift cannot occur solely as a result of the nanorope polarisability. However, when the nanorope is conductive, the charge stored on the nanorope/Si capacitor can be spread along the whole length of the nanorope, L. In effect, the second term in equation (1) becomes much larger because the capacitance is determined by L instead of Rtip. Equation (1) also exhibits a parabolic dependence of the tangent of the phase shift on the applied dc voltage. This contrasts with the linear dependence of the phase shift on potential that arises from the electrostatic force caused by trapped charges: the different dependences on applied voltage has been used before to distinguish the effects of static charge and conductance in EFM.

It is known that in SCM experiments one-dimensional nanostructures will only produce a negative phase shift relative to the substrate background if they are electrically conducting.[8, 12, 22]

Silicon wafers with a 200 nm thick silicon oxide layer on top were diced into approximately 1 cm^2 pieces and prepared as detailed in the experimental section.[8, 12, 22] A drop of **[DNA ⊃ PD] + pent-TP** was then deposited on the silicon surface and the chip left to dry in a vacuum hood for 2 hours before imaging by SCM. The SCM image of **[DNA ⊃ PD] + pent-TP** (Figure 7) shows a negative phase shift (black image) as the tip crosses the wire, this is typical of a conductive structure.
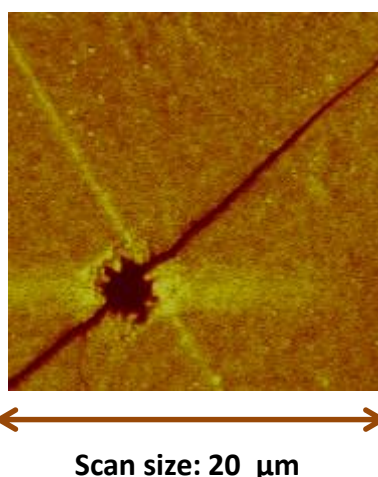
Scan size: 20 μm

Figure 7. SCM phase image of **[DNA⊃PD] + pent-TP**, negative phase shift corresponds to the position of the nanowire in the image and is indicative of it being conductive (scan size: 20 μm).

The observation that the [DNA ⊃ **PD**] + **pent-TP** product is conductive indicates that the monomer units **Pent-TP** are sufficiently closely packed along the DNA helix for them to be able to bridge with their nearest neighbour and hence polymerise. Conductance was not observed in samples prepared in carefully deoxygenated solutions and we conclude that the polymerization is initiated by residual oxygen species in the solvent,[23] and facilitated by the reduced localised pH along the DNA helix.[24]

A parabolic dependence of the phase shift on bias for voltages between -7 and +7 V was observed, see Figure 8. This is in line with the tip-sample interactions being dominated by capacitance effects, rather than the influence of static charges present on the sample (which would be expected to result in a linear relationship between the applied bias potential and measured phase shifts).[16, 25, 26]
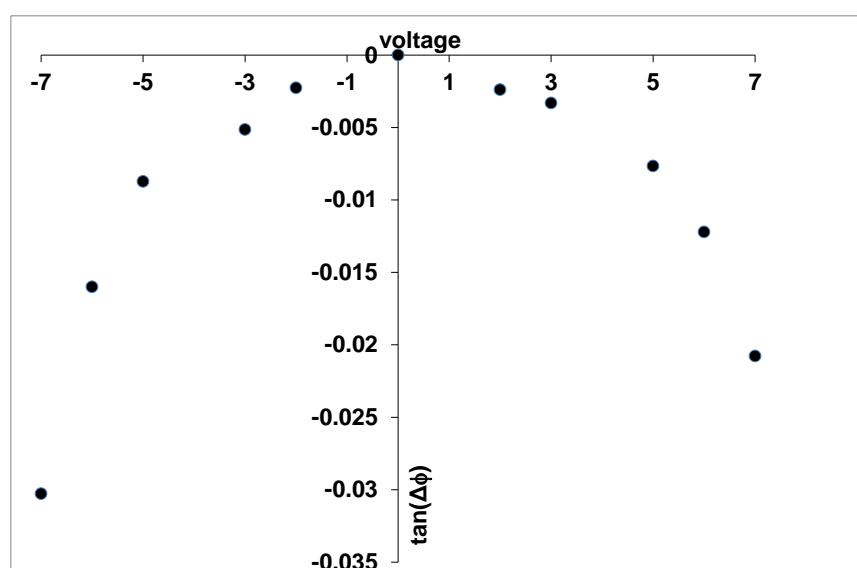
Figure 8 Parabolic dependence of phase shift on bias for voltages between -7 and +7 V for nanowire formed from click reaction of **PD** with **pent-TP** intercalated into λ-DNA, [DNA ⊃ **P/D] +pent TP**.

107

4.3.2.3 UV/vis spectroscopy of [DNA ⊃ PD] + pent-TP

According to previous binding studies, the absorbance λ_{max} of free **PD** and [DNA ⊃ **PD**] appear at 379 nm and 414 nm respectively. The UV spectra of free **PD** and **[DNA⊃PD]** are similar, see Figure 9a. The UV/vis spectrum associated with the *in-situ* click product [DNA ⊃ **PD**] + **pent-TP**, showed a λ_{max} of 387 nm which differs from the absorbance λ_{max} of free **PD** and [DNA ⊃ **PD**] see Figure 9b. In addition, the comparison of the UV/vis spectra of the synthetic click product, **PD** + **pent-TP** with [DNA ⊃ **PD**] + **pent-TP** showed similar absorption peaks at 385 nm and 387 nm respectively. This could infer that the *in-situ* click reaction was successful. Figure 9b indicates that the **PD** absorption band in **[DNA ⊃ PD]** (414 nm) is considerably different from the absorption band from **PD** in the *in-situ* click reaction, [DNA ⊃ **PD**] + **pent-TP** (387 nm). Figure 9c showed the similarity of the UV band for the synthetic click product, **PD** + **pent-TP**, (λ_{max} 387 nm) and the click reaction *in-situ*, [DNA ⊃ **PD**] + **pent-TP** (λ_{max} 385 nm).
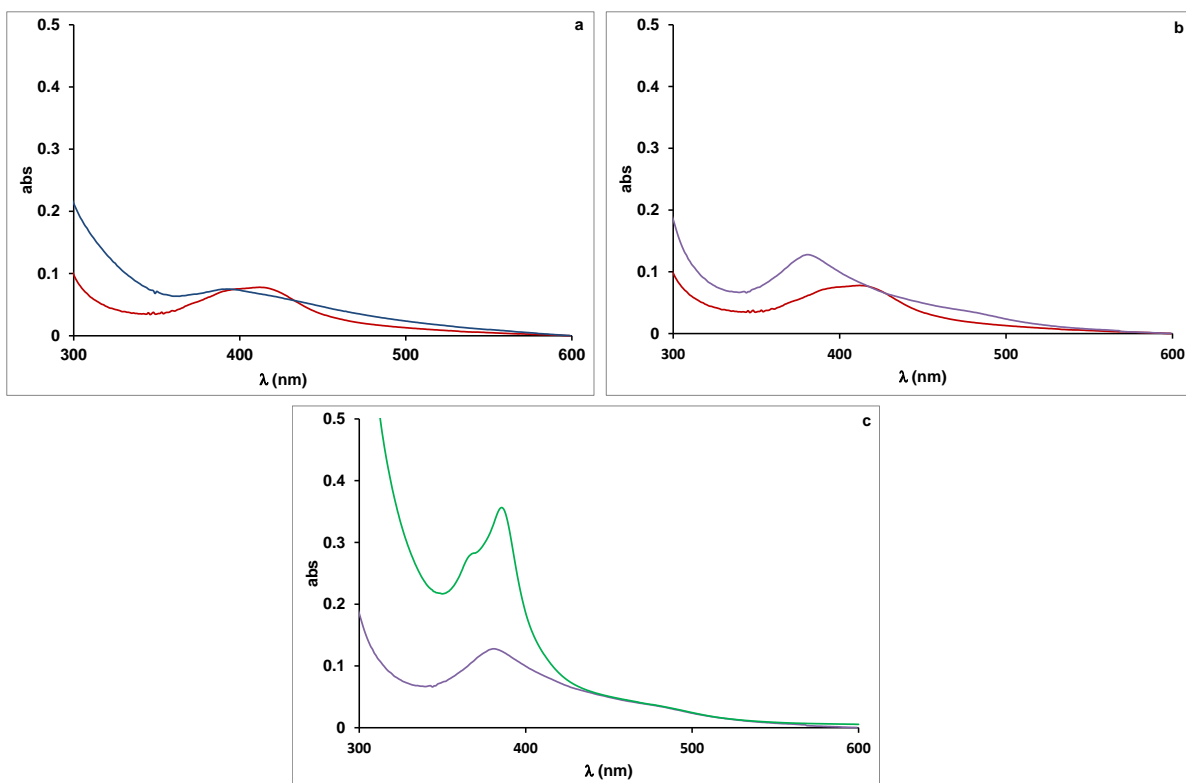
Figure 9. Comparison of UV/vis spectra of **a)** blue free **PD** and red [DNA⊃**PD**]; **b)** purple *in-situ* click [DNA ⊃ **PD**] + **pent-TP** and red [DNA ⊃ **PD**]; **c)** green synthetic click product **PD** +**pent- TP** and purple *in-situ* click [DNA ⊃ **PD**] + **pent-TP**.

FTIR can give valuable information about functional groups involved in the click reaction and how successful performance of the click reaction can be monitored is explained below.

4.3.2.4 FTIR spectroscopy of [DNA ⊃PD] + pent-TP

The IR spectra of **[DNA ⊃ PD] + pent-TP**, **[DNA ⊃ PD]** and **pent-TP** are discussed here. The IR spectrum of **[DNA ⊃ PD** showed a peak at 2108 cm^{-1} relating to the azide group of the intercalated **PD**. The spectrum of **pent-TP** indicated two peaks at 2112 cm^{-1} and 3283 cm^{-1} regarding to stretching modes of C≡C and C≡C–*H* respectively. The spectrum of the product after the click reaction with **pent-TP** implied the successful performance of the *in-situ* click modification of DNA, **[DNA ⊃ PD] + pent-TP**, due to the disappearance of the peaks associated with the alkyne and azide groups as seen in Figure 10.
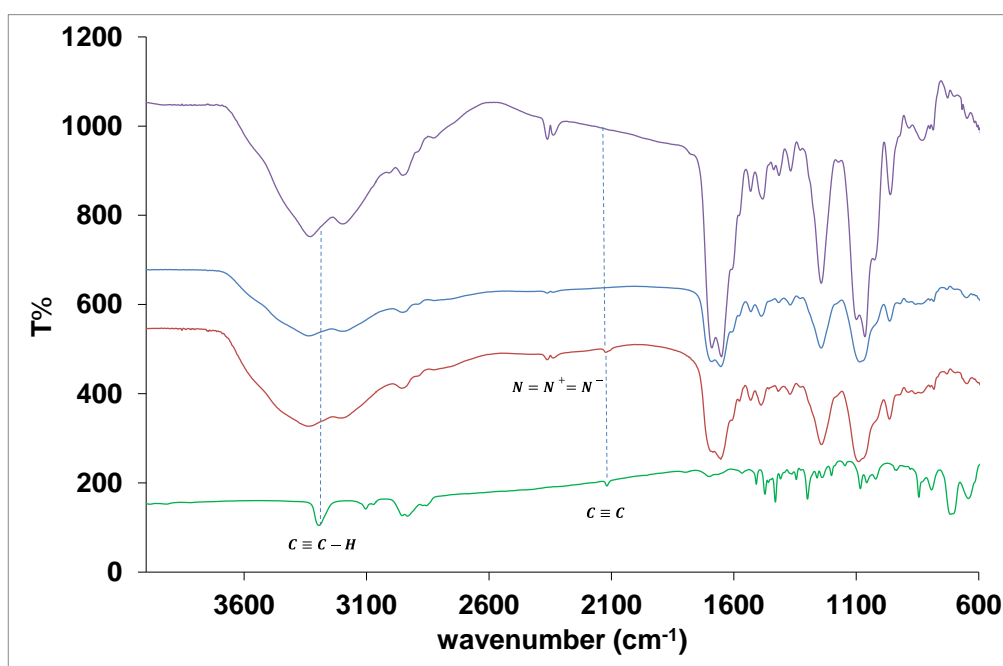
Figure 10. FTIR spectra of *in-situ* click reaction of **PD** with **pent-TP** (purple), calf thymus **DNA** (blue), **[DNA ⊃ PD]** (red) and **pen-TP** (green) from top to bottom.

4.3.2.5 Mass spectrometry of [DNA ⊃ PD] + pent-TP

The *in-situ* click reaction solution was denatured by heating to remove the DNA from the click product which was then extracted by DCM from the aqueous layer. Organic and aqueous layers were evaporated in a vacuum centrifuge and the residues were diluted in pure methanol for analysis by mass spectrometry. The organic residue showed the formation of **[DNA ⊃ PD] + pent-TP** or click product in its high resolution ES-MS

due to the appearance of a molecular ion peak of mass [M+Na]$^+$ 828.2632 which correlates well with the calculated mass of **PD** + **pent-TP,** 828.2628 see Figure.11.
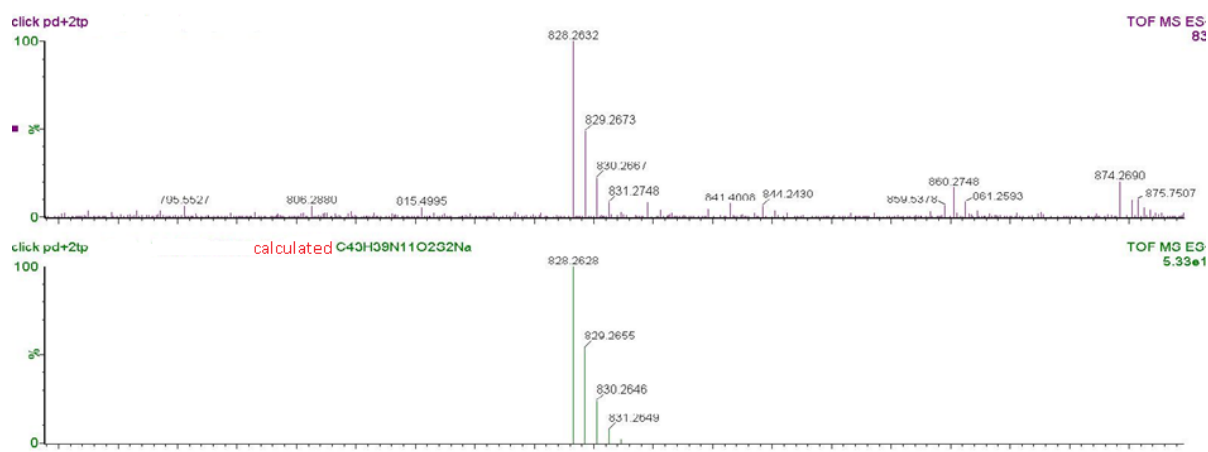
Figure 11. Mass spectra of [DNA ⊃ **PD**] + **pent-TP** in the top real mass and in the bottom calculated mass.

4.3.3 Fluorescence Microscopy of [DNA⊃PD] + APCR

The click reaction was also performed using **APCR** a green fluorescence dye in order to monitor whether the reaction product was localised along the DNA to yield [DNA ⊃ **PD**] + **APCR**. **APCR** was chosen because its excitation wavelength at 501 nm was higher than the excitation wavelength of **PD** and so could be used to identify the *in-situ* click product.

A drop of [DNA ⊃ **PD**] + **APCR** was then deposited on the silicon surface and the chip left to dry in a vacuum hood for 2 hours before imaging by fluorescence microscope.

The fluorescence micrograph shown, see Figure12, is the same sample of [DNA ⊃ **PD**] + **APCR** that had been combed onto a silicon wafer and imaged by AFM, shown in Figure 12. The image shows a linear strand of fluorescing decorated DNA, approximately 17 μm in length. No such image was obtained when bare λ−DNA was treated with **APCR** under the same click reaction conditions discounting simple electrostatics as a possible cause of the association of **APCR** with [DNA ⊃ **PD**].
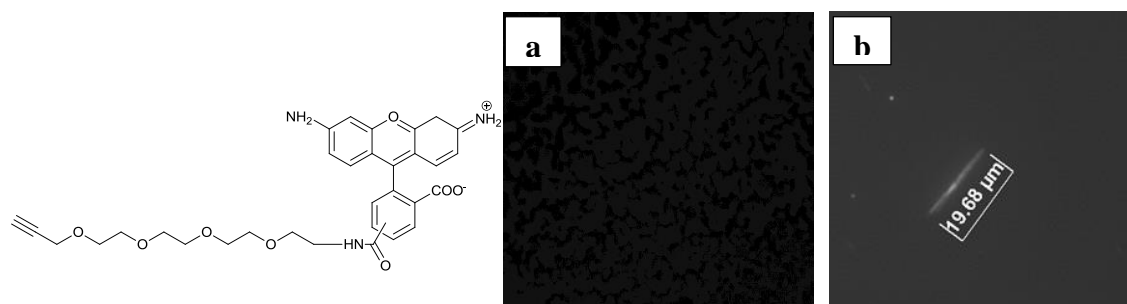
Figure 12. Left hand side: **APCR** and right hand side fluorescence image of a) DNA + **APCR** with click catalyst and b) **[DNA + PD]** + **APCR** with click catalyst, length of the observed decorated **DNA** nanostructure in b is approximately 17 μm.

110

Having investigated the click modification of **PD** while intercalated into DNA, attention turned to studying the *in-situ* click reaction using the **[DNA ⊃ PDMe⁺]** complex. The association constant with DNA of **PDMe⁺**, 2×10^6 M⁻¹, is higher than **PD**, 5.3×10^5 M⁻¹, as discussed in Chapter 2. In addition, the solubility of **PDMe⁺** in water is higher than **PD** due to the positive charge on the ring nitrogen. Therefore, the affinity of **PDMe⁺** to DNA increases due to the improved electrostatic interactions between **PDMe⁺** and the negatively charged DNA backbone. In addition, the solubility of components could affect the morphology of the DNA nanostructure. Therefore, in the next sections some experiments designed to explore the suitability of **PDMe⁺** for performing the *in-situ* click using **pent-TP** and **APCR** are described.

4.4 Assembly at DNA via maximum PDMe⁺ intercalator loading

The binding of **PDMe⁺** to DNA has been studied in Chapter 2 and found to associate with the double helix nearly 100 times more strongly than **PD**. Therefore the following sections discuss the assembly of conductive polymer units, **pent-TP** and the fluorescent dye **APCR** with **PDMe⁺**, at a ratio of intercalator to base-pairs of 1 : 2 and 1 : 4 respectively..
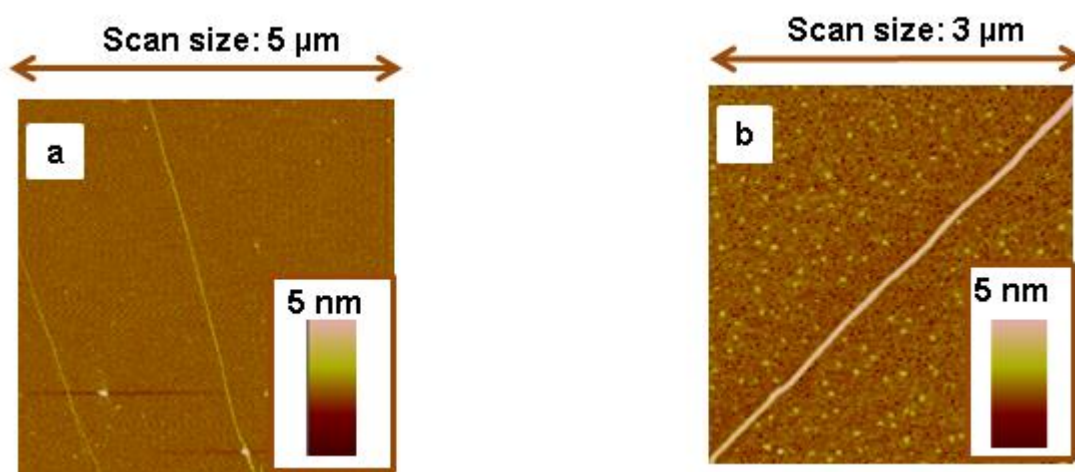
Figure 13. AFM image of **a)** λ-DNA deposited onto a silicon wafer, scan size: 5 μm, DNA shown has typical height of 1.6 nm; **b)** **[DNA ⊃ PDMe⁺]** scan size: 3 μm, height ranges 2.9-5.4 nm.

Once again as in the **PD** case, the AFM images of [DNA ⊃ **PDMe⁺**], Figure 13b, indicated that the linear topology of DNA is not disturbed by the interaction of **PDMe⁺** and are similar to naked DNA, Figure 13a. As for **PD**, the minimum observed heights of the intercalated complexes according with the concluded expectation that intercalation of **PDMe⁺** increases the DNA bulk (height 1.6 nm). However, the increased height of DNA after intercalation of **PDMe⁺** showed that the increased height cannot be due to

111

the simple association of the intercalator into the helix but it could be due to be more than a single helix in many of the observed nanostructures. Therefore the intercalation of **PDMe⁺** in DNA appears again to aid the bundling of two or more helices into larger diameter nanostructures, at least under the surface attachment conditions.

4.4.1 [DNA ⊃ PDMe⁺] clicked with pent-TP

The *in-situ* click modification of DNA, **[DNA ⊃ PDMe⁺] + pent-TP** was performed in order to form conductive nanostructures. The following section discusses some AFM images which illustrate the structural modification of **[DNA ⊃ PDMe⁺]** to give **[DNA ⊃ PDMe⁺] + pent-TP.**

4.4.1.1 AFM study of [DNA ⊃ PDMe⁺] + pent-TP

Aqueous solutions of [DNA ⊃ **PDMe⁺**] and [DNA ⊃ **PDMe⁺**] + **pent-TP** were deposited via molecular combing onto the surface of silanised silicon oxide wafers prepared as previously.[15-17] Tapping mode AFM indicated the formation of wire-like structures aligned on the surface in both cases, see Figure 6a and Figure 6b

Tapping mode AFM indicated the formation of wire-like features aligned on the surface for [DNA ⊃ **PDMe⁺**] and [DNA ⊃ **PDMe⁺**] + **pent-TP** see Figure 14a and Figure14b respectively. The observed 1-D nanostructures of [DNA ⊃ **PDMe⁺**] and [DNA ⊃ **PDMe⁺**] + **pent-TP** are comparable in topology to those of bare λ-DNA, see Fig.13a. The ranges in height of the nanostructures of λ-DNA, [DNA ⊃ **PDMe⁺**] and [DNA ⊃ **PDMe⁺**] + **pent-TP** were 0.5 − 2.1 nm, 2.9 − 5.4 nm and 8.6 − 16.58 nm respectively. These findings indicate that **PDMe⁺** is similar to **PD** and has more than a simple insertion effect on the observed increase in height, and likewise the click reaction with **pent-TP** is not solely responsible for the larger diameters observed.
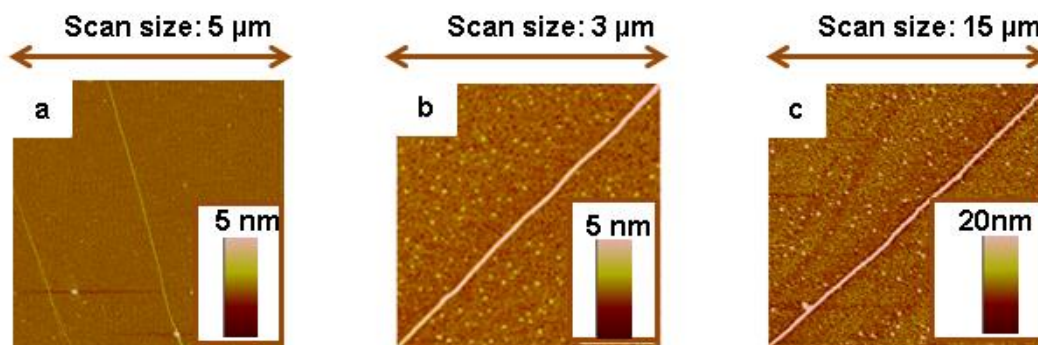
Figure 14: AFM images of **a**) bare DNA, scan size: 5 μm, typical height of 1.6 nm **b**) [DNA ⊃ **PDMe⁺**]**,** scan size: 3.μm, height ranges 2.9-5.4 nm and **c**) [DNA ⊃ **PDMe⁺**] + **pent- TP,** scan size: 15 μm, 10.52 nm height.

4.4.1.2 SCM study of [DNA ⊃ PDMe⁺] + pent-TP

A silicon wafer prepared as described in the experimental section was used as a substrate to deposit a sample of **[DNA ⊃ PDMe⁺] + pent-TP**. The chip was then dried in a vacuum hood for 2 hours before imaging by SCM. The SCM image of the observed nanostructure of **[DNA ⊃ PDMe⁺] + pent-TP** shows a similar result to **[DNA ⊃ PD] + pent-TP,** a negative phase shift as the tip crosses the wire; typical of a conductive structure.[22]
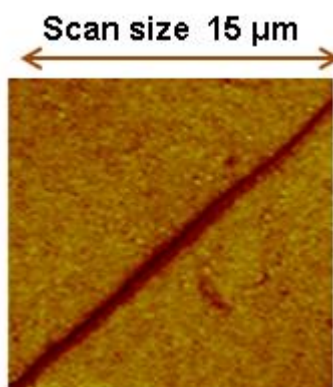
Figure 15 SCM phase image of **[DNA ⊃ PDMe⁺] + pent-TP**, negative phase shift corresponds to the position of the nanowire in the image and is indicative of it being conductive (scan size: 20 μm).

A parabolic dependence of phase shift was observed for bias voltages between -7 and +7 V, see Figure 16. This is consistent with the tip-sample interactions being dominated by capacitance effects, rather than the influence of static charges present on the sample (which would be expected to result in a linear relationship between the applied bias potential and measured phase shifts).[16, 25, 26]
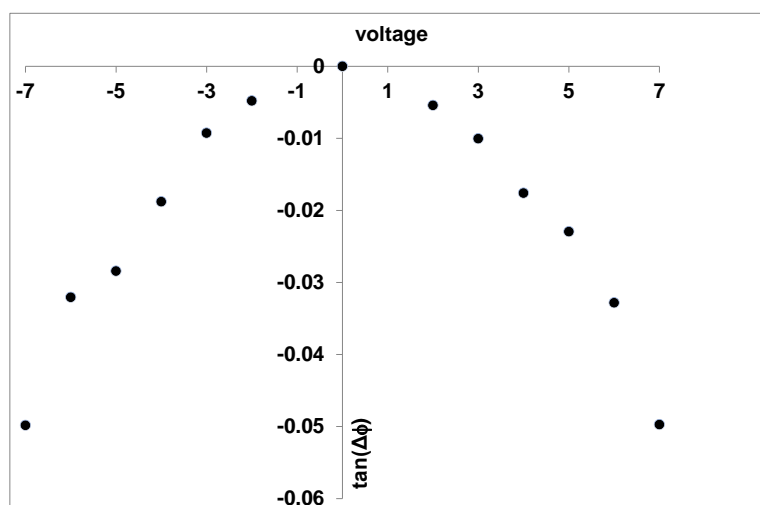
Figure 16 Parabolic dependence of phase shift on bias for voltages between -7 and +7 V for nanowire formed from click reaction of **PDMe⁺** with **pent-TP** intercalated into **λ-DNA**, **[DNA ⊃ PDMe⁺] +pent-TP**.

4.4.1.3 UV/vis spectroscopy of [DNA $\supset$ PDMe$^+$] + pent-TP

The conversion of **PDMe$^+$** to the synthetic click product, **PDMe$^+$ + pent-TP**, was monitored by UV/vis while it remained intercalated in DNA. UV/vis spectroscopy was used to study the electronic structure and compare the two click products; **PDMe$^+$ + pent-TP,** and [DNA $\supset$ **PDMe$^+$**] + **pent-TP.**

According to previous binding studies, the absorbance λ_{max} of **PDMe$^+$** and [DNA $\supset$ **PDMe$^+$**] appear at 413 nm (blue) and 428 nm (red), respectively as shown in Figure 17a, confirming the intercalation of **PDMe$^+$** into **DNA** due to the observed bathochromic shift. The spectrum in Figure 17b associated with the *in-situ* click reaction, [DNA $\supset$ **PDMe$^+$**] + **pent-TP** showed a λ_{max} at 424 nm. This differs from the absorbance λ_{max} of free **PDMe$^+$** (413 nm) but only slightly from the intercalated complex [DNA $\supset$ **PDMe$^+$**] (428 nm). A comparison of the UV/vis spectra of the click product formed in solution (**PDMe$^+$ + pent-TP**) and formed on DNA [DNA $\supset$ **PDMe$^+$**] + **pent-TP** showed peaks at 430 nm and 424 nm, respectively (Figure 17c). There is a strong underlying UV absorption from **pent-**TP that provides a rising background in these spectra, which makes comparison difficult. Nevertheless, the observance of a single major peak in each spectrum that is red shifted compared to free **PDMe$^+$** suggests that the click reaction proceeds while the intercalator remains bound to the DNA.
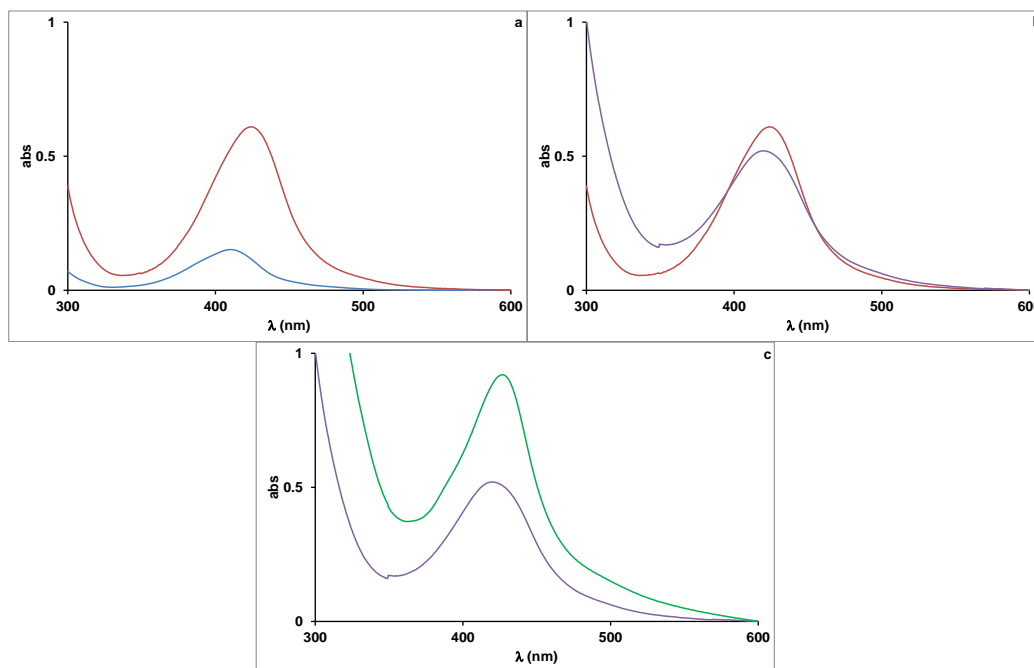
Figure 17 (a) blue free **PDMe$^+$**, red [DNA $\supset$ **PDMe$^+$**] (b) red [DNA $\supset$ **PDMe$^+$**] and Purple *in-situ* click [PD $\supset$ **PDMe$^+$**] +**pent-TP** (c) Purple *in-situ* click [DNA $\supset$ **PDMe$^+$**] +**pent-TP** and green synthetic click product **PDMe$^+$ + pent-TP**.

4.4.1.4 FTIR spectroscopy of [DNA ⊃ PDMe⁺] + pent-TP

The IR spectra of **[DNA ⊃ PDMe⁺] + pent-TP**, **[DNA ⊃ PDMe⁺]** and **pent-TP** are discussed. The IR spectrum of **[DNA ⊃ PDMe⁺]** showed a peak at 2085 cm^{-1} relating to the azide group and the spectrum of **pent-TP** indicated two peaks at 2102 cm^{-1} and 3280 cm^{-1} relating to the stretching modes of C≡C and C≡C–*H* respectively. The spectrum of **[DNA ⊃ PDMe⁺] + pent-TP** implied the successful performance of the click modification due to the disappearance of the peaks associated with both the alkyne and azide groups, see Figure 18.
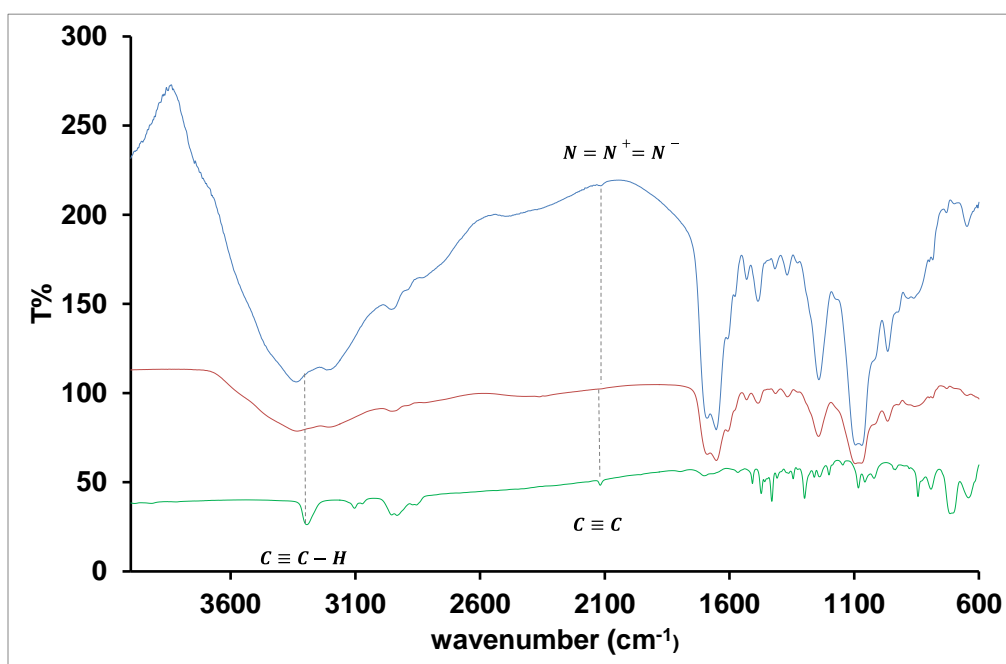
Figure.18 FTIR spectra of **[DNA ⊃ PDMe⁺]** (blue), *in-situ* click reaction of DNA, **[DNA ⊃ PDMe⁺] + pent-TP** (red) and **pent-TP** (green).

4.4.1.5 Mass spectroscopy of [DNA ⊃ PDMe⁺] + pent-TP

The *in-situ* click reaction solution was denatured by heating to remove the DNA from the click product which was then extracted by DCM from the aqueous layer. Organic and aqueous layers were evaporated in a vacuum centrifuge and the residues were diluted in pure methanol for analysis by mass spectrometry. The organic residue showed the formation of **[DNA ⊃ PDMe⁺] + pent-TP** was obtained from its high resolution ES-MS. A molecular ion of mass [M]⁺ 820.3698 was found which correlates well with the calculated mass for **PDMe⁺ + pent-TP** of 820.2964.

4.4.1.6 Linear dichroism spectroscopy of [DNA ⊃ PDMe$^+$] + pent-TP

LD^r investigations discussed in Chapter 2 indicated the negative LD of the DNA band at around the wavelength which nucleobases absorb, 260 nm. In addition the negative LD band for the **PDMe$^+$** due to intercalation of **PDMe$^+$** into DNA was observed.

After the *in-situ* click reaction at high dye loading, **[DNA ⊃ PDMe$^+$] + pent-TP,** the LD^r signal at 425 nm for the **PDMe$^+$** absorption band remained negative, see Figure 19. A new negative signal is observed in the 300-350 nm region, where **PDMe$^+$** has no contribution, which corresponds to the **pent-TP** substituent. If the orientation of the DNA bases (260 nm) is set at 90° to the helix axis, the calculated angles are 74° for **PDMe$^+$** (425 nm) and 63° for **pent-TP** (350 nm). In this orientation, the **TP** molecules can polymerize to give a conducting polymer chain.
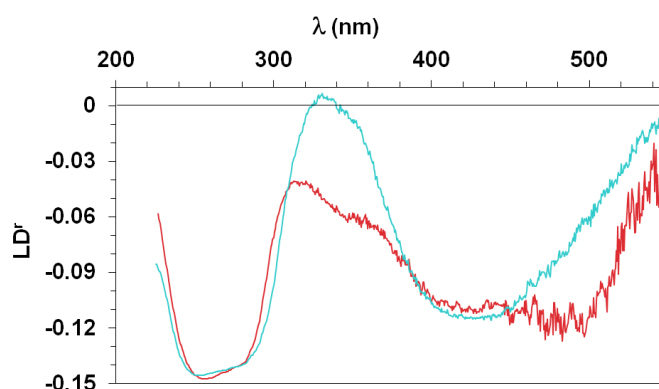
Figure 19. Reduced linear dichroism (LD^r = LD/Abs) spectra of (red) **[DNA ⊃ PDMe$^+$] + pent-TP** in *in- situ* click reaction on DNA at high loading and (blue) **[DNA ⊃ PDMe$^+$]** [**PDMe$^+$**] = 20 μM; [DNA] = 1 mM; [**pent -TP**] = 40 μM; 5 mM phosphate (pH 6.9)/1% DMSO. Shear gradient = 3170 s^{-1} (1000 rpm rotation speed).

4.4.2 AFM and Fluorescence Microscopy of [DNA ⊃ PDMe$^+$] + APCR

AFM studies indicate that the intercalated complexes, [DNA ⊃ **PDMe$^+$**] and [DNA ⊃ **PDMe$^+$**] + **APCR,** remain stable during deposition from solution and interrogation by an AFM tip, with little observed change in the linear wire-like structures observed for native λ-DNA, Figure 20a. However there was a noticeable change in the range of heights of the nanostructures observed, from 5.2 nm to 10.4 nm. Therefore, the click reaction of [DNA ⊃ **PDMe$^+$**] with **APCR,** an alkyne bearing green fluorescent dye, was also monitored through fluorescence microscopy to ascertain that **PDMe$^+$** remains assembled in the helical stack of the λ-DNA even after decoration with **APCR**. The fluorescence micrographs shown in Figure 20b and 20c are of the same sample of [DNA ⊃ **PDMe$^+$**] + **APCR** that had been combed onto a silicon wafer and imaged by **AFM**, shown in Figure 20a. Several linear strands of fluorescing decorated DNA, each approximately 17 μm in length were observed. No such images were obtained when bare λ−DNA was treated with **APCR** under the same click reaction conditions discounting simple electrostatics as a possible cause of the association of **APCR** with [DNA ⊃ **PDMe$^+$**].
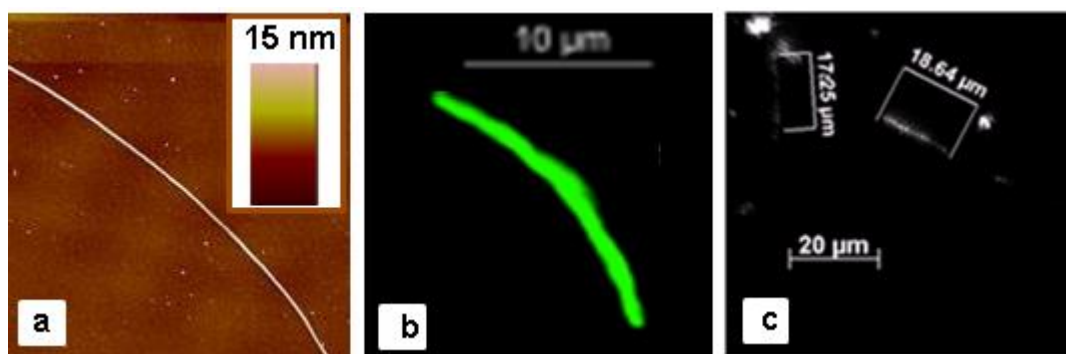
Figure 20. **a)** AFM image, **b)** and **c)**: fluorescence images of [DNA⊃**PDMe$^+$**] + **APCR**, the length of the observed decorated DNA nanostructure is approximately 17 μm.

APCR illuminates the 1-D nanostructures, and confirms that the intercalator remains bound to the DNA even after click modification.

These studies at maximum loading of DNA with **PD** and **PDMe$^+$** show that the assembly of functional alkyne units (conductive polymers, redox active groups and fluorescent dyes) along the DNA helix can be achieved via intercalation followed by click modification. The following sections discuss how the assembly of materials can be controlled by varying the level of intercalative loading of DNA with **PD**.

4.5 Reduced loading of DNA with PD, [DNA ⊃ PD].

In the previous work the ratio of intercalator to base-pairs was kept at the maximum possible loading, 1:2, here a reduced loading of the intercalator **PD** with DNA was investigated where the DNA base ratio was 1:70. Therefore the average separation between two adjacent intercalators, about 12 nm, would be far greater than in the maximum loaded situation. Therefore the interaction between the decorated functional groups will be different and a range of new nanostrucutres may be realised. For example, the assembly of the **pent-TP** group at maximum loading was seen to from a conductive nanowire as the monomer units were close enough to link together to form the polymer. However at the now reduced level of intercalator loading it is possible that intramolecular cyclisation may occur due to low local pH[27] and macrocycle could be formed, see Figure 21.
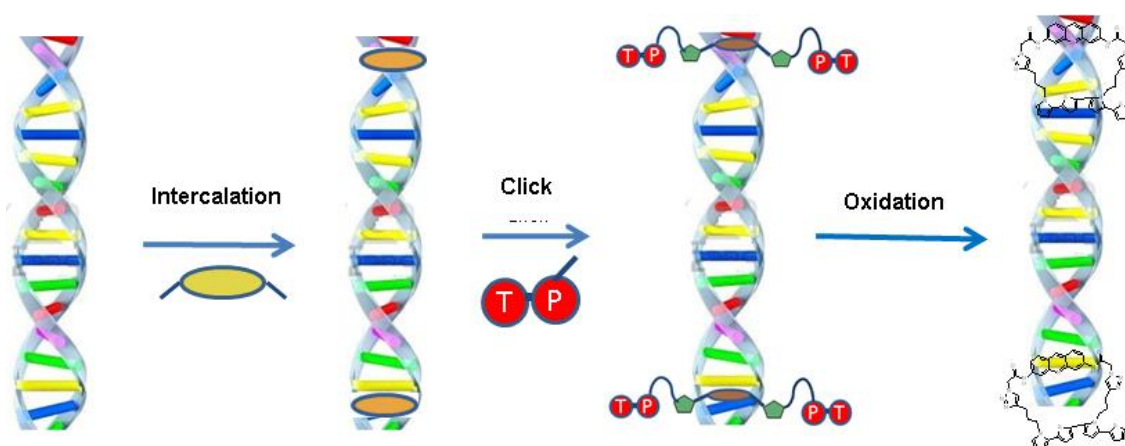
Figure 21. Cartoon model of intercalation then click chemistry in the case of low loading.

4.5.1 In-situ click reaction of reduced loaded [DNA ⊃ PD] with pent-TP

The *in-situ* click reaction of low loaded **[DNA ⊃ PD]** with **pent-TP,** where the ratio of **PD** per DNA base-pair was 1 to 35 was performed with the aim of forming the macrocycle structures proposed in Figure 21. In the following sections UV, IR and Mass spectroscopy characterize the formation of **[DNA ⊃ PD]** + **pent-TP** in this reduced loading case.

4.5.2 UV/vis spectroscopy of [DNA ⊃ PD] + pent-TP at low loading

According to previous binding studies, the absorbance λ_{max} of free **PD** and [DNA ⊃ **PD**] appear at 379 nm and 414 nm respectively, see Figure 22a. Therefore the UV/Vis spectra confirmed the intercalation of **PD** into DNA. The UV/vis spectrum associated with the *in-situ* click product from **[DNA ⊃ PD]** + **pent-TP** see Figure 22b, showed a

λ_{max} at 387 nm that differs from the λ_{max} of free **PD** (379 nm) and the unmodified but intercalated situation **[DNA ⊃ PD]** (414 nm). In addition, the comparison of the UV/vis spectra of the synthetic click product, **PD + pent-TP**, (Figure 22c, green) and the *in situ* click reaction of **[DNA ⊃ PD] + pent-TP**, showed similar maximum at 385 nm and 387 nm respectively. Therefore it could be concluded that the click reaction was successfully performed while **PD** remained intercalated.
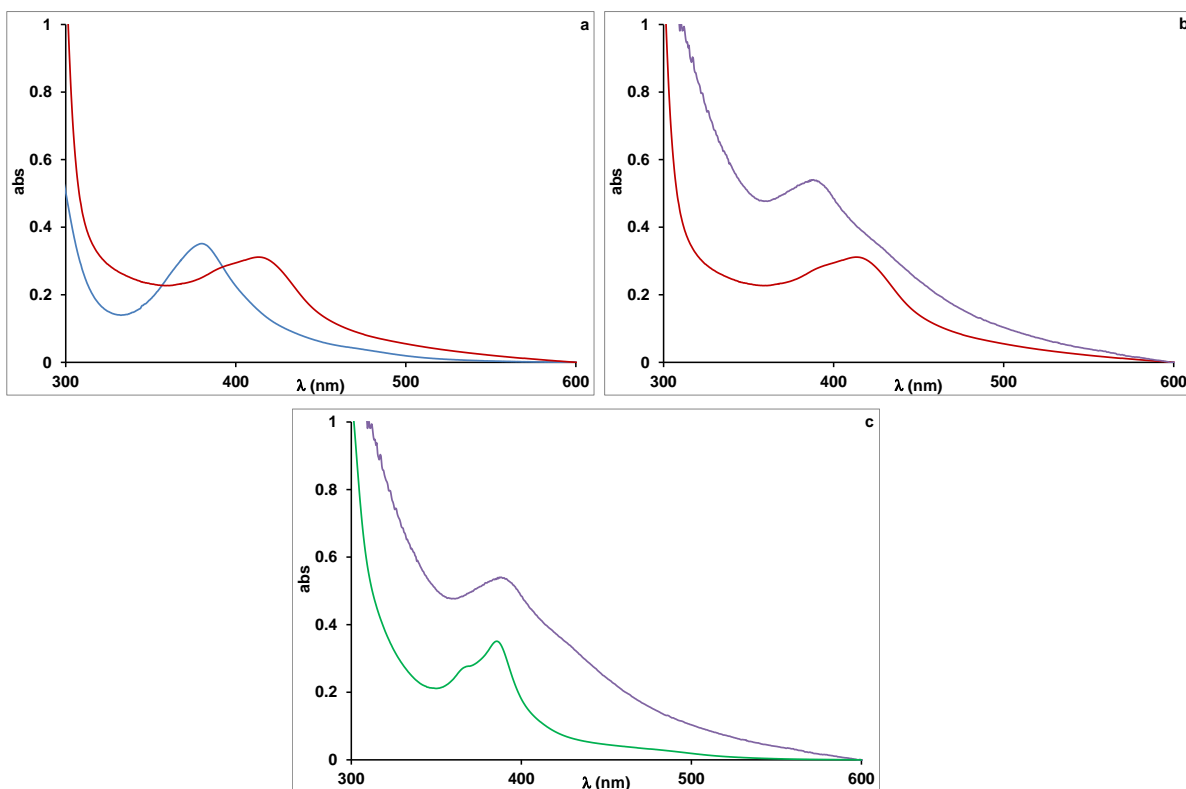
Figure 22. (a) UV/vis spectra of red free **PD,** blue **[DNA ⊃ PD]** (b) blue **[DNA ⊃ PD]** and Purple *in-situ* click **[PD ⊃ PD] +pent-TP**.(c) Purple *in-situ* click **DNA ⊃ PD] +pent-TP** and green synthetic click product, **PD + pent-TP**.

5.3 FTIR spectroscopy of [DNA ⊃ PD] + pent TP at low loading

The IR spectra of DNA, **[DNA ⊃ PD]**, **pent-TP** are discussed together with the products after click reaction. The IR spectrum of **PD** loaded on DNA showed a peak at 2108 cm^{-1} relating to the azide group. The spectrum of **pent-TP** indicated two peaks at 2112 cm^{-1} and 3283 cm^{-1} due to the C≡C and C≡C–*H* stretches respectively. The spectrum of the click-product, **PD + pent-TP** implied the successful performance of the modification due to the disappearance of the peaks associated with both the alkyne and azide groups, see Figure 23.
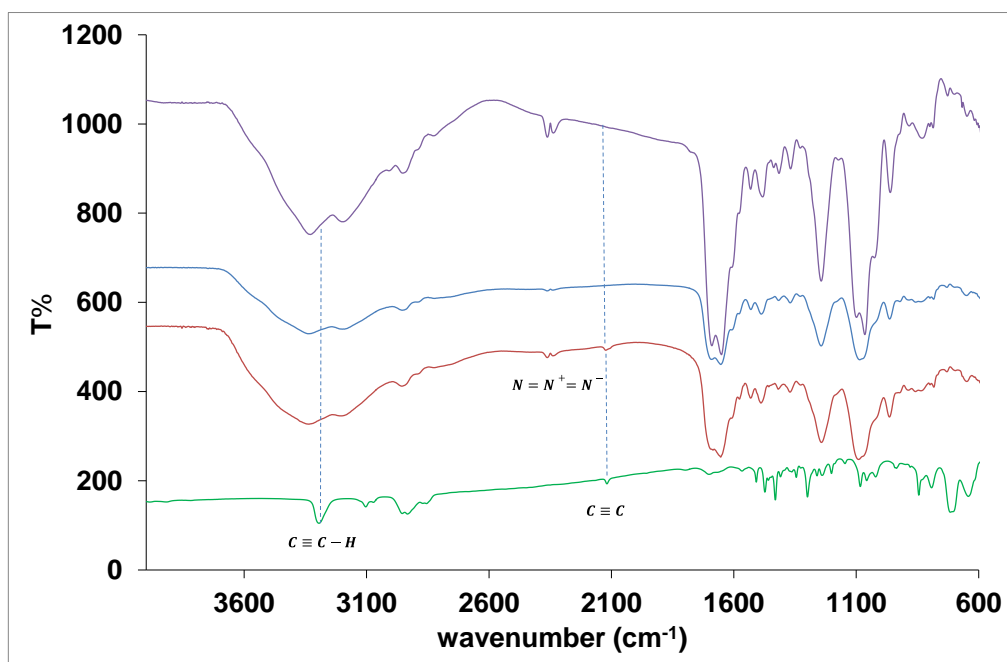
Figure 23. FTIR spectra of click in situ of **DNA, [DNA ⊃ PD] + pent-TP,** (purple); calf thymus **DNA** (blue); **PD** loaded on Calf thymus DNA, [DNA ⊃ PD], (red) and **pen-TP** (green) from top to bottom respectively.

4.5.4 Mass spectroscopy of [DNA ⊃ PD] + pent-TP at low loading

The *in-situ* click reaction solution was denatured by heating to remove the DNA from the click product which was then extracted by DCM from the aqueous layer. Organic and aqueous layers were evaporated in a vacuum centrifuge and the residues were diluted in pure methanol for analysis by mass spectrometry. The organic residue showed the formation of **[DNA ⊃ PD] + pent-TP** was obtained from its high resolution ES-MS. A molecular ion of mass $[M + Na]^+$ 828.2566 was found which correlates well with the calculated mass for **PD + pent-TP** of 828.26, see Figure.24.
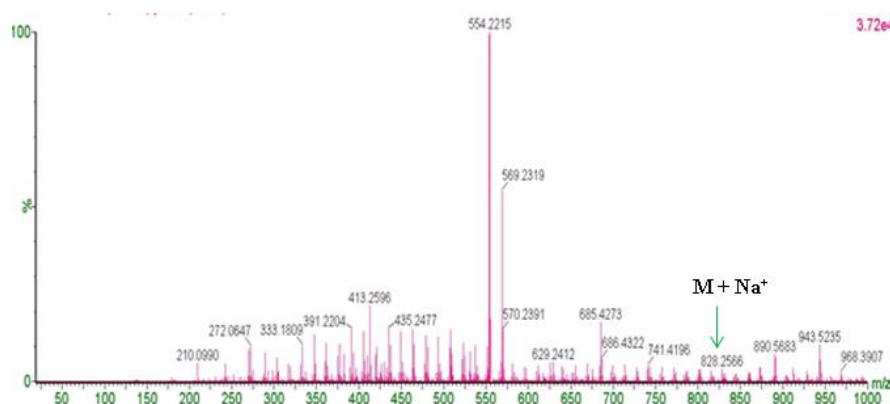
Figure 24. Mass spectrum of extracted organic residue sample of click in situ of DNA, [DNA ⊃ PD] + **pent-TP**, in the case low loading.

4.5.5 Linear Dichroism Spectroscopy of [DNA ⊃ PD or PDMe⁺] + pent-TP at low loading

As previously explained in Chapter 2, LD^r investigation indicated the negative LD of the DNA band in the UV area around the wavelength of absorption of the nucleobases, 260 nm. Linear dichroism spectroscopy also shows that the ring systems of **PD** and **PDMe⁺** remain intercalated in DNA after their azide groups undergo click reactions with **pent-TP**. At low dye loading see Figure 25, the LD^r signal at 300-350 nm is slightly positive whilst the signal in the **PD** absorption band at 430 nm remains negative. Assuming that the DNA band at 260 nm represents an orientation of 90° with respect to to the helix axis, the **pent-TP** substituents in this sample lie at 52° while the **PD** unit is at 66°. This suggests that in the ring-closed product, the **TP** units have an alignment that is close to the plane of the acridine chromophore.
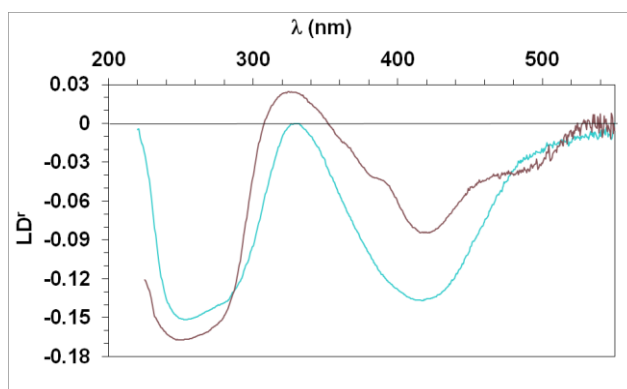
Figure 25. Reduced linear dichroism (LD^r = LD/Abs) of [DNA ⊃ **PD** + pent- **TP** in *in-situ* click reaction at low dye loading. [**PD**] = 7 μM; [DNA] = 1.25 mM; [**pent-TP**] = 14 μM; 5 mM phosphate (pH 6.9)/1% DMSO. Shear gradient = 1900 s^{-1} (600 rpm rotation speed).

4.6 Investigation of [DNA ⊃ PD] + pent-TP complexes and possible structures resulted from controlling the concentration of DNA intercalators

Pent-TP has been used in previous work to form conductive nanowires through templating onto DNA.[14, 28, 29] Therefore by modifying **PD** and **PDMe⁺** with **pent-TP** it is possible to gain more control over the assembly of the monomer units along the DNA helix to form a conductive wire of controlled composition. However, it is also possible that macrocyclic structures could be formed by controlling the loading of the azido intercalator in DNA. Here some investigations into the polymerisation of **PD** + **pent-TP** by chemical oxidation with FeCl$_3$ are described. The polymerization is followed by UV spectroscopy to investigate the extent of conjugation observed in the oligomer/polymer products.

4.6.1 UV/Vis spectroscopy after chemical oxidation of low concentration of synthetic click product (PD + pent-TP) to clarify the behaviour of just click product in low concentration equal with low loading concentration with DNA

The oxidation of the click-product **PD + pent-TP,** was monitored by UV/Vis spectroscopy for 48 hours, see Figure 26. Before polymerization, the peak appearing at 385 nm is assigned to the absorption of the click product. After polymerization, this peak moves slightly to 388 nm and a new peak appears at 410 nm. It is possible that this new absorption band is a result of the linking together of the two ends of the molecule to give a structure with extended conjugation. After 48 hours of polymerization, the peak at 410 nm disappears and a new peak emerges at 480 nm. It is known that as pyrrole polymerises a shift to longer absorption maxima is observed,[29] and the spectra observed in Figure 26 support this and shown structure is expected.
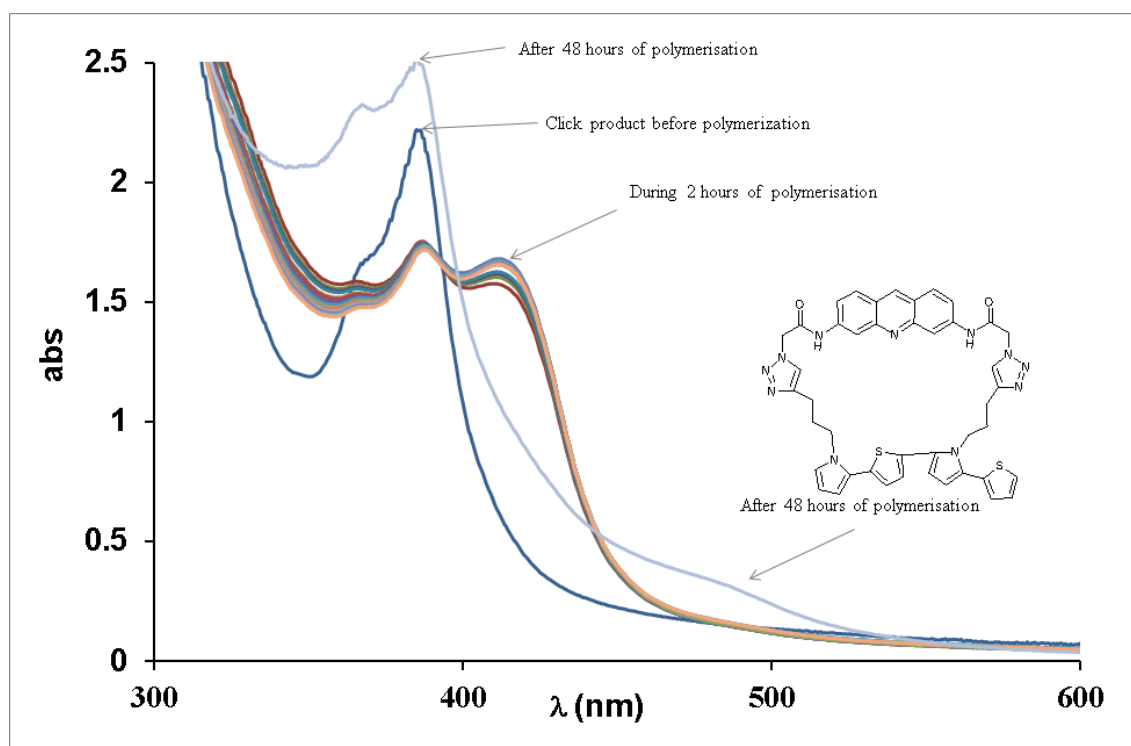
Figure 26 UV/vis spectra of chemical polymerization of 128 μM of synthetic click product, **PD + pent-TP**

4.6.2 UV/vis spectroscopy after chemical oxidation of [DNA ⊃ PD] + pent-TP at low loading

The UV/vis spectrum of **[DNA ⊃ PD] + pent- TP** after chemical polymerisation with FeCl$_3$ indicated the appearance of two π–π* absorption bands at 420 nm and 485 nm which could be due to the formation of larger π-conjugated systems, see Figure 27. This

hypothesis was based on the formation of a macrocycle by the internal dimerization of the two pendant **TP** units attached to the intecalator dye molecule.
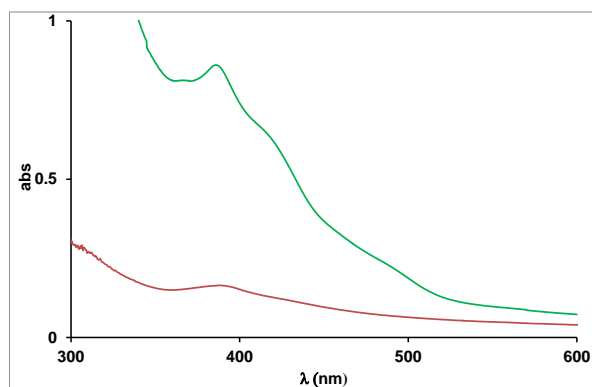
Figure 27. UV/vis spectrum of **[DNA ⊃ PD] + pent-TP** (387 nm, red) and after oxidation (387 nm, 420 nm and 485 nm green).

4.6.3. Mass spectrometry after chemical polymerization of [DNA ⊃ PD] + pent-TP in low loading

The *in-situ* click reaction solution was denatured by heating to remove the DNA from the click product which was then extracted by DCM from the aqueous layer. Organic and aqueous layers were evaporated in a vacuum centrifuge and the residues were diluted in pure methanol for analysis by mass spectrometry, see Figure 28.
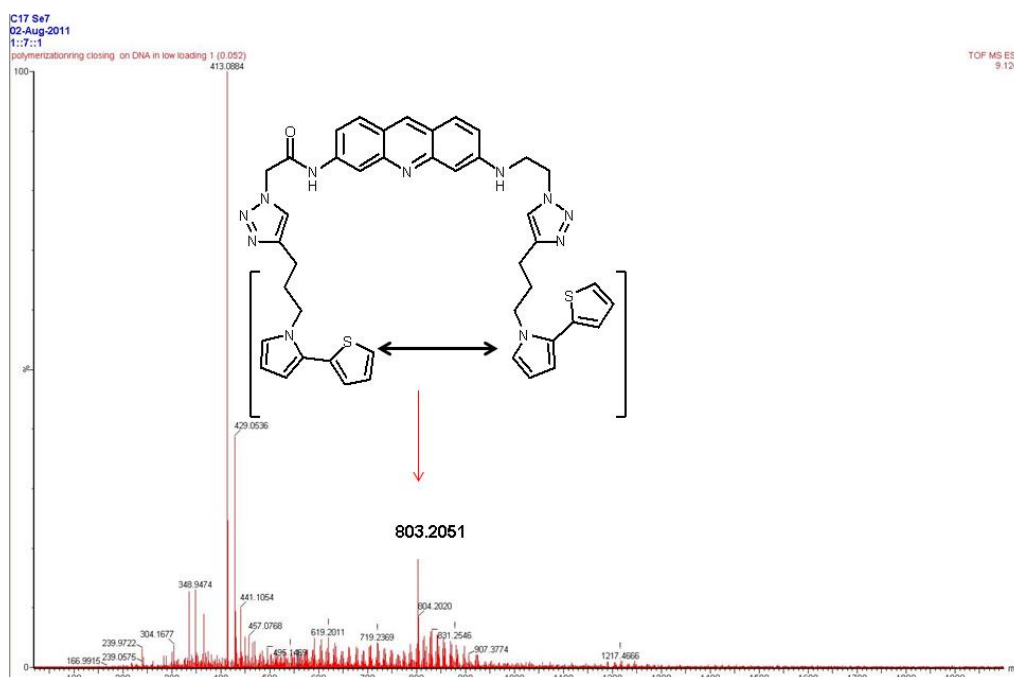
Figure 28. Mass spectrum of the organic extract from **[DNA ⊃ PD] + pent- TP** showing the possible formation of a macrocycle after oxidative polymerisation of either the thiophene or pyrrole heterocyles into a nano-ring.

123

The high resolution ES-MS of the organic residue was used to identify the *in-situ* click product **PD + pent-TP**, with expected molecular ions of [M+Na]$^+$ 828.2632 or [M+H]$^+$ 806.2632. However, a molecular ion of mass [M]$^+$ 803.2051 was found which correlates to a possible ring product by losing two protons from the **TP** heterocycles, ($C_{43}H_{39}N_{11}NaO_2S_2$ -2H), see Figure 28. The macrocycle formed could result from the oxidation at either the pyrrole or thiophene rings and could be one of three possible sizes, see Scheme 1.
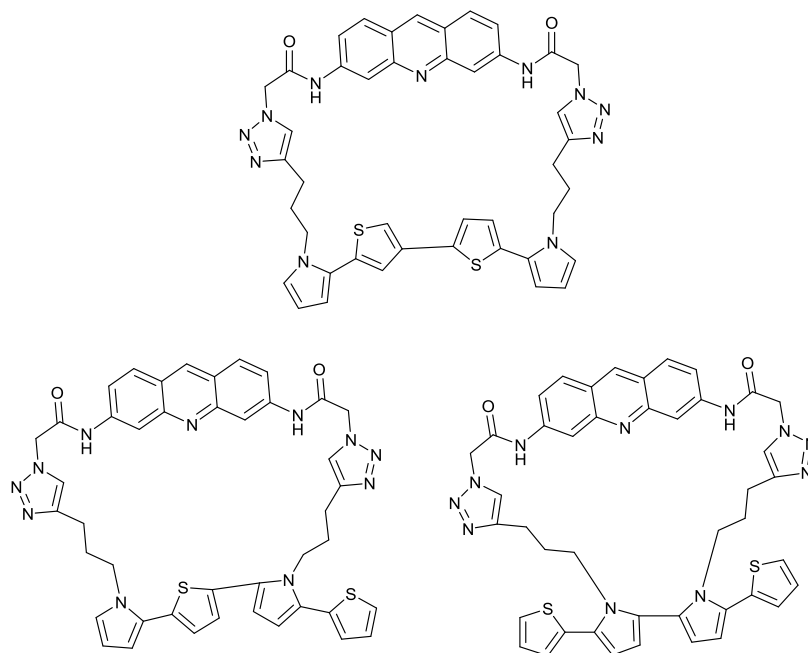
Scheme 1. Three possible macrocycle structures after polymerization of [DNA ⊃ **PD**] + **pent-TP**, the number of thiophene or pyrrole units involved in the ring can vary between 2, 3, or 4.

The following section describes some molecular modelling studies into the possible products from the intra-molecular cyclisation of the [DNA ⊃ **PD**] + **pent- TP** system with a view to understanding the modes of connecting the two **TP** units into a nano-ring.

4.7 Molecular modelling of intra-molecular cyclisation of PD + pent- TP

Molecular modelling analyses were carried out using Materials Studio 4.3 to investigate the minimized energy, rings size, and predicted UV/vis spectrum of the possible nano-rings formed from the internal polymerisation of the DNA intercalated **PD + TP** product. It is envisaged that the **TP** unit could polymerise in three different ways, to yield three macrocycles of different sizes. A ring containing all four heterocycles is formed when the two thiophene units are connected together. A smaller three member macrocyclic forms when one thiophene ring connects to a pyrrole unit on the second **TP**

124

group. The smallest macrocycle is formed if the two pyrrole units are connected together, see Scheme1.

4.7.1 Click product PD + pent-TP.

The minimised structure of the click product, **PD + pent-TP**, is shown in Figure 29, and the calculated absorption spectrum shows two peaks at 275 nm and 320 nm. Although these peaks do not accurately match the recorded spectrum (peaks at 270 nm and 385 nm) the underlying trend in absorbance is observed.
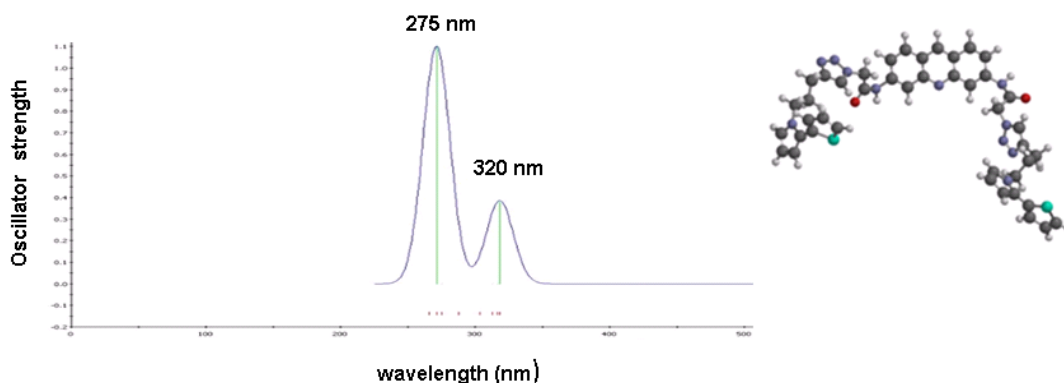
Figure 29 Left: calculated UV/vis spectrum (Materials Studio 4.3 using semi-empirical AM_1 method and ZINDO Hamiltonians) for **PD + pent-TP**, Right: minimised molecular structure of **PD + pent-TP**.

4.7.2 Pyrole-thiophene linked nano-ring [TP-TP]

The minimised structure of a nano-ring formed by closing two pyrole-thiophene ends of the click product, **PD + pent-TP**, is shown in Figure 30. The calculated absorption spectrum shows peaks at 275 nm, 320 nm and 380 nm. Therefore, there is one extra peak at 380 nm which was not seen before ring-closing, and is due to the formation of a four unit oligomer, where three of the heterocycles are involved in the formation of the macro-ring by intramolecular cyclisation. The formed macro-ring contains 32 bond.

The distance between the ring nitrogen of **PD** and the sulfur atom of the central thiophene ring (red line) and the distance between the carbons of the two triazole rings (green line) are 9.29 Å and 7.60 Å respectively (shown in Figure 30).
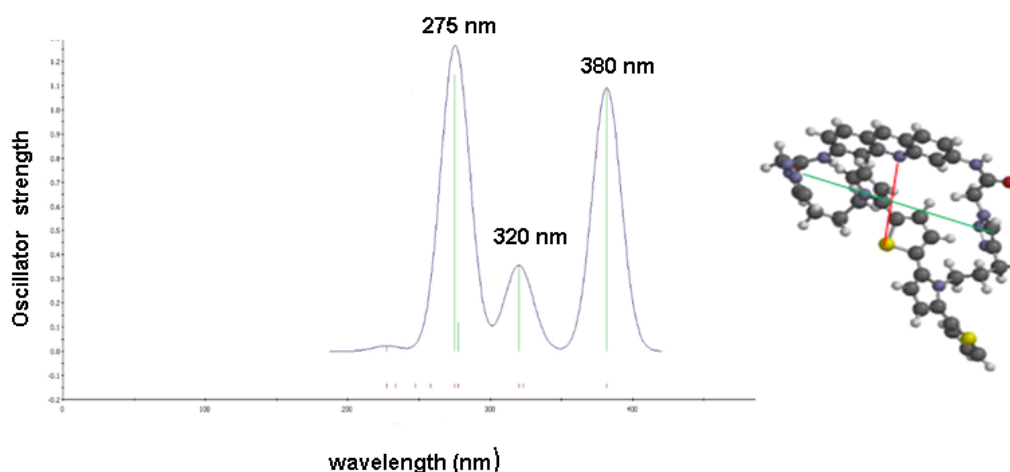
Figure 30 Left: Calculated UV/vis spectrum of ring closing from pyrrole-thiophene ends (molecular internal closing); right: molecular structure of ring after joining thiophene and pyrrole ends.

4.7.3 Thiophene-thiophene linked nano-ring [PT-TP]

The minimised structure of a nano-ring formed by closing two thiophene-thiophene ends of the click product, **PD + pent TP**, is shown in Figure 31. The calculated absorption spectrum shows three peaks at 275 nm, 320 nm and 360 nm. Therefore, there is one extra peak at 380 nm which was not seen before ring-closing, and is due to the formation of a four unit oligomer, where four of the heterocycles are involved in the macro-ring by intramolecular cyclisation. The formed macro-ring contains 37 bond.

The distance between the ring nitrogen of **PD** and the sulfur atom of the central thiophene ring (blue line) and the distance between the carbons of the two triazole rings (red line) are 11.39 Å and 8.36 Å respectively (shown in Figure 31). As expected the dimensions of the space inside the four unit nano-ring is larger than in the three unit case previously described.
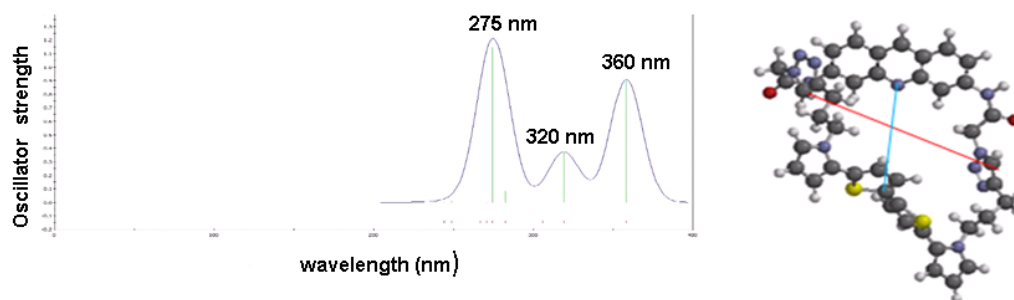
Figure 31 Left: calculated UV/vis spectrum of ring closing from thiophene -thiophene ends (molecular internal closing); right: molecular structure of ring after joining two thiophene ends.

126

4.7.4 Pyrrole-pyrrole linked nano-ring [TP-PT]

The minimised structure of a nano-ring formed by closing two pyrrole-pyrrole ends of the click product, **PD + pent TP**, is shown in Figure 32. The calculated absorption spectrum shows three peaks at 275 nm, 320 nm and 410 nm. Therefore, there is one extra peak at 380 nm which was not seen before ring-closing, and is due to the formation of a four unit oligomer, where two of the heterocycles are involved in the formation of the nano-ring. The formed macro-ring contains 29 bond.

The distance between the ring nitrogen of **PD** and the sulfur atom of the central thiophene ring (red line) and the distance between the carbons of the two triazole rings (red line) are 9.29 Å and 8.04 Å respectively (shown in Figure 32).
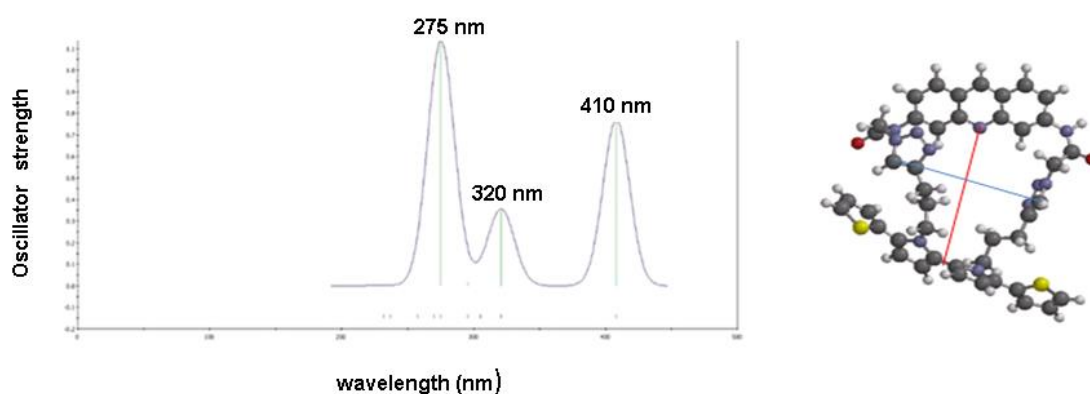
Figure 32 Left: UV/vis spectrum calculated by Material Studio Programme for **PD + pent-TP** after oxidation with FeCl$_3$, ring closing from pyrrole-pyrrole ends (molecular internal closing); right: molecular structure of ring after joining two pyrrole ends.

The calculated UV/vis spectrum of each possible nanoring showed peaks at 275 nm, 320 nm and a third peak at 360, 380 or 410 nm depending on the size of the nano-ring formed. The calculated UV/vis spectra are similar to the experimental data for the **[DNA ⊃ PD] + pent-TP** product which had peaks at 275, 387, 420 and 485 nm, see Figure 27. All three possible structures indicated the appearance of a new peak at longer wavelengths which is due to the increasing π-conjugation within the system after polymerisation. However, the recorded UV spectrum after polymerisation of **[DNA ⊃ PD] + pent-TP** showed the appearance of two peaks at 420 nm and 485 nm which could be assumed to be due to the formation of two of the possible macro-ring structures, see Table 2.

In addition, the calculated heat of formation of the three possible macrocycles is shown in Table 2, 350.8, 359.1 and 434 kcal/mole for **[TP-TP], [TP-PT]** and **[PT-TP]** respectively. Assuming that the structures with the lowest heat of formation are the

most likely to form and considering calculated λ_{maxes} in table 2 (380 nm, 410 nm) more or less matched with 420 nm and 485 nm resulted from experimental data, the expected products of the intra-molecular cyclisation of the isolated **PD + pent-TP** could be **[TP-TP]** and **[TP-PT]** macro-rings.
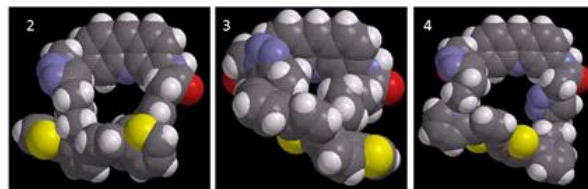
Ring closing way	T P P T	T P T P	T P T P
Distance between N of PD and TP bridge (A°)	9.3	9.3	11.4
Distance between two triazole rings (A°)	8.0	7.8	8.4
Heat formation (Kcal / mole)	359.1	350.8	434
λ (nm)	410	380	360

Table 2 possible arrangements of ring closing and data derived of material studio programme as mentioned in the text.

4.8 Conclusion

AFM studies showed that the 1-D nanostructures of [DNA ⊃ **PD or PDMe$^+$**] and [DNA ⊃ **PD or PDMe$^+$**] + **pent-TP** have comparable topologies to naked λ-DNA but have greater diameter dimensions. The ranges in height of λ-DNA, [DNA ⊃ **PD**], [DNA ⊃ **PDMe$^+$**], [DNA ⊃ **PD**] + **pent-TP** and [DNA ⊃ **PDMe$^+$**] + **pent-TP** were 0.5 − 2.1 nm, 2.8 − 22.2 nm, 2.9 − 5.4 nm, 4.1 − 18.8 nm and 8.6 − 16.58 nm respectively. The minimum observed heights of the intercalated and clicked complexes accord with the expectation that intercalation of **PD** or **PDMe$^+$** and click coupling with **pent-TP** increases the DNA bulk. However, there is clearly more than a single helix in many of the observed nanostructures, which explains the increased diameters beyond the simple association of the intercalator into the helix. Therefore the intercalation of **PD** or **PDMe$^+$** in DNA appears to aid the bundling of two or more helices into larger diameter nanostructures, at least under the surface attachment conditions. The minimum height of AFM image results has been summarised in Table 3 that refer to the height changes of DNA nano structures after loading and after *in-situ* click reaction and it can be due to happening intercalation and click chemistry with bundling of more than two duplex of DNA.

AFM and SCM studies of [DNA ⊃ **PD**] + **pent-TP** and [DNA ⊃ **PDMe$^+$**] + **pent TP** suggest that this intercalative approach is a more controlled method over standard templating reactions for the production of DNA based conductive polymer nanowires.

Compounds	Observed minimum heights of DNA hybrids by AFM (nm)
DNA	0.5
[DNA ⊃ PD]	2.8
[DNA ⊃ PDMe$^+$]	2.9
[DNA ⊃ PD] + EFc	4.8
[DNA ⊃ PD] + pent-TP	4.1
[DNA ⊃ PDMe$^+$] + pent-TP	8.6
[DNA ⊃ PDMe$^+$] + APCR	5.2

Table 3: Summary table of observed minimum heights by AFM of λ-**DNA**, **[DNA ⊃ PD], [DNA ⊃ PDMe$^+$], [DNA ⊃ PD] +EFc, [DNA ⊃ PD] + Pent-TP, [DNA ⊃ PDMe$^+$] + Pent-TP** and **[DNA ⊃ PDMe$^+$] + APCR,**

In addition, further evidence that the intercalated **PD** and **PDMe$^+$** underwent the click reaction was obtained by fluorescence microscopy. The fluorescence micrographs of **[DNA ⊃ PD] + APCR** and **[DNA ⊃ PDMe$^+$] + APCR** showed structures approximately ∼17-19 μm in length, comparing well with the known length of λ-DNA. Therefore, the successful clicking of the fluorescent alkyne to **PD** and **PDMe$^+$** while still assembled along DNA was observed. Consequently, it can be concluded that **PD** and **PDMe$^+$** undergo click chemistry whilst remaining intercalated in the DNA helix. The compounds **PD** and **PDMe$^+$** are promising reagents for the assembly of functional units along DNA.

In the LD^r spectrum of [DNA ⊃ **PDMe$^+$**] + **pent-TP**, a magnitude of the negative signal below 350 nm suggests that the two **pent-TP** groups are not constrained and have sufficient flexibility to align for polymerisation. The pendant **pent-TP** groups are therefore in a favourable orientation along the DNA axis so that during polymerization they could connect to their nearest neighbour in order to produce two parallel strands of conductive polymer aligned by the DNA nanostructure.

UV/vis spectra of the products from the click reaction of **PD** + **pent-TP** and the *in-situ* equivalent **[DNA ⊃ PD] + pent-TP**, were similar with λ$_{max}$ of 385 nm and 387 nm respectively. In the similar comparison for **PDMe$^+$** + **pent-TP** and the *in-situ* click product of **[DNA ⊃ PDMe$^+$] + pent-TP** the spectra showed λ$_{max}$ of 430 nm and 424 nm respectively. Moreover, the IR spectrum of *in-situ* click reaction of

[DNA $\supset$ **PD or PDMe$^+$**] + **pent-TP**, implied the successful performance of the click modification due to the disappearance of the peaks associated with alkyne and azide groups. In addition, mass spectrometry confirmed successful click reaction from the isolated products, **PD** or **PDMe$^+$** + **pent-TP** after removal from DNA.

The UV/vis, IR, Mass spectroscopy and LD^r results presented here confirmed the successful click reaction of **pent-TP** with **PD** after reduced loading into DNA. In addition UV/vis spectra before and after polymerisation and molecular modelling data suggest that the **pent-TP** groups form intramolecular nano-rings. Therefore, the **PD** molecules incorporated into DNA are sufficiently far away from each other so that after the "click" reaction, the products will not interact with each other during polymerisation by FeCl$_3$. However it was envisaged that at high-loading of **PD** into DNA, the **pent–TP** "click" product could arrange into polymeric chains along the DNA.

PD and **PDMe** can act as reagents to assembly of nanomaterial into DNA and then "clicked" with an alkyne group to yield a stoichiometrically controlled nanoscale material bearing the properties of the chosen alkyne moiety.

4.9 Experimental

Material and Methods

Reagents were purchased from Sigma aldrich. Lambda DNA was purchased from New England Biolabs. **PD**, **PDMe$^+$ and** N-pentynyl-2-(2-thienyl)-pyrrole, **pent-TP ,**were synthesised as described in previous chapters. UV, IR and mass spectra were recorded on a Cary 100 Bio UV/visible spectrophotometer, a Bio-Rad FTS-7 FT-IR Spectrometer and a Waters Micromass LCT premier mass spectrometer, respectively. Fluorescence images were collected on an Zeiss Axioplan 2 microscope using Axiovision Viewer 3 software (Zeiss). CV analyses were carried out on the analytical workstation which was an electrochemical analyser/Workstation CH1760B, Model 700B Series by CH Instruments, Inc., USA with sensitivity of up to picoamperes.

Topographical AFM data was acquired using both a Multimode Nanoscope IIIa and Dimension Nanoscope V system (Veeco Instruments Inc., Metrology Group, Santa Barbara, CA, USA) in TappingMode operation. Etched Si AFM probes (TESP model, n-doped Si cantilevers, resonant frequency range, f_o = 230–280 kHz, spring constant, k = 20–80 Nm^{-1}, Veeco Instruments Inc., Metrology Group) were employed during Tapping Mode operation. Data acquisition was carried out using Nanoscope version

5.12b36 and version 7.00b19 software (Veeco Instruments Inc., Digital Instruments) on the Multimode Nanoscope IIIa and Nanoscope Dimension V AFM systems, respectively. For reducing vibration noise an isolation table/acoustic enclosure was used (Veeco Inc., Metrology Group).

Insitu-Click reaction of PD and pent-TP using Calf Thymus DNA, [DNA ⊃ PD] + pent-TP (high loading)

39.6 mg of Calf Thymus DNA was dissolved using 9.9 ml of 5 mM phosphate buffer (pH 7) and stirred for 2 hours and then 100 µL of 0.226 M **PD** in DMSO was added and stirred for 4days and then to perform click reaction, 5ml of (2.26 mM PD+ 9.02 mM DNA) solution was taken and to it, 4.88 mg of **pent-TP**, 1.61 mg of $CuSO_4$, 3.42 mg TBTA and 5.2 mg of Na-ascorbate dissolved in 1 ml of solution containing 19.8% tert-BuOH and 80.2% 5 mM phosphate buffer (pH 7), was added and then this solution was stirred for one week.

Chemical Polymerization of in-situ click reaction of PD and pent-TP using Calf Thymus DNA, [DNA ⊃ PD] + pent-TP (high loading)

452 µL of $FeCl_3$ (0.1 M) as oxidant reagent was added to a 6 mL of solution resulted after click reaction as detailed in above section.

The preparation of in-situ click PDMe[+] and pent-TP sample for LD experiments

552 µL of CT-DNA (10.86 mM) was diluted to a 4 ml solution by 5 mM phosphate buffer (pH 7) then 60 µL of **PDMe[+]** (2 mM) was added and stirred for 48 h to give **[DNA ⊃ PDMe[+]]**. 1 mL of an aqueous solution of nanopure water/t-BuOH (40:60) containing 240 µM **pent-TP** and 68.4 µM TBTA and 1 mL of solution containing 68.4 µM $CuSO_4$, 276 µM Sodium Ascorbate was added and stirred for 48 hours at room temperature.

Intercalation of PD into DNA: [DNA ⊃ PD]

5 μL of solution **PD** (0.6 mM) was added to 10 μL of λ-DNA (500 μg/mL) and diluted by 10 mL deionised water and stirred for 48 h to give **[DNA ⊃ PD].**

Click reaction PD with ethynylferrocene, [DNA ⊃ PD] + EFc

5 μL of an aqueous solution of nanopure water/t-BuOH (1:1) containing 1.2 mM ethynylferrocene, **EFc**, 0.34 mM $CuSO_4$, 1.38 mM Na-ascorbate and 0.34 mM TBTA (tris[(1-benzyl-1H-1,2,3-triazol-4-yl)methyl]amine) was added to the previously prepared 15 μL solution of **[DNA ⊃ PD]** and the solution made up to a total volume of 25 μL with nanopure water and stirred for 16 hours at room temperature.

Click reaction of PD with pent TP, [DNA ⊃ PD] + pent-TP

5 μL of an aqueous solution of nanopure water/t-BuOH (1:1) containing 1.2mM **pent-TP**, 0.34 mM $CuSO_4$, 1.38 mM Na-ascorbate and 0.34 mM TBTA was added to the previously prepared 15 μL solution of **[DNA ⊃ PD]** and the solution made up to a total volume of 25 μL with nanopure water and stirred for 16 hours at room temperature.

Intercalation of PDMe$^+$ into DNA: [DNA ⊃ PDMe$^+$]

5 μL of solution **PDMe$^+$** (0.366 mM) was added to 10 μL of λ-DNA (500 μg/mL) and the volume made up to 27 μL with nanopure water before stirring for 48 h to give **[DNA ⊃ PDMe$^+$].**

Click reaction of PD with APCR, [DNA ⊃ PD] + APCR

10 μL of 0.374 mM of **APCR** and 2 μL of an aqueous solution of nanopure water/t-BuOH (1:1) containing, 0.53 mM $CuSO_4$, 2.1 mM Na-ascorbate and 0.53 mM TBTA were added to a previously prepared solution of **[DNA ⊃ PD]** (5 μL of solution **PD** (0.366 mM) added to 10 μL of λ-DNA (500 μg/mL)) and stirred for 48 hours.

Click reaction of PDMe$^+$ with APCR, [DNA ⊃ PDMe$^+$] + APCR

10 μL of 0.374 mM of **APCR** and 2 μL of an aqueous solution of nanopure water/t BuOH (1:1) containing, 0.53 mM $CuSO_4$, 2.1 mM Na-ascorbate and 0.53 mM TBTA were added to a previously prepared solution of **[DNA ⊃ PDMe$^+$]** (5 μL of solution **PDMe$^+$** (0.366 mM) added to 10 μL of (500 μg/mL)) and stirred for 48 hours.

FTIR study of click reactions

A silicon wafer (n-100) was diced into chips approximately 1 cm^2 which were sequentially cleaned using cotton buds soaked in acetone, propanol and finally water.

The chips were then dried using a nitrogen stream and then placed in an oven for half an hour. These clean and dry substrates were used to deposit reaction samples for analysis by FTIR.

Cyclic Voltammetry

Preparation of solutions for elctrochemical analysis:

i) Lithium perchlorate solution (0.1 M):

Lithium perchlorate (217.76 mg) was dissolved in 20 mL of dry acetonitrile to obtain a solution of 0.1 M.

ii) Ethynylferrocene, EFc

1 mM aqueous solutions of **EFc** was diluted with 10 mL solution of 0.1 M lithium perchlorate (prepared in acetonitrile as above) to prepare 2.4 μM solution of **EFc.**

iii) PD and PDMe$^+$ solutions, 600 μL of 10 mM DMSO solutions of **PD** and **PDMe$^+$** were diluted into a 10 mL solution of 0.1 M lithium perchlorate (prepared in acetonitrile as above) to prepare 0.6 mM **PD** or **PDMe$^+$**. Dry nitrogen was bubbled through the solution for at least 30 min to deoxygenate the solution.

iv) [DNA ⊃ PD] + EFc

5 μL of an aqueous solution of nanopure water/t-BuOH (1:1) containing 1.2 mM ethynylferrocene, **EFc**, 0.34 mM CuSO$_4$, 1.38 mM Na-ascorbate and 0.34 mM TBTA (tris[(1-benzyl-1H-1,2,3-triazol-4-yl)methyl]amine) was added to the previously prepared 15 μL solution of **[DNA ⊃ PD]** and the solution made up to a total volume of 25 μL with nanopure water and stirred for 16 hours at room temperature.

This solution was diluted to a 2.5 mL volume with 0.1 M lithium perchlorate (prepared in acetonitrile as above).

Cyclic voltammetry experiments of PD, EFc, (PD + EFc) and [DNA ⊃ PD] + EFc.

Gold, tungsten and silver wires were used as working, counter and reference electrodes respectively. Cyclic voltammograms were then recorded using the following parameters: Initial potential -0.2 V, high potential 2 V, low potential -0.2 V, scan rate 0.1 V / sec.

AFM Studies

Preparation silicon chips for AFM

A piece of Silicon wafer of n-100 was diced into chips approximately 1 cm^2 and were sequentially cleaned using a cotton bud socked in aceton, propanol and finally water and dried using a nitrogen stream and then the chips were placed in 'piranha solution' (4:1, H_2SO_4:H_2O_2 for 50-60 minutes, washed with nanopure water and dried using a nitrogen stream and dried in an oven for 15 minutes. The surface of chips exposed to TMS for 10 minutes to provide a hydrophobic surface for AFM measurments [12]

Deposition and imaging of DNA:

10 µL of λ-DNA (500 µg/mL) was diluted with nanopure water to a volume of 25 µL to provide a 200 µg/mL concentration of λ-DNA. A silicon chip prepared as above was used as a surface to deposit a 5 µL drop of the λ-DNA solution. The chip was left to dry in a vacuum hood for 3 hours. Range of observed height of λ-DNA was 0.5 - 2.0 nm.

Deposition and imaging of [DNA ⊃ PD]

A 5 µL drop of **[DNA ⊃ PD]** solution. was deposited onto a prepared silicon wafer and left to dry in a vacuum hood for 2 hours before imaging by AFM. Range of observed height was 2.8 - 3.7 nm.

Fluorescence images

Fluorescence images were obtained by excitation using light from a Hg lamp source passed through a 455-495 nm band-pass filter with a maximum transmission at 475 nm. The emitted light was separated from scattered light using a long pass filter with a cut-off at 505-555 nm.

Deposition of [DNA ⊃ PD] and imaging by fluorescence microscope

A 5 µL drop of **[DNA ⊃ PD]** solution. was deposited onto a prepared silicon wafer surface as cleaned for AFM study and left to dry in a vacuum hood for 2 hours before imaging by fluorescence microscope.

Deposition of [DNA ⊃ PDMe$^+$] and imaging by fluorescence microscope

A 5 µL drop of **[DNA ⊃ PDMe$^+$]** solution. was deposited onto a prepared silicon wafer surface as cleaned for AFM study and left to dry in a vacuum hood for 2 hours before imaging by fluorescence microscope.

Deposition of in-situ click reaction of PD with APCR, [DNA ⊃ PD] + APCR and imaging by fluorescence microscope

A 5 µL drop of **[DNA ⊃ PD] + APCR** solution. was deposited onto a prepared silicon wafer surface as cleaned for AFM study and left to dry in a vacuum hood for 2 hours before imaging by fluorescence microscope.

Deposition of in-situ click reaction of PDMe$^+$ with APCR, [DNA ⊃ PDMe$^+$] + APCR and imaging by fluorescence microscope

A 5 µL drop of **[DNA ⊃ PDMe$^+$] + APCR** solution. was deposited onto a prepared silicon wafer surface as cleaned for AFM study and left to dry in a vacuum hood for 2 hours before imaging by fluorescence microscope.

Preparation of silicon chips for SCM studies

Silicon wafers with a 200 nm thick silicon oxide layer (Si<n-100>, 3 inch diameter, 525±50 µm thickness, arsenic doped, <0.0005 Ω cm resistance, thermal oxide layer 2000 ±10% Å thickness, double side polished) were diced into approximately 1 cm^2 pieces. The oxide layer was removed from one side of the wafer using a cotton bud soaked in HF, followed by washing with nanopure water and dried using a nitrogen stream. Removal of the oxide layer was evident by a change in the surface wetting of the etched surface (i.e. hydrophilic to hydrophobic). The surface of the wafer with the oxide layer still present was sequentially cleaned using a cotton bud socked in acetone, propanol and finally water, and then dried under a stream of nitrogen gas. The wafers were placed in 'piranha solution' (4:1, H$_2$SO$_4$:H$_2$O$_2$) (Caution! Piranha solution should be handled with extreme care. It is a strong oxidant and will react violently with many organic materials. It also presents an explosion danger) for 50-60 minutes. Upon removal from the piranha solution, the wafers were washed with nanopure water, dried under a stream of nitrogen gas, followed by further drying in an oven for 15 minutes. The surface of wafers were exposed to the vapour of chlorotrimethylsilane for a period of 10 minutes at ambient temperature and pressure to geneate a hydrophobic surface for subsequent alignment of the DNA-based structures.

SCM data was acquired using conductive, metalized AFM probes (MESP model, metallic Co/Cr coated n-doped Si cantilevers, resonant frequency range, f$_o$ = 60–100 kHz, spring constant, k = 1-5 Nm^{-1}, Veeco Instruments Inc., Metrology Group). Data was collected via a "two-pass" method in which topographical data is collected in

standard Tapping Mode operation during the first pass of the tip of a scan line, and SCM phase data is collected during the second pass of the tip over the same scan line, with the tip maintained at a constant lift height (70 nm in this instance) above the sample surface. A scan rate of 0.5 Hz was typically used. During data acquisition the AFM tip was grounded and an independently controlled dc bias was applied to the sample. Data acquisition was carried out using Nanoscope Version 7.00b19 software (Veeco Inc., Metrology Group). Vibrational noise was again reduced using an isolation table / acoustic enclosure (Veeco Inc., Metrology Group).

Insitu-Click reaction of PD and pent-TP using Calf Thymus DNA, [DNA ⊃ PD] + pent-TP (low loading)

39.6 mg of Calf Thymus DNA was dissolved using 9.9 ml of 5 mM phosphate buffer (PH 7) and stirred for 2 hours and then 100 μL of a solution of 12.8 mM **PD** in DMSO was added and stirred for 3 hours and then UV spectrum of **[DNA ⊃ PD]** solution was taken.

The solution of **[DNA ⊃ PD]** was stirred for 2 weeks and then to perform click chemistry, 2ml of **[DNA ⊃ PD]** solution was taken and to it, 0.11 mg of **pent-TP**, 0.036 mg of $CuSO_4$, 0.077 mg TBTA and 0.116 mg of Na-ascorbate dissolved in 1 ml of solution containing 10% tert-BuOH, 90% 5 mM phosphate buffer (pH 7), was added and then this solution was stirred for one week.

Oxidation of in-situ click reaction of PD and pent-TP using Calf Thymus DNA, [DNA ⊃ PD] + pent-TP (low loading)

20 μL of $FeCl_3$ (17 mM) as oxidant reagent was added to 0.5 mL of solution of click reaction (85.33 μM) and stirred for overnight.

Oxidation of synthetic click product (PD + pent-TP)

The total volume of solvent was 10 mL. The solvent was 90% DMF and 10% aqueous solution. 1.1 mg of click product, **PD** + **pent-TP**, was dissolved by 9 mL of DMF and after 1 mL of 5.1 mM $FeCl_3$ was added for polymerisation, total concentration of polymerized solution was 128 uM of click produt (**PD + pent-TP**).

The sample preparation of in-situ click PD with pent-TP sample for LD experiments

552 μL of CT-DNA (10.86 mM) was diluted to 4 ml solution by 5 mM phosphate buffer (pH 7) then 60 μL of solution **PD** (2 mM) was added stirred for 48 h to give

136

[DNA ⊃ PD]. 1 mL of an aqueous solution of nanopure water/t-BuOH (40:60) containing 240 μM **pent-TP** and 68.4 μM TBTA and 1 mL of solution containing 68.4 μM CuSO$_4$, 276 μM Na-ascorbate was added and stirred for 48 hours at room temperature.

Isolation of click product from DNA for mass spectroscopy:

0.5 mL of click reaction solution in the presence of DNA was placed in a 1 mL eppendorf tube and heated on water bath at 95°C for 10 minutes to denaturate DNA then 0.5 mL DCM added for extracting organic layer and aqueous layer containing yellow liquid and white precipitate. Organic layer and yellow liquid of aqueous layer were placed in vacuum centrifuge to evaporate solvent for 10 minutes. 1 mL of methanol was added to the the rest of centrifuge to prepare MS samples.

References

1. N. C. Seeman, *Nature*, 2003, **421**, 427-431.
2. N. C. Seeman, *Annual review of biochemistry*, **79**, 65-87.
3. U. Feldkamp and C. M. Niemeyer, *Angewandte Chemie International Edition*, 2006, **45**, 1856-1876.
4. H. A. Becerril and A. T. Woolley, *Chemical Society Reviews*, 2009, **38**, 329-337.
5. G. Qun, C. Chuanding, G. Ravikanth, S. Shivashankar, A. Sathish, D. Kun and T. H. Donald, *Nanotechnology*, 2006, **17**, R14.
6. H. Ihmels and D. Otto, Editon edn., 2005, vol. 258, pp. 161-204.
7. M. J. G. G Michael Blackburn, David Loakes and David M Williams, *Nucleic Acids in Chemistry and Biology*, 2006.
8. S. Pruneanu, S. A. F. Al-Said, L. Dong, T. A. Hollis, M. A. Galindo, N. G. Wright, A. Houlton and B. R. Horrocks, *Advanced Functional Materials*, 2008, **18**, 2444-2454.
9. D. Schweinfurth, R. Pattacini, S. Strobel and B. Sarkar, *Dalton Transactions*, 2009, 9291-9297.
10. A. R. Pike, L. C. Ryder, B. R. Horrocks, W. Clegg, B. A. Connolly and A. Houlton, *Chemistry – A European Journal*, 2005, **11**, 344-353.
11. C. A. M. Seidel, A. Schulz and M. H. M. Sauer, *The Journal of Physical Chemistry*, 1996, **100**, 5541-5553.
12. M. Bockrath, N. Markovic, A. Shepard, M. Tinkham, L. Gurevich, L. P. Kouwenhoven, M. W. Wu and L. L. Sohn, *Nano Letters*, 2002, **2**, 187-190.
13. S. A. Farha Al-Said, R. Hassanien, J. Hannant, M. A. Galindo, S. Pruneanu, A. R. Pike, A. Houlton and B. R. Horrocks, *Electrochemistry Communications*, 2009, **11**, 550-553.
14. J. Hannant, J. H. Hedley, J. Pate, A. Walli, S. A. Farha Al-Said, M. A. Galindo, B. A. Connolly, B. R. Horrocks, A. Houlton and A. R. Pike, *Chemical Communications*, 2010, **46**, 5870-5872.
15. Z. Deng and C. Mao, *Nano Letters*, 2003, **3**, 1545-1548.
16. L. Dong, T. Hollis, S. Fishwick, B. A. Connolly, N. G. Wright, B. R. Horrocks and A. Houlton, *Chemistry – A European Journal*, 2007, **13**, 822-828.
17. J. Li, C. Bai, C. Wang, C. Zhu, Z. Lin, Q. Li and E. Cao, *Nucleic Acids Research*, 1998, **26**, 4785-4786.
18. T. Thundat, D. P. Allison and R. J. Warmack, *Nucleic Acids Research*, 1994, **22**, 4224-4228.
19. M. Yan and G. H. Bernstein, *Surface and Interface Analysis*, 2007, **39**, 354-358.
20. B. D. Terris, J. E. Stern, D. Rugar and H. J. Mamin, *Physical Review Letters*, 1989, **63**, 2669-2672.
21. T. S. Jespersen and J. Nygård, *Nano Letters*, 2005, **5**, 1838-1841.
22. C. Staii, A. T. Johnson and N. J. Pinto, *Nano Letters*, 2004, **4**, 859-862.
23. B. S. Lamb and P. Kovacic, *Journal of Polymer Science*, 1980, **18**, 1759-1770.
24. S. Suzuki, T. Yamanashi, S. Tazawa, O. Kurosawa and M. Washizu, *Industry Applications, IEEE Transactions on*, 1998, **34**, 75-83.
25. L. Dong, T. Hollis, B. A. Connolly, N. G. Wright, B. R. Horrocks and A. Houlton, *Advanced Materials*, 2007, **19**, 1748-1751.
26. Y. Zhou, M. Freitag, J. Hone, C. Staii, J. A. T. Johnson, N. J. Pinto and A. G. MacDiarmid, *Applied Physics Letters*, 2003, **83**, 3800-3802.
27. H. Suzuki and Y. Tanaka, *The Journal of Organic Chemistry*, 2001, **66**, 2227-2231.
28. A. V. Pinheiro, D. Han, W. M. Shih and H. Yan, *Nat Nano*, 2011, **6**, 763-772.

29.	G. Zhang, S. P. Surwade, F. Zhou and H. Liu, *Chemical Society Reviews*, 2013.

Chapter 5- *Conclusion and future work*

Chapter 5- Conclusion and future work

Two diazido acridine drivatives, N,N'-(acridine-3,6-diyl)bis(2-azidoacetamide), **PD** and 3,6-bis(2-azidoacetamido)-10-methylacridin-10-ium, **PDMe$^+$**, were successfully synthesised from 3,6-diamino acridine, **Pf.** These azido intercalators were designed to bind to DNA and present the two azido groups for later functionalization by the 1,3 dipolar cycloaddition click reaction with an alkyne bearing moiety.

The interaction of **PD** and **PDMe$^+$** with DNA was investigated by UV, fluorescence, CD and LD spectroscopy, thermal denaturation and viscometry experiments. **PD** and **PDMe$^+$** were found to intercalate at high P/D values as evidenced by linear dichroism studies and viscosity experiments. **PDMe$^+$** showed similar DNA binding properties as **Pf**, giving hypochromic and bathochromic shifts in UV titration experiments. However, **PD** is poorly soluble in water because of its low pKa of 4.3 for protonation. However, it becomes protonated on binding to DNA, resulting in an apparent **pK$_a$** of ≥ 7 producing unusual hyperchromic binding data in UV studies. The observed DNA binding constants of **PD** (5.3×10^5) and **PDMe$^+$** (2×10^6) were less than for **Pf** (3.8×10^6), but sufficient that they remain intercalated into the DNA framework at micromolar concentrations this places the azido groups in the major groove, available for further modification via an *in-situ* click reaction.

PD and **PDMe$^+$** were functionalised by click chemistry with different alkyne-bearing groups; phenylacetylene, ethynyl ferrocene **EFc**, N-pentynyl-2-(2-thienyl)-pyrrole **pent-TP** and acetylene-PEG4-carboxyrhodamine, **APCR**. The click reaction products were characterised by ^{1}H NMR spectroscopy, ^{13}C NMR spectroscopy, ES-MS, IR and where appropriate cyclic voltammetry. IR studies showed the disappearance of the azide and alkynyl stretching signals at 2114 cm^{-1} and 2112 cm^{-1} respectively after the click reaction of **PD** with **pent-TP**. Cyclic voltammetry revealed that the click product with **EFc** was redox active, E = 346 mV compared to 441 mV for **EFc**, a negative shift due to the electron donating effect of the triazole ring.

The electrochemical polymerisation of **PDMe$^+$** + **pent-TP** indicated that the click product forms a polymer film at the working electrode. This is an interesting material for the possible binding of DNA to the electrode surface through intercalation and may have applications in the detection of DNA.

After the ability of **PD** and **PDMe$^+$** to undergo click chemistry was established, these findings opened up studies into the functionalization of the intercalated complexes [DNA ⊃ **PD**] and [DNA ⊃ **PDMe$^+$**] to give decorated DNA via a two-step approach, intercalation followed by click coupling. Therefore, the *in-situ* modification of DNA ⊃ **PD**] and [DNA ⊃ **PDMe$^+$**] with the same range of alkyne-bearing groups via click chemistry to produce highly controlled nanoscale materials was performed.

The click functionalization of the complexes [DNA ⊃ **PD**] and [DNA ⊃ **PDMe$^+$**] with the conductive polymer unit **pent-TP**, was successfully performed and the resulting DNA hybrid nanomaterial characterised by UV, IR, , LD spectroscopy, atomic force microscopy (AFM) and scanned conductance microscopy (SCM) and fluorescence microscopy.

LD studies showed that DNA-bound **PD** and **PDMe$^+$** undergoes *in-situ* click functionalization with **pent-TP**, and remains intercalated after reaction thus placing the monomers in the major groove ready for polymerization to form a conducting chain. Negative LD and LD^r values in the visible region for the *in-situ* click products [DNA ⊃ **PD**] + **pent-TP** and [DNA ⊃ **PDMe$^+$**] + **pent-TP** were strong evidence for stable intercalation after modification.

The AFM studies indicated that the DNA helix loaded with the intercalators, **PD** and **PDMe$^+$**, can be used to assemble a range of functional nanomaterials. The "click" modified nanostructures of **EFc**, **pent-TP** and **APCR** showed 1-D features which were similar to naked DNA in topology but a little larger in diameter. Comparison of the height changes were monitored by AFM. The intercalated complexes remained stable during deposition from solution and interrogation by the AFM tip, with little observed change in the linear wire-like structures. The minimum observed heights of the intercalated and clicked complexes agreed with the expectation that intercalation of **PD** or **PDMe$^+$** and click coupling with **pent-TP** increases the DNA diameter. However, the size of the observed nanostructures was often more than the expected dimensions of a single helix. Therefore, the intercalation of **PD** or **PDMe$^+$** in DNA appears to aid the bundling of two or more helices into larger diameter nanostructures, at least under the surface attachment conditions.

The SCM images of **[DNA ⊃ PD] + pent-TP** and **[DNA ⊃ PDMe⁺] + pent-TP** showed negative phase shifts as the AFM tip crossed the complex, being typical of a conductive structure and supporting the formation of conductive nanowires in both cases.

The click reaction of [DNA ⊃ **PD**] and [DNA ⊃ **PDMe⁺**] with a green fluorescent dye (acetylene-PEG4-carboxyrhodamine), **APCR,** was monitored through fluorescence microscopy to ascertain that the intercalators, **PD** and **PDMe⁺** remain assembled in the helical stack of λ-DNA during decoration. After the click reaction, **APCR** illuminates the 1-D nanostructures, and confirms that the intercalator remains bound to the DNA even after modification.

Future work

Assembly of complex nanostructures, for example DNA origami, has been a growing area of research. However the design of functional nanostructures has been more limited. It is hoped that by using the diazido intercalators developed here, **PD** and **PDMe⁺**, and their now established click chemistry, that the goal of novel DNA-based hybrid materials may be realised. In the case of DNA origami, a suitable structure with pre-programmed shape will be designed and folded. Then in two steps, intercalation with an off-the-shelf azido-intercalator, **PD** or **PDMe⁺** followed by click decoration with the targeted alkyne-bearing group, designer functional nanomaterials of the desired shape will be fabricated.

Appendix

Synthesis and binding of proflavine diazides as functional intercalators for directed assembly on DNA†

Shahrbanou MoradpourHafshejani,[a] Joseph H. Hedley,[ab] Alexandra O. Haigh,[ac] Andrew R. Pike*[a] and Eimer M. Tuite*[a]

Proflavine diazide (PD) with amido-azide substituents on the amine groups and its *N*-methylated analogue (MePD) bind strongly to DNA by nearest-neighbour intercalation with little sequence selectivity, presenting reactive azide groups in the major groove. PD is neutral in aqueous solution but experiences binding-coupled protonation on interaction with DNA with an apparent pK_a shift of 2.5 units. MePD can be click modified *in situ* on DNA with alkyne-functionalised thienyl-pyrrole as a precursor for conducting polymer synthesis, and remains intercalated after reaction with the substituents aligned in the groove.

Introduction

The use of DNA as an architectural material was revolutionized by the seminal work of Seeman and coworkers in constructing 2D and 3D DNA nanostructures,[1] which resulted in an explosion of research in this field. The exquisite specificity of nucleic acid recognition, together with chemical stability, has made DNA the polymer of choice for the construction of increasingly intricate nano-architectures.[2] The DNA duplex is an attractive candidate as a 1D template or scaffold for assembly of functional materials *via* chemical reactions, coordination chemistry, or non-covalent association.[3]

Assembly of conducting polymers, *e.g.* polyaniline,[4] polypyrrole and polythienylpyrrole[5,6] on DNA has been a key area of interest for development of molecular wires. Control of polymerization can be achieved by tethering monomers to DNA on the bases, sugars, or modified backbones.[7] Herein, we present first generation molecules for an alternative strategy which uses unmodified DNA as a scaffold to facilitate the linear assembly of functional materials. This strategy uses small molecules (ligands) that bind strongly to DNA with specific recognition modes (*e.g.* intercalation or groove binding)[8] to present reactive substituents in one DNA groove. Hence, the duplex becomes an adaptable scaffold without the requirement for chemical modification of DNA. Proflavine is the framework we have chosen initially for development of functional intercalators.[9] The strong and well-characterized intercalative binding of acridines has led to their development as anticancer drugs,[10] and these properties also make them attractive candidates for anchoring supramolecular architectures to a DNA scaffold.

Previously, 9-aminoacridine has been used as an intercalative ligand to assemble a copper catalyst on DNA for asymmetric synthesis,[11] and proflavine has been modified with platinum complexes for improved therapeutics.[12] Searcey and coworkers produced a library of substituted acridine intercalators using click chemistry in solution,[13] one of which drove formation of Holliday junctions.[13b] 9-Aminoacridine azide was used for *in situ* click with an alkene peptide, where the reactants were pre-assembled.[14a] More recently, Balasubramanian and coworkers have used *in situ* click substitution of well-known tetraplex binders to identify drugs that bind selectively to G4 motifs.[14b] Also, minor groove binding azido-ligands have been used for assembly of functional molecules on AT-rich DNA.[14c] In this paper we report the synthesis of novel proflavine derivatives with amido-azide substituents that intercalate DNA and undergo *in situ* click reactions[15] with molecules such as alkyne-substituted thienylpyrrole (TP). In this paper, we fully characterize their binding to DNA and *in situ* click reaction, and in related work[5f] we have shown that conducting poly(TP)$_n$ nanowires can be formed from the resultant assembly.

[a]Chemical Nanoscience Laboratory, School of Chemistry, Bedson Building, Newcastle University, Newcastle upon Tyne, NE1 7RU, UK. E-mail: andrew.pike@ncl.ac.uk; eimer.tuite@ncl.ac.uk
[b]QuantuMDx, International Centre for Life, Times Square, Newcastle upon Tyne, NE1 4EP, UK
[c]Churchill Community College, Sixth Form, Churchill Street, Wallsend, NE28 7TN, UK
† Electronic supplementary information (ESI) available: Detailed experimental methods, spectra, calculations, physical data. See DOI: 10.1039/c3ra43090a

Results

Synthesis and absorbance of diazido-proflavines

Modification of proflavine (**1**, Pf)‡ with azide groups produces a ligand that presents "click" functionalities along DNA after intercalation. Initially, the exocyclic amines were converted to azides but that product was relatively unreactive. Thus, an
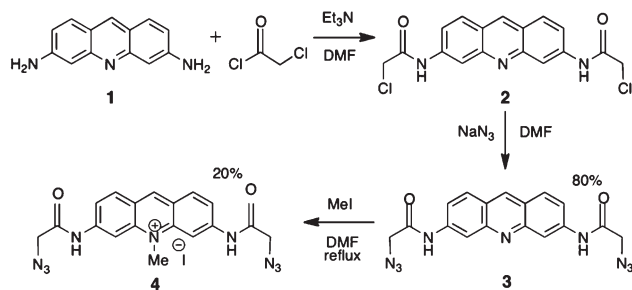
Scheme 1 Synthesis of azide-modified proflavines.

Table 1 Maximum wavelengths and extinction coefficients for absorption of the acridine dyes in the visible, and comparison with calculated energies for the HOMO–LUMO gap[a]

Species	pH	λ_{max}/nm	ε_{max}/M^{-1} cm^{-1}	ΔE/eV
Pf	12	393	19 000	3.51
PfH$^+$	7	445	41 000	3.29
PD	7	381	5800	3.62
PDH$^+$	3	403	13 200	3.27
MePD$^+$	7	409	9200	3.35

[a] λ_{max} and ε_{max}, measured; ΔE, calculated.

extended amide linker was introduced to increase accessibility of the azides, and overcome the reduced reactivity of Pf exocyclic amines after intercalation with DNA[16] (Scheme 1).

Product **3** (proflavine diazide, PD) was obtained in good yield but proved poorly soluble in water, although it dissolved in polar solvents and in DNA solution. Consequently, methylated proflavine diazide (**4**, MePD) was synthesized, in which the ring nitrogen is quaternized to give a cationic species at pH 7. For direct comparison of **1**, **3** and **4**, all experiments were carried out in aqueous buffered solution containing 1% DMSO by volume. This allowed dissolution of PD to tens of millimolar and did not perturb the DNA conformation as judged by circular dichroism.

Aqueous solutions of Pf, PD, and MePD are yellow-orange due to absorbance in the 300–500 nm region (Fig. 1). The modified acridines absorb at higher energy with smaller extinction coefficients than Pf, as previously reported for spin-labelled Pf.[17] All compounds also have significant absorbance in the 260 nm DNA region. Protonation on the ring nitrogen of Pf and PD is calculated to lower the energy of the absorption (supplementary information†), consistent with observed shifts to longer wavelength of the absorption maxima at low pH (Table 1).

pK_as for Pf in aqueous solution are reported at 0.3 and 9.5,[18] and our data (supplementary information†) concur. At pH 7 the dominant monocation has an S$_0$ → S$_1$ absorption maximum at 445 nm with an extinction coefficient of 41 000 M^{-1} cm^{-1}.[19] At high pH, deprotonation of the ring nitrogen produces the neutral form absorbing at higher energy (λ_{max} = 393 nm) with a smaller extinction efficient. The spectra of the di- and tri-cationic forms (pH < 0), for further protonation on the exocyclic nitrogens, are reported to have maxima at 350–360 nm and extinction coefficients comparable to the neutral species.[18,20] MePD is also monocationic at pH 7 with a pK_a of 9.6 for deprotonation. The poor aqueous solubility of PD is consistent with a dominant neutral form at pH 7, which renders the compound very hydrophobic. As pH drops from 9 to 1, the PD spectrum changes substantially with an isosbestic point at 365 nm (Fig. 2a). A pK_a is observed at pH ~4.4, and is assigned to protonation of the ring nitrogen.

Partial charges calculated for the neutral and monocation forms of PD, Pf, and MePD (supplementary information†) explain the change of pK_a when Pf carries amido-azide substituents. For neutral Pf, the ring nitrogen carries a high negative partial charge with partial positive charges on the exocyclic amines, and the charge density changes significantly after protonation of the ring nitrogen. For neutral PD, the negative charge on the ring nitrogen is much smaller due to significant negative charge density on the amide linker and azide nitrogens. After protonation of the ring nitrogen, the

Fig. 1 Absorption spectra of the proflavine dyes in aqueous solution.

‡ Abbreviations: CD, circular dichroism; CT-DNA, calf thymus DNA; PD, proflavine diazide; Pf, proflavine; LD, linear dichroism; LD^r, reduced linear dichroism; MePD, methylated proflavine diazide; P/D, nucleotide phosphate/dye ratio; [poly(dA–dT)]$_2$, poly(deoxyadenylic-thymidylic) acid; [poly(dG–dC)]$_2$, poly(deoxyguanylic-cytidylic) acid; TM, transition moment.

Fig. 2 Effect of pH on the absorption spectrum of PD. (a) spectra and calculated partial charges, and (b, inset) titration, [PD] = 54 µM.
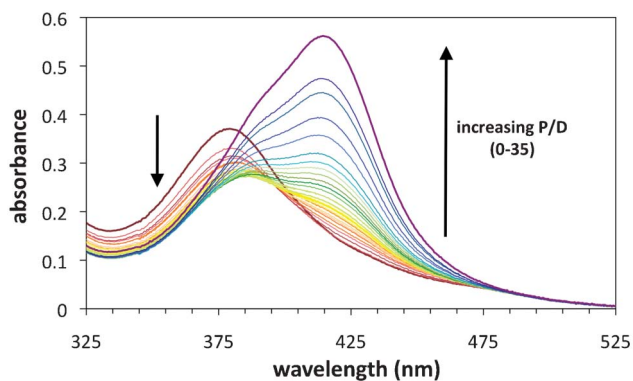
Fig. 3 Effect of binding to calf thymus(CT)-DNA on the absorption spectrum of PD. The spectrum without DNA is shown in dark red. P/D is the DNA (nucleotide phosphate) to dye ratio. [PD] = 56 μM.

negative charges remain localized on the amido-azide substituents. Cationic MePD has a similar partial charge distribution to PD monocation.

Interaction of diazido-proflavines with DNA

Absorption spectroscopy. The binding of Pf, MePD and PD to calf thymus (CT) DNA is readily observed by monitoring visible absorbance.[21] For Pf and MePD, addition of DNA results in red-shifts of ∼15 nm and hypochromicity. This is typical of the effects of insertion between DNA basepairs during intercalation, a binding mode previously shown for Pf.

For PD, a dramatically different behaviour is observed (Fig. 3). A 35 nm red-shift is accompanied by a *hyperchromism* of >50%. Although this apparently indicates a different mode of binding, it is actually consistent with intercalation where binding is coupled to protonation. The maximum absorption of the DNA-bound dye at 416 nm represents a 13 nm shift from the maximum of PDH^+. Additionally, the large absorbance increase compared to the PD spectrum represents a hypochromic change compared to the spectrum of free PDH^+. Thus, the changes in PD absorbance on addition of DNA can be rationally interpreted in terms of the dominant DNA-bound species being the monocationic PDH^+.

Coupled protonation and DNA binding has been reported previously for neutral dibenzoacridine[22a] as well as other intercalators,[22b] minor groove binders[22c] and proteins.[22d] It is also known that the apparent pK_a of cytosine is raised significantly from ∼4.5 when it protonates on formation of CGC-triplexes, with a 3–5 unit increase reported for internal positions.[23] Moreover theory predicts that the DNA minor groove is more acidic than the surrounding solvent,[24a] with experiments indicating a drop of up to 2 units.[24b] This is likely a result of the high negative potential in the minor groove caused by electrostatic focussing.[25] Thus, the increase of apparent pK_a of PD on binding to DNA is not without precedent.

Absorption changes were analysed by the Scatchard method to obtain binding constants and apparent site sizes as shown in Table 2. Proflavine binds very strongly to CT-DNA and only a lower limit for the association constant could be determined at

Table 2 Association constants (K) and apparent binding site sizes (n) for the modified proflavine dyes with calf thymus (CT)-DNA[a]

Dye	[Na$^+$]/mM	K/M^{-1}	n[b]
Pf	7.5	$\geqslant 3.8 \times 10^6$	0.26
Pf	508	1.4×10^5	0.28
PD	7.5	5.3×10^5	0.33
MePD	7.5	2.0×10^6	0.36

[a] Determined by absorption titration in 5 mM phosphate–1% DMSO; [b] n = number of binding sites per nucleotide unit.

low ionic strength. As the salt concentration was raised, binding weakened and an association constant was readily determined with 500 mM NaCl added to buffer. The binding constant in 5 mM phosphate was estimated theoretically using Record/Manning theory, which states that K for a monocationic intercalator varies with added inert monocation according to eqn (1), with B = 0.24, Z = 1, and $\Psi = 0.82$[26] or 1.[27]

$$\frac{d(\ln K_{obs})}{d(\ln[Na^+])} = -(B + Z\psi) \tag{1}$$

A binding constant of K ≈ 1.5×10^7 M^{-1} was predicted at 7.5 mM Na$^+$, which is higher than the experimental value, and represents an upper limit at low ionic strength. The binding constants measured for Pf have similar magnitudes to previously reported values.[28,29] PD and MePD also show high affinities for DNA, with site sizes that are close to nearest-neighbour, although their binding constants are lower than that for Pf. Nonetheless, at low ionic strength, both PD and MePD are quantitatively bound to DNA at high ratios of DNA basepair to dye concentrations, expressed as P/D ([nucleotide phosphate]/[dye]).

Circular dichroism spectroscopy. Pf, PD and MePD are achiral in aqueous solution. On binding to DNA, all three exhibit small induced circular dichroism (ICD) signals in their visible absorption bands (Fig. 4). ICD occurs when an achiral molecule is placed in a chiral environment, e.g., when a dye is
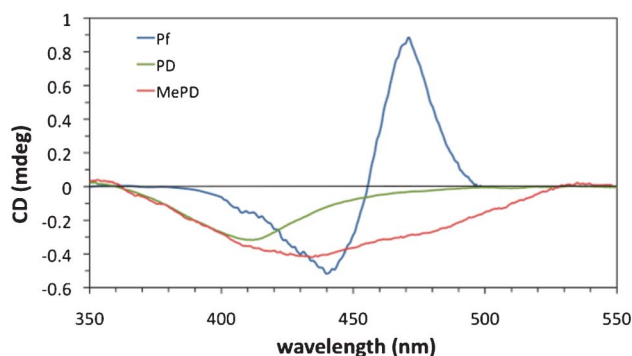
Fig. 4 CD spectra in the visible region showing induced CD of the dyes in the presence of calf thymus (CT)-DNA. [Pf] = 10 μM, P/D = 50; [PD] = 50 μM, P/D = 20; [MePD] = 50 μM, P/D = 10. P/D is the DNA (nucleotide phosphate) to dye ratio. Data are smoothed (see supplementary information† for raw data).

bound to the right-handed helix of DNA.[30] The ICD signals are weak, consistent with intercalative binding.[31]

The ICD for Pf resembles that reported previously for similar binding ratios at low ionic strength in native DNA, [poly(dA–dT)]$_2$, and [poly(dG–dC)]$_2$.[29,32–34] The non-conservative splitting pattern has been attributed to degenerate vibronic exciton coupling between intercalated and externally bound dyes.[28c,34] External binding is found to be minimal at high salt concentrations but to occur to some extent at low salt concentrations even at the high P/D ratios used in this work.[34,35] The deconvoluted CD spectrum of pure intercalated Pf is reported to be positive but that of acridine orange, which is tetramethylated on the exocyclic nitrogens, is negative.[34] This was attributed to different intercalation geometries of the two dyes, since the transition moment involved is the same long-axis polarized π–π^* transition for each.[34–36] It was suggested that H-bonds between Pf and the DNA backbone, as observed in crystal structures, are responsible for that difference since the magnitude of the Pf ICD was sensitive to increasing ionic strength. Negative ICD spectra for PD and MePD suggest that these dyes might have intercalation orientations more similar to acridine orange than Pf; indeed, small slides or twists of the dye in the intercalation pocket can cause a sign inversion.[37] The absence of splitting in the ICD spectra of PD and MePD suggests that external binding is less important for these dyes than for Pf, perhaps because the increased bulk of the side chains hinders association of additional dyes in the groove as observed when Pf external binding is blocked by glycosylation of the major groove in T2-DNA.[32]

Linear dichroism spectroscopy. In flow linear dichroism (LD) spectroscopy, high molecular weight DNA is oriented by shear flow in a Couette cell.[30] LD is defined by eqn (2), where A_{iso} is the isotropic absorption of the sample (i.e., without orientation), S is an orientation factor, and α represents the angle between the polarization of the absorbing transition moment and the orientation axis.

$$LD^r(\lambda) = LD(\lambda)/A_{iso}(\lambda) = 1.5\, S\, (3\, \langle \cos^2\alpha \rangle - 1) \qquad (2)$$

The LD signal of DNA is negative in the 200–350 nm absorption region, where the strongly absorbing transition moments (TM) are polarized in the planes of the basepairs. Since the helix axis of aligned DNA is oriented parallel to the flow direction, negative LD indicates that the basepairs are oriented more perpendicular than parallel to the helical axis, as expected for B-form DNA. For all three acridines, the LD signals in the visible spectrum are also negative (supplementary information†). This implies that the TMs responsible for visible absorption, which are polarized in the acridine aromatic planes,[34,36] also have an average orientation >54° to the helix axis.

For structural interpretation of LD, reduced linear dichroism (LD^r) spectra were computed (Fig. 5) using eqn (2). In general, the LD^r signals at 260 nm for DNA with and without dye report on changes in base orientation induced by dye binding, although overlap of strong dye absorption with DNA at 260 nm precludes quantitative analysis. The ratio of LD^r signals in the visible and UV regions allows calculation of the
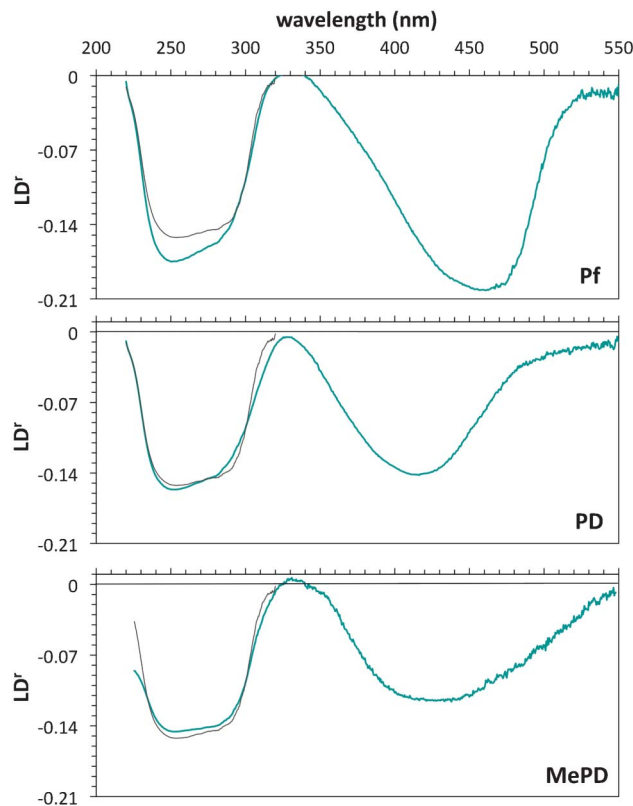
Fig. 5 Reduced linear dichroism (LD^r) spectra of acridine dyes with calf thymus (CT)-DNA. P/D = 50; [DNA] = 1 mM. Shear gradient = 1900 s^{-1} (600 rpm). P/D is the DNA (nucleotide phosphate) to dye ratio. The free DNA spectrum is shown in grey.

angle between the dye and base pair planes. An important caveat is that the latter comparison is valid only if all the dye absorption arises from bound material, since free dye contributes to isotropic absorption but not to LD. Therefore, spectra were measured under conditions (low salt and high P/D) that favour complete binding. For our samples, there was good correspondence between the isotropic absorption and LD spectra, showing close to 100% of dye is bound.

Negative LD^r signals in the dye visible absorption bands (Fig. 5) are consistent with the chromophore long axes lying approximately parallel to the base pair planes. For Pf, this agrees with previous electric LD results which showed the ring system was parallel to the base planes for DNA with various base compositions.[38] Pf shows greater magnitude LD^r in the visible than in the UV. For PD and MePD, the visible LD^r magnitude is lower than that in the UV. Previous studies have inferred an effective value of 80–86° for the orientation of the basepairs to the helix axis.[29,39] Nevertheless, significantly more negative LD^r in the dye than the DNA band, as observed for Pf, has also been reported for other intercalators such as methylene blue.[37c,d] Previous spectral analysis[36] of Pf and related dyes assigned the 465 nm absorption solely to a long-axis polarized transition, and 263 nm absorption predominantly to long-axis polarized transitions with a small contribution from a short-axis polarized transition. Similar assignments are likely for PD and MePD. Thus different
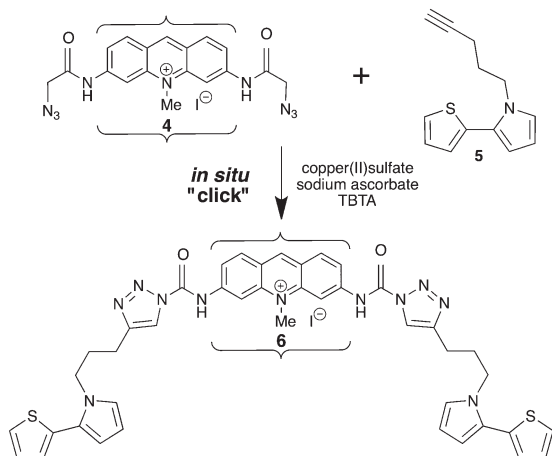
Scheme 2 In situ ''click'' reaction of MePD (4) and pTP (5) to generate MePD-pTP (6). Brackets represent the intercalation site in DNA. Arrows represent presumed main transition moment directions.

values of $LD^r(vis)/LD^r(UV)$ suggest that PD and MePD adopt slightly different intercalation geometries than Pf, as also inferred from CD spectra. Wedging intercalation from the major groove, due to the bulky substituents impeding full insertion between the basepairs, would result in smaller LD^r for the dye since the chromophore would sample a range of orientation, as observed for piperazinecarbonyloxyalkyl derivatives of anthracene and pyrene.[40]

Linear dichroism spectroscopy shows that the ring systems of PD and MePD remain intercalated in DNA after their azide groups undergo click reactions (Scheme 2) with 5-pentenyl-thienyl-pyrrole (pTP). On the other hand, 6 formed in solution did not bind strongly to DNA. Thus, an in situ click reaction is necessary to assemble such a molecule on DNA.

At high dye loading (Fig. 6), the LD^r signal at 425 nm in the MePD absorption band remains negative after the click reaction. A new negative signal is observed in the 300–350 nm region, where MePD has no contribution, which corresponds to absorption of the pTP substituent (supplementary information†). The absorbing transition moment of the clicked TP chromophore thus has an average orientation of <54° to
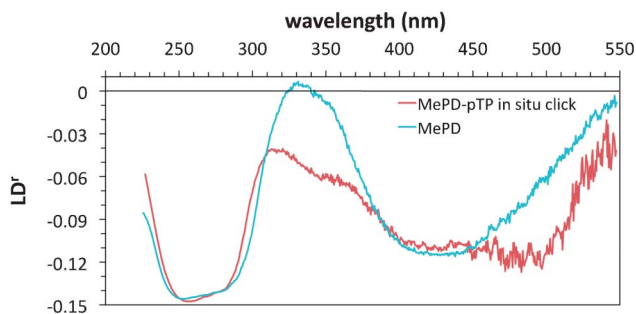
Fig. 6 Reduced linear dichroism (LD^r) spectrum of in situ generated MePD-pTP (6) bound to calf thymus (CT)-DNA compared with DNA-bound MePD.[5f] P/D = 50; [DNA] = 1 mM. P/D is the DNA (nucleotide phosphate) to dye ratio. Shear gradient = 3170 s^{-1} (1000 rpm).
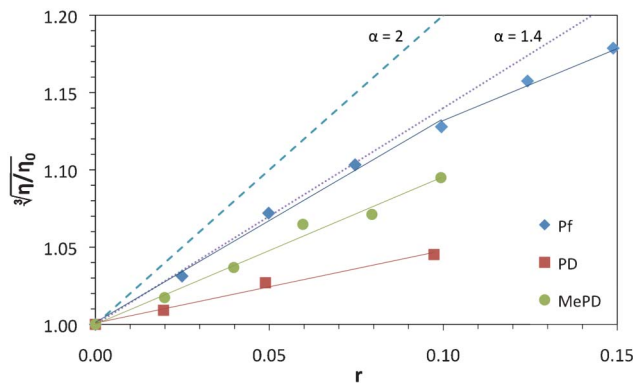
Fig. 7 Relative intrinsic viscosity of calf thymus (CT)-DNA on addition of acridine dyes. [DNA] = 300 μM; 25 °C.

the helix axis. If we set the DNA basepair (260 nm) orientation at 90° to the helix axis, the calculated angles are 74° for MePD (425 nm) and 63° for pTP (350 nm). By contrast, at low dye loading (supplementary information†), the LD^r signal at 300–350 nm is positive whilst the signal in the PD absorption band at 430 nm remains negative, and the angle for pTP substituents in this case is calculated as 52°. Thus, the proximity of nearest neighbour intercalated PD forces the TP residues into an orientation somewhat more parallel to the basepairs. Nonetheless, the TP residues can polymerise into long conducting $poly(TP)_n$ nanowires from this orientation, as we have demonstrated elsewhere.[5f]

Viscometry. Binding of proflavine increases DNA viscosity (Fig. 7), as expected for a classical intercalator, and consistent with previous reports.[29,41,42] Studies with different DNAs found greater apparent elongation for AT-rich than GC-rich DNA,[42,43] due to Pf having a greater tendency to bind externally with the latter and distort the binding ratio. Fig. 7 shows that PD and MePD also increase the viscosity of CT-DNA, but to a lesser extent. Pf is quantitatively bound under the conditions used, and the initial slope of 1.40 (up to r = 0.1) is consistent with monointercalation into high molecular weight DNA with no significant change of persistence length (supplementary information†). An absence of persistence length change on bis-intercalation of YOYO-1 has been reported.[44]

PD and MePD are also quantitatively bound, and although their slopes (0.99 and 0.50, respectively) are lower than for Pf, they are consistent with intercalation. The slope for PD is substantially lower than for Pf or MePD, and its low value implies either that some bound PD is externally associated, or that binding causes a reduction in persistence length that counteracts the increase in contour length due to intercalation. However, the lack of splitting in CD spectroscopy indicates that external binding is not important for PD and MePD, certainly not to the extent of 50% being externally bound.

Minor groove binders cause little change in viscosity[45] but partial intercalators decrease DNA viscosity by bending through wedging,[46] whilst covalent binding of cisplatin decreases DNA viscosity through static bending.[47] These bending interactions decrease the viscosity of rod-like DNA

by shortening the axial length. In long DNA, the bending effect is translated to a decrease of persistence length, which reduces the relative viscosity according to eqn (3). Since MePD and PD still increase viscosity, albeit less so than Pf, they cannot be considered to behave as true partial intercalators that bind by wedging open the basepairs toward one groove. Nonetheless, the results suggest that they adopt an intercalation geometry that reduces DNA persistence length.

$$\sqrt[3]{\frac{[\eta]}{[\eta]_0}} = \frac{L}{L_0} = 1 + \alpha r \qquad (3)$$

Thermal denaturation. Each dye increases the thermal stability of CT-DNA (supplementary information†), as previously reported for Pf.[19a,29] The degree of stabilization correlates with binding affinity, so that Pf has a slightly larger effect than MePD, which in turn has a much larger effect than PD. The greater stabilizing effect of Pf compared to MePD is more dramatic at P/D = 1, suggesting that Pf has greater tendency for electrostatically-driven external binding at high loading and low ionic strength than does MePD, as also inferred from CD. Similar results were observed with [poly(dA–dT)]$_2$ but comparative experiments with [poly(dG–dC)]$_2$ were impossible because of the high melting temperature (95 °C) observed for the naked polynucleotide, so that addition of dye raised the T_m to >100 °C.

Fluorescence. The emission of all three acridines is quenched on binding to calf-thymus DNA, as shown in Fig. 8. For Pf, as for related dyes,[48] this is attributed to electron transfer from guanine to the dye singlet state.[28a,49] Our observations that the emission intensity of Pf bound to CT-DNA decreases in the range P/D = 0–20 and thereafter slowly rises (Fig. 8), mirrors previously reported behaviour.[49] Pf emission is quenched by guanine but enhanced by adenine from comparison of emission in the presence of [poly(dA–dT)]$_2$ and [poly(dG–dC)]$_2$. The quenching observed at low P/D with [poly(dA–dT)]$_2$ is attributed to self-quenching by externally stacked dyes,[21,28c,35] and at high binding ratios the intensity reflects the increase in reported lifetime.[41]

Both PD and MePD$^+$ are quenched by adenine as well as guanine in polynucleotides, indicating that their singlet states are more readily reduced than ^{1}Pf. Ground state reduction is predicted to occur more readily than for Pf due to lower electron densities on their aromatic ring systems, and their (0,0) transitions are at higher energy than that of Pf. Taken together, these features rationalize why the excited singlet states of PD and MePD are significantly more oxidizing than that of Pf. Emission titrations indicate that PD and MePD show little selectivity in binding to [poly(dA–dT)]$_2$, [poly(dG–dC)]$_2$ or mixed sequence CT-DNA. Pf binds most strongly to [poly(dG–dC)]$_2$ under our conditions, other studies report little selectivity at higher ionic strength.[29] However, recent molecular modelling[50] suggests that Pf should indeed bind more strongly to [poly(dG–dC)]$_2$ than [poly(dA–dT)]$_2$ due to greater π–π stacking in the former case. We interpret our observations in terms of the smaller substituents on Pf allowing it to intercalate deeply into the base pair pockets, thus benefiting from enhanced π–π stacking in the GC pockets. By contrast, if
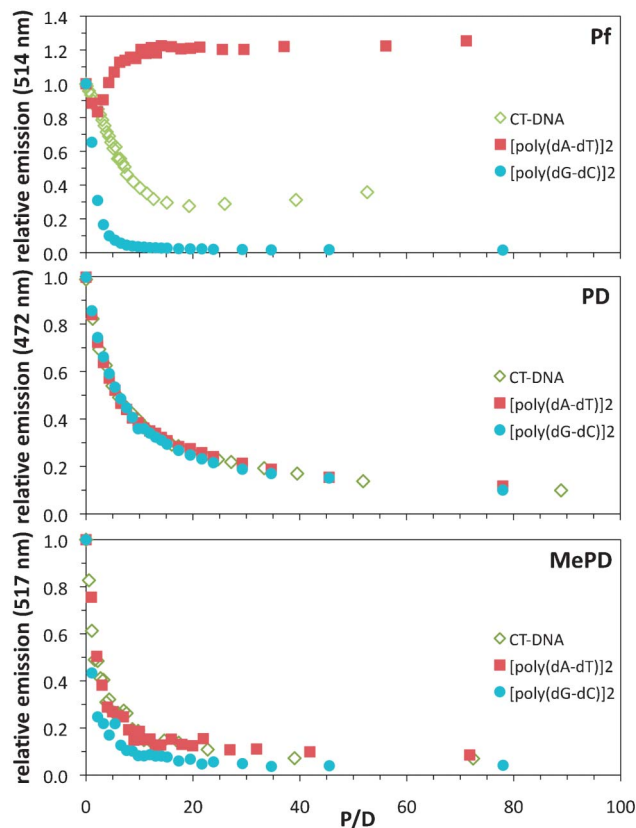
Fig. 8 Variation of emission intensity of acridine dyes on addition of calf thymus (CT)-DNA and alternating homopolynucleotides. P/D is the DNA (nucleotide phosphate) to dye ratio. [dye] = 5 μM.

PD and MePD cannot intercalate as deeply as Pf from the major groove due to their bulky substituents, they will experience similar stacking interactions in all types of base pair pockets.

Discussion

Linear dichroism and viscometry results demonstrate that Pf, PD and MePD intercalate between the DNA base pairs. The small induced CD signals are also consistent with intercalative binding. Other results such as absorption, emission, and thermal denaturation titrations reflect the relative binding affinities of the three compounds. Proflavine was chosen as the framework molecule for our functional intercalators since it known to be an avid intercalator. A recent PDB deposition (3FT6)[51a] shows a crystal structure of proflavine intercalated at terminal CG/CG steps in a hexamer duplex (supplementary information†). The heterocyclic system is deeply intercalated and the exocyclic amino groups are both oriented towards the major groove but do not protrude. Symmetric intercalation with the dye long axis parallel to the base pair long axis allows the amines to form H-bonds with the phosphate and sugar groups of the backbone. This crystal structure confirms an earlier nmr structure with a tetramer [d(CCGG)]$_2$,[51b] and

crystal structures with RNA[51c] and DNA[51d,e] CG dinucleotide minihelices. By comparison, N,N'-tetramethyl proflavine (or acridine orange, AO) and N-dimethyl proflavine are intercalated asymmetrically in dinucleotide minihelix crystals with $\sim10°$ twist from the symmetric geometry.[52] These dyes are slightly displaced towards the major groove in the basepair pocket, with one dimethyl amine group protruding and the other amine in a position similar to Pf. This small change of conformation is enough to cause a change in ICD signal from positive for Pf to negative for AO.[34] Given the negative ICD spectra for PD and MePD bound to DNA, a reasonable hypothesis is that they adopt an intercalation geometry similar to AO, displaced towards the major groove, but likely with both their bulky azide substituents protruding. The wide major groove should readily accommodate these substituents and present them for reaction with molecules approaching from bulk solution.

Such variation of intercalation geometry also rationalises differences in LD and viscosimetry for different dyes. Partial intercalators with small aromatic groups strongly reduce the viscosity of DNA.[46a] However, although PD and MePD give lower slopes than Pf, they nevertheless markedly increase DNA viscosity. Likewise, the LD^r signals for these compounds are still strongly negative, although smaller than for Pf. Taken together, these observations suggest that PD and MePD bind by intercalation with slightly different geometries and dynamics than Pf, since their bulky substituents probably prevent the aromatic tricycle from embedding deeply in the intercalation pocket. Instead, they may be displaced towards the edges of the basepairs closest to the major groove which could give rise to dynamic or static bending of DNA, as seen for the partial intercalator $[\text{Ru(phen)}_3]^{2+}$ [46b,53] or for covalently bound cisplatin.[47] Smaller LD^r signals for the modified dyes are consistent with this postulate, since partially intercalated dyes can explore a range of orientation angles other than perpendicular to the helix axis.[40] Consequently, PD and MePD show little sequence selectivity which is advantageous for their general application as versatile intercalative anchors for directed assembly on a DNA scaffold.

Conclusions

Proflavine, Pf, can be readily modified with azide groups on its exocyclic amines *via* an amide linker. The resultant compound, PD, is neutral but methylation on the ring nitrogen gives a cationic dye, MePD. PD is poorly soluble in water, but becomes protonated on binding to DNA, resulting in an apparent pK_a shift of >3 units. Like proflavine, PD and MePD intercalate DNA, as evidenced by linear dichroism and viscometry. The Pf exocyclic amines reside in the major groove of DNA, and it is likely that the modified dyes adopt a similar binding geometry. However, their larger substituents appear to hinder deep intercalation, implying displacement towards the edge of the major groove, as reported for acridine orange, so that the basepairs become slightly wedged apart to reduce the

DNA persistence length. DNA-bound PD and MePD undergo *in situ* click functionalization with pTP, and remain intercalated after reaction thus placing the monomers in the major groove ready for polymerization to form a conducting chain. In summary, PD and MePD are good candidates for application as an intercalative anchor for assembly of supramolecular structures on a DNA scaffold since they bind strongly with little sequence selectivity, and remain intercalated after click reactions with bulky functional groups.

Experimental

All chemicals and solvents were of the highest grade available from Sigma-Aldrich. Proflavine hemisulfate salt hydrate was used as received, and proflavine derivatives were synthesized (Scheme 1) and purified as described in the supplementary information.† To ensure complete dissolution of dyes, solids were initially dissolved in 100% DMSO, and diluted with 5 mM phosphate buffer with the required pH to give samples in 5 mM phosphate with 1% DMSO. Polynucleotides [poly(dG–dC)]$_2$ and [poly(dA–dT)]$_2$, and high molecular weight calf-thymus DNA were from Sigma. All nucleic acids were dialyzed extensively against pure water before use to remove excess salts, and were stored in 5 mM sodium phosphate buffer (pH 6.9). All experiments were carried out in 5 mM phosphate buffer/1% DMSO (v/v) at 21 °C, unless otherwise stated, which allowed dissolution of PD to tens of millimolar. Although 10% DMSO can distort binding of ligands,[54] 1% DMSO did not perturb the DNA conformation as judged by circular dichroism, and binding results for Pf were consistent with those reported in the absence of DMSO. The concentrations of all materials were determined by UV/vis absorption spectroscopy using the following extinction coefficients, determined analytically for PD and MePD and obtained from the literature for the other materials. Pf (445 nm) 41 000 M^{-1} cm^{-1};[19] PD (381 nm) 6600 M^{-1} cm^{-1}; MePD (409 nm) 9200 M^{-1} cm^{-1}; CT-DNA (260 nm) 6600 M^{-1} cm^{-1}; [poly(dA–dT)]$_2$ (262 nm) 6700 M^{-1} cm^{-1}; [poly(dG–dC)]$_2$ (254 nm) 8400 M^{-1} cm^{-1}. Nucleic acid concentrations are given per nucleotide. Buffer of required pH was prepared by adjusting the pH of a 5 mM phosphate (pH 6.9) solution using small aliquots of concentrated phosphoric acid or sodium hydroxide.

UV/vis spectra and thermal denaturation were measuring with a Cary 100 Bio UV-visible spectrophotometer, and all data are normalized to a 1 cm pathlength. Titrations with calf thymus DNA solution were performed by adding aliquots of concentrated DNA to a constant concentration of ligand. Corrected fluorescence emission and excitation spectra were measured with a SPEX FluoroMax spectrophotometer. CD spectra were measured on a Jasco J-810 spectropolarimeter, and data were normalized to a 1 cm pathlength. The data are presented, as collected, in mdeg; these data can be converted to absorbance units through division by 32 980 mdeg. LD spectra were measured on an Applied Photophysics Chirascan CD spectropolarimeter, adapted to produce linearly polarized

light. Orientation of the intercalator nucleic acid samples was achieved in a flow Couette cell with an outer rotating cylinder and an inner cylinder of 3 cm diameter. The experimental path length was 1 mm, and data are normalized to a 1 cm path length.

Molecular modelling was performed with Spartan 04 (Wavefunction) using the semi-empirical PM3 method and density functional (DFT) method B3LYP/6-31G* to calculate potential densities and HOMO and LUMO energies of Pf, PD, MePD and their protonated forms.

A Cannon-Manning extra low charge size 75 semi-micro viscometer, immersed in a water bath thermostated at 25 °C, was used to measure the relative intrinsic viscosity[55] of dilute solutions of CT-DNA. The DNA concentration and the viscometer volume (300 mL) were kept constant for a series of added dye concentrations. The flow time for water was 177 s, and for solutions containing DNA was >245 s. Measurements were carried out in triplicate and gave standard deviations of $< \pm 1$ s. For long DNA, if the persistence length does not change on intercalation, a plot of the cube root of the relative intrinsic viscosity against binding ratio yields a slope of 1.4 (supplementary information†).[56]

Acknowledgements

References

1 (a) J. Chen and N. C. Seeman, *Nature*, 1991, **350**, 631; (b) E. Winfree, F. Liu, L. A. Wenzler and N. C. Seeman, *Nature*, 1998, **394**, 539.

2 (a) N. C. Seeman, *Nature*, 2003, **421**, 427; (b) P. W. K. Rothemund, *Nature*, 2006, **440**, 297–302; (c) A. V. Pinheiro, D. Han, W. M. Shih and H. Yan, *Nat. Nanotechnol.*, 2011, **6**, 763; (d) T. J. Bandy, A. Brewer, J. R. Burns, G. Marth, T. Nguyen and E. Stultz, *Chem. Soc. Rev.*, 2011, **40**, 138–148.

3 (a) E. Meggers, P. L. Holland, W. B. Tolman, F. E. Romesberg and P. G. Schultz, *J. Am. Chem. Soc.*, 2000, **122**, 10714; (b) G. H. Clever, K. Kaul and T. Carell, *Angew. Chem., Int. Ed.*, 2007, **46**, 6226; (c) S. Liu, G. H. Clever, Y. Takezawa, M. Kaneko, K. Tanaka, X. Guo and M. Shionoyo, *Angew. Chem., Int. Ed.*, 2011, **50**, 8886; (d) I. Bouamaied, T. Nguyen, T. Ruhl and E. Stultz, *Org. Biomol. Chem.*, 2008, **6**, 3888; (e) F. Menacher and H.-A. Wagenknecht, *Photochem. Photobiol. Sci.*, 2011, **10**, 1275.

4 (a) P. Nickels, W. U. Dittmer, S. Beyer, J. P. Kotthaus and F. C. Simmel, *Nanotechnology*, 2004, **15**, 1524; (b) B. Datta, G. B. Schuster, A. McCook, S. C. Harvey and K. Kakrzewska, *J. Am. Chem. Soc.*, 2006, **128**, 14428.

5 (a) A. R. Pike, S. N. Patole, N. C. Murray, T. Ilyas, B. A. Connolly, B. R. Horrocks and A. Houlton, *Adv. Mater.*,

2003, **15**, 254; (b) S. A. F. Al-Said, R. Hassanien, J. Hannant, M. A. Galindo, S. Pruneanu, A. R. Pike, A. Houlton and B. Horrocks, *Electrochem. Commun.*, 2009, **11**, 550; (c) J. Hannant, J. H. Hedley, J. Pate, A. Walli, S. A. F. Al-Said, M. A. Galindo, B. A. Connolly, B. R. Horrocks, A. Houlton and A. R. Pike, *Chem. Commun.*, 2010, **46**, 5870; (d) M. A. Galindo, J. Hannant, R. W. Harrington, W. Clegg, B. R. Horrocks, A. R. Pike and A. Houlton, *Org. Biomol. Chem.*, 2011, **9**, 1555; (e) A. Mishchenko, M. Abdualla, A. Rudnev, Y. Fu, A. R. Pike and T. Wandlowski, *Chem. Commun.*, 2011, **47**, 9807; (f) S. MoradpourHafshejani, S. M. D. Watson, E. Tuite and A. R. Pike, *Chem. Sci.*, 2013, under review; (g) D. Erts, U. Malinovskis, I. Muiznieks and E. Tuite, *Thin Solid Films*, 2008, **516**, 8969.

6 (a) W. Chen, G. Güler, E. Kuruvilla, G. B. Schuster, H.-C. Chiu and E. Riedo, *Macromolecules*, 2010, **43**, 4032; (b) Z. Ma, W. Chen and G. B. Schuster, *Chem. Mater.*, 2012, **24**, 3916–3922; (c) W. Chen and G. B. Schuster, *J. Am. Chem. Soc.*, 2012, **134**, 840–843.

7 (a) A. Houlton, A. R. Pike, M. A. Galindo and B. R. Horrocks, *Chem. Commun.*, 2009, 1797; (b) Rajesh, T. Ahuja and D. Kumar, *Sens. Actuators, B*, 2009, **136**, 275.

8 *Nucleic Acids in Chemistry and Biology*, ed. G. M. Blackburn, M. J. Gait, D. Loakes and D. M. Williams, RSC Publishing, Cambridge, 3rd edn, 2006.

9 (a) L. S. Lerman, *J. Mol. Biol.*, 1961, **3**, 18; (b) V. Luzzati, F. Masson and L. S. Lerman, *J. Mol. Biol.*, 1961, **3**, 634; (c) W. D. Sasikala and A. Mukherjee, *Phys. Chem. Chem. Phys.*, 2013, **15**, 6446.

10 W. A. Denny, *Curr. Med. Chem.*, 2002, **9**, 1655.

11 (a) G. Roelfes and B. L. Feringa, *Angew. Chem., Int. Ed.*, 2005, **44**, 3230; (b) A. J. Boersma, R. P. Megens, B. L. Feringa and G. Roelfes, *Chem. Soc. Rev.*, 2010, **39**, 2083.

12 (a) E. Ceci, R. Cini, A. Karaulov, M. B. Hursthouse, L. Maresca and G. Natile, *J. Chem. Soc., Dalton Trans.*, 1993, 2491; (b) S. Biagini, A. Bianchi, T. Biver, A. Boggioni, I. V. Nikolayenko, F. Secco and M. Venturini, *J. Inorg. Biochem.*, 2011, **105**, 558.

13 (a) L. A. Howell, A. Howman, M. A. O'Connell, A. Mueller and M. Searcey, *Bioorg. Med. Chem. Lett.*, 2009, **19**, 5880; (b) L. A. Howell, Z. A. E. Walker, R. Bowater, M. O'Connell and M. Searcey, *Chem. Commun.*, 2011, **47**, 8262.

14 (a) S. Imoto, T. Hirohama and F. Nagatsugi, *Bioorg. Med. Chem. Lett.*, 2008, **18**, 5560; (b) M. Di Antonio, G. Biffi, A. Mariani, E.-A. Raiber, R. Rodriguez and S. Balasubramanian, *Angew. Chem., Int. Ed.*, 2012, **51**, 11073; (c) M. I. Sánchez, O. Vázquez, J. Martínez-Costas, M. E. Vázquez and J. L. Mascareñas, *Chem. Sci.*, 2012, **3**, 2383.

15 (a) H. C. Kolb, M. G. Finn and K. B. Sharpless, *Angew. Chem., Int. Ed.*, 2001, **40**, 2004; (b) C. R. Becer, R. Hoogenboom and U. S. Schubert, *Angew. Chem., Int. Ed.*, 2009, **48**, 4900; (c) A. H. El-Sagheer and T. Brown, *Chem. Soc. Rev.*, 2010, **39**, 1388; (d) A. H. El-Sagheer and T. Brown, *Acc. Chem. Res.*, 2012, **45**, 1258.

16 L. S. Lerman, *J. Mol. Biol.*, 1964, **10**, 367.

17 K. Yamaoka, S. Noji and M. Yoshida, *Bull. Chem. Soc. Jpn.*, 1981, **54**, 31.

18 S. G. Schulman, D. V. Naik, A. C. Capomacchia and T. Roy, *J. Pharm. Sci.*, 1975, **64**, 982.

19 (a) N. F. Gersch and D. O. Jordan, *J. Mol. Biol.*, 1965, **13**, 138; (b) G. R. Haugen and W. H. Melhuish, *Trans. Faraday Soc.*, 1964, **60**, 386.

20 N. Mataga, Y. Kaifu and M. Koizumi, *Bull. Chem. Soc. Jpn.*, 1956, **29**, 373.

21 (a) A. R. Peacocke and J. N. H. Skerrett, *Trans. Faraday Soc.*, 1956, **52**, 261; (b) E. Tuite and J. M. Kelly, *Biopolymers*, 1995, **35**, 419.

22 (a) J. Booth and E. Boyland, *Biochim. Biophys. Acta*, 1953, **12**, 75; (b) F. Pierard, A. Del Guerzo, A. Kirsch-De Mesmaeker, M. Demeunynck and J. Lhomme, *Phys. Chem. Chem. Phys.*, 2001, **3**, 2911; (c) B. Njuyen, J. Stanek and W. D. Wilson, *Biophys. J.*, 2006, **90**, 1319; (d) F. M. Dullweber, T. Stubbs, J. Musil, J. Sturzebecher and G. Klebe, *J. Mol. Biol.*, 2001, **313**, 593.

23 (a) W. D. Wilson, H. P. Hopkins, S. Mizan, D. D. Hamilton and G. Zon, *J. Am. Chem. Soc.*, 1994, **116**, 3607; (b) J. L. Asensio, A. N. Lane, J. Dhesi, S. Bergqvist and T. Brown, *J. Mol. Biol.*, 1998, **275**, 811.

24 (a) G. Lamm and G. R. Pack, *Proc. Natl. Acad. Sci. U. S. A.*, 1990, **87**, 9033; (b) S. Hanlon, L. Wong and G. R. Pack, *Biophys. J.*, 1997, **72**, 291.

25 R. Rohs, A. M. West, A. Sosinsky, P. Liu, R. S. Mann and B. Honig, *Nature*, 2009, **461**, 1248.

26 (a) M. T. Record, C. F. Anderson and T. M. Lohman, *Q. Rev. Biophys.*, 1978, **11**, 103; (b) W. D. Wilson and I. G. Lopp, *Biopolymers*, 1984, **23**, 3025.

27 (a) G. S. Manning, *Quart. Rev. Biophys.*, 1978, **11**, 179; (b) R. A. G. Friedmann and G. S. Manning, *Biopolymers*, 1984, **23**, 2671.

28 (a) J. C. Thomes, G. Weill and M. Daune, *Biopolymers*, 1969, **8**, 647; (b) F. Quadrifoglio, V. Crescenzi and V. Giancotti, *Biophys. Chem.*, 1974, **1**, 319; (c) R. W. Armstrong, T. Kurucsev and U. P. Strauss, *J. Am. Chem. Soc.*, 1970, **92**, 3174.

29 B. García, J. M. Leal, R. Ruiz, T. Biver, F. Secco and M. Venturini, *J. Phys. Chem. B*, 2010, **114**, 8555.

30 B. Nordén, A. Rodger and T. Dafforn, *Linear Dichroism and Circular Dichroism: A Textbook on Polarized Light Spectroscopy*, RSC Publishing, Cambridge, 2010.

31 R. Lyng, T. Härd and B. Nordén, *Biopolymers*, 1987, **26**, 1327.

32 H. J. Li and D. M. Crothers, *Biopolymers*, 1969, **8**, 217.

33 M. Kamiya, *Biochim. Biophys. Acta*, 1979, **562**, 70.

34 D. Fornasiero and T. Kurucsev, *J. Phys. Chem.*, 1981, **85**, 613.

35 H. J. Li and D. M. Crothers, *J. Mol. Biol.*, 1969, **39**, 461.

36 Y. Matsuoka and K. Yamaoka, *Bull. Chem. Soc. Jpn.*, 1979, **52**, 3163.

37 (a) R. Lyng, A. Rodger and B. Nordén, *Biopolymers*, 1991, **31**, 1709; (b) R. Lyng, A. Rodger and B. Nordén, *Biopolymers*, 1992, **32**, 1201; (c) E. Tuite and B. Nordén, *J. Am. Chem.*

Soc., 1994, **116**, 7548; (d) E. Tuite and B. Nordén, *Chem. Comm.*, 1995, 53–54.

38 J. Ramstein, C. Houssier and M. Leng, *Biochim. Biophys. Acta*, 1973, **335**, 54.

39 (a) Y. Matsuoka and B. Nordén, *Biopolymers*, 1982, **21**, 2433; (b) P. J. Chou and J. Johnson, *J. Am. Chem. Soc.*, 1993, **115**, 1205.

40 H.-C. Becker and B. Nordén, *J. Am. Chem. Soc.*, 2000, **122**, 8344.

41 G. Cohen and H. K. Eisenberg, *Biopolymers*, 1969, **8**, 45.

42 J. Ramstein, M. Dourlent and M. Leng, *Biochem. Biophys. Res. Comm.*, 1972, **47**, 874.

43 J. Ramstein, M. Ehrenberg and R. Rigler, *Biochemistry*, 1980, **19**, 3938.

44 K. Günther, M. Mertig and R. Seidel, *Nucl. Acids Res.*, 2010, **38**, 6526.

45 D. Suh and J. B. Chaires, *Bioorg. Med. Chem.*, 1995, **3**, 723.

46 (a) L. Kapiak and E. J. Gabbay, *J. Am. Chem. Soc.*, 1975, **97**, 403; (b) S. Satyanarayana, J. C. Dabrowiak and J. B. Chaires, *Biochemistry*, 1992, **31**, 9319.

47 J.-L. Butour and J.-P. Macquet, *Biochim. Biophys. Acta*, 1981, **653**, 305.

48 (a) E. Tuite, J. M. Kelly, G. S. Beddard and G. D. Reid, *Chem. Phys. Lett.*, 1994, **226**, 517; (b) G. D. Reid, D. J. Whittaker, M. A. Day, C. M. Creely, E. M. Tuite, J. M. Kelly and G. S. Beddard, *J. Am. Chem. Soc.*, 2001, **123**, 6953.

49 Y. Kubota and R. F. Steiner, *Biophys. Chem.*, 1977, **6**, 279.

50 R. Ruiz, B. García, G. Ruisi, A. Silvestri and G. Barone, *J. Mol. Struct: THEOCHEM*, 2009, **915**, 86.

51 (a) T. Maehigashi, O. Persil, N. V. Hud and L. D. Williams, *RCSB Protein Databank ID 3FT6*, DOI: 10.2210/pdb3ft6/pdb; (b) D. J. Patel and L. L. Canuel, *Proc. Natl. Acad. Sci. USA*, 1977, **74**, 2624; (c) S. Neidle, A. Achari, G. L. Taylor, H. M. Berman, H. L. Carrell, J. P. Glusker and W. C. Stallings, *Nature*, 1977, **269**, 304; (d) H.-S. Shieh, H. M. Berman, M. Dabrow and S. Neidle, *Nucl. Acids Res.*, 1980, **8**, 85; (e) B. Schneider, S. L. Ginell and H. M. Berman, *Biophys. J.*, 1992, **63**, 1572.

52 (a) A. H.-J. Wang, G. J. Quigley and A. Rich, *Nucl. Acids Res.*, 1979, **6**, 3879; (b) B. S. Reddy, T. P. Seshadri, T. D. Sakore and H. M. Sobell, *J. Mol. Biol.*, 1979, **135**, 787; (c) T. D. Sakore, K. K. Bhandary and H. M. Sobell, *J. Biomol. Struct. Dyn.*, 1984, **1**, 1219.

53 (a) P. Lincoln and B. Nordén, *J. Phys. Chem. B*, 1998, **102**, 9583; (b) A. Reymer and B. Nordén, *Chem Comm.*, 2012, **48**, 4941.

54 (a) H.-K. Kim, P. Lincoln, B. Nordén and E. Tuite, *Chem. Commun.*, 1997, 2375; (b) A. W. McKinley, P. Lincoln and E. M. Tuite, *Dalton Trans.*, 2013, **42**, 4081.

55 E. L. Gilroy, M. R. Hicks, D. J. Smith and A. Rodger, *Analyst*, 2011, **136**, 4159.

56 H. Yamakawa and M. Fujii, *Macromolecules*, 1974, **7**, 128.

Diazido-Proflavines as Intercalative Anchors for Directed Assembly of Functional Molecules on DNA

Shahrbanou Moradpourhafshejani,[a] Joseph H. Hedley,[a,b] Alexandra O. Haigh,[a,c] Andrew R. Pike[a]* and Eimer M. Tuite[a]*

[a] Chemical Nanoscience Laboratory, School of Chemistry, Bedson Building, Newcastle University, Newcastle upon Tyne, NE1 7RU, UK. E-mail: andrew.pike@ncl.ac.uk; eimer.tuite@ncl.ac.uk

[b] QuantuMDx, International Centre for Life, Times Square, Newcastle upon Tyne, NE1 4EP, UK.

[c] Churchill Community College, Sixth Form, Churchill Street, Wallsend, Tyne & Wear NE28 7TN, UK.

Supporting Information

A. Synthetic Methods
B. Experimental Methods
C. Dye Extinction Coefficients & Absorption Spectra in Aqueous Solution
D. Minimized Structures and MOs calculated with SPARTAN
E. pH Spectral Titrations and pK_a Determination
F. Minimized Structures and Partial Charges calculated with SPARTAN
G. Absorption Spectral Titrations with CT-DNA
H. Absorption Changes as a Function of Added CT-DNA
I. Scatchard Plots for Binding to CT-DNA
J. Linear Dichroism with CT-DNA
K. Reduced Linear Dichroism with CT-DNA
L. Spectroscopy of Methylated Proflavine Diazide after Click Reaction with pTP
M. Spectroscopy of Proflavine Diazide after Click Reaction with pTP
N. Circular Dichroism with CT-DNA
O. Dilute Solution Viscometry with CT-DNA
P. Thermal Denaturation with CT-DNA
Q. Thermal Denaturation with [poly(dA-dT)]$_2$
R. Emission Spectral Titrations with CT-DNA, [poly(dA-dT)]$_2$, and [poly(dG-dC)]$_2$
S. PDB Structure of Proflavine/DNA Structure

A. Synthetic Methods

Synthesis of Proflavine Diazide (PD)

Anhydrous DMF (400 mL) and triethyl amine (2 mL, 14.4 mmol) were added to proflavine (1 g, 3.87 mmol). This solution was stirred vigorously for 30 min at room temperature and then chloroacetyl chloride (6 mL, 75.3 mmol) was added dropwise at 0 °C. The solution was stirred for 3 h. TLC was performed in chloroform/methanol (90:10) to show that the reaction had gone to completion. Water (100 mL) was added to quench the reaction. Solvent was removed *in vacuo* and the residue was filtered and washed with water (3×50 mL) and then dried in vacuum-oven under 60°C temperature to afford an orange solid in yield of 1.12 g, 79.7%. In the next step DMF (375 mL) was added to the orange solid (500 mg, 1.38 mmol). Sodium azide (0.55 g, 9.1 mmol) was then added and then the reaction solution was stirred and heated (80 °C) overnight. TLC showed that the reaction had proceeded to completion. The reaction mixture was cooled to room temperature and solvent was removed *in vacuo*. The ^{1}H-NMR spectrum of the residue confirmed the successful synthesis of proflavine diazide derivative. ^{1}H-NMR (300 MHz, DMSO-d_6, 25°C) step 1: δ 11.47 (s, 2H, NH), 9.65 (s, 1H, CH) 8.86 (S, 2H, CH) 8.41 (d, 2H, CH, J=9.21) 7.8 (dd, 2H, CH, J=1.61,9.10) 4.48 (S, 4H, CH$_2$) step 2: δ (300 MHz, DMSO, 25 °C) 10.82 (s, 2H, NH) 8.90 (s, 1H, CH) 8.50 (s, 2H, CH) 8.1 (d, 2H, CH, J=9.05) 7.7 (dd, 2H, CH, J=1.99, 9.05) 4.2 (s, 4H, CH$_2$). ^{13}C-NMR (400 MHz, DMSO-d_6, δ 167.24, 149.70, 140.07, 135.32, 129.24, 122.65, 120.01, 114.47, 51.50). HRMS (ESI, m/z): [M+H]$^+$ calculated for C$_{17}$H$_{14}$N$_9$O$_2$, 376.1270; found, 376.1266.

Synthesis of Methylated Proflavine Diazide (MePD)

Proflavine diazide derivative (PD) (200 mg, 0.53 mmol) was placed under vacuum and after an hour, 50 mL anhydrous DMF was added. The solution was stirred vigorously for 30 min then methyl iodide (100 µL, 1.6 mmol) was added. The solution was stirred under N$_2$ with reflux (86°C) for 48 hours. TLC showed that the reaction had proceeded to completion. Solvent was removed *in vacuo* and the residue was extracted with ethyl acetate. The organic layer was dried with MgSO$_4$ and evaporated to afford a orange-red solid which was purified by column chromatography using DCM/methanol (95:5) This gave a dark red solid with a yield of 10%. ^{1}H-NMR (300 MHz, DMSO-d_6, 25°C). δ 11.296 (s, 2H, NH), 9.742 (s, 1H, CH), 8.994 (s, 2H, CH), 8.505 (d, 2H, CH), 7.885 (dd, 2H, CH), 4.49 (s, 3H, CH$_3$), 4.31 (s, 4H, CH$_2$). ^{13}C-NMR (400 MHz, DMSO-d_6) δ 169.36, 147.84, 143.29, 133.91, 122.90, 120.92, 103.92, 55.45, 52.33, 49.13, 38.13.
HRMS (ESI, m/z): [M+H]$^+$ calculated for C$_{17}$H$_{14}$N$_9$O$_2$, 390.1427; found, 390.1437.

B. Experimental Methods

Reagents

All chemicals and solvents were purchased from Sigma-Aldrich and were of the highest grade available. Proflavine hemisulfate salt hydrate from was used as received, and proflavine derivatives were synthesized and purified as described below.
Polynucleotides [poly(dG-dC)]$_2$ and [poly(dA-dT)]$_2$, and high molecular weight calf-thymus DNA were from Sigma. All nucleic acids were dialyzed extensively against pure water before use to remove excess salts, and were stored in 5 mM sodium phosphate buffer (pH 6.9).

Instruments and Measurements

Spectroscopic, thermal denaturation and viscometry experiments were carried out in 5 mM phosphate buffer/1% DMSO at 21 °C, unless otherwise stated.

UV/vis Absorption and Emission Spectroscopy
UV/vis measurements were carried out on a Cary 100 Bio UV-Visible spectrophotometer, and all

data are normalized to a 1 cm pathlength. Titrations with calf thymus DNA solution were performed by adding aliquots of concentrated DNA to a constant concentration of ligand.

The concentrations of all materials were determined by UV/vis absorption spectroscopy using the following extinction coefficients, determined analytically for PD and MePD and obtained from the literature for the other materials. Pf (445 nm) 41,000 M^{-1} cm^{-1} [N. F. Gersch and D. O. Jordan, *J. Mol. Biol.*, 1965, **13**, 138; G. R. Haugen and W. H. Melhuish, *Trans. Faraday Soc.*, 1964, **60**, 386.]; PD (381 nm) 6,600 M^{-1} cm^{-1}; MePD (409 nm) 9,200 M^{-1} cm^{-1}; CT-DNA (260 nm) 6,600 M^{-1} cm^{-1}; [poly(dA-dT)]$_2$ (262 nm) 6,700 M^{-1} cm^{-1}; [poly(dG-dC)]$_2$ (254 nm) 8,400 M^{-1} cm^{-1}.

Corrected fluorescence emission and excitation spectra were measured with a SPEX FluoroMax spectrophotometer.

Circular Dichroism

CD spectra were measured on a Jasco J-810 spectropolarimeter, and data were normalized to a 1 cm pathlength. The data are presented, as collected, in mdeg; these data can be converted to absorbance units through division by 32,980 mdeg. Although proflavine and its derivatives are achiral, they show induced CD signals when bound to nucleic acids as a result of coupling of their electric-dipole-allowed transition moments with the transition moments of the chirality organized nucleobases.

Linear Dichroism and Reduced Linear Dichroism

LD spectra were measured on an Applied Photophysics Chirascan CD spectropolarimeter, adapted to produce linearly polarized light. Orientation of the intercalator nucleic acid samples was achieved in a flow Couette cell with an outer rotating cylinder and an inner cylinder of 3 cm diameter. The experimental path length was 1 mm, and data were normalized to a 1 cm path length. Samples containing pTP showed scattering phenomena which introduced significant errors in quantitative analysis of these spectra; nonetheless, qualitative interpretations are justifiable.

LD is the differential absorption of light plane polarized parallel and perpendicular to the flow direction in the Couette cell. The magnitude of the LD signal depends on the degree of orientation of the sample as well as the molar absorptivity and concentration of the sample [*Linear Dichroism and Circular Dichroism: A Textbook on Polarized Light Spectroscopy*, B. Nordén, A. Rodger and T. Dafforn; RSC Publishing, Cambridge, 2010.]. At the magic angle of 54°, LD = 0.

The reduced dichroism is defined as:

$$LD^r(\lambda) = LD(\lambda)/A_{iso}(\lambda) \tag{S1}$$

Where A_{iso} is the isotropic absorption of the sample (*i.e.*, without orientation). It is related to the orientation of the chromophore as:

$$LD^r(\lambda) = 1.5\, S\, (3\, \langle \cos^2\alpha \rangle - 1) \tag{S2}$$

Where α represents the angle between the polarization of the absorbing transition moment and DNA helix axis (which is parallel to the orientation axis). S is an orientation factor describing the degree of orientation of the DNA helix such that $S = 1$ is equivalent to perfect orientation and $S = 0$ to random orientation. $\langle \cos^2\alpha \rangle$ represents an average over the angular distribution. S depends on the DNA stiffness and length, the flow rate, and the viscosity of the medium. S can be determined from the dichroism of DNA at 260 nm, where the π-π* transitions are polarized in the plane of the bases. Previous studies have inferred an effective value of 80-86° for the orientation of the basepairs to the helix axis [Y. Matsuoka and B. Nordén, *Biopolymers*, 1982, **21**, 2433; P. J. Chou and J. Johnson, *J. Am. Chem. Soc.*, 1993, **115**, 1205.].

Thermal Denaturation

Thermal denaturation experiments were performed by monitoring the absorbance at 260 nm versus temperature. Nucleic acid concentrations were typically 49 μM for these experiments.

pH Titrations

Buffer of required pH was prepared by adjusting the pH of a 5 mM phosphate (pH 6.9) solution using small aliquots of concentrated phosphoric acid or sodium hydroxide.

To ensure complete dissolution of dyes, solids were initially dissolved in 100% DMSO, and diluted with 5 mM phosphate buffer with the required pH to give samples in 99% 5 mM phosphate/1% DMSO. Samples typically contained 15 µM proflavine, 19 µM MePD and 49 µM PD.

Dilute Solution Viscosimetry

A Cannon-Manning extra low charge size 75 semi-micro viscometer, immersed in a water bath thermostated at 25 °C, was used to measure the relative intrinsic viscosity [E. L. Gilroy, M. R. Hicks, D. J. Smith and A. Rodger, *Analyst*, 2011, **136**, 4159.] of dilute solutions of CT-DNA. The DNA concentration and the viscometer volume (300 mL) were kept constant for a series of added dye concentrations. The flow time for water was 177 s, and for solutions containing DNA was >245 s. Measurements were carried out in triplicate and gave standard deviations of <±1 s. The flow times are related to the relative intrinsic viscosity according to Equation (S3), where $[\eta]$ is the intrinsic viscosity in the presence of dye, $[\eta]_0$ is the intrinsic viscosity of free DNA. t_0, t_d, and t represent the flow times for buffer only, naked DNA, and dye-bound DNA, respectively.

$$\frac{[\eta]}{[\eta]_0} = \frac{t - t_0}{t_d - t_0} \qquad (S3)$$

For rigid rod DNA, the relative contour length, L, is related to the relative intrinsic viscosity and the binding ratio according to Equation (5), where r is bound dye per base [G. Cohen and H. K. Eisenberg, *Biopolymers*, 1969, **8**, 45.]. L is the contour length in the presence of dye and L_0 is the contour length of free DNA. For monointercalation, every bound dye extends DNA by the equivalent of two bases (or one base pair). Thus, a plot of the cube root of the relative intrinsic viscosity against binding ratio yields a slope of $\alpha = 2$.

$$\sqrt[3]{\frac{[\eta]}{[\eta]_0}} = \frac{L}{L_0} = 1 + \alpha r \qquad (S4)$$

Experiments with sonicated DNA from Sigma gave no significant difference in viscosity from that of water up to a concentration of 900 µM. Experiments were therefore carried out with high molecular weight CT-DNA, which means that changes in contour length and changes in flexibility cannot be readily distinguished. Nevertheless, this method is useful for comparing the effects of different dyes on the hydrodynamics of DNA. Applying the wormlike chain model for a random coil, the intrinsic viscosity of DNA, is [H. Yamakawa and M. Fujii, *Macromolecules*, 1974, **7**, 128.]:

$$[\eta] \propto L^{3/2} \times l_P^3 \qquad (S5)$$

where l_P is persistence length (50 nm for DNA). Thus, if the persistence length does not change on intercalation, a plot of the cube root of the relative intrinsic viscosity against binding ratio yields a slope of 1.4. If the persistence length changes on intercalation, the slope will additionally reflect that change.

$$\sqrt[3]{\frac{[\eta]}{[\eta]_0}} = \sqrt{\frac{L}{L_0} \cdot \frac{l_P}{l_P^0}} = 1 + \sqrt{2}\frac{l_P}{l_P^0} r \qquad (S6)$$

Molecular Modelling

Molecular modelling was performed with Spartan 04 (Wavefunction) using the semi-empirical PM3 method and density functional (DFT) method B3LYP/6-31G* to calculate potential densities and HOMO and LUMO energies of Pf, PD, MePD and their protonated forms.

C. Dye Extinction Coefficients & Absorption Spectra in Aqueous Solution
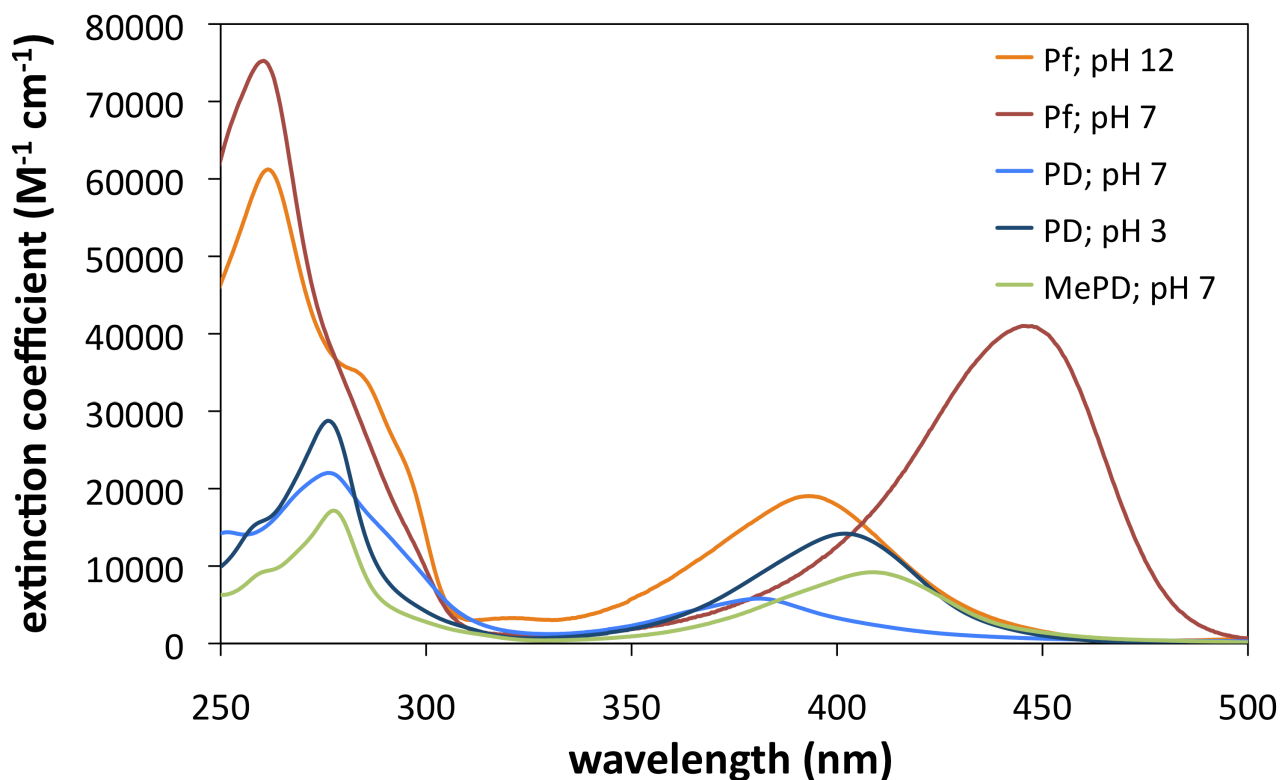
Figure S1. Absorption spectra of **Pf**, **PD** and **MePD** in aqueous solution with 1% DMSO .

Table S1. Extinction coefficients of the proflavine dyes in aqueous solution with 1% DMSO.

Dye	pH	λ_{max} / nm	ε_{max} / M^{-1} cm^{-1}	HOMO-LUMO gap / eV	λ_{max}(DNA) / nm
Pf	12	393	19,000	3.51	-
PfH$^+$	7	445	41,000	3.29	460
PD	7	381	5,800	3.62	-
PDH$^+$	3	403	13,200	3.27	416
MePD$^+$	7	409	9,200	3.35	425

D. Minimized Structures and MOs calculated with SPARTAN

Pf	**HOMO**	**LUMO**
-666 au	-4.83 eV	-1.32 eV
	ΔE = 3.51 eV	

PfH$^+$	**HOMO**	**LUMO**
-667 au	-8.95 eV	-5.66 eV
	ΔE = 3.29 eV	

PD	**HOMO**	**LUMO**
-1300 au	-6.02 eV	-2.40 eV
	ΔE = 3.62 eV	

PDH$^+$	**HOMO**	**LUMO**
-1299 au	-9.46 eV	-6.19 eV
	ΔE = 3.27 eV	

MePD$^+$	**HOMO**	**LUMO**
-1338 au	-9.44 eV	-6.09 eV
	ΔE = 3.35 eV	
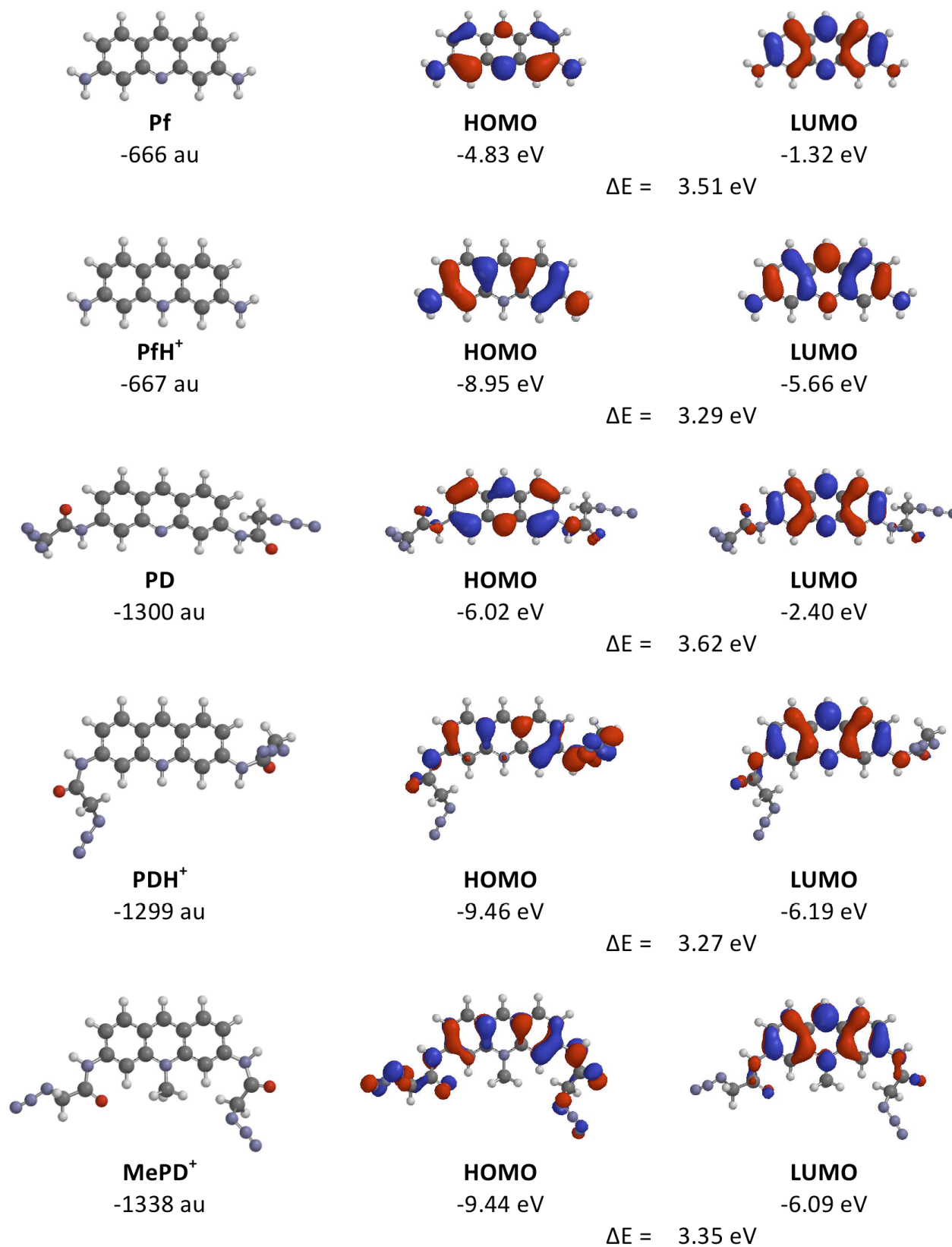
Figure S2. Frontier orbitals calculated for **Pf**, **PD** and **MePD** and their protonated forms. Semi-empirical structure minimization (PM3) was followed by DFT calculations (B3LYP/6-31G*) of energies and molecular orbitals.

E. pH Spectral Titrations and pKa Determination
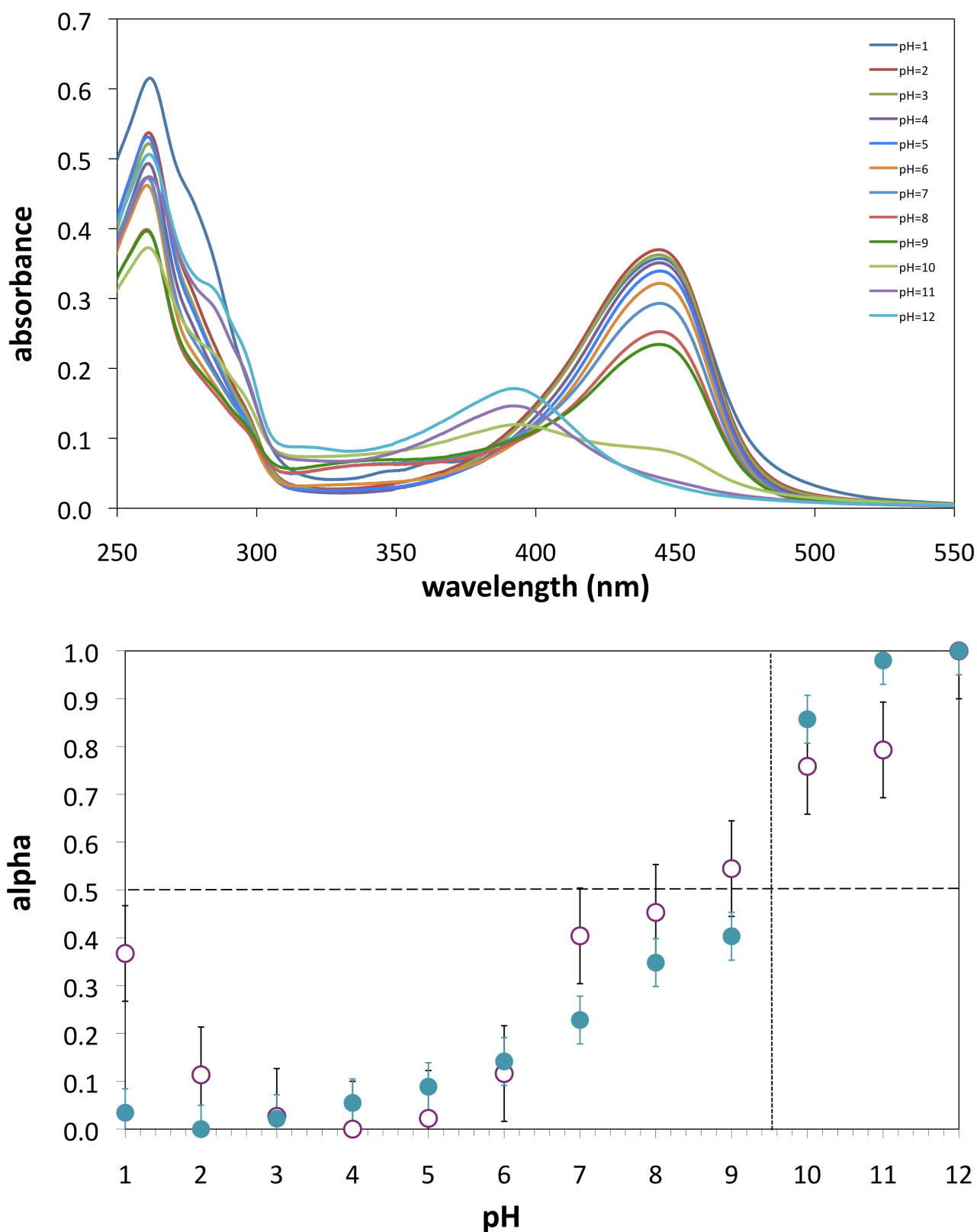
Figure S3. Variation of the absorption spectra of **Pf** with pH. *alpha* represents the proportion of the species that is prevalent at high pH. (●) 448 nm; (○) 317 nm. Pf (7 μM); 5 mM phosphate (pH 6.9)/1% DMSO; pH adjusted with NaOH or H_3PO_4; 21 °C.
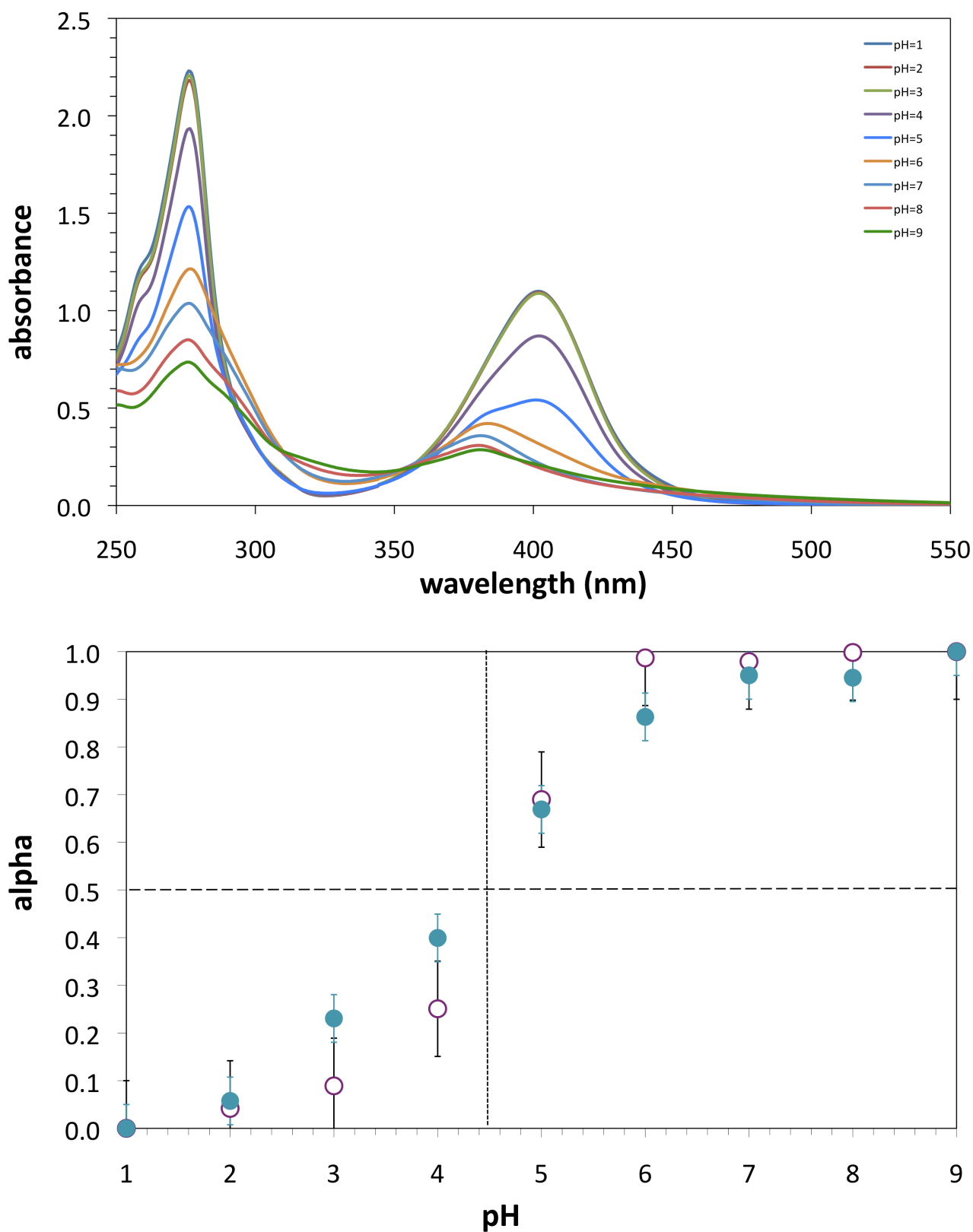
Figure S4. Variation of the absorption spectra of **PD** with pH. *alpha* represents the proportion of the species that is prevelant at high pH. (●) 406 nm; (○) 331 nm. PD (54 µM); 5 mM phosphate (pH 6.9)/1% DMSO; pH adjusted with NaOH or H_3PO_4; 21 °C.
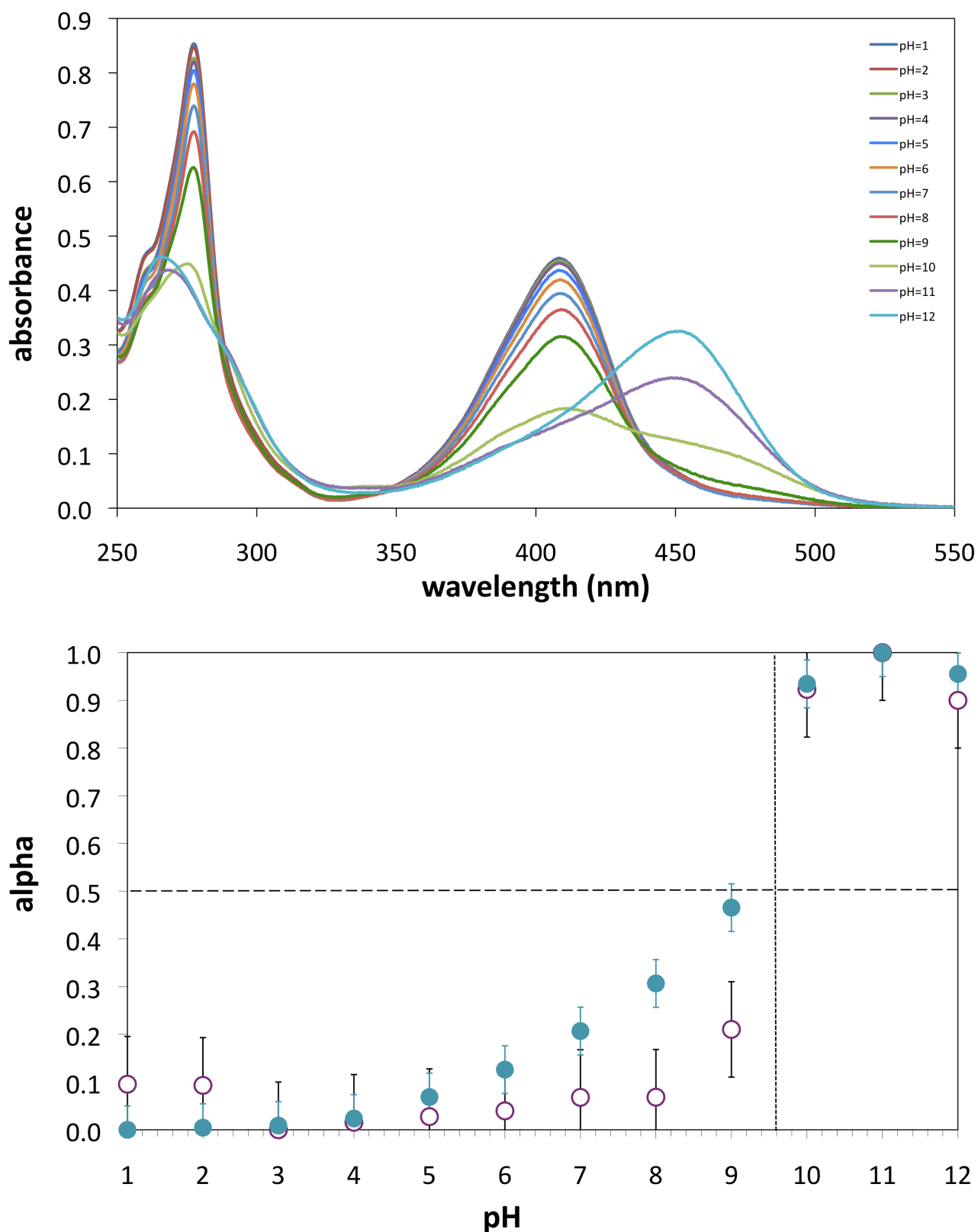
Figure S5. Variation of the absorption spectra of **MePD** with pH. *alpha* represents the proportion of the species that is prevalent at high pH. (●) 407 nm; (○) 323 nm. PDMe (43 μM); 5 mM phosphate (pH 6.9)/1% DMSO; pH adjusted with NaOH or H_3PO_4; 21 °C.

F. Minimized Structures and Partial Charges calculated with SPARTAN

	Pf	0.68 D
	PfH$^+$	2.32 D
	PD	0.53 D
	PDH$^+$	4.84 D
	MePD$^+$	5.90 D
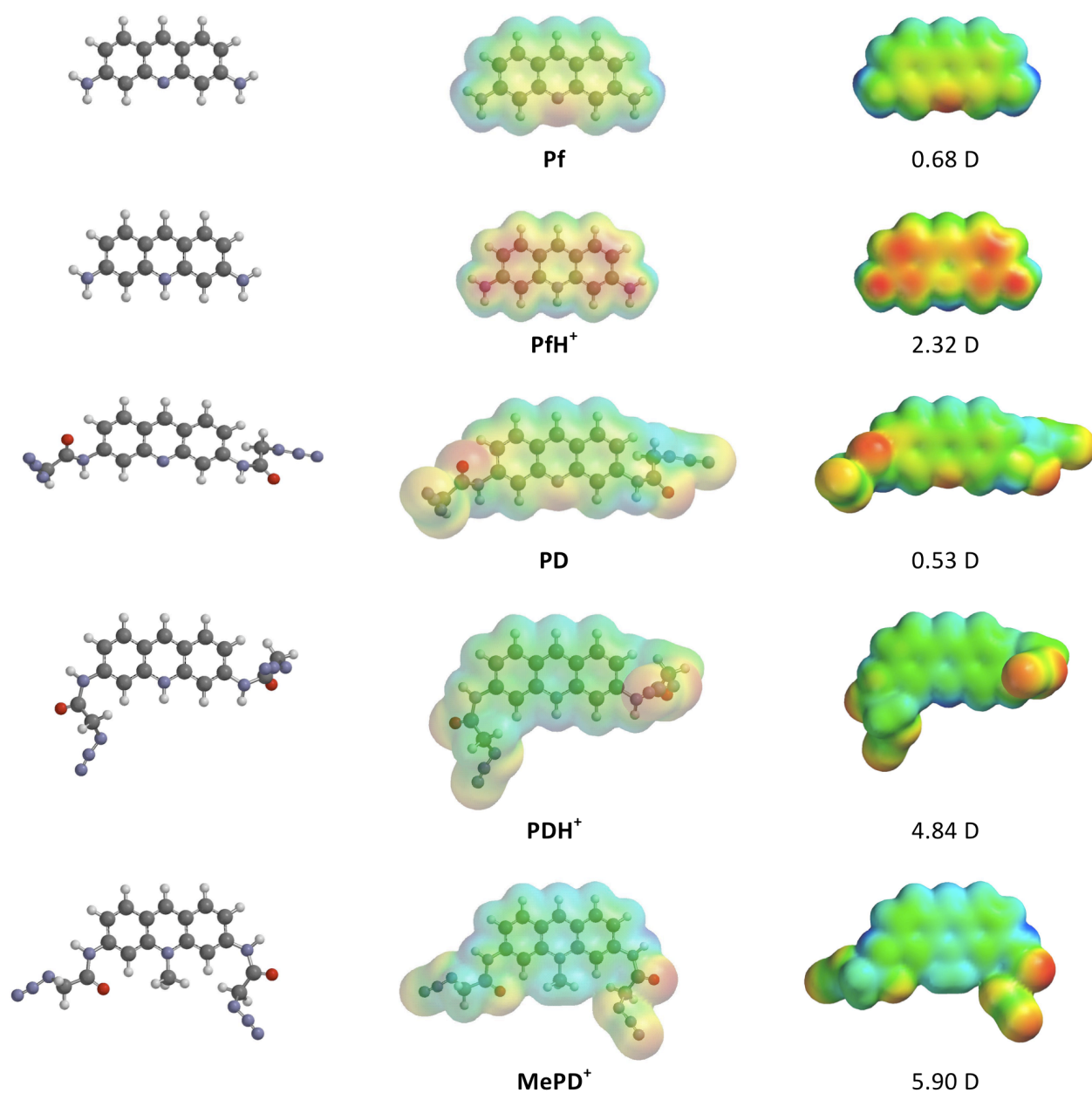
Figure S6. Partial charges for the minimized structures (left column) of **Pf**, **PD** and **MePD** and their protonated forms rendered as transparent (middle column) and solid surfaces (right column). Semi-empirical structure minimization (PM3) was followed by DFT calculations (B3LYP/6-31G*) of partial charge distributions. Positive and negative partial charges are represented, respectively, by blue and red.

G. Absorption Spectral Titrations with CT-DNA
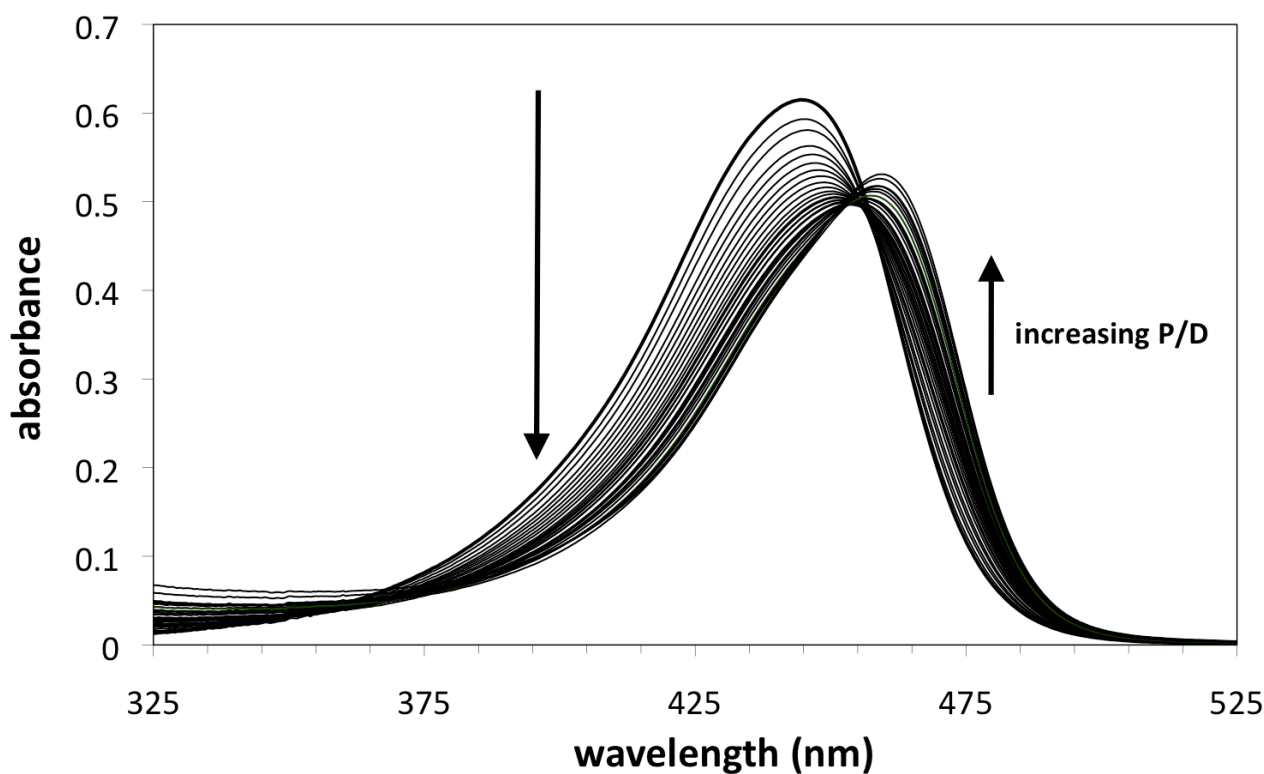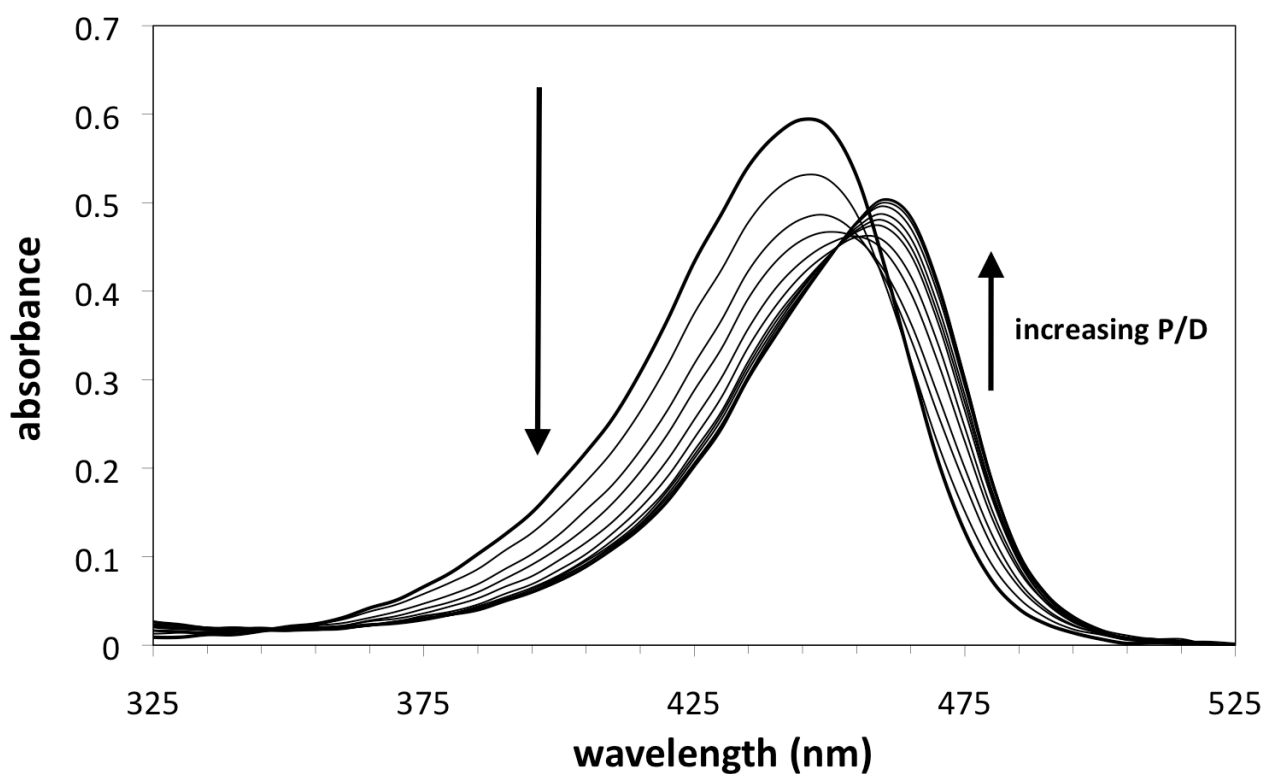
Figure S7. Absorption titrations of **Pf** in 5 mM phosphate/1% DMSO (top; 14.5 µM) and 5 mM phosphate/0.5 M NaCl/1% DMSO (bottom; 15 µM) with added CT-DNA.
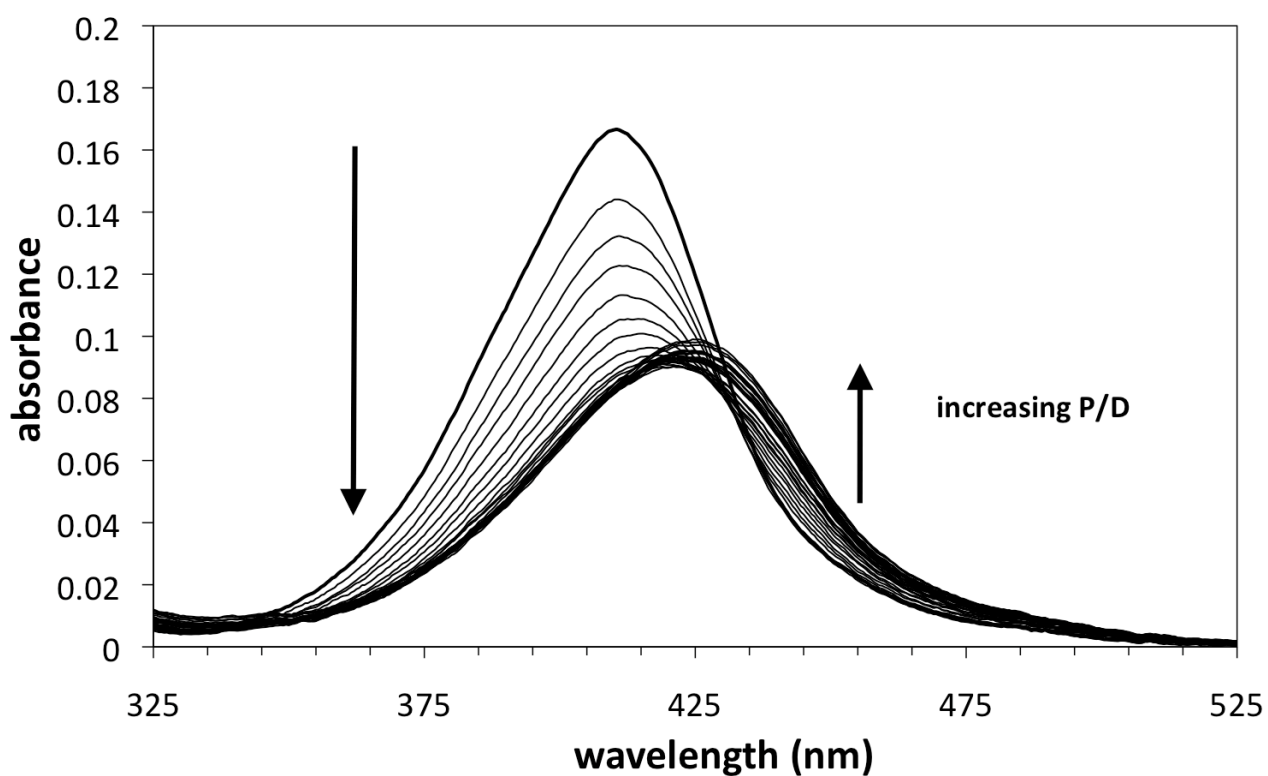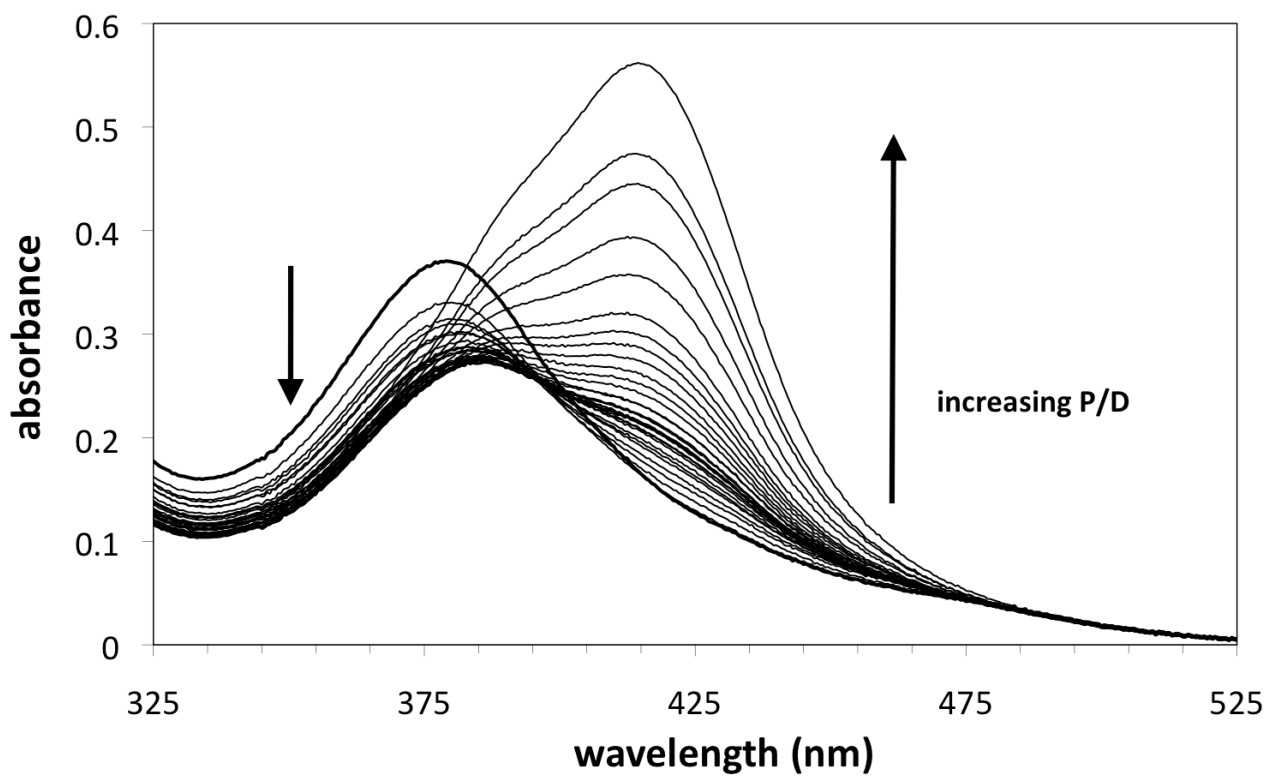
Figure S8. Absorption titrations of **PD** (top; 56 μM) and **MePD** (bottom; 18 μM) in 5 mM phosphate/1% DMSO with added CT-DNA.

H. Absorption Changes as a Function of Added CT-DNA
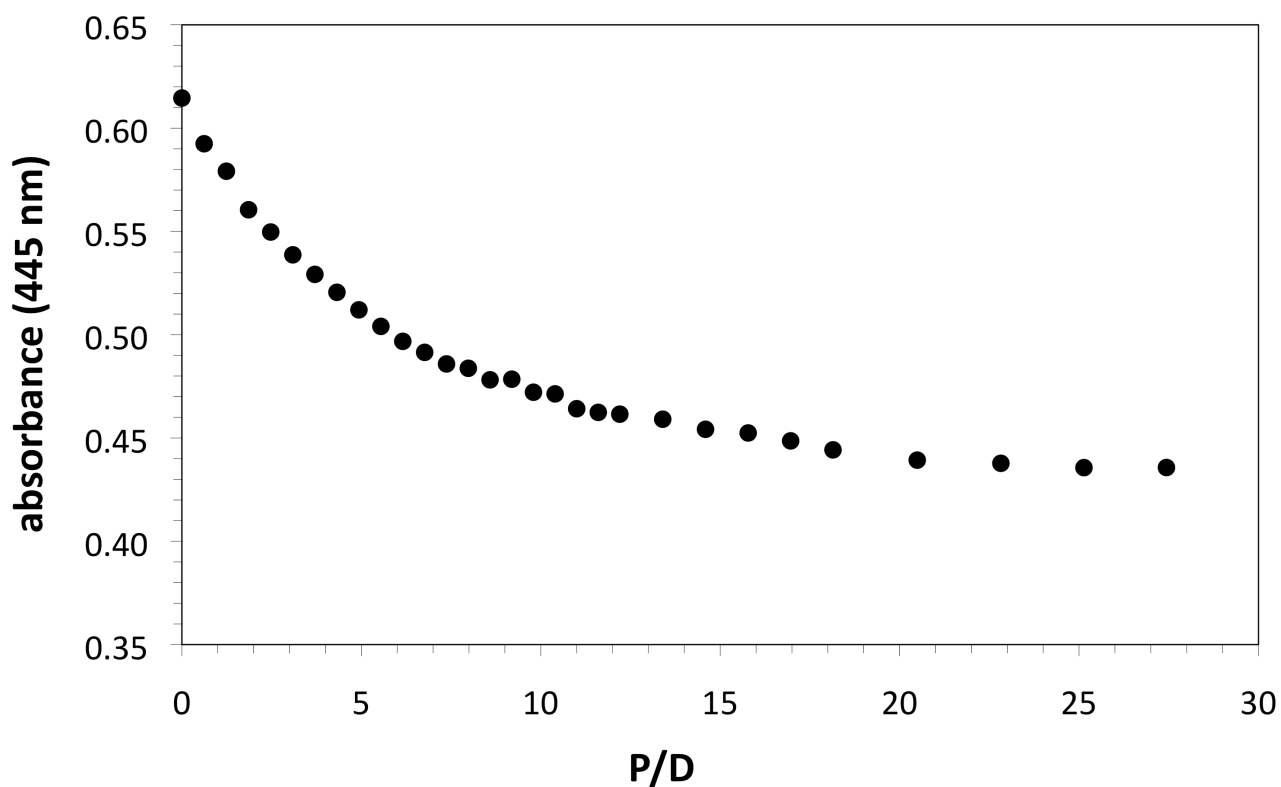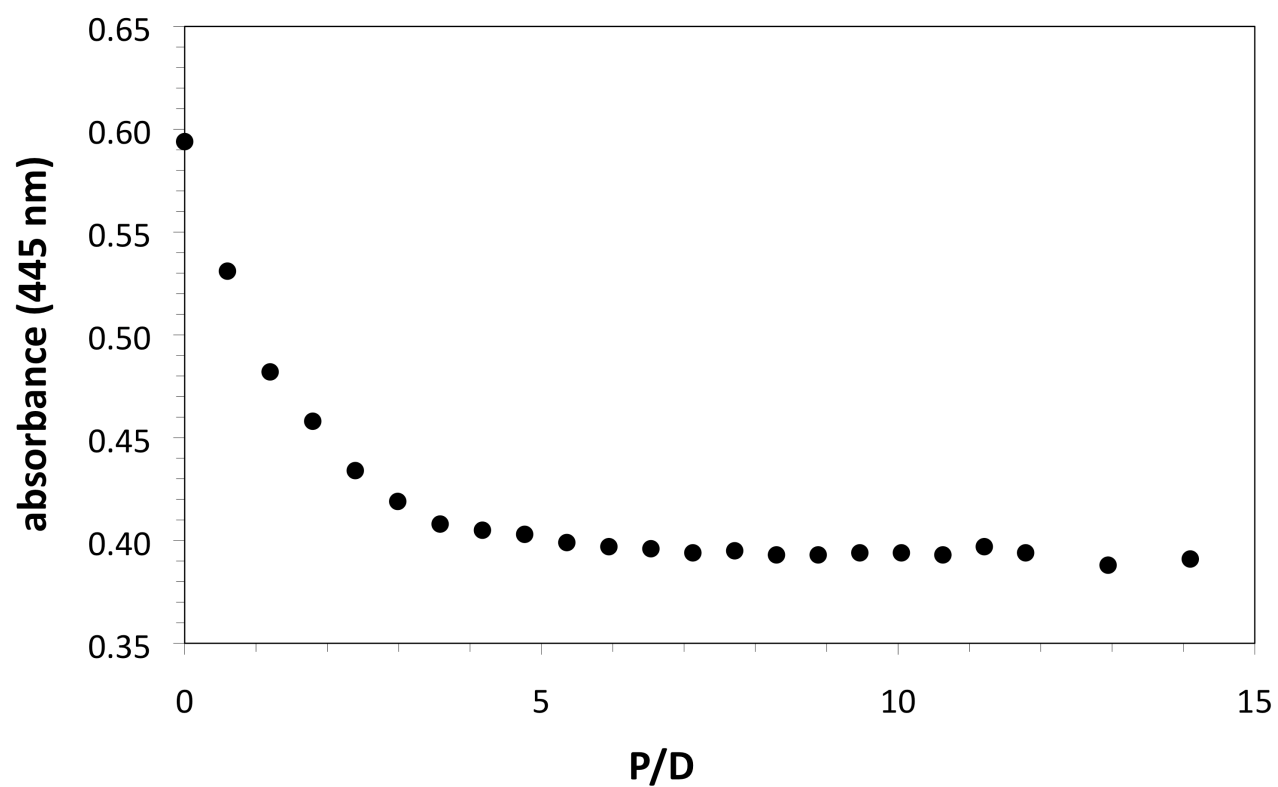
Figure S9. Absorption titrations of **Pf** in 5 mM phosphate/1% DMSO (top; 14.5 µM) and 5 mM phosphate/0.5 M NaCl/1% DMSO (bottom; 15 µM) with added CT-DNA.
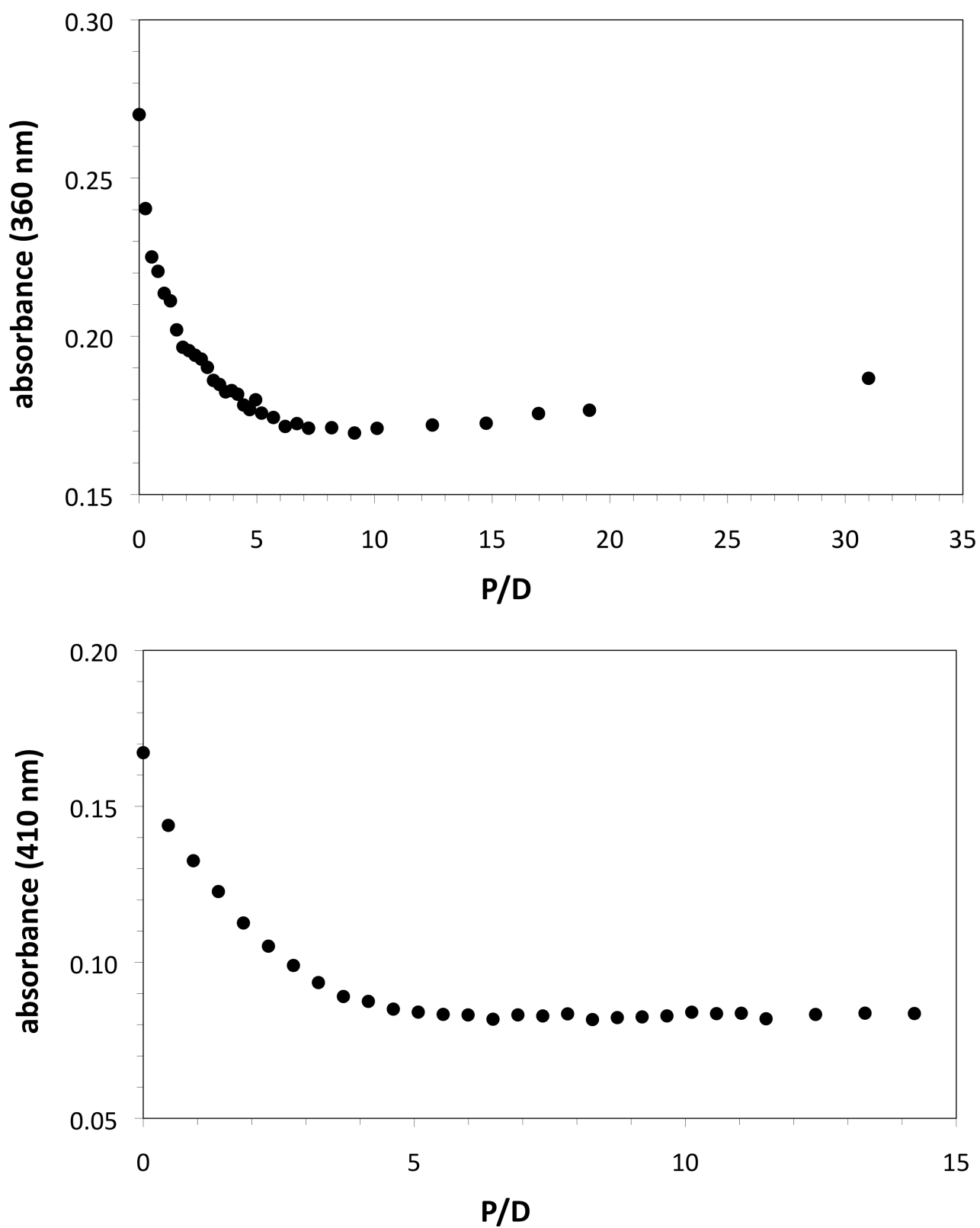
Figure S10. Absorption titrations of **PD** (top; 56 µM) and **MePD** (bottom; 18 µM)in 5 mM phosphate/1% DMSO with added CT-DNA.

I. Scatchard Plots for Binding to CT-DNA
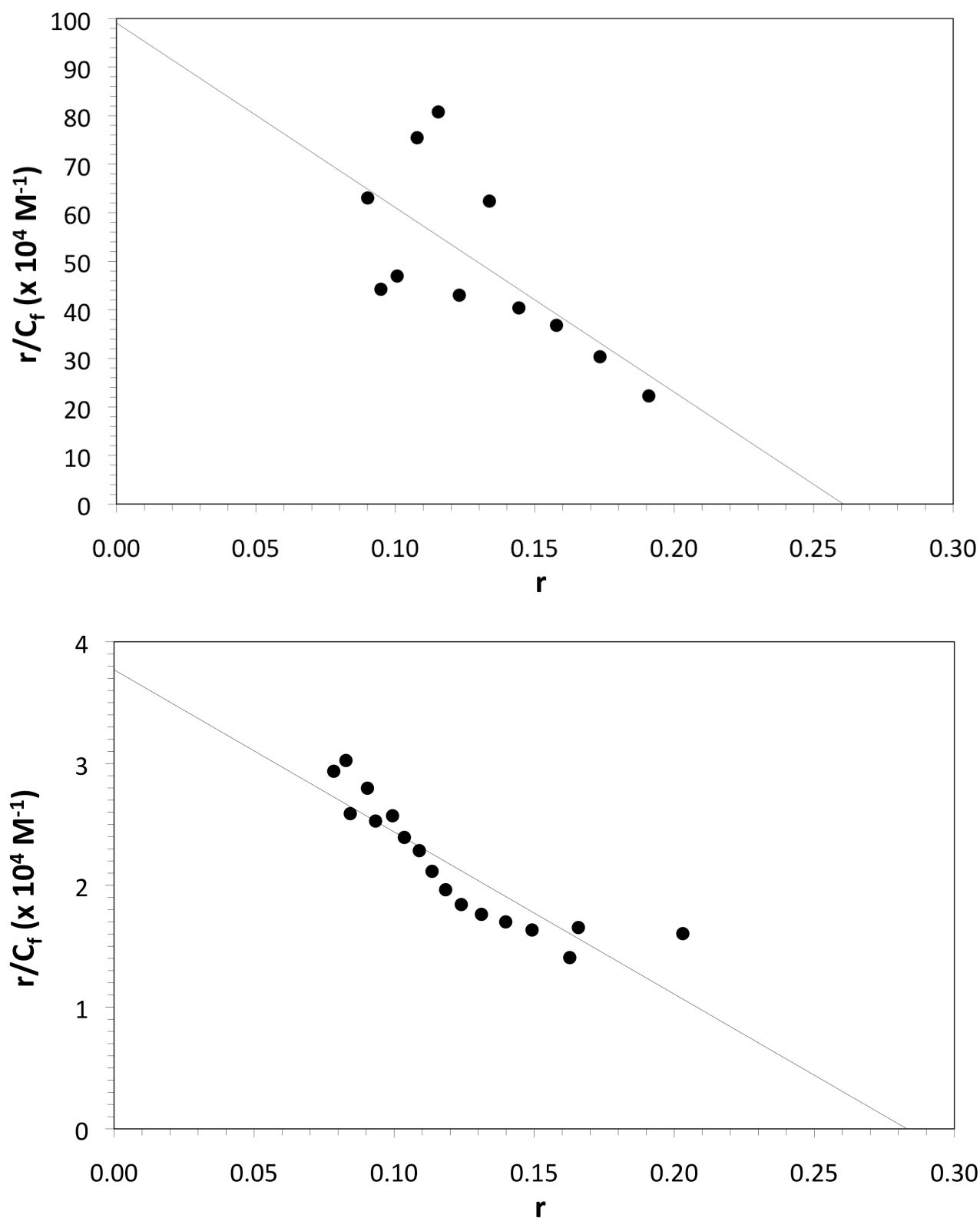
Figure S11. Scatchard plots for **Pf** in 5 mM phosphate/1% DMSO (top; 14.5 μM) and 5 mM phosphate/0.5 M NaCl/1% DMSO (bottom; 15 μM) with added CT-DNA.

Top: $K \geq 3.8 \times 10^6$ M^{-1}; n = 0.26

Bottom: $K = 1.4 \times 10^5$ M^{-1}; n = 0.28
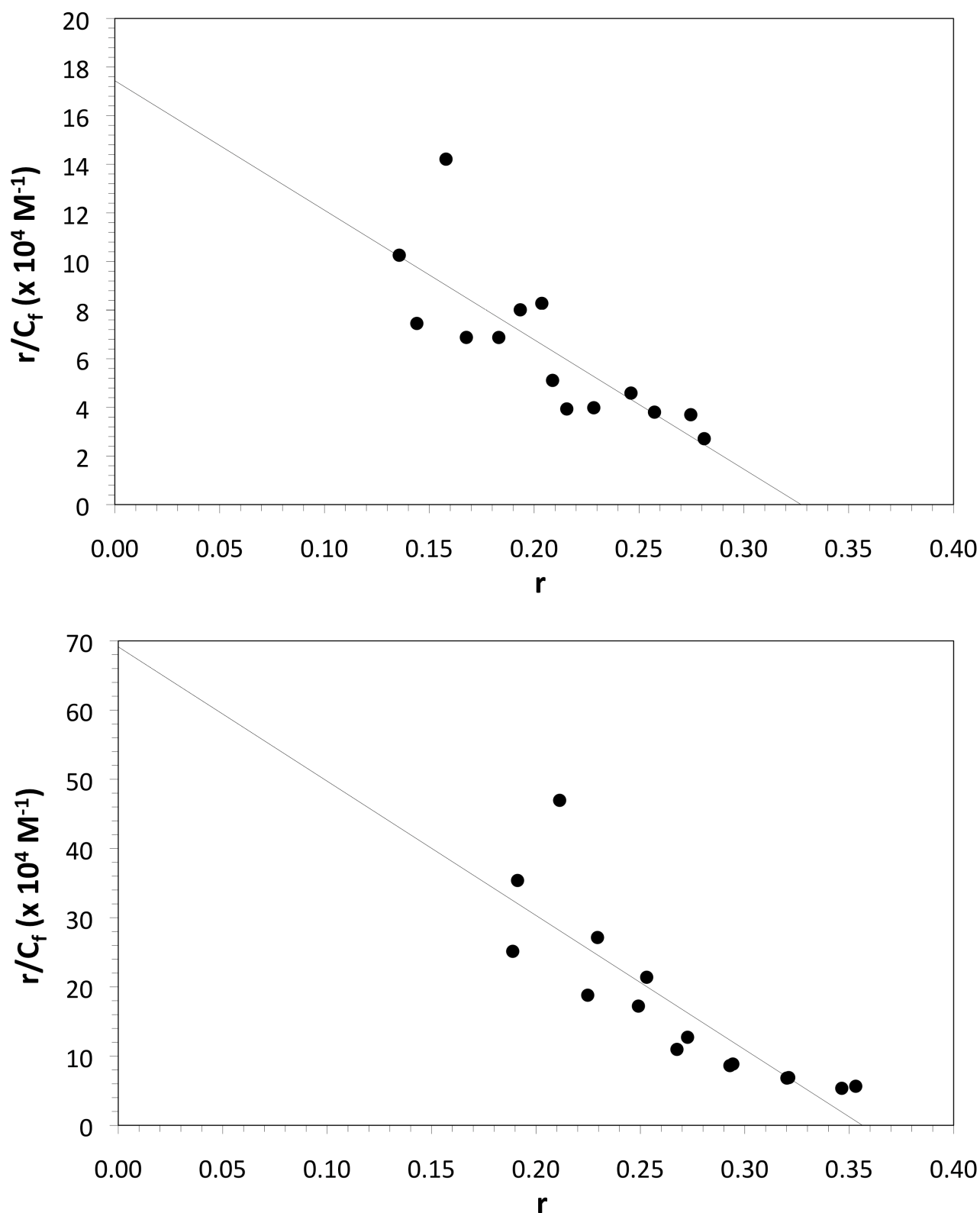
Figure S12. Scatchard plots for **PD** (top; 56 µM) and **MePD** (bottom; 18 µM) in 5 mM phosphate/1% DMSO with added CT-DNA.

Top: $K = 5.3 \times 10^5$ M^{-1}; $n = 0.33$

Bottom: $K = 2.0 \times 10^6$ M^{-1}; $n = 0.36$

J. Linear Dichroism with CT-DNA
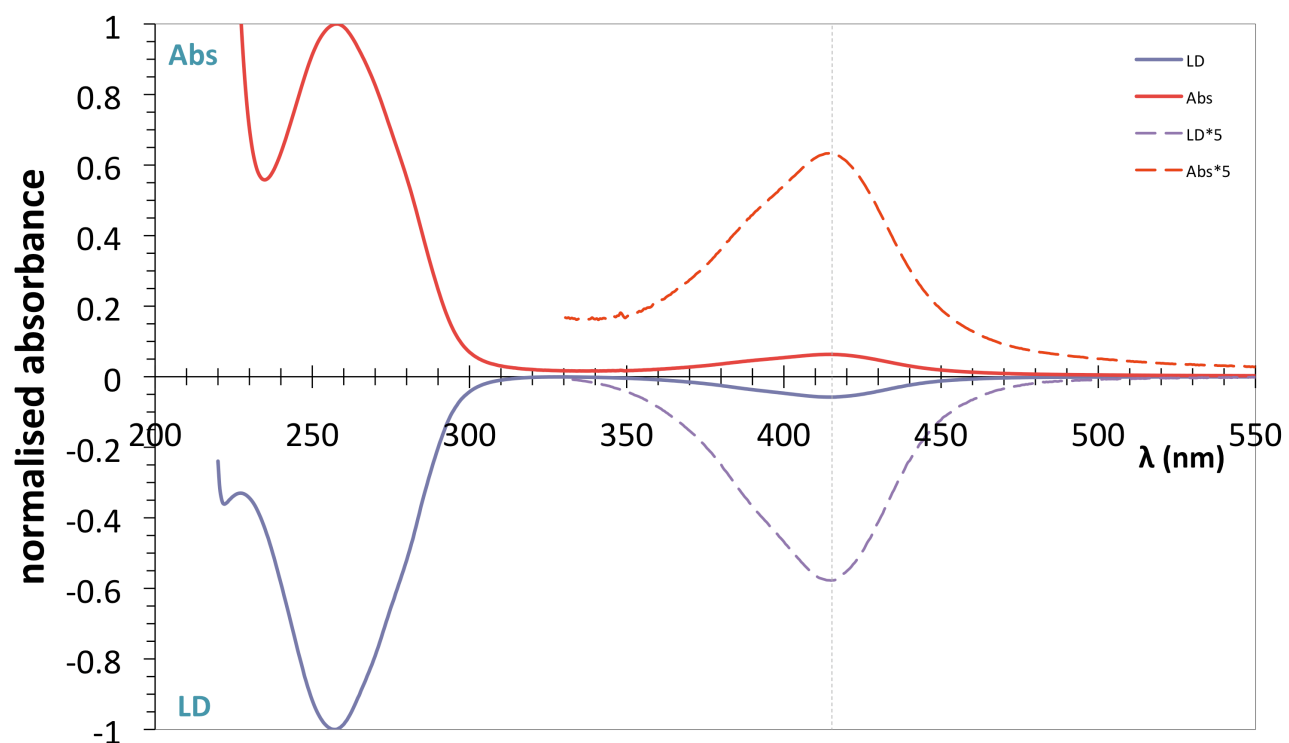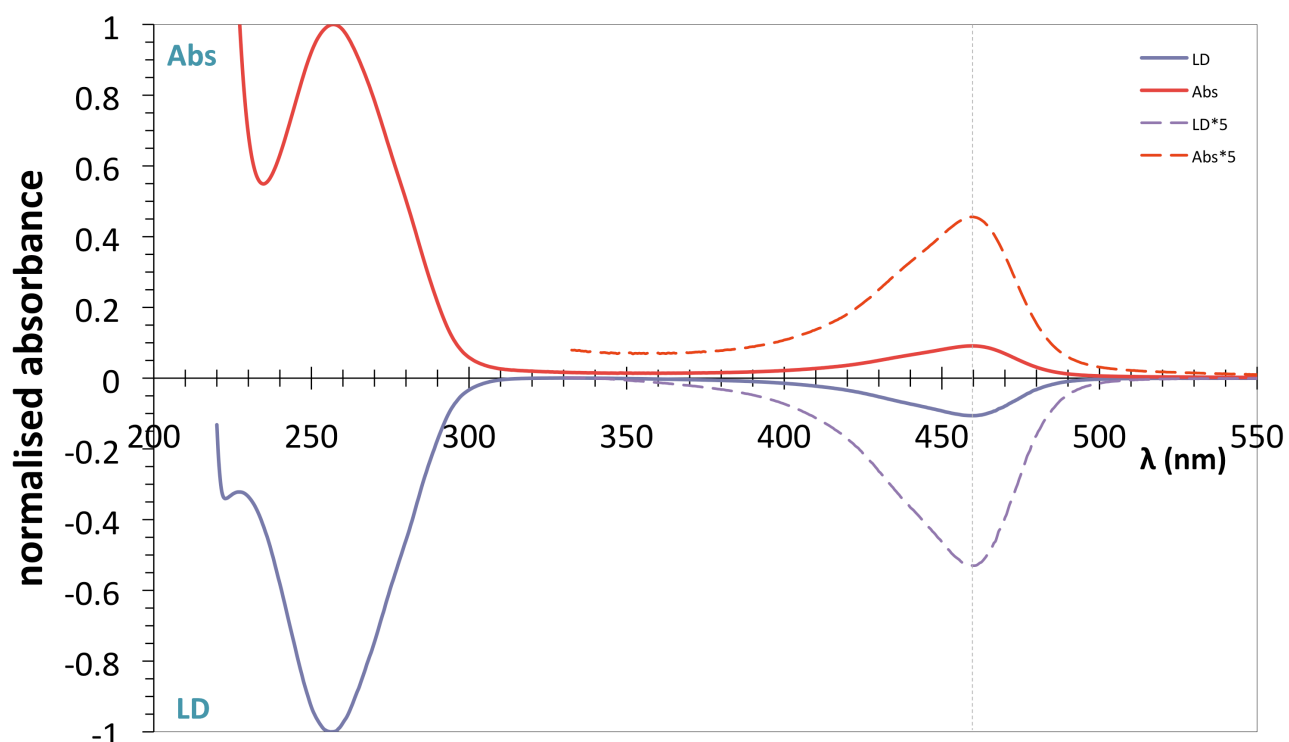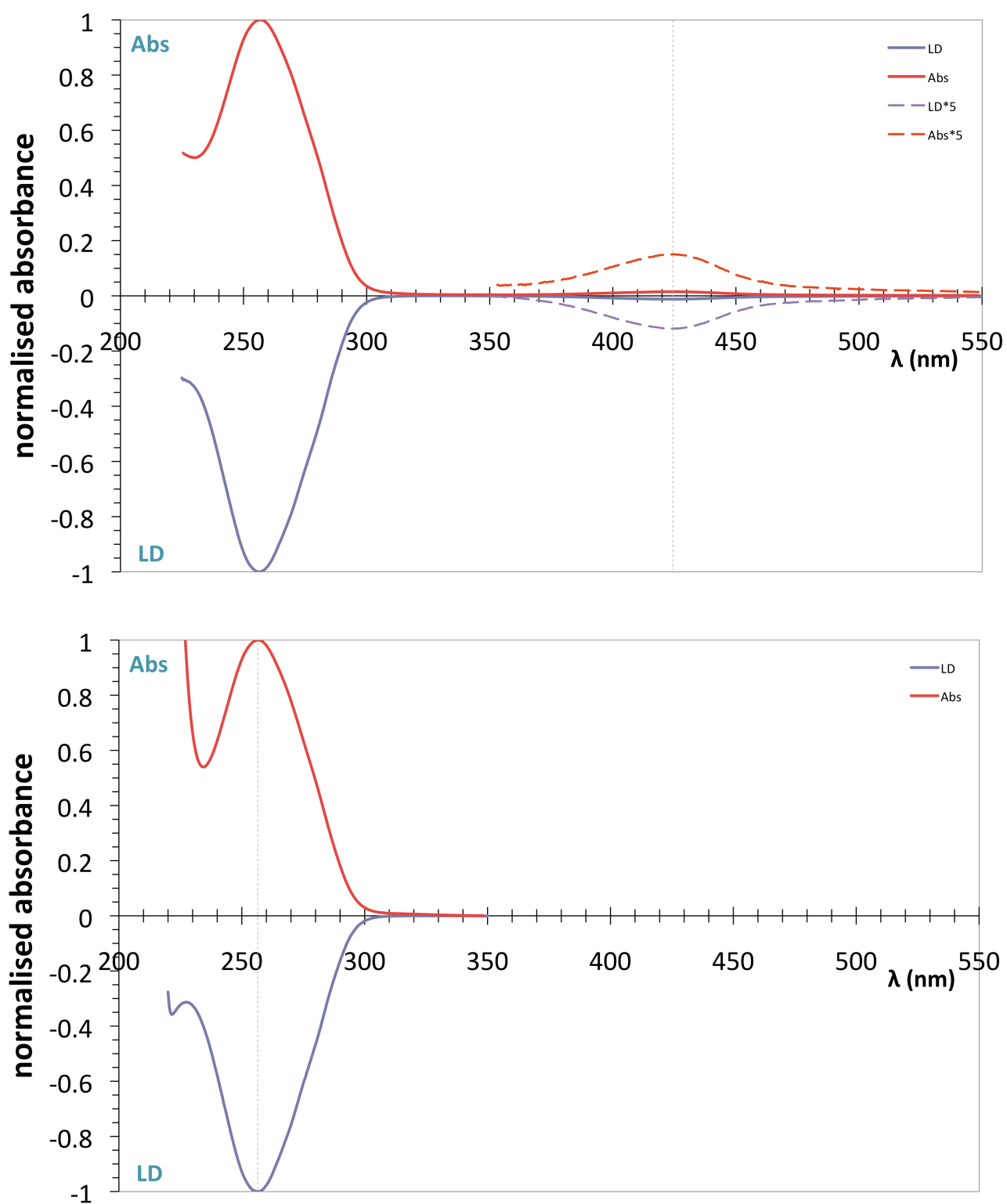
Figure S13. Linear dichroism (LD) and absorption (Abs) spectra of **Pf**, **PD** and **MePD** in the presence of CT-DNA, and CT-DNA alone (top-bottom). Data are normalised to ±1 at 258 nm. [Pf] = 16 μM; [PD] = 28 μM; [MePD] = 20 μM; [DNA] = 1 mM; 5 mM phosphate (pH 6.9)/1% DMSO. Shear gradient = 1900 s^{-1} (600 rpm rotation speed).

K. Reduced Linear Dichroism with CT-DNA
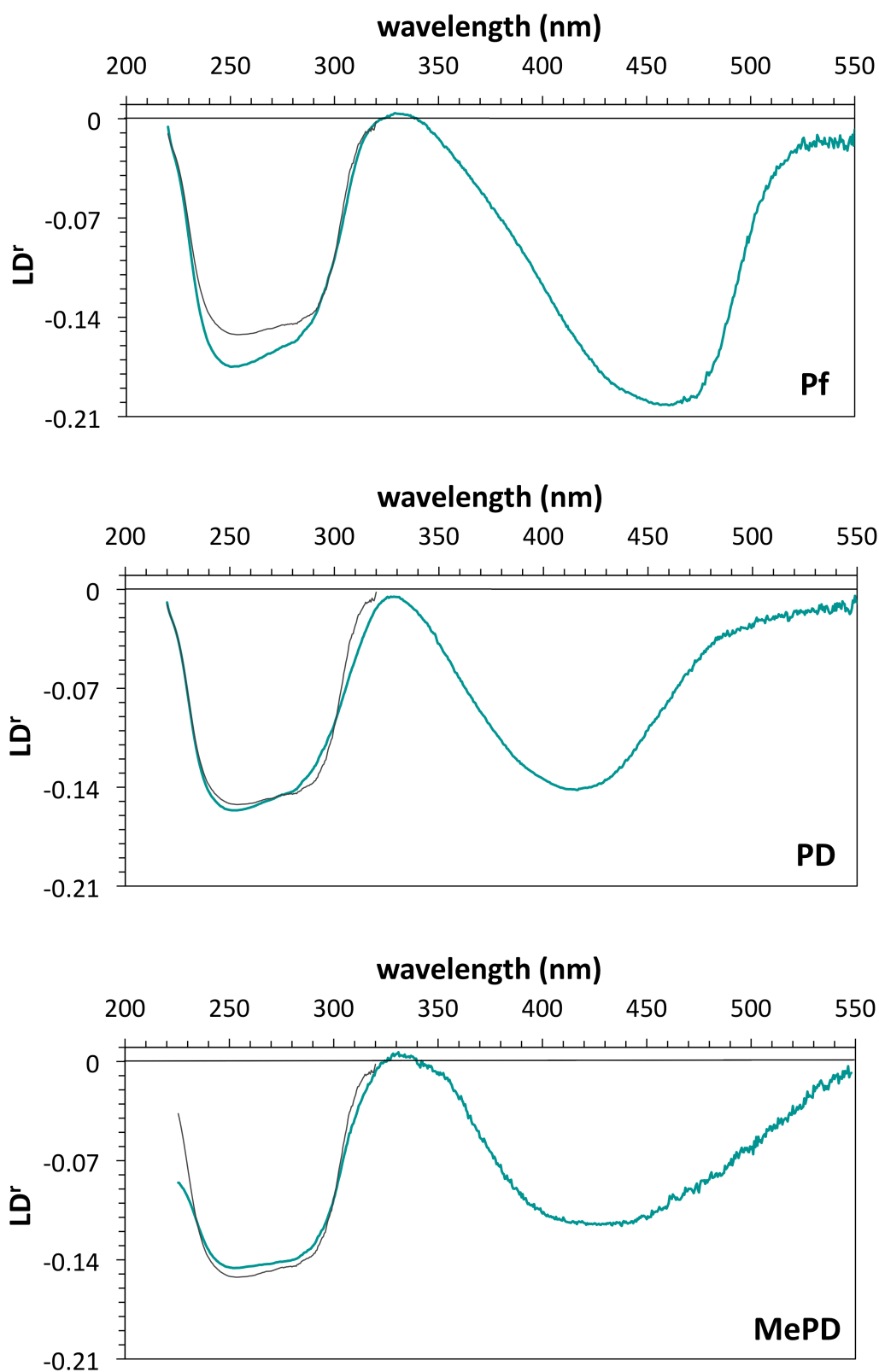
Figure S14. Reduced linear dichroism (LD^r = LD/Abs) spectra of **Pf**, **PD** and **MePD** (top-bottom) in the presence of CT-DNA. [Pf] = 16 µM; [PD] = 28 µM; [MePD] = 20 µM; [DNA] = 1 mM; 5 mM phosphate (pH 6.9)/1% DMSO. Shear gradient = 1900 s^{-1} (600 rpm rotation speed).

L. Spectroscopy of Methylated Proflavine Diazide after Click Reaction with pTP
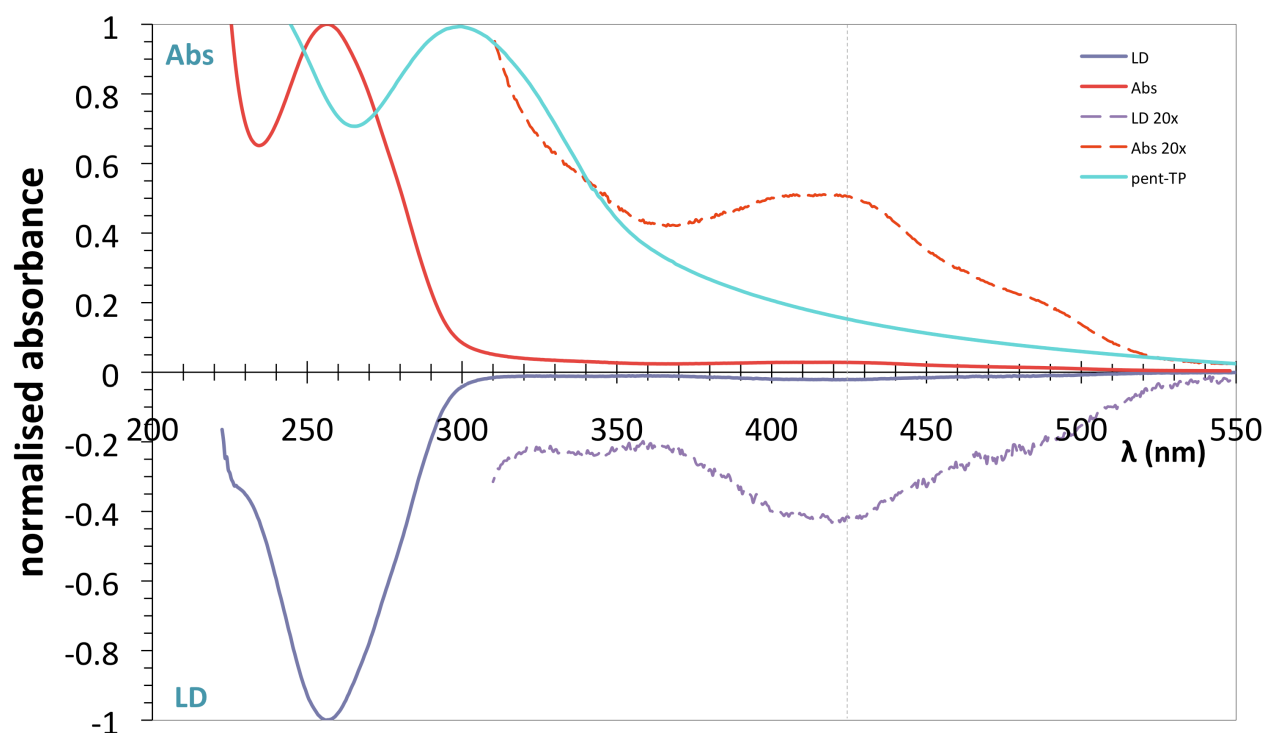
Figure S15. Linear dichroism (LD) and absorption (Abs) spectra of **MePD-pTP** with CT-DNA after click reaction in situ on DNA at high dye loading. Data are normalised to ±1 at 258 nm. [MePD] = 20 μM; [DNA] = 1 mM; [pTP] = 40 μM; 5 mM phosphate (pH 6.9)/1% DMSO. Rotation speed = 1000 rpm. The absorption spectrum of **pTP** in 5 mM phosphate (pH 6.9)/3% BuOH is shown for comparison.
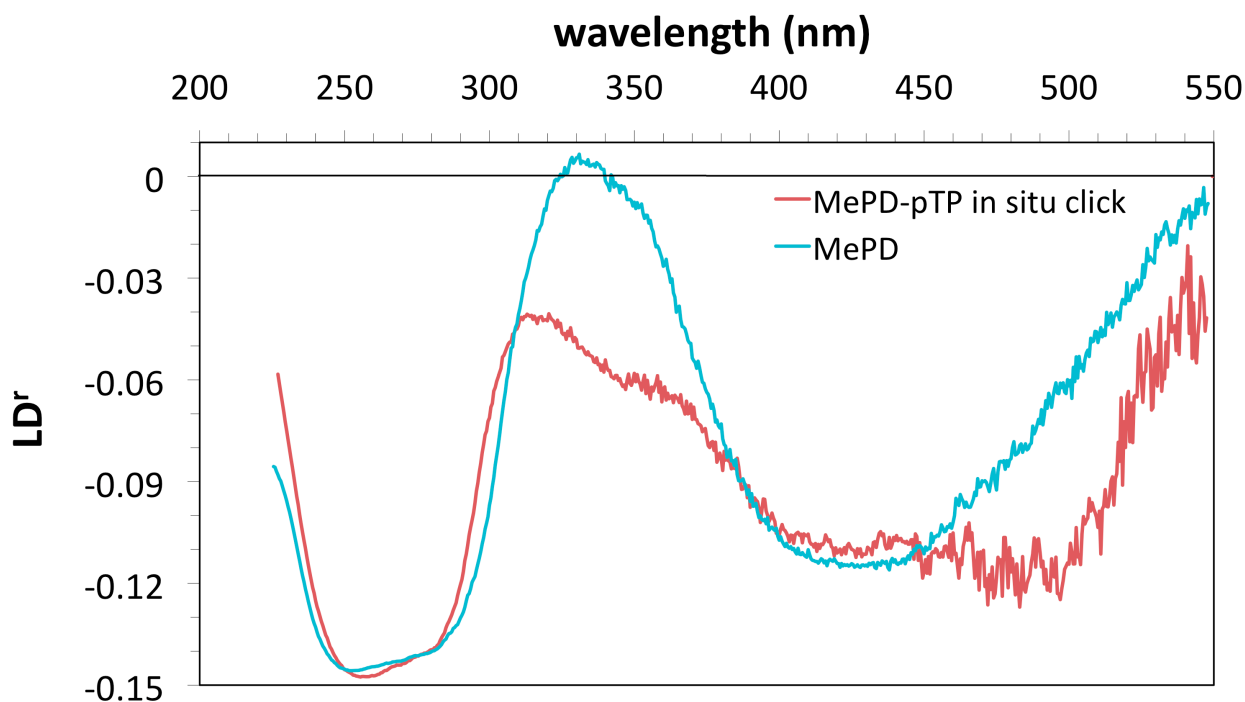
Figure S16. Reduced linear dichroism (LD^r = LD/Abs) spectra of **MePD-pTP** with CT-DNA after click reaction *in situ* on DNA at high dye loading. [MePD] = 20 μM; [DNA] = 1 mM; [pTP] = 40 μM; 5 mM phosphate (pH 6.9)/1% DMSO. Shear gradient = 3170 s^{-1} (1000 rpm rotation speed).

M. Spectroscopy of Proflavine Diazide after Click Reaction with pTP
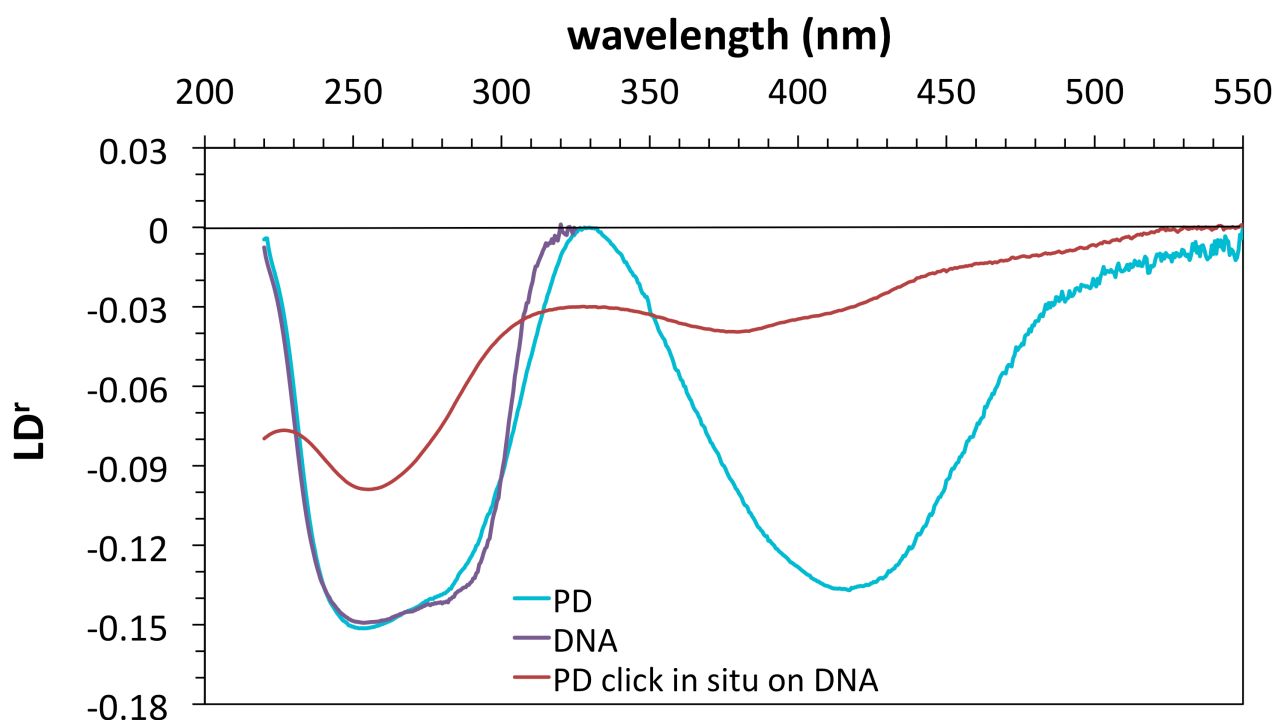
Figure S17. Reduced linear dichroism (LD^r = LD/Abs) spectra of **PD-pTP** with CT-DNA after click reaction *in situ* on DNA at high dye loading. [PD] = 60 µM; [DNA] = 240 mM; [pTP] = 120 µM; 5 mM phosphate (pH 6.9)/1% DMSO. Shear gradient = 1900 s^{-1} (600 rpm rotation speed).
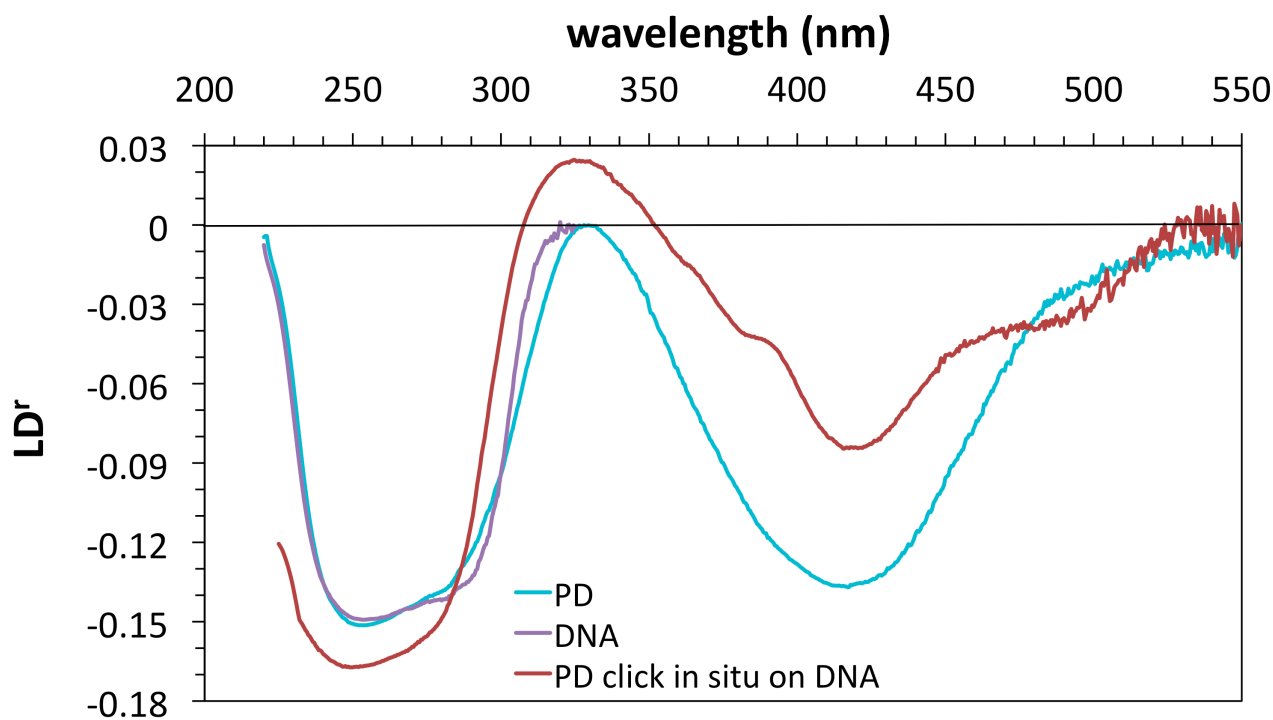
Figure S18. Reduced linear dichroism (LD^r = LD/Abs) spectra of **PD-pTP** with CT-DNA after click reaction *in situ* on DNA at low dye loading. [PD] = 7 µM; [DNA] = 1.25 mM; [pTP] = 14 µM; 5 mM phosphate (pH 6.9)/1% DMSO. Shear gradient = 1900 s^{-1} (600 rpm rotation speed).

N. Circular Dichroism with CT-DNA
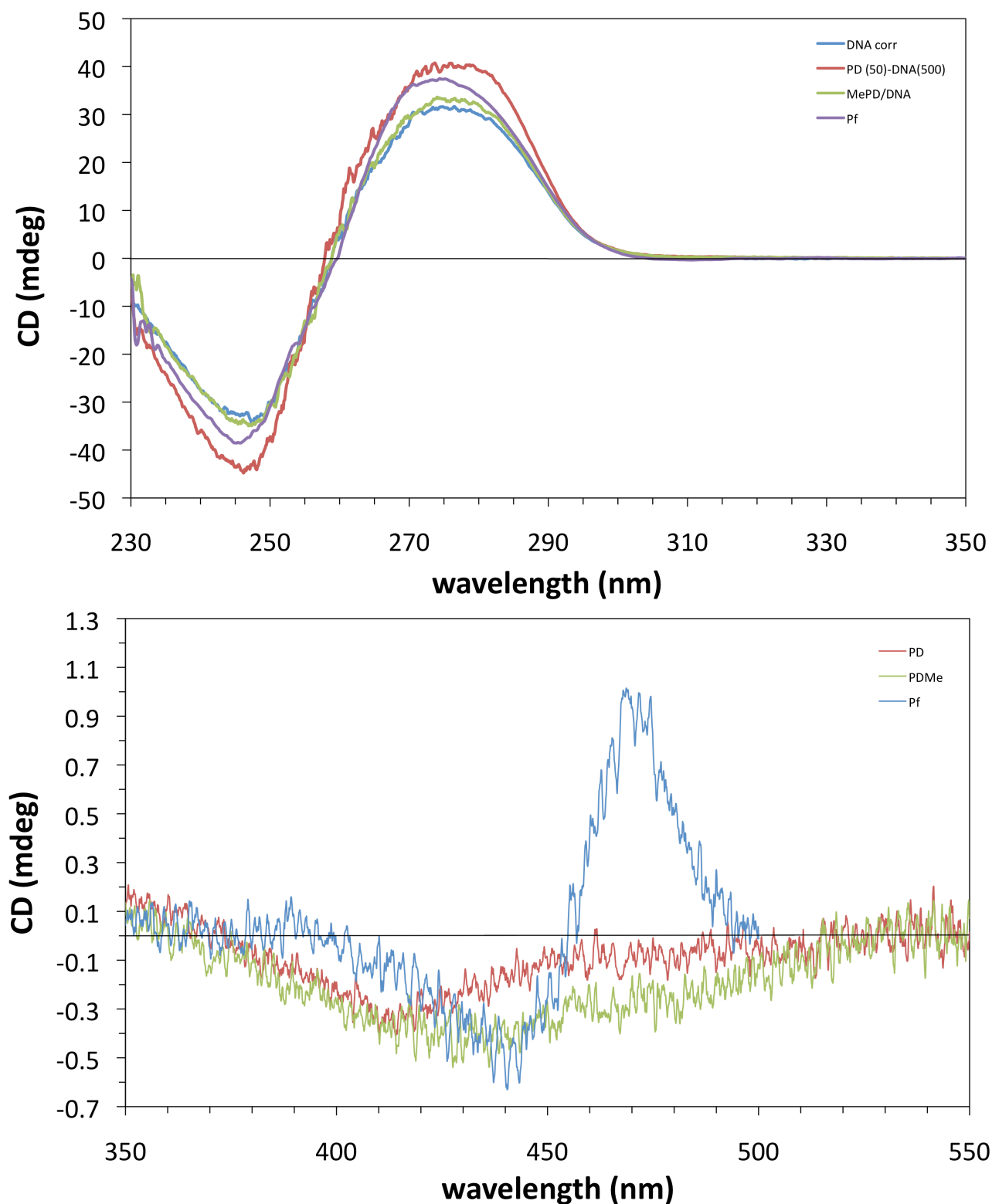
Figure S19. Circular dichroism (CD) spectra of **Pf**, **PD** and **MePD** in the presence of CT-DNA. [Pf] = 10 µM/[DNA] = 500 µM; [PD] = 50 µM/[DNA] = 1000 µM; [MePD] = 50 µM/[DNA] = 500 µM; 5 mM phosphate (pH 6.9)/1% DMSO. Raw data is presented for single runs in the UV and an average of 4 runs in the visible.

O. Viscosimetry with CT-DNA
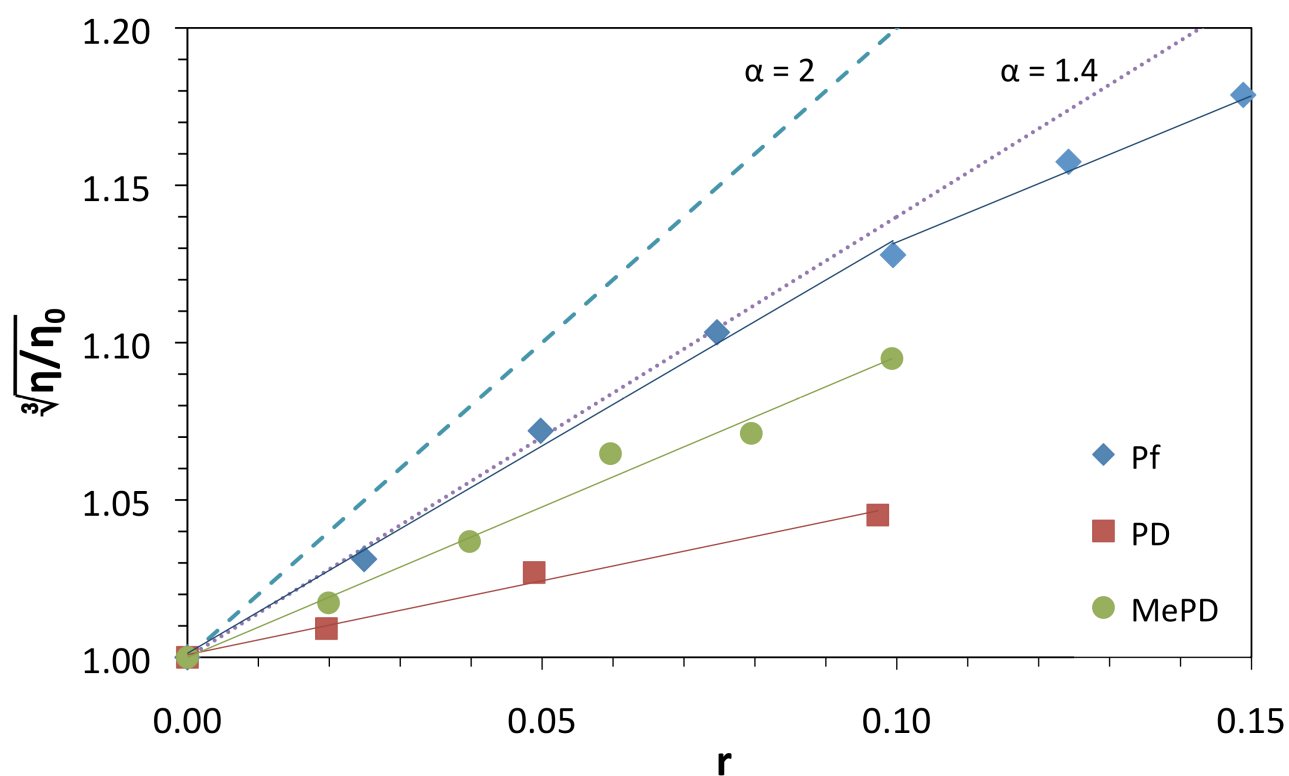
Figure S20. Relative intrinsic viscosity of CT-DNA on addition of **Pf**, **PD**, and **MePD**. 5 mM phosphate/1% DMSO; [DNA] = 300 µM; 25 °C. The dashed line represents a slope of 2 as predicted for mono-intercalation with rodlike DNA. The dotted line represents a slope of 1.4 as predicted for mono-intercalation with random coil DNA.

P. Thermal Denaturation with CT-DNA
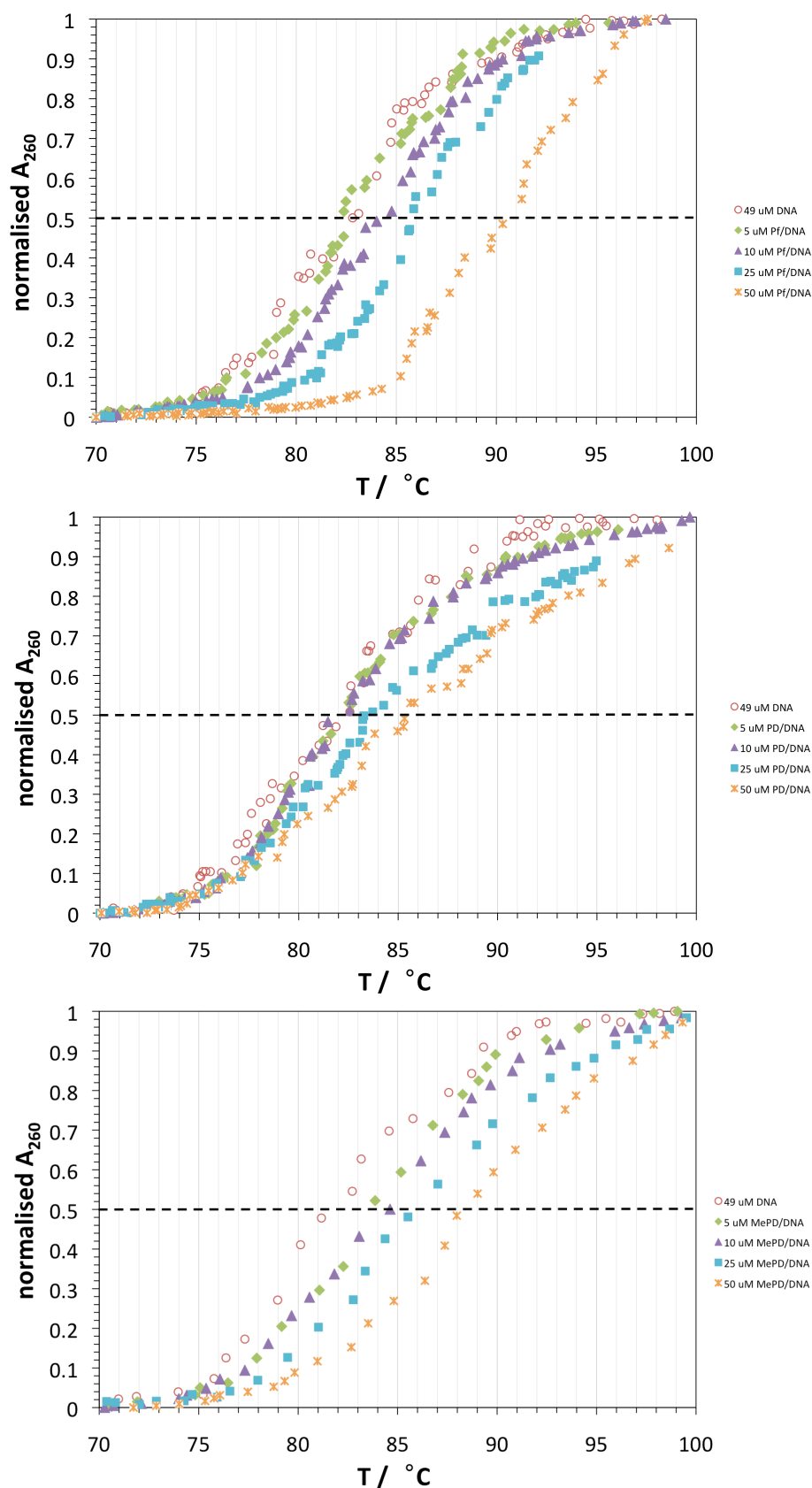
Figure S21. Thermal denaturation of CT-DNA in the presence of **Pf**, **PD** and **MePD** (top-bottom). [DNA] = 49 µM; 100 mM phosphate (pH 6.9)/1% DMSO. absorbance monitored at 260 nm.

Q. Thermal Denaturation with [poly(dA-dT)]₂
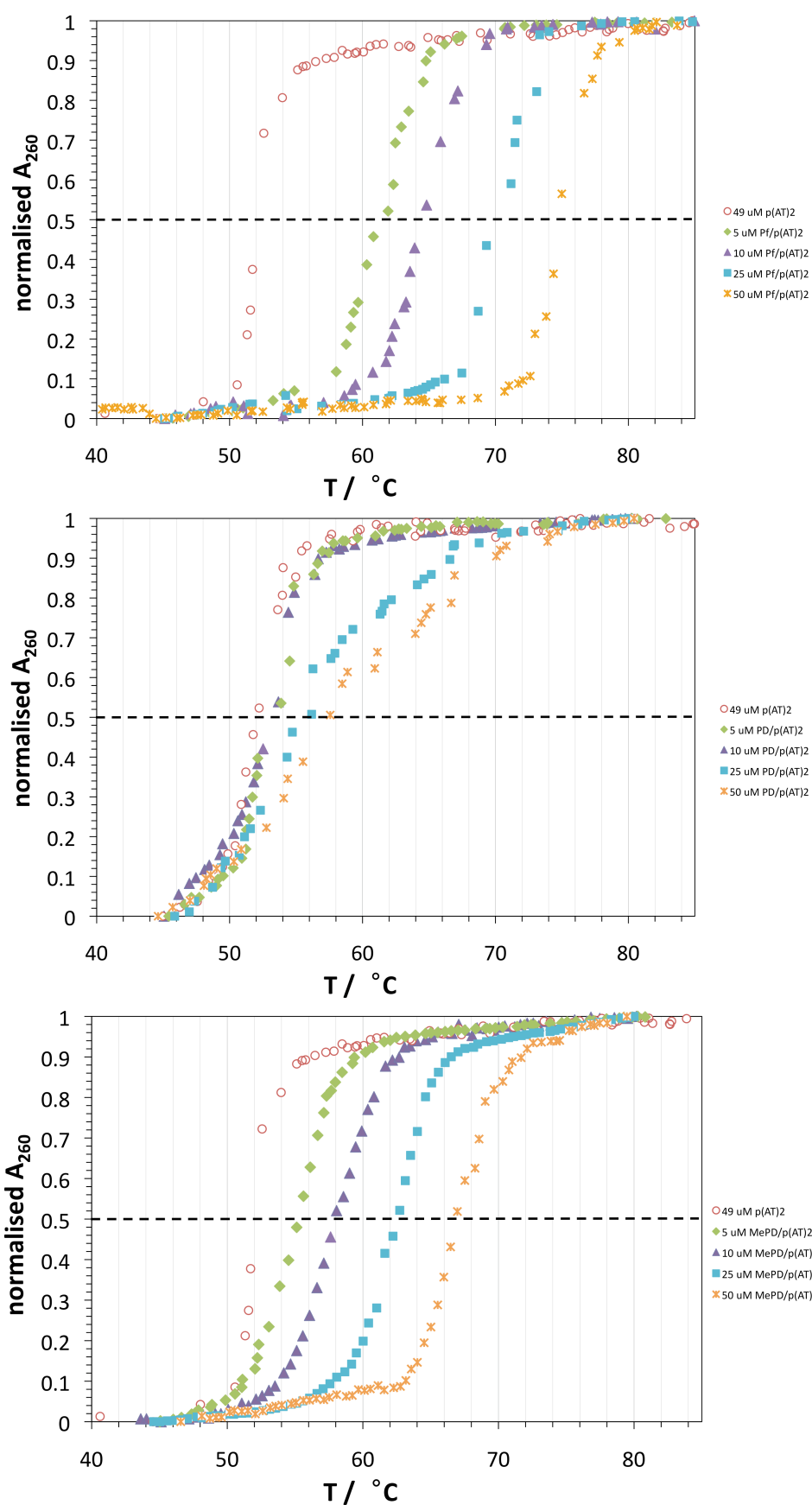
Figure S22. Thermal denaturation of [poly(dA-dT)]₂ in the presence of **Pf**, **PD** and **MePD** (top-bottom). [DNA] = 49 µM; 50 mM phosphate (pH 6.9)/1% DMSO. absorbance monitored at 260 nm.

R. Emission Spectral Titrations with CT-DNA, [poly(dA-dT)]₂, and [poly(dG-dC)]₂
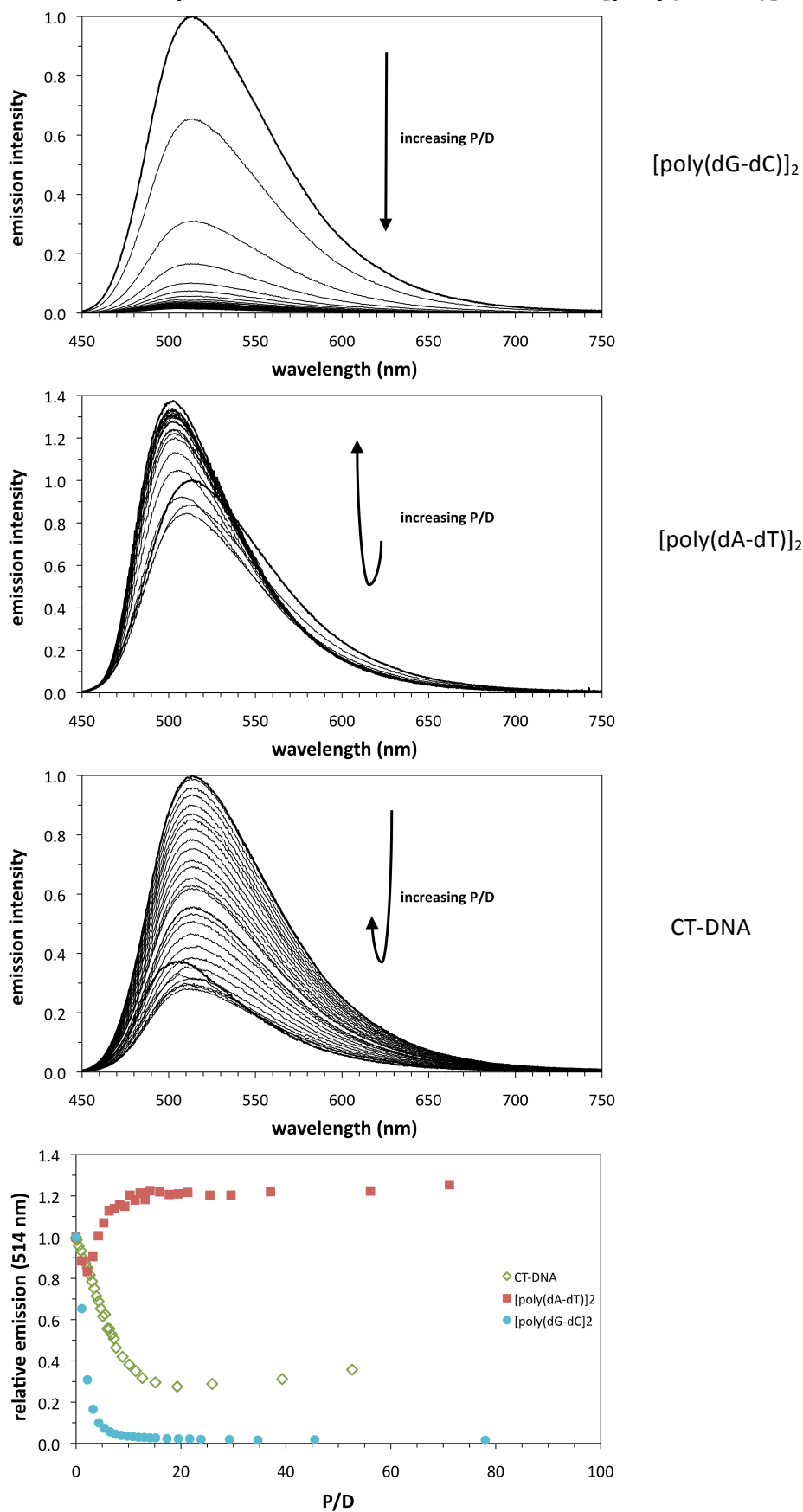
Figure S23. Emission spectra for titration of **Pf** with added [poly(dG-dC)]₂, [poly(dA-dT)]₂, CT-DNA(bottom), and comparative relative emission intensities. [dye] = 5 μM; 5 mM phosphate (pH 6.9)/1% DMSO; 21 °C. Excitation wavelength: Pf (430 nm).
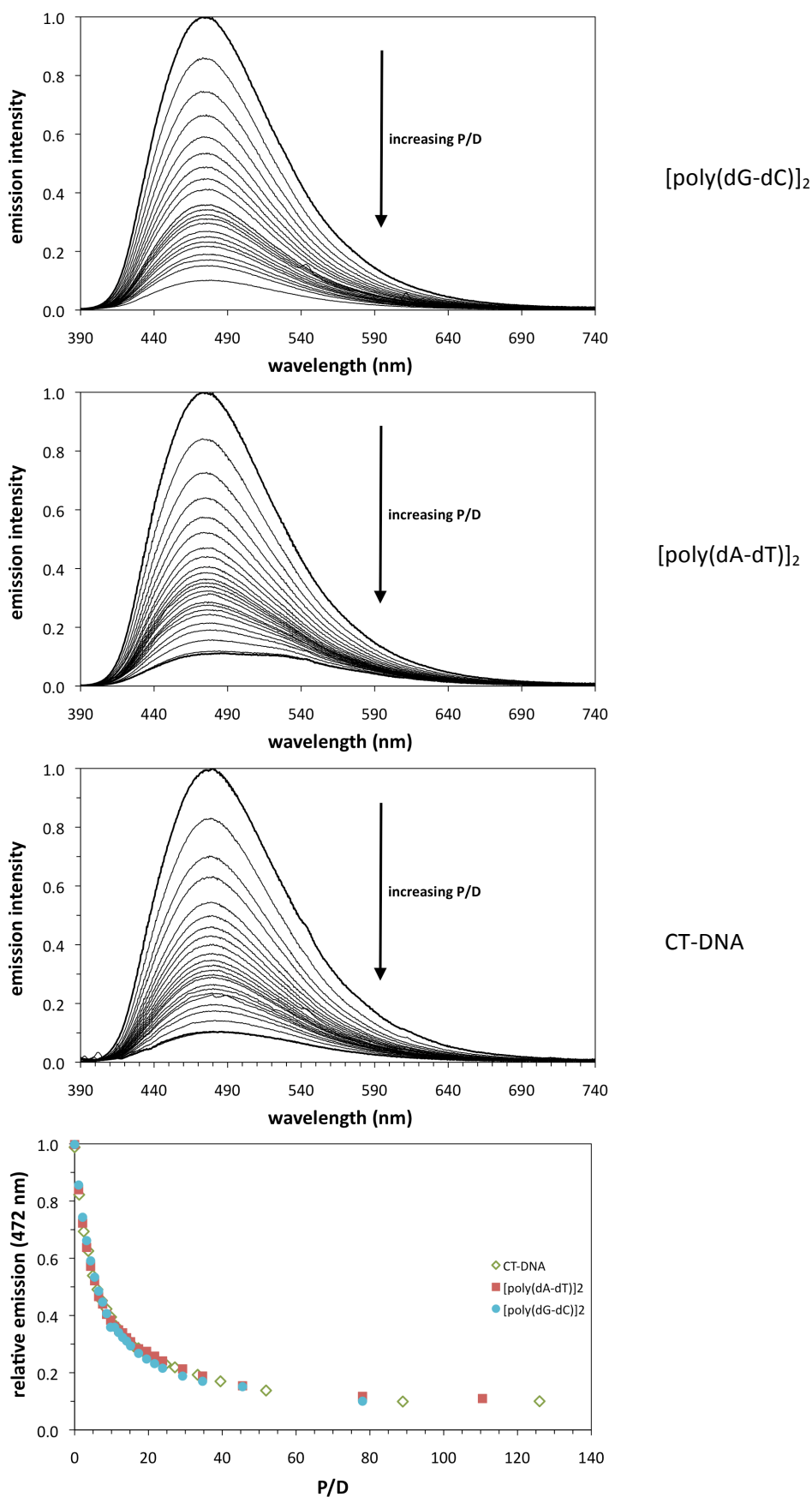
Figure S24. Emission spectra for titration of **PD** with added [poly(dG-dC)]$_2$, [poly(dA-dT)]$_2$, CT-DNA(bottom), and comparative relative emission intensities. [dye] = 5 μM; 5 mM phosphate (pH 6.9)/1% DMSO; 21 °C. Excitation wavelength: PD (380 nm).
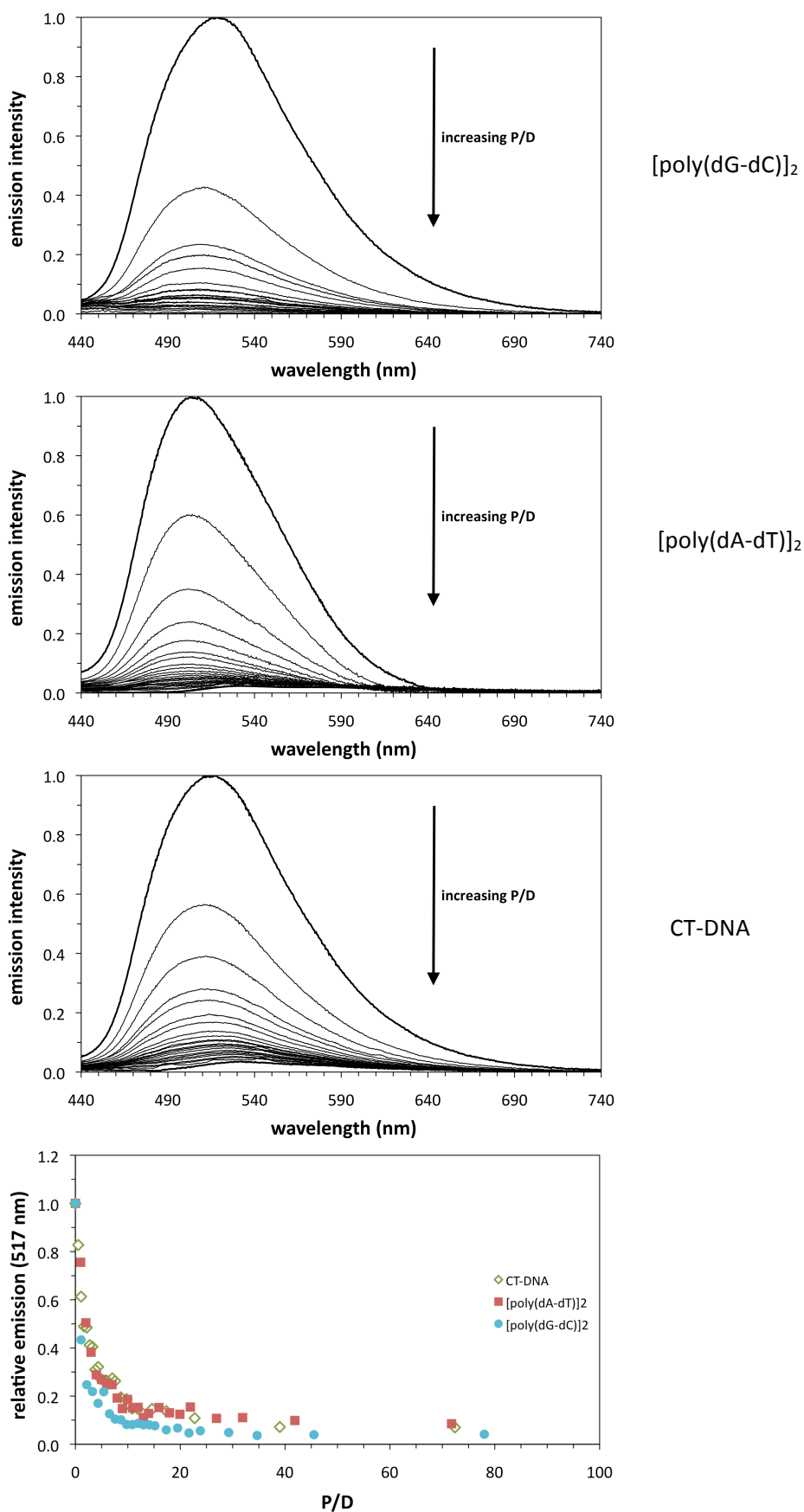
Figure S25. Emission spectra for titration of **MePD** with added [poly(dG-dC)]$_2$, [poly(dA-dT)]$_2$, CT-DNA(bottom), and comparative relative emission intensities. [dye] = 5 μM; 5 mM phosphate (pH 6.9)/1% DMSO; 21 °C. Excitation wavelength: MePD (415 nm).

S. PDB Structure of Proflavine/DNA Structure
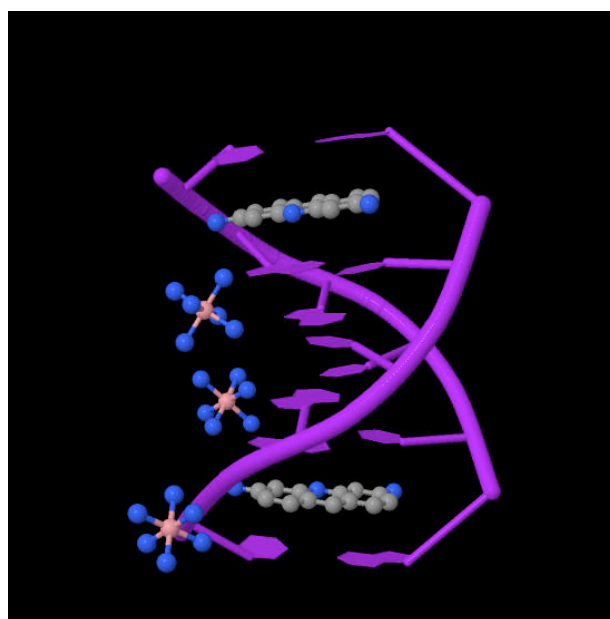
Figure S26. Crystal structure of **Pf** bound to the self-complimentary oligonucleotide 5'-[d(CGATCG)]-3', downloaded from Protein Data Bank (3FT6). Maehigashi, T.; Persil, O.; Hud, N. V.; Williams, L. D. RCSB Protein Databank ID 3FT6, DOI: 10.2210/pdb3ft6/pdb.